Physics and Astrophysics of Compact Objects

Contents

1 Topics

The study of compact objects such as white dwarfs, neutron stars, and black holes requires the interplay between nuclear and atomic physics together with relativistic field theories, e.g., general relativity, quantum electrodynamics, quantum chromodynamics, as well as particle physics. In addition to the theoretical physics aspects, studying astrophysical scenarios characterized by the presence of at least one of the above compact objects is the focus of extensive research within our group, e.g., the physics of pulsars. This research can be divided into the following topics:

- **Nuclear and Atomic Astrophysics**. We study the properties and processes occurring in compact stars in which nuclear and atomic physics have to be necessarily applied. We focus on the properties of nuclear matter under extreme conditions of density, pressure, and temperature in compact star interiors. The matter equation of state is studied in detail, considering all the interactions between the constituents within a fully relativistic framework.

- **White Dwarfs Physics and Structure**. The aim of this part of our research is to construct the white dwarf structure within a self-consistent description of the equation of state of the interior together with the solution of the hydrostatic equilibrium equations in general relativity. Non-magnetized, magnetized, non-rotating, and rotating white dwarfs are studied. The interaction and evolution of a central white dwarf with a surrounding disk, as occurred in the aftermath of white dwarf binary mergers, is also a subject of study.

- **White Dwarfs Astrophysics**. We are interested in the astrophysics of white dwarfs, both isolated and in binaries. Magnetized white dwarfs, soft gamma repeaters, anomalous X-ray pulsars, white dwarf pulsars, cataclysmic variables, binary white dwarf mergers, and type Ia supernovae are studied. The role of a realistic white dwarf interior structure is particularly emphasized.

- **Neutron Stars Physics and Structure**. We calculate the properties of the interior structure of neutron stars using realistic models of the nuclear matter equation of state within the general relativistic equilibrium equations. Strong, weak, electromagnetic, and gravitational interactions have to be jointly taken into due account within a self-consistent, fully relativistic framework. Non-magnetized, magnetized, non-rotating, and rotating neutron stars are studied.

- **Neutron Stars Astrophysics**. We study astrophysical systems harboring neutron stars, such as isolated and binary pulsars, low and intermediate X-ray binaries, and merging double neutron stars and neutron star-white dwarf binaries. Most extreme cataclysmic events involving neutron stars and their role in explaining extraordinarily energetic astrophysical events such as gamma-ray bursts are analyzed in detail.

- **Black Hole Physics and Astrophysics**. We study the role of black holes in relativistic astrophysical systems such as gamma-ray bursts, active galactic nuclei, and galactic cores. Special attention is given to applying the theory of test particle motion both in the neutral and charged case and general relativity tests.

- **Radiation Mechanisms of Compact Objects**. We here study possible emission mechanisms of compact objects such as white dwarfs, neutron stars, and black holes. We are interested in the electromagnetic, neutrino, and gravitational-wave emission in compact object magnetospheres and accretion disks surrounding them, as well as inspiraling and merging relativistic binaries (double neutron stars, neutron star-white dwarfs, white dwarf-white dwarf, and neutron star-black holes). We also study the radiation from particle acceleration near stellar-mass and supermassive black holes by surrounding electromagnetic fields.

- **Exact and Numerical Solutions of the Einstein and Einstein-Maxwell Equations in Astrophysics**. We analyze the ability of analytic exact solutions of the Einstein and Einstein-Maxwell equations to describe the exterior spacetime of compact stars such as white dwarfs and neutron stars. For this, we compare and contrast exact (analytic) solutions with numerical solutions of the stationary axisymmetric Einstein equations. The problem of matching between interior and exterior spacetime is addressed in detail. The effect of the quadrupole moment on the properties of the spacetime is also investigated. Particular attention is given to applying exact solutions in astrophysics, e.g., the dynamics of particles around compact stars and their relevance in astrophysical systems such as X-ray binaries and gamma-ray bursts.

- **Critical Fields and Non-linear Electrodynamics Effects in Astrophysics**. We study the conditions under which ultrastrong electromagnetic fields can develop in astrophysical systems such as neutron stars and the process of gravitational collapse to a black hole. The effects of non-linear electrodynamics minimally coupled to gravity are investigated. New analytic and numeric solutions to the Einstein-Maxwell equations representing black holes or the exterior field of a compact star are obtained and analyzed. The consequences on extreme astrophysical systems, for instance, gamma-ray bursts, are studied.

2 Participants

2.1 ICRANet

- C. L. Bianco (ICRANet, Italy)
- J. A. Rueda (ICRANet, Italy)
- R. P. Kerr (ICRANet, Italy; University of Canterbury, New Zeland)
- R. Ruffini (ICRANet, Italy)
- N. Sahakyan (ICRANet, Armenia)
- G. Vereschagin (ICRANet, Italy)
- S.-S. Xue (ICRANet, Italy)
- Y. Wang (ICRANet, Italy)

2.2 External collaborations: professors and senior researchers

- C. Arguelles (Universidad de La Plata, Argentina)
- E. A. Becerra (Universidad Industrial de Santander, Colombia)
- L. Becerra (Universidad Mayor, Chile)
- M. Bulla (Università degli Studi di Ferrara, Italy)
- R. Camargo (Universidade do Estado de Santa Catarina, Brazil)
- F. Cipolletta (Barcelona Supercomputing Center, Spain)

- C. Cherubini (Università Campus Biomedico, Italy)
- J. G. Coelho (Universidade Federal do Espírito Santo, Brazil)
- R. C. dos Anjos (Universidade Federal do Paraná, Brazil; Universidade Federal da Fronteira Latino-Americana, Brazil; Universidade Tecnológica Federal do Paraná, Brazil)
- A. Drago (INFN, Università degli Studi di Ferrara, Italy)
- C. L. Fryer (Los Alamos National Laboratory, USA; University of Arizona, USA)
- C. Guidorzi (Università degli Studi di Ferrara, Italy)
- D. P. Menezes (Universidade Federal de Santa Catarina, Brazil)
- M. F. Mestre (Universidad de La Plata, Argentina; Instituto de Astrofisica de La Plata, Argentina)
- R. Moradi (Institute of High-Energy Physics, China)
- L. A. Nuñez (Universidad Industrial de Santander, Colombia)
- G. Pagliara (INFN, Università degli Studi di Ferrara, Italy)
- J. P. Pereira ((Universidade Federal do Espírito Santo, Brazil)
- C. Providência (University of Coimbra, Portugal)
- H. Quevedo (Universidad Autonoma de Mexico, Mexico)
- F. Rastegarnia (Institute of High-Energy Physics, China)
- J. D. Uribe-Suarez (Universidad Santiago de Cali, Colombia)
- J. I. Zuluaga (Universidad de Antioquia, Colombia)

2.3 Postdocs

- R. V. Lobato (Universidad de los Andes, Bogotá, Colombia; Texas A&M University-Commerce, Commerce, USA)
- J. F. Rodriguez (Universidad Industrial de Santander, Colombia)
- M. F. Sousa (Universidade Federal do Paraná, Brazil)

2.4 Graduate Students

- S. V. Borges (University of Wisconsin-Milwaukee, USA)
- V. Crespi (Universidad de La Plata, Argentina)
- T. Oliveira (Universidade Federal do Espírito Santo, Brazil)
- T. Ottoni (Universidade Federal do Espírito Santo, Brazil)
- K. Kianfar (Instituto Tecnológico de Aeronáutica, Brazil)
- A. Rodrigues (Universidade Federal do Espírito Santo, Brazil)
- S. Zhang (University of Science and Technology of China, China; Università degli Studi di Ferrara, Italy)

3 Highlights 2024

The year 2024 has seen the consolidation of the scientific production trend of ICRANet on the topic of compact objects. It has been very prolific in terms of the number of publications and, more importantly, in terms of the quality and relevance of our publications.

Analyzing astrophysical sources requires the interplay of different areas of physics and astronomy. For this reason, some articles on this topic could be placed in any of the different reports. To avoid such an overlapping, the Editors discuss which section of the annual report would be the best place to include a publication with such features. In this report, we have included six published articles, one accepted for publication (in press) and one under review process for publication. The report reproduces the PDFs of the selected six already published articles in 2024. In the other reports of the annual scientific report of ICRANet, you will also find articles where the physics and astrophysics of compact objects have been relevant, e.g., the section dedicated to gamma-ray bursts and dark matter. We refer the reader to those sections for further details on those publications.

We want to highlight the strengthening of our international collaborations for these achievements. The publications summarized in this report have seen the participation of scientists from Argentina, Brazil, Chile, China, Colombia, Italy, Mexico, Portugal, Spain, and the United States.

All results have been discussed at international conferences. In particular, we highlight the presentations at the 17th Marcel Grossmann Meeting, held in Pescara on 7-12 July 2024.

4 Publications 2024

4.1 Refereed Journals

4.1.1 Printed

1. Rueda, J. A.; Becerra, L.; Bianco, C. L.; Della Valle, M.; Fryer, C. L.; Guidorzi, C.; Ruffini, R., *Long and short GRB connection*, Physical Review D 111, 023010, 2025.

   Long and short gamma-ray bursts (GRBs) are thought to arise from different and unrelated astrophysical progenitors. The association of long GRBs with supernovae (SNe) and the difference in the distributions of galactocentric offsets of long and short GRBs within their host galaxies have often been considered strong evidence of their unrelated origins. Long GRBs have been thought to result from the collapse of single massive stars, while short GRBs come from mergers of compact-object binaries. Our present study challenges this conventional view. We demonstrate that the observational properties, such as the association with SNe and the different galactic offsets, are naturally explained within the framework of the binary-driven hypernova model, suggesting an evolutionary connection between long and short GRBs.

2. S. R. Zhang, J. A. Rueda, R. Negreiros, *Can the central compact object in HESS J1731–347 be indeed the lightest neutron star observed?*, The Astrophysical Journal 978, 1 2025.

   The exceptionally low mass of $0.77^{+0.2}_{-0.17} M_{\odot}$ for the central compact object (CCO) XMMU J173203.3–344518 (XMMU J1732) in the supernova remnant (SNR) HESS J1731–347 challenges standard neutron star (NS) formation models. The nearby post-AGB star IRAS 17287–3443 ($\approx 0.6 M_{\odot}$), also within the SNR, enriches the scenario. To address this puzzle, we advance the possibility that the gravitational collapse of a rotating pre-SN iron core ($\approx 1.2 M_{\odot}$) could result in a low-mass NS. We show that angular momentum conservation during the collapse of an iron core rotating at $\approx 45\%$ of the Keplerian limit results in a mass loss of $\approx 0.3M_{\odot}$, producing a stable newborn NS of $\approx 0.9M_{\odot}$. Considering the possible spin-down, this indicates that the NS is now slowly rotating, thus fulfilling the observed mass-radius relation. Additionally, the NS's surface temperature ($\approx 2 \times 10^6$ K) aligns with canonical thermal evolution for its ≈ 4.5 kyr age. We propose the pre-SN star, likely an ultra-stripped core of $\approx 4.2M_{\odot}$, formed a tidally locked binary with IRAS 17287–3443, having a 1.43-day orbital period. The supernova led to a $\approx 3M_{\odot}$ mass loss, imparting a kick velocity $\lesssim 670$ km s^{-1}, which disrupted the binary. This scenario explains the observed 0.3 pc offset between XMMU J1732 and IRAS 17287–3443 and supports the possibility of CCOs forming in binaries, with rotation playing a key role in core-collapse, and the CCO XMMU J1732 being the lightest NS ever observed.

3. Ottoni, Tulio; Coelho, Jaziel G.; de Lima, Rafael C. R.; Pereira, Jonas P.; Rueda, Jorge A., *X-ray pulsed light curves of highly compact neutron stars as probes of scalar-tensor theories of gravity*, Eur. Phys. J. C, 84, 1337, 2024.

   The strong gravitational potential of neutron stars (NSs) makes them ideal astrophysical objects for testing extreme gravity phenomena. We explore the potential of NS X-ray pulsed lightcurve observations to probe deviations from general relativity (GR) within the scalar-tensor theory (STT) of gravity framework. We compute the flux from a single, circular, finite-size hot spot, accounting for light bending, Shapiro time delay, and Doppler effect. We focus on the high-compactness regime, i.e., close to the critical GR value $GM/(Rc^2) = 0.284$, over which multiple images of the spot appear and impact crucially the lightcurve. Our investigation is motivated by the increased sensitivity of the pulse to the scalar charge of the spacetime in such high compactness regimes, making these systems exceptionally suitable for scrutinizing deviations from GR, notably phenomena such as spontaneous scalarization, as predicted by STT. We find significant differences in NS observables, e.g., the flux of a single spot can differ up to 80% with respect to GR. Additionally, reasonable choices for the STT parameters that satisfy astrophysical constraints lead to changes in the NS radius relative to GR of up to approximately 10%. Consequently, scalar parameters might be better constrained when uncertainties in NS radii decrease, where this could occur with the advent of next-generation gravitational wave detectors, such as the Einstein Telescope and LISA, as well as future electromagnetic missions like eXTP and ATHENA. Thus, our findings suggest that accurate X-ray data of the NS surface emission, jointly with refined theoretical models, could constrain STTs.

4. Pereira, Jonas P.; Ottoni, Tulio; Coelho, Jaziel G.; Rueda, Jorge A.; de Lima, Rafael C. R., *Impact of stratified rotation on the moment of inertia of neutron stars* , Physical Review D 110, 103014, 2024.

   Rigid (uniform) rotation is usually assumed when investigating the properties of mature neutron stars (NSs). Although it simplifies their description, it is an assumption because we cannot observe the NS's innermost parts. Here, we analyze the structure of NSs in the simple case of almost rigidity, where the innermost and outermost parts rotate with different angular velocities. This is motivated by the possibility of NSs having superfluid interiors, phase transitions, and angular momentum transfer during accretion processes. We show that, in general relativity, the relative difference in angular velocity between different parts of an NS induces a change in the moment of inertia compared to that of rigid rotation. The relative change depends nonlinearly on where the angular velocity jump occurs inside the NS. For the same observed angular velocity in both configurations, if the jump location is close to the star's surface—which is possible in central compact objects (CCOs) and accreting stars—the relative change in the moment of inertia is close to that of the angular velocity (which is expected due to total angular momentum aspects). If the jump occurs deep within the NS, for instance, due to phase transitions or superfluidity, smaller relative changes in the moment of inertia are observed; we found that if it is at a radial distance smaller than approximately 40% of the star's radius, the relative changes are negligible. Additionally, we outline the relevance of systematic uncertainties that nonrigidity could have on some NS observables, such as radius, ellipticity, and the rotational energy budget of pulsars, which could explain the x-ray luminosity of some sources. Finally, we also show that nonrigidity weakens the universal I-Love-Q relations.

5. Rueda, J. A.; Ruffini, R., *Kerr black hole energy extraction, irreducible mass feedback, and the effect of captured particles charge*, The European Physical Journal C 84, 1166, 2024.

We analyze the extraction of the rotational energy of a Kerr black hole (BH) endowed with a test charge and surrounded by an external test magnetic field and ionized low-density matter. For a magnetic field parallel to the BH spin, electrons move outward(inward) and protons inward(outward) in a region around the BH poles(equator). For zero charge, the polar region comprises spherical polar angles $-60^\circ \lesssim \theta \lesssim 60^\circ$ and the equatorial region $60^\circ \lesssim \theta \lesssim 120^\circ$. The polar region shrinks for positive charge, and the equatorial region enlarges. For an isotropic particle density, we argue the BH could experience a cyclic behavior: starting from a zero charge, it accretes more polar protons than equatorial electrons, gaining net positive charge, energy and angular momentum. Then, the shrinking(enlarging) of the polar(equatorial) region makes it accrete more equatorial electrons than polar protons, gaining net negative charge, energy, and angular momentum. In this phase, the BH rotational energy is extracted. The extraction process continues until the new enlargement of the polar region reverses the situation, and the cycle repeats. We show that this electrodynamical process produces a relatively limited increase of the BH irreducible mass compared to gravitational mechanisms like the Penrose process, hence being a more efficient and promising mechanism for extracting the BH rotational energy.

6. Becerra, L. M.; Cipolletta, F.; Fryer, C. L.; Menezes, Débora P.; Providência, Constança; Rueda, J. A.; Ruffini, R., *Occurrence of Gravitational Collapse in the Accreting Neutron Stars of Binary-driven Hypernovae*, The Astrophysical Journal 976, 80, 2024.

   The binary-driven hypernova (BdHN) model proposes long gamma-ray bursts (GRBs) originate in binaries composed of a carbon-oxygen (CO) star and a neutron star (NS) companion. The CO core collapse generates a newborn NS and a supernova that triggers the GRB by accreting onto the NSs, rapidly transferring mass and angular momentum to them. This article aims to determine the conditions under which a black hole (BH) forms from NS collapse induced by the accretion and the impact on the GRB's observational properties and taxonomy. We perform three-dimensional, smoothed particle hydrodynamics simulations of BdHNe using up-to-date NS nuclear equations of state, with and without hyperons, and calculate the structure evolution in full general relativity. We assess the binary parameters leading either NS in the binary to the critical mass for gravitational collapse into a BH and its occurrence time, t_{col}. We include a nonzero angular momentum of the NSs and find that t_{col} ranges from a few tens of seconds to hours for decreasing NS initial angular momentum values. BdHNe I are the most compact (about 5 minute orbital period), promptly form a BH, and release $\gtrsim 10^{52}$ erg of energy. They form NS-BH binaries with tens of kiloyears merger timescales by gravitational-wave emission. BdHNe II and III do not form BHs, and release $\sim 10^{50}$–10^{52} erg and $\lesssim 10^{50}$ erg of energy, respectively. They form NS-NS binaries with a range of merger timescales larger than for NS-BH binaries. In some compact BdHNe II, either NS can become supramassive, i.e., above the critical mass of a nonrotating NS. Magnetic braking by a 10^{13} G field can delay BH formation, leading to BH-BH or NS–BH with tens of kiloyears merger timescales.

4.1.2 Accepted for publication (in press)

1. Ruffini, R.; Bianco, C. L.; Prakapenia, M.; Quevedo, H.; Rueda, J. A.; Zhang, S. R., *The role of the irreducible mass in repetitive Penrose energy extraction processes in a Kerr black hole*, accepted for publication in Physical Review Research, preprint: arXiv:2405.10459.

   The concept of the irreducible mass ($M_{\rm irr}$) has led to the mass-energy (M) formula of a Kerr black hole (BH), in turn leading to its surface area $S = 16\pi M_{\rm irr}^2$. This also allowed the coeval identification of the reversible and irreversible transformations, soon followed by the concepts of *extracted* and *extractable* energy. This new conceptual framework avoids inconsistencies recently evidenced in a repetitive Penrose process. We consider repetitive decays in the ergosphere of an initially extreme Kerr BH and show the processes are highly irreversible. For each decay, the particle that the BH captures causes an increase of the irreducible mass (so the BH horizon), much larger than the extracted energy. The energy extraction process stops when the BH reaches a positive spin lower limit set by the process boundary conditions. Thus, the reaching of a final non-rotating Schwarzschild BH state through this accretion process is impossible. We have assessed such processes for selected decay radii and incoming particle with rest mass 1% of the BH initial mass M_0. For $r = 1.2M$ and $1.9M$, the sequence stops after 8 and 34 decays, respectively, at a spin 0.991 and 0.857, the energy extracted has been only 1.16%, and 0.42%, the extractable energy is reduced by 17% and 56%, and the irreducible mass increases by 5% and 22%, all values in units of M_0. These results show the highly nonlinear change of the BH parameters, dictated by the BH mass-energy formula, and that the BH rotational energy is mainly converted into irreducible mass. Thus, evaluating the irreducible mass increase in any energy extraction processes in the Kerr BH ergosphere is mandatory.

4.1.3 Submitted for publication

1. Becerra, L. M.; Fryer, C. L.; Rueda, J. A.; Ruffini, R., *On the formation of compact-object binaries from binary-driven hypernovae*, submitted to The Astrophysical Journal. Preprint: arXiv:2401.15702.

   We present smoothed-particle-hydrodynamics (SPH) simulations of the binary-driven hypernova (BdHN) scenario of long gamma-ray bursts (GRBs), focusing on the binary stability during the supernova (SN) explosion. The BdHN progenitor is a binary comprised of a carbon-oxygen (CO) star and a neutron star (NS) companion. The core collapse of the CO leads to an SN explosion and a newborn NS (νNS) at its center. Ejected material accretes onto the NS and the νNS. BdHNe of type I have compact orbits of a few minutes, the NS reaches the critical mass, forming a black hole (BH), and the energy release is $\gtrsim 10^{52}$ erg. BdHNe II have longer periods of tens of minutes to hours; the NS becomes more massive, remains stable, and the system releases $\sim 10^{50}$–10^{52} erg. BdHN III have longer periods, even days, where the accretion is negligible, and the energy released is $\lesssim 10^{50}$ erg. We assess whether the system remains gravitationally bound after the SN explosion, leading to an NS-BH in BdHN I, an NS-NS in BdHN II and III, or if the SN explosion disrupts the system. The existence of bound systems predicts an evolutionary connection between the long and short GRB populations. We determine the binary parameters for which the binary remains bound after the BdHN event. For these binaries, we derive fitting formulas of the numerical results for the main parameters, e.g., the mass loss, the SN explosion energy, orbital period, eccentricity, center-of-mass velocity, and the relation between the initial and final binary parameters, which are useful for outlined astrophysical applications.

Long and short GRB connection

J. A. Rueda,[1,2,3,4,5] L. Becerra,[6,1] C. L. Bianco,[1,2,5] M. Della Valle,[7,1] C. L. Fryer,[8,9,10,11,12] C. Guidorzi,[13,14] and R. Ruffini[1,2,15,16,*]

[1]*ICRANet, Piazza della Repubblica 10, I-65122 Pescara, Italy*
[2]*ICRA, Dipartimento di Fisica, Sapienza Università di Roma, Piazzale Aldo Moro 5, I-00185 Roma, Italy*
[3]*ICRANet-Ferrara, Dipartimento di Fisica e Scienze della Terra, Università degli Studi di Ferrara, Via Saragat 1, I-44122 Ferrara, Italy*
[4]*Dipartimento di Fisica e Scienze della Terra, Università degli Studi di Ferrara, Via Saragat 1, I–44122 Ferrara, Italy*
[5]*INAF, Istituto di Astrofisica e Planetologia Spaziali, Via Fosso del Cavaliere 100, 00133 Rome, Italy*
[6]*Centro Multidisciplinario de Física, Vicerrectoría de Investigación, Universidad Mayor, Santiago de Chile 8580745, Chile*
[7]*INAF - Osservatorio Astronomico di Capodimonte, Salita Moiariello 16, I-80131 Napoli, Italy*
[8]*Center for Theoretical Astrophysics, Los Alamos National Laboratory, Los Alamos, New Mexico 87545, USA*
[9]*Computer, Computational, and Statistical Sciences Division, Los Alamos National Laboratory, Los Alamos, New Mexico 87545, USA*
[10]*The University of Arizona, Tucson, Arizona 85721, USA*
[11]*Department of Physics and Astronomy, The University of New Mexico, Albuquerque, New Mexico 87131, USA*
[12]*The George Washington University, Washington, DC 20052, USA*
[13]*INFN - Sezione di Ferrara, Via Saragat 1, 44122 Ferrara, Italy*
[14]*INAF - Osservatorio di Astrofisica e Scienza dello Spazio di Bologna, Via Piero Gobetti 101, 40129 Bologna, Italy*
[15]*Université de Nice Sophia-Antipolis, Grand Château Parc Valrose, Nice, CEDEX 2, France*
[16]*INAF, Viale del Parco Mellini 84, 00136 Rome, Italy*

(Received 17 July 2024; accepted 16 December 2024; published 6 January 2025)

Long and short gamma-ray bursts (GRBs) are thought to arise from different and unrelated astrophysical progenitors. The association of long GRBs with supernovae (SNe) and the difference in the distributions of galactocentric offsets of long and short GRBs within their host galaxies have often been considered strong evidence of their unrelated origins. Long GRBs have been thought to result from the collapse of single massive stars, while short GRBs come from mergers of compact-object binaries. Our present study challenges this conventional view. We demonstrate that the observational properties, such as the association with SNe and the different galactic offsets, are naturally explained within the framework of the binary-driven hypernova model, suggesting an evolutionary connection between long and short GRBs.

DOI: 10.1103/PhysRevD.111.023010

I. INTRODUCTION

The binary nature of short gamma-ray bursts (GRBs) was recognized and widely accepted since the first proposals based on mergers of binaries formed of two neutron stars (NS-NS) or an NS and a black hole (NS-BH; e.g., [1–4]). On the other hand, long GRBs have been mostly considered to arise from the core collapse of a single massive star into a BH (or a magnetar), a "collapsar" [5], surrounded by a massive accretion disk [6,7].

Therefore, the above theoretical models of long and short GRBs have treated them as two different and unrelated classes of astrophysical sources from different progenitors. This assumption has been further enhanced by the fact that only the long GRBs are associated with supernovae (SNe) and by the differences in the observed projected galactocentric offsets of short and long GRBs in the host galaxies. This work shows that such apparent differences are instead explained through an evolutionary connection between the long and the short GRBs that naturally arises when considering the role of binaries in the stellar evolution of massive stars.

Indeed, multiwavelength observations in the intervening years point to a key role of binaries in the evolution of massive stars and GRBs. The BeppoSAX satellite capabilities led to the discovery of the x-ray afterglow of GRBs [8],

*Contact author: jorge.rueda@icra.it

and the accurate position, which allowed the optical follow-up by ground-based telescopes, led to two major results: determining the GRB cosmological nature [9] and observing long GRBs in temporal and spatial coincidence with type Ic SNe. The first GRB-SN association was GRB 980425-SN 1998bw [10]. The follow-up by the Neil Gehrels Swift Observatory [11–13] of the optical afterglow has confirmed about twenty GRB-SN associations [14–18]. The SNe Ic associated with the long GRBs show similar optical luminosity and peak time independent of the GRB energetics, which spans nearly 7 orders of magnitude in the sample of GRB-SN (see Ref. [18], for details). Explaining the GRB-SN association is one of the most stringent constraints for GRB models.

GRB-SN systems are related to massive star explosions [19–21], and most massive stars belong to binaries [22,23]. The SN associated with long GRBs are of type Ic, and theoretical models and simulations show that they are more plausibly explained via binary interactions to aid the hydrogen and helium layers of the pre-SN star to be ejected [24–30]. Further discussion on binary and single-star model progenitors of GRB-SNe can be found in Aimuratov *et al.* [18].

The above theoretical and observational considerations suggest that long GRBs associated with SNe likely occur in binaries. A possible crucial role of binaries in GRBs had been envisaged in Fryer *et al.* [31]. The binary-driven hypernova (BdHN) model has proposed a binary progenitor for long GRBs to respond to the above exigences. In this model, the GRB-SN event arises from a binary comprising a carbon-oxygen (CO) star and an NS companion. The collapse of the iron core of the CO star leads to a newborn NS (νNS) and a type Ic SN. The explosion and expelled matter in the presence of the NS companion in a tight orbit triggers a series of physical processes that lead to the observed emission episodes (see, e.g., Refs. [18,32–38] and references therein). Most relevant is the hypercritical accretion of SN ejecta onto the νNS and NS companion [39], allowed by the copious emission of MeV neutrinos [35,40]. The accretion rate, highly dependent on the orbital period, leads to various BdHN types.

In the few-minute-orbital-period CO-NS binaries, the NS reaches the critical mass, collapsing into a rotating (Kerr) BH. These systems are called BdHN I and are the most energetic long GRBs with an energy release $\gtrsim 10^{52}$ erg. Some examples are GRB 130427A [41], GRB 180720B [42], and GRB 190114C [43,44]. The accretion rate is lower in less compact binaries with periods from tens of minutes to hours, so the NS remains stable as a more massive, fast-rotating NS. These systems, called BdHNe II, release energies $\sim 10^{50}$–10^{52} erg. An example is GRB 190829A [45]. Wide CO-NS binaries with periods of up to days, called BdHNe III, release $\lesssim 10^{50}$ erg, such as GRB 171205A [46].

The above picture predicts that BdHN events (long GRBs) may lead to three possible fates of the CO-NS binary: an NS-BH (BdHNe I) and NS-NS (BdHNe II) or two runaway NSs (most BdHNe III). The gravitational wave emission will lead the new compact-object binaries that remain bound to merge, producing short GRBs [33,47–49]. We refer to this evolutionary process as the "long-short GRB connection." We have recently performed a suite of numerical simulations to determine the binary parameters that form NS-BH, NS-NS, and those that become unbound by BdHN events [50]. Here, we use those new results to assess the long-short GRB connection from the theoretical and observational viewpoint. In particular, we analyze information from the GRB density rates, the distribution as a function of redshift, the host galaxy types, and the projected offset position of long and short GRBs.

Section II summarizes the observational constraints for the long-short GRB connection imposed by the observed GRB populations, density rates, the host galaxies, and the sources' position projected offsets. Section III shows the main results of the three-dimensional numerical simulations of the BdHN scenario relevant to the analysis of this work. Specifically, we calculate the merger times and the difference of the position offsets between the long and short GRBs, predicted by the BdHN model simulations. In Sec. IV, we discuss our results and draw the main conclusions.

II. OBSERVATIONAL CONSTRAINTS FOR THE LONG-SHORT GRB CONNECTION

A. GRB density rates

A clue for the long-short GRB connection may arise from the GRB occurrence rates. Here, we use the rates estimated in Ruffini *et al.* [47], following the method by Sun *et al.* [51]. Suppose ΔN_i bursts are detected by various instruments in a logarithmic luminosity bin from $\log L$ to $\log L + \Delta \log L$. Thus, the total local density rate between observed minimum and maximum luminosities $L_{\rm min}$ and $L_{\rm max}$ can be estimated as

$$\mathcal{R} = \sum_i \sum_{L_{\rm min}}^{L_{\rm max}} \frac{4\pi}{\Omega_i T_i} \frac{1}{\ln 10} \frac{1}{g(L)} \frac{\Delta N_i}{\Delta \log L} \frac{\Delta L}{L}, \qquad (1)$$

where Ω_i and T_i are the instrument field of view and observing time, $g(L) = \int_0^{z_{\rm max}} (1+z)^{-1} dV(z)$, being $V(z)$ the comoving volume given in a flat ΛCDM cosmology by $dV(z)/dz = (c/H_0) 4\pi d_L^2 / [(1+z^2)\sqrt{\Omega_M (1+z)^3 + \Omega_\Lambda}]$, with H_0 the Hubble constant, d_L the luminosity distance, Ω_M and Ω_Λ the cosmology matter and dark energy density parameters, and $z_{\rm max}$ is the maximum redshift at which a burst of luminosity L can be detected. We refer the reader to Sec. X in [47] for further details.

Using a sample of 233 long bursts with $E_{\rm iso} \gtrsim 10^{52}$ erg, peak energy $0.2 \lesssim E_p \lesssim 2$ MeV, and measured redshifts $0.169 \leq z \leq 9.3$, Ruffini *et al.* [47] estimated the observed (isotropic) density rate of BdHN I, $\mathcal{R}_{\rm I} \approx 0.7$–$0.9\ {\rm Gpc}^{-3}\,{\rm yr}^{-1}$. As expected from the above definitions, this rate agrees with the estimated rate of the so-called high-luminous ($L \gtrsim 10^{50}\ {\rm erg\,s}^{-1}$) long GRBs, e.g., 0.6–1.9 [52] and 0.7–0.9 ${\rm Gpc}^{-3}\,{\rm yr}^{-1}$ [51].

As discussed in [33], the BdHN I subclass can arise from a small subset of the ultrastripped binaries. The rate of ultrastripped binaries, $\mathcal{R}_{\rm USB}$, is expected to be 0.1%–1% of the total SN Ic [53]. The rate of SN Ic (not the total core-collapse SN) has been estimated to be $\mathcal{R}_{\rm SNIc} \approx 2.6 \times 10^4\ {\rm Gpc}^{-3}\ {\rm yr}^{-1}$ (see, e.g., [54]). This estimate is compatible with more recent estimates, e.g., $\mathcal{R}_{\rm SNIc} \sim 2.4 \times 10^4\ {\rm Gpc}^{-3}\ {\rm yr}^{-1}$ [55]. Therefore, the rate of ultrastripped binaries may be $\mathcal{R}_{\rm USB} \sim 24$–$240\ {\rm Gpc}^3\ {\rm yr}^{-1}$, which implies that ∼0.4%–4% of them may explain the BdHNe I observed population.

Turning now to the BdHNe II and III, the above method leads to the total density rate $\mathcal{R}_{\rm II+III} \approx 66$–$145\ {\rm Gpc}^{-3}\,{\rm yr}^{-1}$, which was estimated in [47] with a sample of 10 long bursts with $E_{\rm iso} \lesssim 10^{52}$ erg, $4 \lesssim E_p \lesssim 200$ keV, and measured redshifts $0.0085 \leq z \leq 1.096$. As expected from the above features, this rate agrees with independent estimates of the density rate of the so-called low-luminous ($L \lesssim 10^{48}\ {\rm erg\,s}^{-1}$) long GRBs, e.g., 148–677 [56], 155–1000 [54], ∼200 [57], and 99–262 ${\rm Gpc}^{-3}\ {\rm yr}^{-1}$ [51]. Therefore, the BdHNe II and III dominate the long GRB rate, i.e., $\mathcal{R}_{\rm long} \equiv \mathcal{R}_{\rm I+II+III} \approx \mathcal{R}_{\rm II+III}$.

Let us now discuss the post-BdHN binaries formed by the BdHNe I, II, and III. The ("pre-BdHN") CO-NS progenitors of BdHNe I have orbital periods of a few minutes, so most of them remain bound after the SN explosion [33,36]. The bursts from the NS-BH mergers formed after BdHNe I are expected to have compact and potentially low-mass disks, leading to very short durations. Hence, they have been called ultrashort GRBs (U-GRBs). The above properties make U-GRBs hard to detect, and it is thought that no U-GRB has been observed [33]. Thus, we can assume the rate of BdHN I as the upper limit to the U-GRBs from NS-BH mergers, i.e., $\mathcal{R}_{\rm U\text{-}GRB} \lesssim \mathcal{R}_{\rm I}$.

In BdHNe II and III, the SN can either disrupt the binary, leading to runaway NSs or, if it remains bound, to an NS-NS binary. The mergers of the NS-NS binaries are expected to produce short GRBs. As for BdHN I and II energy separatrix of $\sim 10^{52}$ erg related to the energy required to bring the NS companion to the critical mass for BH formation, in Ruffini *et al.* [47,48], two subclasses of short bursts from NS-NS mergers have been distinguished. The mergers that overcome the NS critical mass, so those forming a BH, should release an energy $\gtrsim 10^{52}$ erg. These systems have been called authentic short GRBs (S-GRBs). The NS-NS mergers leading to a stable, massive NS have been called short gamma-ray flashes (S-GRFs) and release $\lesssim 10^{52}$ erg. It has been there estimated that $\mathcal{R}_{\rm S\text{-}GRF} \approx 4$ and $\mathcal{R}_{\rm S\text{-}GRB} \approx 0.002\ {\rm Gpc}^3\,{\rm yr}^{-1}$. Hence, the S-GRFs dominate the rate of short bursts, i.e., $\mathcal{R}_{\rm short} \equiv \mathcal{R}_{\rm S\text{-}GRF} + \mathcal{R}_{\rm S\text{-}GRB} + \mathcal{R}_{\rm U\text{-}GRB} \approx \mathcal{R}_{\rm S\text{-}GRF}$. This implies that NS-NS mergers dominate the observed local short GRB rate. The above estimates agree with independent assessments of the short GRB rate (see Table 2 in [58] for a summary) and the current upper limit of AT 2017gfo kilonovalike events $< 900\ {\rm Gpc}^3\,{\rm yr}^{-1}$ [59]. We refer to Mandel and Broekgaarden [60] for a recent review.

We summarize in Table I all the above information for the various BdHN and short GRB subclasses. The fact that $\mathcal{R}_{\rm long} > \mathcal{R}_{\rm short}$ supports the expectation that the SN event disrupts a non-negligible fraction of binaries. Indeed, if we require the short-burst population to derive from the long-burst population, the fraction of binaries that remain bound should be $\mathcal{R}_{\rm short}/\mathcal{R}_{\rm long} \approx 2\%$–$8\%$. Thus, the SN explosion would disrupt the 92%–98% of NS-NS binaries from BdHNe II and III. However, the latter dominates the percentage of unbound systems given their much wider pre-SN orbits [50]. Interestingly, this inferred ∼1% fraction of survived NS-NS binaries only based on the GRB rates and the BdHN prediction that short GRBs are long GRB descendants agrees with estimates from population synthesis simulations (see, e.g., [61–65] and references therein). See also Kochanek *et al.* [66], Chrimes *et al.* [67], Luitel and Rangelov [68], and Chrimes *et al.* [69] for more recent analyses. All the above has triggered new observational campaigns searching for bound or ejected companions of SN explosions (see, e.g., [69–74] and references therein).

TABLE I. Summary of some physical and observational properties of the GRB subclasses relevant for this work. The first three columns indicate the GRB subclass name and the corresponding pre-BdHN and post-BdHN binaries. In columns 4 and 5, we list the ranges of peak energy ($E_{\rm p,i}$) and isotropic energy released ($E_{\rm iso}$) (rest frame 1–10^4 keV). Columns 6 and 7 list the maximum observed redshift and the local observed rate $\mathcal{R}$ obtained in Ruffini *et al.* [47].

Subclass	Pre-BdHN	Post-BdHN	$E_{\rm p,i}$ (MeV)	$E_{\rm iso}$ (erg)	$z_{\rm max}$	$\mathcal{R}$ (${\rm Gpc}^{-3}{\rm yr}^{-1}$)
BdHN I	CO-NS	NS-BH	∼0.2–2	$\sim 10^{52}$–10^{54}	9.3	$0.77^{+0.09}_{-0.08}$
BdHN II + III	CO-NS	NS-NS	$\lesssim 0.2$	$\sim 10^{48}$–10^{52}	1.096	100^{+45}_{-34}
S-GRF	NS-NS	NS	$\lesssim 2$	$\sim 10^{49}$–10^{52}	2.609	$3.6^{+1.4}_{-1.0}$
S-GRB	NS-NS	BH	$\gtrsim 2$	$\sim 10^{52}$–10^{53}	5.52	$(1.9^{+1.8}_{-1.1}) \times 10^{-3}$
U-GRB	NS-BH	BH	$\gtrsim 2$	$\gtrsim 10^{52}$	$\lesssim z^{\rm I}_{\rm max}$	$\lesssim \mathcal{R}_{\rm I}$

B. GRB redshift distribution

In Bianco *et al.* [75], the redshift distribution of a sample of 301 GRBs observed by Swift before December 2018 was analyzed. Based on the definition of long GRB types within the BdHN scenario and that of short GRBs, the above Swift sample was subdivided into three subsamples: 216 BdHNe I, 64 BdHNe II and III, and 21 short GRBs. The redshift distribution of the BdHNe I subsample shows a single peak between $z \sim 2$ and $z \sim 2.5$ and a sort of plateau for $0.5 \lesssim z \lesssim 2$. The distribution of the subsample formed by BdHNe II and III shows a single peak around $z \sim 1$. Therefore, the distribution of BdHN I + II + III has a double-peak structure [75], which, as expected, agrees with previous analysis of the long GRB population (see, e.g., [52,76] and Fig. 8 in Grieco *et al.* [77]). The sample of short GRBs shows a single peak at $z \lesssim 0.5$. In this paper, we updated this GRB sample by considering 34 additional short GRBs until the end of 2023. The total number of short GRBs in this new sample is, therefore, 55, and the total number of GRBs in the entire sample is 335. Figure 1 shows the distributions of the BdHNe I (upper panel), BdHNe II + III (middle panel), and short GRBs (lower panel) subsamples. It shows the following qualitative features:

(i) The BdHN I population is responsible for the long GRB peak at $z_p^I \sim 2$–2.5 [75]. The BdHN II + III distribution peaks at $z_p^{\mathrm{II+III}} \approx 0.72$. One of the reasons for $z_p^{\mathrm{I}} > z_p^{\mathrm{II+III}}$ is the BdHN I higher energetics, which allows their detection at larger redshifts.

(ii) The distributions of BdHNe II + III and short GRBs show a similar shape [75]. The former is wider than the latter, and their peaks occur at slightly different redshifts. The peak of the short GRB distribution occurs at $z_p^{\mathrm{short}} \approx 0.42$, which is lower than $z_p^{\mathrm{II+III}} \approx 0.72$ by $\Delta z \approx 0.3$.

We have performed a Kolmogorov-Smirnov test on the relation hypothesis between the BdHN I, BdHN II + III, and short GRB distributions. The following conclusions can be drawn:

(i) The p-value testing the BdHN I and short GRB distribution similarity is 4.5×10^{-10}. This very low value suggests their relationship is unlikely.

(ii) The p-value testing the BdHN II + III and short GRB distribution similarity is 0.011. This much larger value indicates similarity. The difference in the position of the peaks dominates the difference in the distributions. In fact, by shifting any of the distributions by the difference of their peaks, $\Delta z \approx 0.3$, the p-value increases to ≈ 0.35.

The above results agree with our previous conclusions based on the GRB density rates: the observed population of short GRBs appears dominated by NS-NS mergers and not by NS-BH mergers, so it is not evolutionarily connected with the BdHN I population but with that of BdHNe II and III, i.e., the latter may form the NS-NS binaries that become the short GRB progenitors. This conclusion finds further support from the estimated merger times. The most recent numerical simulations of the BdHN scenario [50] lead to a wide range of merger timescales $\sim 10^4$–10^9 yr (see Fig. 2 below). The rapidly merging binaries are those of short orbital periods, so they are mostly NS-BH, which have merger times $\tau_{\mathrm{merger}} \sim 10$ kyr [33]. As we discussed above, those NS-BH are post-BdHN I products. Thus, given the peak of the BdHN I distribution at $z \sim 2$ and the NS-BH short merging times, these binaries should not be expected to contribute to the short GRB population at low redshifts.

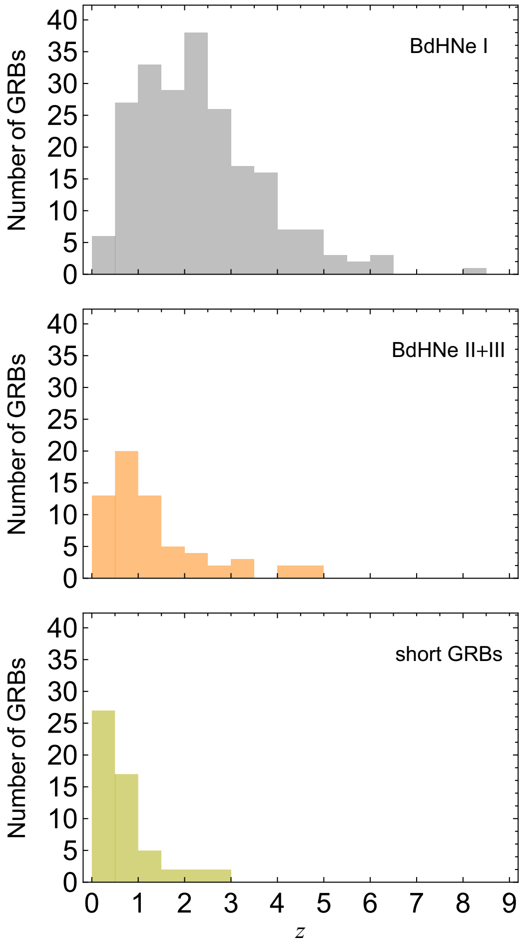

FIG. 1. Distributions of a sample of 335 GRBs as a function of the cosmological redshift. The sample is divided into three subsamples: BdHNe I (upper panel, 216 sources, gray), BdHNe II + III (middle panel, 64 sources, orange), and short GRBs (lower panel, 55 sources, green). This GRB sample is an updated version, with 34 additional short GRBs until the end of 2023, of the one considered by Bianco *et al.* [75]. We refer to Sec. VI of Bianco *et al.* [75] for additional details on the definition of the sample.

C. GRB host galaxies and projected offsets

Concerning the short GRB host galaxies, Nugent *et al.* [78] shows that 84% are star forming, like long GRB hosts. This

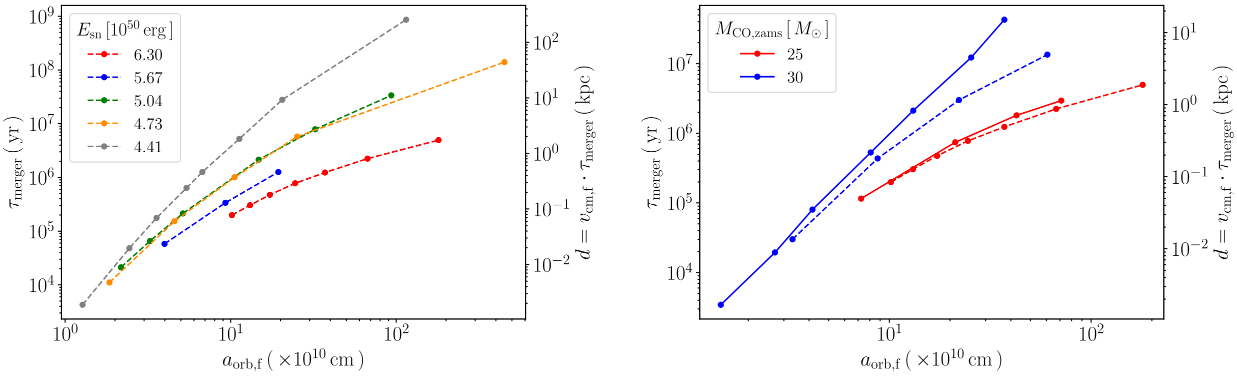

FIG. 2. Characteristic merger time by gravitational-wave emission (left axis) and distance travel (right axis) for the binary systems that remain bound (negative total energy) after a BdHN event as a function of the final binary separation. Left: the initial binary comprises a CO-evolved star from a ZAMS progenitor of $M_{\rm zams} = 25 M_\odot$ and a $2 M_\odot$ NS companion and the curves correspond to selected SN explosion energies. Right: simulations for the SN explosion energy 6.30×10^{50} erg for two CO-evolved stars from ZAMS progenitors: $M_{\rm zams} = 25 M_\odot$ (red) and $30 M_\odot$ (blue). The dashed (solid) curves correspond to symmetric (asymmetric) SN explosions (see [50] for details).

fraction decreases significantly at low redshift ($z \lesssim 0.25$), in line with galaxy evolution. Interestingly, high-mass galaxies are less abundant among the short GRB hosts than field galaxies, which becomes more evident at $z \gtrsim 0.5$ and more similar to the analogous distribution for long GRB hosts. Moreover, they found evidence for both a short delay-time population, mostly for star-forming hosts at $z > 1$, and a long delay-time one, which becomes prevalent at lower redshift in quiescent hosts.

The projected physical offsets from the host galaxy center of short GRBs are, on average, larger than those of long GRBs. Recent work by Fong *et al.* [79] including 90 short GRB host galaxies, the majority of which are robust associations, finds offsets ranging from a fraction of kiloparsec to ≈60 kpc, with a median offset value 5–8 kpc (see also O'Connor *et al.* [80]). These values must be compared with the median value of long GRBs of 1.28 kpc. Indeed, 90% of long GRB offsets are < 5 kpc [81].

The above observational properties evidence that, for long and short GRBs to share a common progenitor, the delay-time distribution of the compact-object binary mergers must include short and long values. We shall discuss these points in the next section.

III. POST-BdHN NS-NS/NS-BH TIME AND DISTANCE TRAVELED TO MERGER

We have recently presented in Becerra *et al.* [50] a new set of numerical simulations performed with the SN-SPH code [82] of the evolution of the binary system from the CO star SN explosion. The code follows the structure evolution of the νNS and the NS companion as they move and accrete matter from the SN ejecta. The initial setup has been described in detail in Becerra *et al.* [36] (see also [38]).

The code tracks the SN ejecta and point-mass particles' position and velocity. The total energy of the evolving νNS-NS system, $E_{\rm tot}$, is given by the sum of the total kinetic energy relative to the binary's center of mass and the gravitational binding energy. The system is bound if $E_{\rm tot} < 0$. In that case, the orbital separation can be determined from the binary total energy, the orbital period from Kepler's law, and the eccentric from the orbital angular momentum (see [50] for further details).

To examine the conditions under which the binary remains bound, we perform simulations for various initial orbital periods, keeping fixed the initial mass of the NS companion, $M_{\rm NS,i} = 2 M_\odot$, the zero-age main-sequence (ZAMS) of the CO star ($M_{\rm zams} = 25 M_\odot$), and the SN explosion energy. The pre-SN CO star has a total mass of $M_{\rm CO} = 6.8 M_\odot$ and leaves a νNS of $M_{\nu{\rm NS},i} = 1.8 M_\odot$. Thus, it ejects $M_{\rm ej} \approx 5 M_\odot$ in the SN explosion. We recall that $M_{\rm CO} = M_{\nu{\rm NS},i} + M_{\rm ej}$. We record the final values of the νNS mass $M_{\nu{\rm NS,f}}$, the NS companion mass $M_{\rm NS,f}$, orbital separation $a_{\rm orb,f}$, orbital period $P_{\rm orb,f}$, and eccentricity e_f. Another key quantity is the final binary center of mass velocity $v_{\rm c.m.,f}$. We end the simulation when most of the ejecta have left the system, i.e., when the mass gravitationally bound to the stars (νNS and NS) is gravitationally negligible, e.g., $\lesssim 10^{-3} M_\odot$.

The final total energy of the systems in the simulations is well fitted by the following polynomial function:

$$E_{\rm tot,f} \approx -\frac{1}{2}\frac{G M_{\rm CO} M_{\rm ns,i}}{a_{\rm orb,i}}(a + bx + cx^2), \qquad x \equiv \frac{a_{\rm orb,i} P_{\rm orb,i}}{v_{\rm sn}}, \tag{2}$$

where $v_{\rm sn} = \sqrt{2E_{\rm sn}/M_{\rm ej}}$ is an indicative average expansion velocity of the SN ejecta of mass $M_{\rm ej}$. For the present binary, $a = 0.294$, the constants b and c depend on the SN explosion energy and are listed in Table 2 of Becerra *et al.* [50]. For example, for $E_{\rm sn} = 6.3 \times 10^{50}$ erg, $b = -3.153$ and

$c = 5.219$. The maximum initial period for the system to hold bound is obtained by setting the final total energy to zero. In the present example, the energy becomes zero at $x = 0.115$, which implies $P_{\rm orb,max} \approx 7.15$ min.

The final bound systems will be compact binary systems (NS-NS or NS-BH), which will eventually merge through the emission of gravitational waves. The time to merger is given by (see, e.g., [83])

$$\tau_{\rm merger} = \frac{c^5}{G^3}\frac{5}{256}\frac{a_{\rm orb}^4}{\mu M^2}F(e), \tag{3}$$

$$F(e) = \frac{48}{19}\frac{1}{g(e)^4}\int_0^e \frac{g(e)^4(1-e^2)^{5/2}}{e(1+\frac{121}{304}e^2)}de, \tag{4}$$

where $g(e) = e^{12/19}(1-e^2)^{-1}(1+121e^2/304)^{870/2299}$, being $M = m_1 + m_2$, $\mu = m_1 m_2/M$, and e the orbit total mass, reduced mass, and eccentricity.

We have calculated the time to merger from Eq. (3), using the parameters obtained from the numerical simulations, i.e., $a_{\rm orb} = a_{\rm orb,f}$, $m_1 = M_{\nu{\rm NS,f}}$, $m_2 = M_{\rm NS,f}$, and $e = e_f$. With this information, the distance traveled by the newly formed compact-object binary from the BdHN event location to the merger site is

$$d = v_{\rm c.m.,f}\tau_{\rm merger}. \tag{5}$$

Figure 2 shows $\tau_{\rm merger}$ (left axis) and d (right axis) as a function of $a_{\rm orb,f}$. We show the results when the CO star's companion is an NS of $M_{{\rm NS},i} = 2M_\odot$, while we adopt two models for the CO star. The first is the model of the previous example, i.e., a CO-evolved star from a ZAMS progenitor of $M_{\rm zams} = 25M_\odot$; $M_{\rm CO} = M_{\nu{\rm NS},i} + M_{\rm ej} \approx 6.8M_\odot$, where $M_{\nu{\rm NS},i} \approx 1.8M_\odot$ and $M_{\rm ej} \approx 5M_\odot$. The second model is the CO star from a $M_{\rm zams} = 30M_\odot$; $M_{\rm CO} \approx 8.9M_\odot$, where $M_{\nu{\rm NS},i} = 1.7M_\odot$ and $M_{\rm ej} \approx 7.2M_\odot$. Each point in each curve corresponds to a different value of the parameter x defined in Eq. (2), so for fixed initial component masses, ejecta mass, and SN explosion energy, it explores a range of orbital periods $P_{\rm orb,i}$ (or, equivalently, $a_{\rm orb,i}$). In the right panel plot, we compare the results for a symmetric and asymmetric SN explosion of the same energy.

For the various SN explosion energies, the left panel of Fig. 2 shows a range of merger times $\tau_{\rm merger} = 10^4$–10^9 yr. Correspondingly, we obtain systemic velocities $v_{\rm c.m.,f} \sim 10$–$100~{\rm km\,s^{-1}}$ for those newly formed binaries. From the above, we find that the distance traveled by these binaries (NS-NS or NS-BH) after the BdHN event ranges $d = 0.01$–100 kpc.

The measured projected offsets of long and short GRBs in the host galaxies differ about 1 order of magnitude (see [79] and Sec. II B). While most long GRBs have offsets < 5 kpc, with a median value $\sim$1 kpc, short GRBs show an equally broad distribution but shifted to larger values by about one decade, that is, from a fraction of kiloparsec to $\approx$70 kpc. The short GRB offset median is $\approx$8 or $\approx$5 kpc for the golden sample of the most robust associations. The offsets of the short GRBs in the sample of Fig. 1 are 0.15–70.19 kpc. This range of values strikingly agrees with that obtained for the distance traveled by the NS-NS and NS-BH binaries produced by BdHNe.

It is worth mentioning that the above conclusions have been obtained within the model's hypotheses and are limited to the parameter space we have explored. Such a parameter space (e.g., CO star mass and orbital period) is not arbitrary; it corresponds to the conditions that, from our simulations, lead to the three subclasses of BdHNe (I, II, III). However, these conditions may vary according to the various physical conditions in population synthesis simulations leading to the pre-BdHN CO-NS binaries. Such simulations are still missing in the literature and represent an interesting new research topic.

IV. DISCUSSION AND CONCLUSIONS

We have reached the following conclusions:

(1) GRB rates. The inequality $\mathcal{R}_{\rm short} < \mathcal{R}_{\rm long}$ is explained as follows (see Sec. II A). First and foremost, the short GRB is dominated by NS-NS mergers, and only a subset of the BdHNe can produce NS-NS (BdHNe II and III). Thus, the subset leading to short GRBs is given by the BdHNe II and III that lead to bound NS-NS binaries [50]. Further, BdHNe I lead to NS-BH binaries. These binaries can produce short GRBs only if the BH is low enough mass; otherwise, tidal disruption of the NS by the BH is more likely to occur.

(2) Redshift distribution. First, we have shown in Sec. II B that $z_p^{\rm I}(\approx 2$–$2.5) > z_p^{\rm II+III}(\approx 0.72)$ (see also Fig. 1), which reflects the higher energetics of the BdHN I relative to BdHN II and III that allows their observation at higher redshifts. Then, we showed that the short GRB distribution peaks at $z_p^{\rm short} \approx 0.42$. The inequality $z_p^{\rm short} \ll z_p^{\rm I}$ suggests that BdHN I remnant binaries have a negligible role in the distribution of short GRBs. Indeed, in the BdHN scenario, BdHNe I produce compact-orbit NS-BH binaries, rapidly merging on timescales $< 10^5$ yr [33]. At the peak redshift of the BdHN I distribution, $z_p^I \approx 2$–2.5, such a timescale implies a negligible redshift interval, so their contribution at $z_p^{\rm short} \approx 0.42$ is negligible. On the other hand, the distribution of BdHN II + III shows similarities with that of the short GRBs, and $z_p^{\rm II+III} \approx 0.72$, which differs from $z_p^{\rm short}$ by $\Delta z = 0.3$. The merger timescales of NS-NS products by BdHN II and III (see Fig. 2) could explain the time delay (redshift difference) between the two distributions. The above analysis suggests a link between the NS-NS

remnant binaries from BdHN II and III as possible progenitors of the short GRBs. Thus, further detailed calculations are needed to deepen this connection, such as simulating the merger time-delay distribution accounting for the occurrence rate and intrinsic distribution of binary periods at different redshifts and the cosmological expansion. Such a calculation goes beyond the exploratory character of the present article and is left for future analyses.

(3) Host galaxies. Short-GRB host stellar-population ages support the picture of a short delay-time population within young and star-forming galaxies at $z > 0.25$, along with a long delay-time population which characterizes older and quiescent galaxies at lower z [78]. The above observations suggest compact-orbit NS-NS binaries should be more abundant in the former galaxies, while wide-orbit NS-NS binaries dominate in the latter. This suggestive information deserves further attention from combined cosmology and population synthesis models, which, combined with the BdHN simulations, could be used to estimate the expected galactocentric offsets and circum-merger conditions for NS-NS merging systems (see, e.g., [84]).

(4) Galactocentric offsets. The NS-NS produced by BdHNe II and III have a distribution of binary periods, eccentricities, and systemic velocities, which predict a wide distribution of systemic velocities 10–100 $\mathrm{km\,s^{-1}}$ and merger times 10^4–10^9 yr, leading to distances of 0.01–100 kpc traveled by these systems from the BdHN site to their merger site at which the short GRBs are expected to be produced (see Fig. 2). In the BdHN scenario, this distance traveled by the post-BdHN binary directly measures the distance separating the long and short GRB occurrence sites. Therefore, our modeling does not give information on the offset of the long or the short GRB but on their relative offset. Indeed, most long GRBs have offsets < 5 kpc, while short GRB offsets span from a fraction of kiloparsec to ≈ 70 kpc. This difference in the offset of about a decade agrees with the BdHN numerical simulations presented here.

There are additional consequences of the present scenario. Current distributions of merger times and large systemic postformation velocities are in tension with observations of short GRBs in dwarf galaxies. The velocities larger than the galaxy escape velocities and the long merger times predict offsets larger than observed would impede the r-process enrichment of the galaxy [85]. In this regard, our results imply two possibilities. First, a population of short-merger-time binaries (< 100 kyr) do not have time to move outside the dwarf galaxy, even for velocities larger than the galaxy's escape velocity. Second, there are binaries with longer merger times but with velocities lower than the galaxy's escape velocity. The present results, combined with future detailed population studies, may determine the relative relevance of these systems to explain these observations.

In summary, we have shown that observations of the GRB density rates and density distribution, the host galaxy types, and the sources' projected position offsets agree with the expectations from the BdHN scenario and numerical simulations. This constitutes a strong test of the surprising conclusion, as it may sound: short GRBs are long GRB descendants.

All the above implies, at the same time, the binary progenitor nature of long GRBs and, consequently, the associated preceding binary stellar evolution. Therefore, further theoretical and observational scrutiny from the GRB, x-ray binaries, population synthesis, stellar evolution, and cosmology communities is highly encouraged.

ACKNOWLEDGMENTS

The simulations were performed on LANL HPC resources provided under the Institutional Computing program.

[1] J. Goodman, Astrophys. J. Lett. **308**, L47 (1986).
[2] B. Paczynski, Astrophys. J. Lett. **308**, L43 (1986).
[3] David Eichler, Mario Livio, Tsvi Piran, and David N. Schramm, Nature (London) **340**, 126 (1989).
[4] R. Narayan, T. Piran, and A. Shemi, Astrophys. J. Lett. **379**, L17 (1991).
[5] S. E. Woosley, Astrophys. J. **405**, 273 (1993).
[6] P. Mészáros, Annu. Rev. Astron. Astrophys. **40**, 137 (2002).
[7] T. Piran, Rev. Mod. Phys. **76**, 1143 (2004).
[8] E. Costa, F. Frontera, J. Heise, M. Feroci, J. in't Zand, F. Fiore, M. N. Cinti, D. Dal Fiume, L. Nicastro, M. Orlandini *et al.*, Nature (London) **387**, 783 (1997).
[9] M. R. Metzger, S. G. Djorgovski, S. R. Kulkarni, C. C. Steidel, K. L. Adelberger, D. A. Frail, E. Costa, and F. Frontera, Nature (London) **387**, 878 (1997).
[10] T. J. Galama, P. M. Vreeswijk, J. van Paradijs, C. Kouveliotou, T. Augusteijn, H. Böhnhardt, J. P. Brewer, V. Doublier, J. F. Gonzalez, B. Leibundgut *et al.*, Nature (London) **395**, 670 (1998).

[11] S. D. Barthelmy, L. M. Barbier, J. R. Cummings, E. E. Fenimore, N. Gehrels, D. Hullinger, H. A. Krimm, C. B. Markwardt, D. M. Palmer, A. Parsons *et al.*, Space Sci. Rev. **120**, 143 (2005).
[12] D. N. Burrows, J. E. Hill, J. A. Nousek, J. A. Kennea, A. Wells, J. P. Osborne, A. F. Abbey, A. Beardmore, K. Mukerjee, A. D. T. Short *et al.*, Space Sci. Rev. **120**, 165 (2005).
[13] P. W. A. Roming, T. E. Kennedy, K. O. Mason, J. A. Nousek, L. Ahr, R. E. Bingham, P. S. Broos, M. J. Carter, B. K. Hancock, H. E. Huckle *et al.*, Space Sci. Rev. **120**, 95 (2005).
[14] S. E. Woosley and J. S. Bloom, Annu. Rev. Astron. Astrophys. **44**, 507 (2006).
[15] M. Della Valle, Int. J. Mod. Phys. D **20**, 1745 (2011).
[16] J. Hjorth and J. S. Bloom, The gamma-ray burst—supernova connection, in *Gamma-Ray Bursts*, edited by C. Kouveliotou, R. A. M. J. Wijers, and S. Woosley, Cambridge Astrophysics Series Vol. 51 (Cambridge University Press, Cambridge, England, 2012), Chap. 9, pp. 169–190.
[17] Z. Cano, S.-Q. Wang, Z.-G. Dai, and X.-F. Wu, Adv. Astron. **2017**, 8929054 (2017).
[18] Y. Aimuratov, L. M. Becerra, C. L. Bianco, C. Cherubini, M. Della Valle, S. Filippi, L. Li, R. Moradi, F. Rastegarnia, J. A. Rueda *et al.*, Astrophys. J. **955**, 93 (2023).
[19] A. S. Fruchter, A. J. Levan, L. Strolger, P. M. Vreeswijk, S. E. Thorsett, D. Bersier, I. Burud, J. M. Castro Cerón, A. J. Castro-Tirado, C. Conselice *et al.*, Nature (London) **441**, 463 (2006).
[20] C. Raskin, E. Scannapieco, J. Rhoads, and M. Della Valle, Astrophys. J. **689**, 358 (2008).
[21] P. L. Kelly, R. P. Kirshner, and M. Pahre, Astrophys. J. **687**, 1201 (2008).
[22] H. A. Kobulnicky and C. L. Fryer, Astrophys. J. **670**, 747 (2007).
[23] H. Sana, S. E. de Mink, A. de Koter, N. Langer, C. J. Evans, M. Gieles, E. Gosset, R. G. Izzard, J. B. Le Bouquin, and F. R. N. Schneider, Science **337**, 444 (2012).
[24] K. Nomoto and M. Hashimoto, Phys. Rep. **163**, 13 (1988).
[25] K. Iwamoto, K. Nomoto, P. Höflich, H. Yamaoka, S. Kumagai, and T. Shigeyama, Astrophys. J. Lett. **437**, L115 (1994).
[26] C. L. Fryer, P. A. Mazzali, J. Prochaska, E. Cappellaro, A. Panaitescu, E. Berger, M. van Putten, E. P. J. van den Heuvel, P. Young, A. Hungerford *et al.*, Publ. Astron. Soc. Pac. **119**, 1211 (2007).
[27] S.-C. Yoon, S. E. Woosley, and N. Langer, Astrophys. J. **725**, 940 (2010).
[28] N. Smith, W. Li, J. M. Silverman, M. Ganeshalingam, and A. V. Filippenko, Mon. Not. R. Astron. Soc. **415**, 773 (2011).
[29] S.-C. Yoon, Pub. Astron. Soc. Aust. **32**, e015 (2015).
[30] H.-J. Kim, S.-C. Yoon, and B.-C. Koo, Astrophys. J. **809**, 131 (2015).
[31] C. L. Fryer, S. E. Woosley, and D. H. Hartmann, Astrophys. J. **526**, 152 (1999).
[32] J. A. Rueda and R. Ruffini, Astrophys. J. Lett. **758**, L7 (2012).
[33] C. L. Fryer, F. G. Oliveira, J. A. Rueda, and R. Ruffini, Phys. Rev. Lett. **115**, 231102 (2015).
[34] L. Becerra, F. Cipolletta, C. L. Fryer, J. A. Rueda, and R. Ruffini, Astrophys. J. **812**, 100 (2015).
[35] L. Becerra, C. L. Bianco, C. L. Fryer, J. A. Rueda, and R. Ruffini, Astrophys. J. **833**, 107 (2016).
[36] L. Becerra, C. L. Ellinger, C. L. Fryer, J. A. Rueda, and R. Ruffini, Astrophys. J. **871**, 14 (2019).
[37] J. A. Rueda, R. Ruffini, L. Li, R. Moradi, J. F. Rodriguez, and Y. Wang, Phys. Rev. D **106**, 083004 (2022).
[38] L. M. Becerra, R. Moradi, J. A. Rueda, R. Ruffini, and Y. Wang, Phys. Rev. D **106**, 083002 (2022).
[39] C. L. Fryer, J. A. Rueda, and R. Ruffini, Astrophys. J. Lett. **793**, L36 (2014).
[40] L. Becerra, M. M. Guzzo, F. Rossi-Torres, J. A. Rueda, R. Ruffini, and J. D. Uribe, Astrophys. J. **852**, 120 (2018).
[41] R. Ruffini, R. Moradi, J. A. Rueda, L. Becerra, C. L. Bianco, C. Cherubini, S. Filippi, Y. C. Chen, M. Karlica, N. Sahakyan *et al.*, Astrophys. J. **886**, 82 (2019).
[42] J. A. Rueda, L. Li, R. Moradi, R. Ruffini, N. Sahakyan, and Y. Wang, Astrophys. J. **939**, 62 (2022).
[43] R. Moradi, J. A. Rueda, R. Ruffini, L. Li, C. L. Bianco, S. Campion, C. Cherubini, S. Filippi, Y. Wang, and S. S. Xue, Phys. Rev. D **104**, 063043 (2021).
[44] R. Moradi, J. A. Rueda, R. Ruffini, and Y. Wang, Astron. Astrophys. **649**, A75 (2021).
[45] Y. Wang, J. A. Rueda, R. Ruffini, R. Moradi, L. Li, Y. Aimuratov, F. Rastegarnia, S. Eslamzadeh, N. Sahakyan, and Y. Zheng, Astrophys. J. **936**, 190 (2022).
[46] Y. Wang, L. M. Becerra, C. L. Fryer, J. A. Rueda, and R. Ruffini, Astrophys. J. **945**, 95 (2023).
[47] R. Ruffini, J. A. Rueda, M. Muccino, Y. Aimuratov, L. M. Becerra, C. L. Bianco, M. Kovacevic, R. Moradi, F. G. Oliveira, G. B. Pisani *et al.*, Astrophys. J. **832**, 136 (2016).
[48] R. Ruffini, J. Rodriguez, M. Muccino, J. A. Rueda, Y. Aimuratov, U. Barres de Almeida, L. Becerra, C. L. Bianco, C. Cherubini, S. Filippi *et al.*, Astrophys. J. **859**, 30 (2018).
[49] L. M. Becerra, C. Fryer, J. F. Rodriguez, J. A. Rueda, and R. Ruffini, Universe **9**, 332 (2023).
[50] L. M. Becerra, C. L. Fryer, J. A. Rueda, and R. Ruffini, arXiv:2401.15702.
[51] H. Sun, B. Zhang, and Z. Li, Astrophys. J. **812**, 33 (2015).
[52] D. Wanderman and T. Piran, Mon. Not. R. Astron. Soc. **406**, 1944 (2010).
[53] T. M. Tauris, N. Langer, and P. Podsiadlowski, Mon. Not. R. Astron. Soc. **451**, 2123 (2015).
[54] D. Guetta and M. Della Valle, Astrophys. J. Lett. **657**, L73 (2007).
[55] C. Frohmaier, C. R. Angus, M. Vincenzi, M. Sullivan, M. Smith, P. E. Nugent, S. B. Cenko, A. Gal-Yam, S. R. Kulkarni, N. M. Law *et al.*, Mon. Not. R. Astron. Soc. **500**, 5142 (2021).
[56] E. Liang, B. Zhang, F. Virgili, and Z. G. Dai, Astrophys. J. **662**, 1111 (2007).
[57] F. J. Virgili, E.-W. Liang, and B. Zhang, Mon. Not. R. Astron. Soc. **392**, 91 (2009).
[58] M. Della Valle, D. Guetta, E. Cappellaro, L. Amati, M. T. Botticella, M. Branchesi, E. Brocato, L. Izzo, M. A. Perez-Torres, and G. Stratta, Mon. Not. R. Astron. Soc. **481**, 4355 (2018).

[59] I. Andreoni, M. W. Coughlin, E. C. Kool, M. M. Kasliwal, H. Kumar, V. Bhalerao, A. S. Carracedo, A. Y. Q. Ho, P. T. H. Pang, D. Saraogi *et al.*, Astrophys. J. **918**, 63 (2021).
[60] I. Mandel and F. S. Broekgaarden, Living Rev. Relativity **25**, 1 (2022).
[61] M. Dominik, K. Belczynski, C. Fryer, D. E. Holz, E. Berti, T. Bulik, I. Mandel, and R. O'Shaughnessy, Astrophys. J. **759**, 52 (2012).
[62] K. A. Postnov and L. R. Yungelson, Living Rev. Relativity **17**, 3 (2014).
[63] M. Dominik, E. Berti, R. O'Shaughnessy, I. Mandel, K. Belczynski, C. Fryer, D. E. Holz, T. Bulik, and F. Pannarale, Astrophys. J. **806**, 263 (2015).
[64] C. L. Fryer, K. Belczynski, E. Ramirez-Ruiz, S. Rosswog, G. Shen, and A. W. Steiner, Astrophys. J. **812**, 24 (2015).
[65] K. Belczynski, S. Repetto, D. E. Holz, R. O'Shaughnessy, T. Bulik, E. Berti, C. Fryer, and M. Dominik, Astrophys. J. **819**, 108 (2016).
[66] C. S. Kochanek, K. Auchettl, and K. Belczynski, Mon. Not. R. Astron. Soc. **485**, 5394 (2019).
[67] A. A. Chrimes, A. J. Levan, A. S. Fruchter, P. J. Groot, P. G. Jonker, C. Kouveliotou, J. D. Lyman, E. R. Stanway, N. R. Tanvir, and K. Wiersema, Mon. Not. R. Astron. Soc. **513**, 3550 (2022).
[68] S. Luitel and B. Rangelov, Res. Not. Am. Astron. Soc. **6**, 13 (2022).
[69] A. A. Chrimes, A. J. Levan, J. J. Eldridge, M. Fraser, N. Gaspari, P. J. Groot, J. D. Lyman, G. Nelemans, E. R. Stanway, and K. Wiersema, Mon. Not. R. Astron. Soc. **522**, 2029 (2023).
[70] M. Ogata, R. Hirai, and K. Hijikawa, Mon. Not. R. Astron. Soc. **505**, 2485 (2021).
[71] O. D. Fox, S. D. Van Dyk, B. F. Williams, M. Drout, E. Zapartas, N. Smith, D. Milisavljevic, J. E. Andrews, K. A. Bostroem, A. V. Filippenko *et al.*, Astrophys. J. Lett. **929**, L15 (2022).
[72] T. Moore, S. J. Smartt, M. Nicholl, S. Srivastav, H. F. Stevance, D. B. Jess, S. D. T. Grant, M. D. Fulton, L. Rhodes, S. A. Sim *et al.*, Astrophys. J. Lett. **956**, L31 (2023).
[73] H.-P. Chen, S.-J. Rau, and K.-C. Pan, Astrophys. J. **949**, 121 (2023).
[74] P. Chen, A. Gal-Yam, J. Sollerman, S. Schulze, R. S. Post, C. Liu, E. O. Ofek, K. K. Das, C. Fremling, A. Horesh *et al.*, Nature (London) **625**, 253 (2024).
[75] C. L. Bianco, M. T. Mirtorabi, R. Moradi, F. Rastegarnia, J. A. Rueda, R. Ruffini, Y. Wang, M. Della Valle, L. Li, and S. R. Zhang, Astrophys. J. **966**, 219 (2024).
[76] A. Lien, T. Sakamoto, S. D. Barthelmy, W. H. Baumgartner, J. K. Cannizzo, K. Chen, N. R. Collins, J. R. Cummings, N. Gehrels, H. A. Krimm *et al.*, Astrophys. J. **829**, 7 (2016).
[77] V. Grieco, F. Matteucci, G. Meynet, F. Longo, M. Della Valle, and R. Salvaterra, Mon. Not. R. Astron. Soc. **423**, 3049 (2012).
[78] A. E. Nugent, W.-F. Fong, Y. Dong, J. Leja, E. Berger, M. Zevin, R. Chornock, B. E. Cobb, L. Z. Kelley, C. D. Kilpatrick *et al.*, Astrophys. J. **940**, 57 (2022).
[79] W.-f. Fong, A. E. Nugent, Y. Dong, E. Berger, K. Paterson, R. Chornock, A. Levan, P. Blanchard, K. D. Alexander, J. Andrews *et al.*, Astrophys. J. **940**, 56 (2022).
[80] B. O'Connor, E. Troja, S. Dichiara, P. Beniamini, S. B. Cenko, C. Kouveliotou, J. B. González, J. Durbak, P. Gatkine, A. Kutyrev *et al.*, Mon. Not. R. Astron. Soc. **515**, 4890 (2022).
[81] P. K. Blanchard, E. Berger, and W.-f. Fong, Astrophys. J. **817**, 144 (2016).
[82] C. L. Fryer, G. Rockefeller, and M. S. Warren, Astrophys. J. **643**, 292 (2006).
[83] M. Maggiore, *Gravitational Waves. Vol. 1: Theory and Experiments* (Oxford University Press, New York, 2007), ISBN 9780198570745, 9780198520740.
[84] B. K. Wiggins, C. L. Fryer, J. M. Smidt, D. Hartmann, N. Lloyd-Ronning, and C. Belcynski, Astrophys. J. **865**, 27 (2018).
[85] A. E. Nugent, W.-f. Fong, C. Castrejon, J. Leja, M. Zevin, and A. P. Ji, Astrophys. J. **962**, 5 (2024).

The Astrophysical Journal, 978:1 (7pp), 2025 January 01 https://doi.org/10.3847/1538-4357/ad96b5

Can the Central Compact Object in HESS J1731–347 Be Indeed the Lightest Neutron Star Observed?

S. R. Zhang (张书瑞)[1,2,3,4], J. A. Rueda Hernandez[1,2,5,6,7], and R. Negreiros[8,9]
[1] Dipartimento di Fisica e Scienze della Terra, Università degli Studi di Ferrara, Via Saragat 1, I–44122 Ferrara, Italy; zhangsr@mail.ustc.edu.cn, jorge.rueda@icra.it
[2] ICRANet-Ferrara, Dip. di Fisica e Scienze della Terra, Università degli Studi di Ferrara, Via Saragat 1, I-44122 Ferrara, Italy
[3] School of Astronomy and Space Science, University of Science and Technology of China, Hefei 230026, People's Republic of China
[4] CAS Key Laboratory for Research in Galaxies and Cosmology, Department of Astronomy, University of Science and Technology of China, Hefei 230026, People's Republic of China
[5] ICRANet, Piazza della Repubblica 10, I-65122 Pescara, Italy
[6] ICRA, Dipartamento di Fisica, Sapienza Università di Roma, Piazzale Aldo Moro 5, I-00185 Rome, Italy
[7] INAF, Istituto di Astrofisica e Planetologia Spaziali, Via Fosso del Cavaliere 100, 00133 Rome, Italy
[8] Catholic Institute of Technology, 1 Broadway—14th floor, Cambridge, MA 02142, USA; rnegreiros@catholic.tech
[9] Instituto de Física, Universidade Federal Fluminense, Niterói, Rio de Janeiro, Brazil
Received 2024 October 19; revised 2024 November 19; accepted 2024 November 23; published 2024 December 20

Abstract

The exceptionally low mass of $0.77^{+0.2}_{-0.17}M_{\odot}$ for the central compact object (CCO) XMMU J173203.3–344518 (XMMU J1732) in the supernova remnant (SNR) HESS J1731–347 challenges standard neutron star (NS) formation models. The nearby post–asymptotic giant branch star IRAS 17287–3443 ($\approx 0.6M_{\odot}$), also within the SNR, enriches the scenario. To address this puzzle, we advance the possibility that the gravitational collapse of a rotating presupernova (SN) iron core ($\approx 1.2M_{\odot}$) could result in a low-mass NS. We show that angular momentum conservation during the collapse of an iron core rotating at ≈45% of the Keplerian limit results in a mass loss of $\approx 0.3M_{\odot}$, producing a stable newborn NS of $\approx 0.9M_{\odot}$. Considering the possible spin-down, this indicates that the NS is now slowly rotating, thus fulfilling the observed mass–radius relation. Additionally, the NS's surface temperature ($\approx 2 \times 10^6$ K) aligns with canonical thermal evolution for its ≈4.5 kyr age. We propose the pre-SN star, likely an ultrastripped core of $\approx 4.2M_{\odot}$, formed a tidally locked binary with IRAS 17287–3443, with a 1.43 day orbital period. The SN led to a $\approx 3M_{\odot}$ mass loss, imparting a kick velocity $\lesssim 670$ km s^{-1}, which disrupted the binary. This scenario explains the observed 0.3 pc offset between XMMU J1732 and IRAS 17287–3443 and supports the possibility of CCOs forming in binaries, with rotation playing a key role in core collapse, and the CCO XMMU J1732 being the lightest NS ever observed.

Unified Astronomy Thesaurus concepts: Neutron stars (1108); Close binary stars (254)

1. Introduction

Central compact objects (CCOs) are isolated compact stars, thought to be neutron stars (NSs), located at the center of supernova remnants (SNRs) of young ages of a few thousand years (V. Doroshenko et al. 2016; W. C. G. Ho et al. 2021), show low magnetic fields ranging 10^{10}–10^{11} G (J. P. Halpern & E. V. Gotthelf 2010; E. V. Gotthelf et al. 2013; W. C. G. Ho et al. 2021), and emit thermal X-ray radiation with no counterparts at any other wavelength and most do not exhibit pulsations (A. De Luca 2017; J. A. J. Alford & J. P. Halpern 2023). These observational properties make the study of CCOs crucial for understanding the equation of state (EOS), thermal evolution, and formation channel of NSs.

Typically, no observations suggest a binary origin for CCOs, except the CCO in the SNR HESS J1731–347 (see below), XMMU J173203.3–344518, hereafter XMMU J1732 for short. But this is not the only feature that makes XMMU J1732 an exceptional CCO study case: its mass has been recently measured to be $0.77^{+0.2}_{-0.17}M_{\odot}$ and its radius $10.4^{+0.86}_{-0.78}$ km (V. Doroshenko et al. 2022). The above numbers challenge the existing evolutionary channels leading to NSs, e.g., via core collapse, given that only NS masses $\gtrsim 1.17M_{\odot}$ are expected (Y. Suwa et al. 2018). This is generally consistent with observations, except for XMMU J1732. Thus, even if the general relativistic equilibrium configuration sequences of NSs allow for stable low-mass NSs, and the mass and radius of this CCO could provide new constraints on the nuclear EOS, astrophysical formation channels would avoid their formation in nature. Given the above properties of this system, it has been suggested XMMU J1732 could be a strange star (see, e.g., J. E. Horvath et al. 2023; F. Di Clemente et al. 2024), a hybrid star, or a dark matter admixed NS (see, e.g., V. Sagun et al. 2023; P. Laskos-Patkos et al. 2024).

In this article, we argue that XMMU J1732 might indeed be a low-mass NS and advance the possible formation channel in a core-collapse scenario by considering the rotational effects of the progenitor star in a binary, which have not been previously accounted for. The presence of a (likely) post–asymptotic giant branch (post-AGB) star (IRAS 17287–3443) inside the SNR HESS J1731–347 suggests these two stars could have formed a binary that was disrupted by the supernova (SN) event (V. Doroshenko et al. 2016). Binaries are prevalent in the Universe, and binary stellar evolution, their associated SN explosions, and products can differ significantly from those of single stars (P. Podsiadlowski et al. 2004; E. Laplace et al. 2020; E. Laplace et al. 2021). The gravitational and rotational effects may lead to mass transfer and rotational synchronization of the stellar components with the orbital period in compact-orbit binaries. Therefore, the pre-SN star could be a rotating core whose outermost layers may have been stripped, with the composition and structure different from the single-star case (E. Laplace et al. 2020; E. Laplace et al. 2021).

Bearing the above in mind, in the following sections, we explore the possibility that the pre-SN system was a tidally locked binary that led to an ultrastripped SN, forming at its center an NS that becomes low mass owing to mass shedding, and the disruption of the binary. In Section 2, the observational properties of the source are introduced, a model of rotating core collapse to form an NS is constructed, and the rotational evolution of the NS leading to shedding mass during its formation is discussed. Subsequently, in Section 3, we argue a possible evolutionary scenario for the pre-SN binary and discuss its disruption by the SN event. Finally, we summarize and discuss our conclusions in Section 4.

2. The Low-mass NS Formation and Evolution

2.1. Observational Properties

The observations of HESS J1731–347 (also known as G353.6–0.7) indicate the presence of XMMU J1732 at its center with a mass of $0.77^{+0.2}_{-0.17}M_{\odot}$ and a radius of $10.4^{+0.86}_{-0.78}$ km (V. Doroshenko et al. 2022). An optical star, IRAS 17287–3443, likely a post-AGB star with a mass of $0.605M_{\odot}$, is also inside the SNR (V. Doroshenko et al. 2016). The mass of the thick dust shell within which the optical star and the CCO are embedded has been estimated to be 1.5–$3M_{\odot}$ (V. Doroshenko et al. 2016). Gaia parallax measurements constrain the distance to the optical companion to be 2.5(3) kpc (C. A. L. Bailer-Jones et al. 2021). Thus, the observed angular distance of $\approx 25''$ between XMMU J1732 and IRAS 17287–3443 implies their projected separation to be $\approx$0.3 pc. There is another source, HESS J1729–345, where a γ-ray excess has also been observed. This source is located near HESS J1731–347 and shares a common H II cloud association with it, but it lies approximately 1° away from the CCO. As explained in N. Maxted et al. (2018), the TeV emission outside the SNR is produced by escaping cosmic rays, and HESS J1729–345 may represent a new component of target material mass.

2.2. The Rotating Collapse of the Iron Core

We assume XMMU J1732 is an NS formed following the traditional paradigm of gravitational collapse of the iron core of an evolved star. For simplicity, a polytropic sphere model is employed to calculate (solving the Lane–Emden equation) the density profile $\rho(R)$ of the iron core. A polytropic sphere with polytropic index $n = 3$ ($\gamma = 4/3$) is a suitable approximation near the critical mass, with a moment of inertia given by $I = kMR^2$, where $k = 0.075$. Despite the polytropic sphere closely matching the detailed iron core model with $k = 0.074$ (K. Boshkayev et al. 2013), the spherical symmetry does not account for deformations due to rotation. This is safe for our purpose since the collapsing part is the central region of the iron core, where the oblateness is very small, making it accurate to first order. Hence, equal equatorial and polar radii ($R_{\rm eq}$ and $R_{\rm p}$) are assumed, hereafter denoted as R.

The angular momentum of every fluid element is assumed to be conserved during the collapse. The collapsing matter is contained within a cylindrical polar coordinate in the initial model (see, e.g., J. C. Miller & F. de Felice 1985). For a spherical object, the mass and angular momentum contained within the cylindrical polar coordinate x are

$$M_b(x) = \int_0^x \int_0^{\sqrt{R^2 - x'^2}} \rho(\sqrt{x'^2 + z^2}) 4\pi x' \, dz dx', \qquad (1)$$

$$L(x) = \int_0^x \int_0^{\sqrt{R^2 - x'^2}} \rho(\sqrt{x'^2 + z^2}) 4\pi x'^3 \quad \Omega(x') \, dz dx'. \qquad (2)$$

When a rapidly rotating NS is formed with baryonic mass $M_b(x)$, the corresponding gravitational mass is $M(x)$. Following the general relativistic uniformly rotating NS results of F. Cipolletta et al. (2015), the relationship between the above two is $M/M_{\odot} \approx M_b/M_{\odot} - (1/20)(M_b/M_{\odot})^2$, and the upper limit of angular momentum is given by

$$L_{\max} \approx 0.7 \frac{GM^2(x)}{c}. \qquad (3)$$

Thus, the angular momentum of the original components required for the collapse into an NS must fulfill

$$L(x) \leqslant L_{\max}. \qquad (4)$$

This necessary condition allows us to determine the critical cylindrical polar coordinate $x_{\rm crit}$, below which collapse occurs and above it, mass is shed. The equality in Equation (4) indicates the final collapsed object is at the Keplerian sequence.

We turn to exemplify the model with specific cases. Let us assume the initial iron core is uniformly rotating with an angular velocity Ω given by a fraction $\beta < 1$ of the maximum angular velocity set by the mass-shedding, Keplerian limit, $\Omega_{\rm K}$. According to the simulation of a uniformly rotating iron core in general relativity (see, e.g., K. Boshkayev et al. 2013), $\Omega_{\rm K} \approx 0.76\sqrt{GM/R^3}$, so $\Omega = \beta\Omega_{\rm K}$. We adopt an initial mass $M = 1.2M_{\odot}$ and radius $R = 2686$ km, consistent with the structure parameters of the maximum mass configuration of an iron core in the same general relativistic treatment. For rotation parameters $\beta = 0.3$, $\beta = 0.4$, and $\beta = 0.5$, the corresponding angular momenta contained within the cylindrical polar coordinate x are depicted in Figure 1, along with the maximum allowable angular momentum. Additionally, the lower panel of Figure 1 gives the masses contained within the cylindrical polar coordinate x.

In the case of $\beta = 0.3$ and $\beta = 0.4$, the critical coordinate is $x_{\rm crit} = 0.54$ and $x_{\rm crit} = 0.35$, respectively, and the corresponding mass that can collapse to form an NS is $M(x_{\rm crit}) \approx 1.07M_{\odot}$ and $M(x_{\rm crit}) \approx 0.91M_{\odot}$. The case of $\beta = 0.4$ is suitable for XMMU J1732. The actual rotation parameter β may be slightly larger since the central core may not be a pure iron core, so its mass may be somewhat larger than $1.2M_{\odot}$, and the mass of the newly formed NS may be even smaller initially, increasing to its current mass through the accretion of shedding material. However, the exact amount of shed material accreted onto the NS and the unbound portion depends on factors like magnetic field strength, rotation, and the NS collapse process (e.g., P. Chi-Kit Cheong et al. 2024). While dynamic evolution of shed materials merits further numerical simulation, they are beyond the scope of this study. The case $\beta = 0.5$ leads to $L(x)$ above $L_{\max}$ for the appropriate NS mass values. Therefore, values $\beta \sim$ 0.4–0.45 are reasonable.

To summarize, the collapse of an iron core of $M_b \approx M_g = 1.2M_{\odot}$, uniformly rotating at $\Omega = 0.4\Omega_{\rm K} \approx 0.87$ rad s^{-1}, so a rotation period $P \approx 7.2$ s, could lead to an NS of baryonic mass $M_b \approx 0.96M_{\odot}$, so a gravitational mass $M \approx 0.91M_{\odot}$. In the collapse process, $\Delta M = 0.24M_{\odot}$ are shed, in addition to the

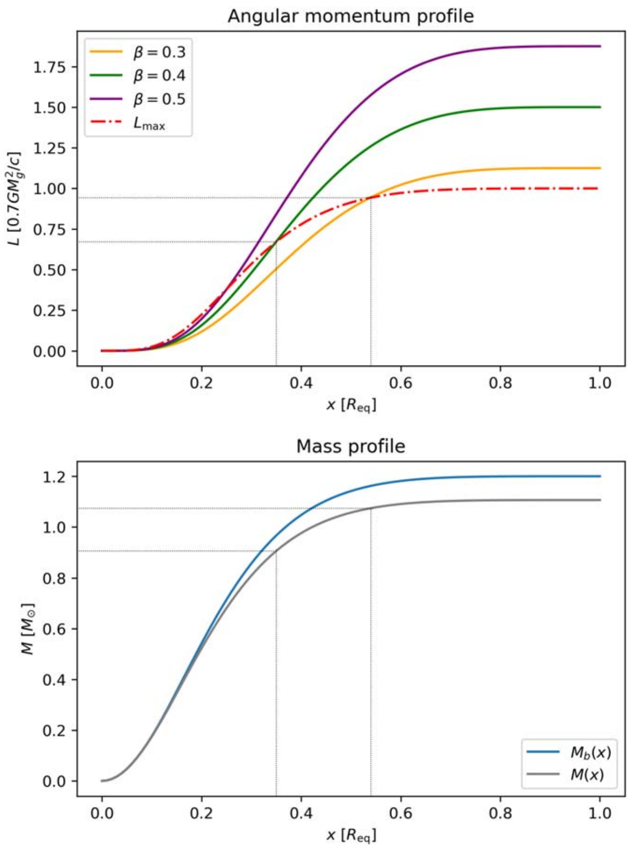

Figure 1. Upper panel: angular momentum contained within the cylindrical polar coordinate x (solid curves), along with the maximum angular momentum for the uniformly rotating sphere (red dashed–dotted curve), for selected values of the initial angular velocity parameter β. The angular momentum is normalized to $L_{\rm max} = 0.7GM^2/c$. Lower panel: baryonic (blue curve) and gravitational (black curve) mass contained within the cylindrical polar coordinate x.

ejected outermost layers of the pre-SN star hosting the iron core.

2.3. Spin-down of the Newborn NS

As indicated above, the newborn NS formed in the core-collapse process will rapidly rotate, with their rotation rate limited by the mass-shedding angular velocity. We now estimate the NS angular velocity at the system's estimated age. For this task, we consider the NS can spin-down as it might be subjected to the torque by magnetic dipole radiation. In this case, the energy conservation equation reads

$$-\dot{E}_{\rm dip} \approx -\frac{d}{dt}\left(\frac{1}{2}I\Omega^2\right) = L_{\rm dip} = \frac{2}{3}\frac{B^2 R_{\rm NS}^6 \Omega^4}{c^3}, \tag{5}$$

where I is the NS moment of inertia. Neglecting the change with time of I, Equation (5) leads to the angular rotation evolution

$$\Omega(t) = \frac{\Omega_0}{\sqrt{1+\frac{t}{\tau}}}, \qquad \tau = \frac{3Ic^3}{4B^2 R_{\rm NS}^6 \Omega_0^2}, \tag{6}$$

where τ is the spin-down timescale and Ω_0 is the initial NS angular velocity, which we adopt to be a maximum value, i.e., $\Omega_0 = \Omega_{\rm K} \approx 0.7\sqrt{GM_{\rm NS}/R_{\rm NS}^3} \approx 7110\,{\rm rad\,s^{-1}}$, corresponding to a rotation frequency $f_0 = \Omega_0/(2\pi) \approx 1131$ Hz ($\approx$0.9 ms period). This is just the initial frequency at the birth of the NS, and it will evolve rapidly.

CCOs are characterized by weak magnetic fields $B \sim 10^{10}$–10^{11} G. For instance, assuming $B = 10^{11}$ G, $M_{\rm NS} = 0.9M_\odot$, $R_{\rm NS} = 10^6$ cm, and $I = 10^{45}\,{\rm g\,cm^2}$, Equation (6) tells that at $t = 4.5$ kyr, the NS rotation frequency will be $\approx$531 Hz. This is an upper limit for the rotation frequency since additional effects could also contribute to the NS spin-down, e.g., the gravitational waves in early evolution (see, e.g., A. Ferrari & R. Ruffini 1969; J. P. Ostriker & J. E. Gunn 1969; S. Chandrasekhar 1970; R. Ruffini & J. A. Wheeler 1971; B. D. Miller 1974), multipolar magnetic field components (see, e.g., A. Mastrano et al. 2013; A. Tiengo et al. 2013; J. Pétri 2015; G. A. Rodrìguez Castillo et al. 2016; J. A. Pons & D. Viganò 2019; J. A. Rueda et al. 2022; Y. Wang et al. 2023), or the magnetic field could have been larger at earlier times at then be buried by fallback accretion (see, e.g., W. C. G. Ho 2011; N. Fraija et al. 2018). Thus, the rotation effect on the NS structure at these times is negligible, so a slow-rotation or nonrotation approximation may suffice to estimate the mass and radius (see, e.g., F. Cipolletta et al. 2015).

We can also use the above estimate to constrain the magnetic field, the frequency, and the X-ray pulsar efficiency, as follows. As for other CCOs, the X-ray observations of XMMU J1732 by XMM-Newton show a stable, i.e., absent of pulsed, emission. The observed flux in the 0.5–10 keV energy band is $F_X \approx 2.5 \times 10^{-12}\,{\rm erg\,s^{-1}\,cm^{-2}}$ (D. Klochkov et al. 2015). The spectrum is consistent with a blackbody emission with surface temperature $T_s = 2 \times 10^6$ K and radius $R_{\rm NS} \approx 10.5$ km, assuming a distance to the source $d = 2.5$ kpc (C. A. L. Bailer-Jones et al. 2021). This implies an intrinsic X-ray luminosity $L_{\rm X} = 4\pi d^2 F_{\rm X} \approx 2 \times 10^{33}\,{\rm erg\,s^{-1}}$. The dipole luminosity in the X-ray band is $L_{\rm X}^{\rm dip} = \eta_{\rm X} L_{\rm dip}$, where $\eta_{\rm X}$ is the X-ray emission efficiency parameter. Therefore, the constraint $L_{\rm X}^{\rm dip} \leqslant L_{\rm X}$ leads to

$$\eta_{\rm X} \leqslant \frac{3}{2}\frac{c^3 L_{\rm X}}{B^2 R_{\rm NS}^6 \Omega_0^4}\left(1+\frac{t}{\tau}\right)^2, \tag{7}$$

which for the above parameters implies $\eta_{\rm X} \lesssim 10^{-7}$ at $t = 4.5$ kyr. This value is consistent with the lowest X-ray emission efficiencies of pulsars (see, e.g., A. A. Abdo et al. 2013). Still, the value of $\eta_{\rm X}$ can be higher since, as we argued above, the rotation angular velocity is an upper limit, so the CCO is likely slower.

2.4. Cooling Evolution

We must also dedicate some time to exploring the thermal properties of XMMU J1732. This object offers a unique opportunity for examining its thermal characteristics, as it is one of the few thermally emitting compact objects for which we have a reliable mass estimate.

We start by revisiting the thermal evolution equations that govern the cooling process of NSs. This cooling is primarily driven by the emission of neutrinos, originating from the star's interior, and photons, emitted from its surface. The equations representing both energy balance and conservation are written as

$$\frac{\partial(le^{2\phi})}{\partial m} = -\frac{1}{\rho\sqrt{1-2m/r}}\left(\epsilon_\nu e^{2\phi} + c_v\frac{\partial(Te^{\phi})}{\partial t}\right), \tag{8}$$

$$\frac{\partial(Te^{\phi})}{\partial m} = -\frac{(le^{\phi})}{16\pi^2 r^4 \kappa\rho\sqrt{1-2m/r}}. \tag{9}$$

Equations (8) and (9) illustrate that the cooling of NSs depends on macroscopic properties—such as radial distance (r), mass ($m(r)$), and the metric function ($\phi(r)$). Additionally, there is a direct correlation with microscopic and thermodynamic quantities, including specific heat $c_v(r, T)$, thermal conductivity $\kappa(r, T)$, neutrino emissivity $\epsilon_\nu(r, T)$, and energy density $\rho(r)$. By solving Equations (8) and (9), one can obtain the temporal evolution of the temperature ($T(r, t)$) and luminosity ($l(r, t)$), which can then be compared against observational data to gauge the quality of the underlying model.

The stellar microscopic composition is crucial for thermal evolution, significantly impacting thermal conductivity, specific heat, and most importantly, neutrino emissivity. Given the nature of our model, we have opted for a conservative approach by using a parameterization of the Akmal–Pandaripande–Ravenhall (APR) EOS (V. R. Pandharipande & D. G. Ravenhall 1998; H. Heiselberg 2000), known for its ab initio formulation. This choice is ideal for modeling low-mass stars, as it provides reliable results for low densities, thereby minimizing uncertainties associated with the microscopic model. Previous studies have employed similar methodologies, such as T. Sales et al. (2020), F. Lyra et al. (2023), and V. Sagun et al. (2023). Assuming the APR EOS, the composition of the stellar core is limited to neutrons, protons, and electrons. The corresponding microscopic properties are utilized to determine all pertinent thermodynamic quantities. Additionally, we consider all potential neutrino emission processes, including the direct Urca, modified Urca, and bremsstrahlung processes.

The crust of the star is modeled using the traditional Baym–Pethick–Sutherland (BPS) approach (G. Baym et al. 1971). In this model, the outer crust consists of heavy ions arranged in a crystalline lattice permeated by electrons. The inner crust begins at the neutron drip density, where, in addition to the electron sea, free neutrons are also present. Thermodynamics of the crust is mostly dominated by the heavy ions and electrons, the latter being responsible for most of the specific heat, with the latter driving most of the heat conduction.

Details of the calculations of thermodynamics properties may be found in great detail in references D. G. Yakovlev et al. (2000), D. Yakovlev & C. Pethick (2004), and D. Page et al. (2004).

Finally, we must enforce the appropriate boundary conditions. These include the vanishing heat flow at the star's center ($l(r = 0) = 0$) and the suitable atmospheric model at the surface, which depends on the ratio and content of light and heavy elements. For more details, refer to E. Gudmundsson (1982), E. H. Gudmundsson et al. (1983), and D. Page & S. Reddy (2006).

Our initial findings are presented in Figure 2, which depicts the thermal evolution of NSs with masses in the range of $0.77^{+0.2}_{-0.17} M_\odot$ against the observed temperature of XMMU J1732 whose age was estimated in V. Doroshenko et al. (2016); this age of between 4 and 10 kyr is supported by the fact that the

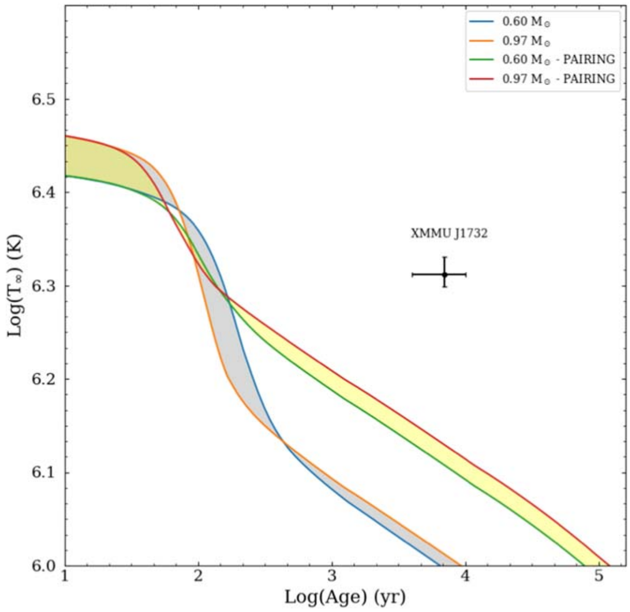

Figure 2. Thermal evolution simulation for 0.6–0.97 $M_\odot$ NSs modeled with the APR EOS. Cooling tracks with pairing indicated were calculated employing neutron singlet and triplet pairing ($^1S_0$ and $^3P_2$) as well as proton singlet ($^1S_0$) model after the SFB and CCDK models (J. M. C. Chen et al. 1993b; A. Schwenk et al. 2003). These simulations considered an envelope of heavy elements. Also shown is the observed temperature of XMMU J1732 and its estimated age according to V. Doroshenko et al. (2016).

observed infrared structure and SNR shell must have comparable ages. Alternatively, we could adopt a more stringent age constraint of 2–6 kyr, as suggested by Y. Cui et al. (2016), which we also examined. However, this narrower age range did not lead to qualitative differences in our results, except that it slightly favors an object with a smaller mass, closer to $0.6 M_\odot$. This figure includes two data sets: one for NSs without pairing and another with pairing. Pairing is a crucial factor in the thermal evolution of NSs. Its significance to cooling lies in the exponential suppression of neutrino emission processes by the pairing gap energy, which affects the primary heat sink in the thermal evolution. At the densities present in NSs, nucleons are expected to form pairs (J. Chen et al. 1993a). Although there are still many uncertainties regarding the strength and prevalence of pairing, it is generally accepted (see, for instance, D. Page et al. 2004; S. Beloin et al. 2018) that, at least for lower densities, neutrons may pair up in singlet ($^1S_0$) states, especially in the lower density regions of the outer crust, as well as triplet ($^3P_2$) states, which can extend into the core. More uncertain, but still possible, is the formation of superconducting protons via singlet proton pairing. We examine both neutron singlet and triplet pairing ($^1S_0$ and $^3P_2$), as well as proton singlet ($^1S_0$) based on the Schwenk–Friman–Brown (SFB) and CCDK models (J. M. C. Chen et al. 1993b; A. Schwenk et al. 2003). Allowing nucleons to pair up results in significantly slower cooling, yet it cannot match the observed temperature of XMMU J1732. As previously noted, the composition of an NS's atmosphere greatly influences its cooling process. Initially, our simulations assumed an atmosphere composed exclusively of heavy elements. Such a setup, which is associated with more efficient cooling, does not align with the specific conditions we propose for XMMU J1732 in this paper.

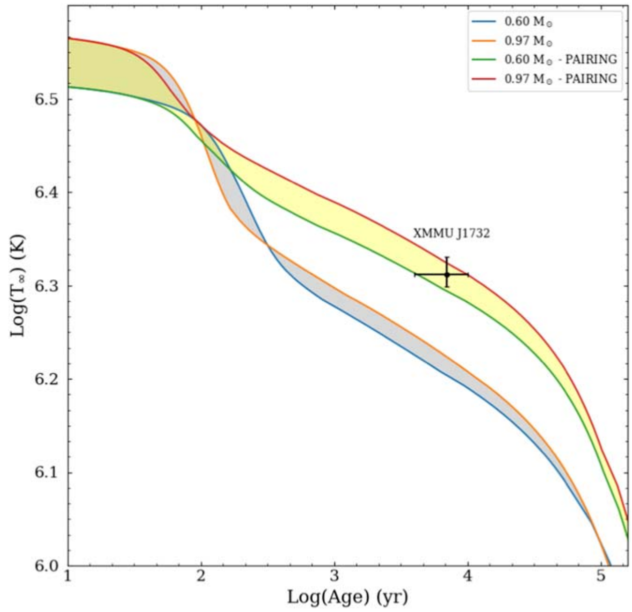

Figure 3. Same as Figure 2, but for a hydrogen-rich envelope with a light-element fraction of $\Delta M/M = 10^{-7}$, which is consistent with a carbon-rich envelope.

The situation significantly improves when considering a light-element-rich envelope. In this case, we have employed an envelope with $\Delta M/M = 10^{-7}$, where ΔM represents the light elements mass in the upper envelope (E. Gudmundsson 1982; E. H. Gudmundsson et al. 1983; A. Y. Potekhin et al. 1997). Figure 3 shows the outcomes for such an envelope.

The selection of $\Delta M/M = 10^{-7}$ is deliberate, aligning with an atmosphere composed of H, He, and C as described by A. Y. Potekhin et al. (1997). This detail is crucial since the most likely scenario for this object is the accretion of material onto the CCO shortly after the SN, resulting in a significant carbon presence in the atmosphere, as it was pointed out by V. Doroshenko et al. (2016). It is thus worth noting that, by accounting for a carbon-rich atmosphere, there is a remarkable concordance between the temperature and estimated age of the central compact object XMMU J1732 and our cooling simulations.

The results suggest the thermal properties of XMMU J1732 concur with the model explored in this study. An ordinary NS with a mass ranging 0.6–0.97 $M_\odot$ can naturally account for the observed data. In this study, we have focused solely on hadronic degrees of freedom. This approach is reasonable because transitions to quark matter are suggested to occur at higher densities (M. Oertel et al. 2017; M. G. Alford et al. 2013; M. Buballa et al. 2014; K. Masuda et al. 2013) than those expected in a compact object with such low mass. Notably, the work published in V. Sagun et al. (2023) and J. Horvath et al. (2023) has demonstrated that exotic degrees of freedom can also explain the thermal data of HESS J1731–347. Therefore, extending our evolutionary model to include exotic degrees of freedom would be an interesting direction for future research.

3. Progenitor System

Having clarified the consistency of XMMU J1732 with a rotating core-collapse event that shed mass, we turn to reconstruct the astrophysical scenario before the SN event.

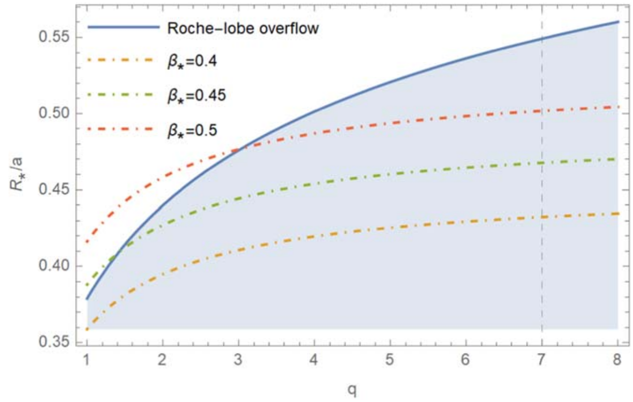

Figure 4. The ratio of the primary star radius to the binary semimajor axis as a function of the ratio of the masses of the two components of the binary star. The blue curve corresponds to the Roche-lobe outflow condition, with the shaded region separating two components larger than the Roche-lobe outflow condition, i.e., Equation (10). The dashed–dotted curves correspond to the tidally locked condition with different rotation parameters. The vertical dashed line indicates the mass ratio of the inferred progenitor binary associated with SNR HESS J1731–347.

Observations indicate that the mass of the dust shell in this SNR is $\sim$1.5–3$M_\odot$, which further supports the suggestion that the pre-SN progenitor should not be a single star but rather an ultrastripped core in a binary. Below, we infer the progenitor binary parameters.

3.1. Binary System Prior to SN

We start by imposing that there is no Roche-lobe overflow in the binary at the SN event. For the primary star, this condition constraints its radius $R_\star$ to satisfy

$$\frac{R_\star}{a} \lesssim \frac{0.49q^{2/3}}{0.6q^{2/3} + \ln(1 + q^{1/3})}, \tag{10}$$

where a is the semimajor axis of the binary orbit, and $q \equiv M_\star/M_c > 1$ is the binary mass ratio. When the equal sign in Equation (10) is taken, it indicates the Roche-lobe outflow condition, corresponding to the blue curve in Figure 4, with the shaded region indicating the range defined by Equation (10).

We assume the binary is tidally locked before the SN occurs, i.e., $\Omega_\star = \Omega_{\rm orb}$. Then, the angular velocity parameter is given by

$$\beta_\star \equiv \frac{\Omega_\star}{\Omega_{K,*}} = \frac{\sqrt{\frac{G(M_\star + M_c)}{a^3}}}{0.76\sqrt{\frac{GM_\star}{R_\star^3}}} = \frac{1}{0.76}\sqrt{\frac{1+q}{q}}\left(\frac{R_\star}{a}\right)^{3/2}. \tag{11}$$

Note that the value 0.76 is consistent with Section 2.2. For a given β_*, Equation (11) relates $R_\star/a$ and q. As discussed in Section 2.2, assuming that the collapsing iron core rotates uniformly to collapse into a low-mass NS, a reasonable value for $\beta_\star$ could be somewhere in the range 0.4–0.5. Figure 4 shows the $R_\star/a$ as a function of q for three selected values, $\beta_* = 0.4$, 0.45, and 0.5.

An SNR mass of $3M_\odot$ (V. Doroshenko et al. 2016) implies the pre-SN star would be $M_* = 4.2M_\odot$. We recall that here we refer to the pre-SN star mass, which can be considerably lower than the mass of its progenitor zero-age main-sequence star. Indeed, for the latter to give rise to an NS, stellar evolution predicts it to be $\gtrsim 8M_\odot$. Therefore, the above numbers suggest the star loses about half of its mass from the main sequence to the pre-SN stage. Given that the companion star is $M_c \approx 0.6M_\odot$, the mass ratio is $q \approx 7$. These parameters are consistent with the ultrastripped SNe simulations: see, for instance, the simulation where the mass of the stripped star is $4.23M_\odot$ and the iron core mass is $1.27M_\odot$ in Table 1 in E. Laplace et al. (2021). The stripped star of $4.23M_\odot$ has a stellar radius $R_\star \approx 4.2R_\odot$. By substituting this value into Equation (11), for $q = 7$, we find the orbital separation $a = 9.04R_\odot$. This implies an orbital period of $P = 1.43$ days. The optical star has $M_c \sim 0.6M_\odot$, so its radius is expected to be $\lesssim R_\odot$ during the post-AGB phase. Thus, at the time of the SN explosion, the separation between the two components is larger than the sum of their radii, placing it below the Roche-lobe outflow condition curve, as shown in Figure 4. Interestingly, this also agrees with the numerical simulations of E. Laplace et al. (2021), which indicate that the primary star in close binaries at solar metallicity and an initial mass above $11M_\odot$ does not interact with its companion after reaching core helium depletion.

3.2. Binary Disruption

We now show that the binary parameters inferred above imply that the SN explosion likely disrupted the binary, as suggested by V. Doroshenko et al. (2016). The SNR mass consists of two parts: the ejecta from the SN explosion, $M_{\rm ej} = 4.23M_\odot$–$1.27M_\odot = 2.96M_\odot$ (the outer layers above the iron core), and the material shed during the core collapse, $M_{\rm shed} \approx 0.3M_\odot$ (i.e., $M_{\rm cco} + M_{\rm shed} \approx 1.27M_\odot$). It is worth noting that the mass ejected from the AGB to post-AGB evolution of the optical star is expected to be only 10^{-5}–$10^{-2.5}M_\odot$ (R. Meijerink et al. 2003; P. Ventura et al. 2012), hence we neglect its contribution to the remnant mass.

For a binary with a circular orbit, an ejected mass larger than half of the total mass, i.e., $M_{\rm ej} > M_{\rm tot}/2$, leads to a 100% probability of disruption (J. G. Hills 1983). As indicated by the model above, $M_{\rm ej} = 2.96M_\odot$ and $M_{\rm tot} = 4.23M_\odot + 0.6M_\odot = 4.83M_\odot$. Therefore, $M_{\rm ej}/M_{\rm tot} > 1/2$, indicating that the SN explosion could have indeed disrupted this binary. Furthermore, the mass of the SNR is consistent with the upper limit of approximately $3M_\odot$ (V. Doroshenko et al. 2016).

Following J. G. Hills (1983), we can estimate an upper limit of the kick velocity, i.e., assuming 100% of the probability of disruption. This leads to a kick of $\Delta v \approx 670\,{\rm km\,s^{-1}}$. The possible large kick velocity imparted to the stars in this scenario agrees with existing simulations of $\sim$1 day orbital period binaries of low-mass components (P. Podsiadlowski et al. 2004). Considering the SNR estimated age of 4.5 kyr, the two objects could have reached a maximum separation of $\approx$3 pc. This value is larger than the observed relative projected offset of $\approx$0.3 pc between the CCO, XMMU J1732, and the optical star, IRAS 17287–3443, which is reasonable because we have used the upper limit of the kick velocity, and the actual distance between the optical star and the CCO can be larger than the observed projected offset, depending on the proper motion direction relative to the line of sight.

4. Discussion and Conclusions

We have advanced a formation scenario for the puzzling, light CCO XMMU J1732, with an optical star neighbor IRAS 17287–3443 within the SNR HESS J1731–347. We have provided a scenario within the traditional framework of NS formation from core-collapse SN. Here are some concluding remarks:

(i) Angular momentum conservation in the collapse process leads to the light NS formation by mass-shedding if the iron core at the collapse moment rotates at about 45% of the Keplerian limit angular velocity, i.e., $\beta \sim 0.45$. The observed CCO, XMMU J1732, is indeed a light NS of $M_{\rm NS} \approx 0.9M_\odot$ formed in the collapse of a fast-rotating iron core of mass $M \approx 1.2M_\odot$, with a rotation period of $\approx$7 s, which sheds $\approx 0.3M_\odot$ during its collapse avoiding to overcome the maximum angular momentum the newborn NS can hold. We refer to Section 2.2 for details.

(ii) Assuming a magnetic dipole braking model for a dipole strength of 10^{11} G, and as NS age the estimated age of the SNR (4.5–10 kyr), we showed the CCO must be currently a modest rotator, given the upper limit of the rotation frequency $\approx$531 Hz (see Section 2.3). Thus, a slow-rotation or nonrotating mass–radius relation could accurately describe it. This implies that the observationally inferred radius of XMMU J1732 can be a relevant constraint in the low-mass region of the NS mass–radius relation.

(iii) We have performed comprehensive cooling simulations for light NSs within the mass range of $0.77^{+0.20}_{-0.17}M_\odot$, specifically for those characterized by the ab initio APR model, and have observed a significant agreement with empirical data. It is important to highlight that our simulations incorporated considerations for nucleon pairing, which align with the prevailing theories on NS thermal evolution. Remarkably by considering a carbon-rich atmosphere, as predicted by V. Doroshenko et al. (2016), our cooling simulations were in excellent agreement with observed thermal data. This concurrence is not merely coincidental but is a testament to the robustness of the underlying assumptions. These findings corroborate the model introduced in this study, demonstrating that the thermal characteristics of XMMU J1732 can be accurately accounted for by a conventional NS cooling model, thereby eliminating the need for more speculative hypotheses and decreasing the number of parameters required to interpret the observed phenomena.

(iv) The obtained parameters from the core-collapse model are generally consistent with simulations of the pre-SN stage in binaries with the primary having a mass of $M_* \sim 4.2M_\odot$ (E. Laplace et al. 2021). We assume XMMU J1732 and IRAS 17287–3443 ($M_c \approx 0.6M_\odot$) formed a binary system before the core-collapse SN event. Adopting tidal locking, we have inferred a semimajor axis of the pre-SN binary $a \approx 9R_\odot$, and the orbital period $P \approx 1.4$ days (see section 3.1). No Roche-lobe overflow occurred before the SN.

(v) The mass loss amounting to $\sim 3M_\odot$, given by the SNR shell mass, led to the disruption of the binary since it is more than half the total binary mass, $M_* + M_c \approx 4.8M_\odot$. This is consistent with the observed projected separation of $\approx$0.3 pc between the CCO and the post-AGB, lower than the maximum separation of $\approx$3 pc, obtained assuming the maximum possible kick ($670\,{\rm km\,s^{-1}}$) that could have been imparted (see Section 3.2).

Although assessed via a simplified model, the above astrophysical scenario highlights the relevance of rotation in the binary evolution and, finally, in the core-collapse process. Accurate calculations from numerical simulations could replace some simplifications. For instance, we have made a hybrid model of the rotating core collapse that joins a simplified Newtonian model to the results of the rotating NS structure obtained in full general relativity. Thus, it would be ideal to perform a full general relativistic calculation of the gravitational collapse of a rotating iron core of a pre-SN star with its interior structure obtained with an evolution code accounting for binary interactions.

To conclude, some comments on the binary evolution path are in order. Typically, ultrastripped SNe do not lead to the binary disruption (T. M. Tauris et al. 2015; N. D. Richardson et al. 2023). However, what makes this system unique is mainly the exceptionally low mass of the newborn NS, i.e., the CCO, and the companion star, resulting in the ejected mass easily exceeding half of the total system mass. The previous evolution of the binary, especially of the low-mass companion, remains an interesting subject of study since the evolution leading to a post-AGB is expected to be longer than that leading to a core-collapse SN and an NS. We can only speculate that our binary could have followed a similar evolutionary path to the E. Laplace et al. (2021) simulations. The crucial condition is that the binary mass ratio be close to unity at the beginning of the evolution. Their simulations involve a secondary with an initial mass of 80% of the primary star. Still, the secondary's state at the time of the SN is uncertain. Therefore, further population synthesis analyses and simulations of the binary stellar evolution, including possible different masses of the secondary, are needed to comprehend this system fully. Such analysis, which is worth it on its own, goes beyond our scope here and is left for future work.

Acknowledgments

We thank Prof. Thomas Tauris for discussing and highlighting important references to binary evolution and Prof. M. Bulla for suggestions on the presentation. J.A.R. also thanks Prof. M. Malheiro and Prof. A. Drago for discussions on the quark star hypothesis of XMMU J1732. S.R.Z. acknowledges the Joint International Relativistic Astrophysics Doctorate Program and support from the China Scholarship Council (CSC No. 202206340085). R.N. acknowledges financial support from CAPES and FAPERJ. This work is part of the project FAPERJ JCNE Proc. No. E-26/201.432/2021.

ORCID iDs

S. R. Zhang (张书瑞) https://orcid.org/0000-0003-0368-384X
J. A. Rueda Hernandez https://orcid.org/0000-0003-4904-0014
R. Negreiros https://orcid.org/0000-0002-9669-905X

References

Abdo, A. A., Ajello, M., Allafort, A., et al. 2013, ApJS, 208, 17
Akmal, A., Pandharipande, V. R., & Ravenhall, D. G. 1998, PhRvC, 58, 1804
Alford, J. A. J., & Halpern, J. P. 2023, ApJ, 944, 36
Alford, M. G., Han, S., & Prakash, M. 2013, PhRvD, 88, 083013
Bailer-Jones, C. A. L., Rybizki, J., Fouesneau, M., Demleitner, M., & Andrae, R. 2021, AJ, 161, 147
Baym, G., Pethick, C., & Sutherland, P. 1971, ApJ, 170, 299
Beloin, S., Han, S., Steiner, A. W., & Page, D. 2018, PhRv, C97, 015804
Boshkayev, K., Rueda, J. A., Ruffini, R., & Siutsou, I. 2013, ApJ, 762, 117
Buballa, M., Dexheimer, V., Drago, A., et al. 2014, JPhG, 41, 123001
Chandrasekhar, S. 1970, ApJ, 161, 571
Chen, J., Clark, J., Dav, R., & Khodel, V. 1993a, NuPhA, 555, 59
Chen, J. M. C., Clark, J. W., Davé, R. D., & Khodel, V. V. 1993b, NuPhA, 555, 59
Chi-Kit Cheong, P., Pitik, T., Longo Micchi, L. F., & Radice, D. 2024, arXiv:2410.10938
Cipolletta, F., Cherubini, C., Filippi, S., Rueda, J. A., & Ruffini, R. 2015, PhRvD, 92, 023007
Cui, Y., Pühlhofer, G., & Santangelo, A. 2016, A&A, 591, A68
De Luca, A. 2017, JPhCS, 932, 012006
Di Clemente, F., Drago, A., & Pagliara, G. 2024, ApJ, 967, 159
Doroshenko, V., Pühlhofer, G., Kavanagh, P., et al. 2016, MNRAS, 458, 2565
Doroshenko, V., Suleimanov, V., Pühlhofer, G., & Santangelo, A. 2022, NatAs, 6, 1444
Ferrari, A., & Ruffini, R. 1969, ApJL, 158, L71
Fraija, N., Bernal, C. G., Morales, G., & Negreiros, R. 2018, PhRvD, 98, 083012
Gotthelf, E. V., Halpern, J. P., & Alford, J. 2013, ApJ, 765, 58
Gudmundsson, E. 1982, ApJ, 259, L19
Gudmundsson, E. H., Pethick, C. J., & Epstein, R. I. 1983, ApJ, 272, 286
Halpern, J. P., & Gotthelf, E. V. 2010, ApJ, 709, 436
Heiselberg, H. 2000, PhR, 328, 237
Hills, J. G. 1983, ApJ, 267, 322
Ho, W. C. G. 2011, MNRAS, 414, 2567
Ho, W. C. G., Zhao, Y., Heinke, C. O., et al. 2021, MNRAS, 506, 5015
Horvath, J., Rocha, L., de Sá, L., et al. 2023, A&A, 672, L11
Horvath, J. E., Rocha, L. S., de Sá, L. M., et al. 2023, A&A, 672, L11
Klochkov, D., Suleimanov, V., Pühlhofer, G., et al. 2015, A&A, 573, A53
Laplace, E., Götberg, Y., de Mink, S. E., Justham, S., & Farmer, R. 2020, A&A, 637, A6
Laplace, E., Justham, S., Renzo, M., et al. 2021, A&A, 656, A58
Laskos-Patkos, P., Koliogiannis, P. S., & Moustakidis, C. C. 2024, PhRvD, 109, 063017
Lyra, F., Moreira, L., Negreiros, R., Gomes, R. O., & Dexheimer, V. 2023, PhRvC, 107, 025806
Mastrano, A., Lasky, P. D., & Melatos, A. 2013, MNRAS, 434, 1658
Masuda, K., Hatsuda, T., & Takatsuka, T. 2013, ApJ, 764, 12
Maxted, N., Burton, M., Braiding, C., et al. 2018, MNRAS, 474, 662
Meijerink, R., Mellema, G., & Simis, Y. 2003, A&A, 405, 1075
Miller, B. D. 1974, ApJ, 187, 609
Miller, J. C., & de Felice, F. 1985, ApJ, 298, 474
Oertel, M., Hempel, M., Klähn, T., & Typel, S. 2017, RvMP, 89, 015007
Ostriker, J. P., & Gunn, J. E. 1969, ApJ, 157, 1395
Page, D., Lattimer, J. M., Prakash, M., & Steiner, A. W. 2004, ApJS, 155, 623
Page, D., & Reddy, S. 2006, ARNPS, 56, 327
Pétri, J. 2015, MNRAS, 450, 714
Podsiadlowski, P., Langer, N., Poelarends, A. J. T., et al. 2004, ApJ, 612, 1044
Pons, J. A., & Viganò, D. 2019, LRCA, 5, 3
Potekhin, A. Y., Chabrier, G., & Yakovlev, D. G. 1997, A&A, 323, 415
Richardson, N. D., Pavao, C. M., Eldridge, J. J., et al. 2023, Natur, 614, 45
Rodrìguez Castillo, G. A., Israel, G. L., Tiengo, A., et al. 2016, MNRAS, 456, 4145
Rueda, J. A., Li, L., Moradi, R., et al. 2022, ApJ, 939, 62
Ruffini, R., & Wheeler, J. A. 1971, in Proc. The Astrophysical Aspects of Weak Interactions, Problemi Attuali di Scienza e di Cultura, ed. L. Radicati (Roma: Accademia Nazionale dei Lincei), 165
Sagun, V., Giangrandi, E., Dietrich, T., et al. 2023, ApJ, 958, 49
Sales, T., Lourenço, O., Dutra, M., & Negreiros, R. 2020, A&A, 642, A42
Schwenk, A., Friman, B., & Brown, G. E. 2003, NuPhA, 713, 191
Suwa, Y., Yoshida, T., Shibata, M., Umeda, H., & Takahashi, K. 2018, MNRAS, 481, 3305
Tauris, T. M., Langer, N., & Podsiadlowski, P. 2015, MNRAS, 451, 2123
Tiengo, A., Esposito, P., Mereghetti, S., et al. 2013, Natur, 500, 312
Ventura, P., di Criscienzo, M., Schneider, R., et al. 2012, MNRAS, 424, 2345
Wang, Y., Becerra, L. M., Fryer, C. L., Rueda, J. A., & Ruffini, R. 2023, ApJ, 945, 95
Yakovlev, D., & Pethick, C. 2004, ARA&A, 42, 169
Yakovlev, D. G., Kaminker, A. D., Gnedin, O. Y., & Haensel, P. 2000, PhR, 354, 1

Eur. Phys. J. C (2024) 84:1337
https://doi.org/10.1140/epjc/s10052-024-13721-6

THE EUROPEAN PHYSICAL JOURNAL C

Regular Article - Theoretical Physics

X-ray pulsed light curves of highly compact neutron stars as probes of scalar–tensor theories of gravity

Tulio Ottoni[1,2,a], **Jaziel G. Coelho**[3,b], **Rafael C. R. de Lima**[4,c], **Jonas P. Pereira**[3,5,6,d], **Jorge A. Rueda**[2,7,8,9,10,e]

[1] PPGCosmo, Universidade Federal do Espírito Santo, Av. Fernando Ferrari, Vitória, Espirito Santo 29075-910, Brazil
[2] ICRANet-Ferrara, Dipartimento di Fisica e Scienze della Terra, Università degli Studi di Ferrara, Via Saragat 1, 44122 Ferrara, FE, Italy
[3] Núcleo de Astrofísica e Cosmologia (Cosmo-Ufes) and Departamento de Física, Universidade Federal do Espírito Santo, Av. Fernando Ferrari, Vitória, ES 29075-910, Brazil
[4] Departamento de Física, Universidade do Estado de Santa Catarina, Rua Paulo Malschitzki, Joinville, SC 89219-710, Brazil
[5] Departamento de Astronomia, Instituto de Astronomia, Geofísica e Ciências Atmosféricas (IAG), Universidade de São Paulo, Rua do Matão 1226, Cidade Universitária, São Paulo 05508-090, Brazil
[6] Nicolaus Copernicus Astronomical Center, Polish Academy of Sciences, Bartycka 18, 00-716 Warsaw, Poland
[7] ICRANet, Piazza della Repubblica 10, 65122 Pescara, Italy
[8] ICRA, Dipartamento di Fisica, Sapienza Universitá di Roma, Piazzale Aldo Moro 5, 00185 Rome, Italy
[9] Department of Physics and Earth Science, University of Ferrara, Via Saragat 1, 44122 Ferrara, Italy
[10] INAF, Istituto di Astrofisica e Planetologia Spaziali, Via Fosso del Cavaliere 100, 00133 Rome, Italy

Received: 10 September 2024 / Accepted: 15 December 2024

Abstract The strong gravitational potential of neutron stars (NSs) makes them ideal astrophysical objects for testing extreme gravity phenomena. We explore the potential of NS X-ray pulsed light curve observations to probe deviations from general relativity (GR) within the scalar–tensor theory (STT) of gravity framework. We compute the flux from a single, circular, finite-size hot spot, accounting for light bending, Shapiro time delay, and Doppler effect. We focus on the high-compactness regime, i.e., close to the critical GR value $GM/(c^2R) = 0.284$, over which multiple images of the spot appear and impact crucially the light curves. Our investigation is motivated by the increased sensitivity of the pulse to the scalar charge of the spacetime in such high compactness regimes, making these systems exceptionally suitable for scrutinizing deviations from GR, notably phenomena such as spontaneous scalarization, as predicted by STT. We find significant differences in NS observables, e.g., the flux of a single spot can differ up to 80% with respect to GR. Additionally, reasonable choices for the STT parameters that satisfy astrophysical constraints lead to changes in the NS radius relative to GR of up to approximately 10%. Consequently, scalar parameters might be better constrained when uncertainties in NS radii decrease, where this could occur with the advent of next-generation gravitational wave detectors, such as the Einstein Telescope and LISA, as well as future electromagnetic missions like eXTP and ATHENA. Thus, our findings suggest that accurate X-ray data of the NS surface emission, jointly with refined theoretical models, could constrain STTs.

1 Introduction

Neutron stars (NSs) are natural laboratories for testing fundamental physics, ranging from interactions above nuclear saturation density to the strong gravitational field in the stellar interior and surroundings. Their astrophysical observations can probe fundamental interactions in a very unique regime [1,2]. Regarding the gravitational field, the extreme conditions of density and pressure in NSs can activate non-minimally coupled fields to gravity. The simplest case is that of scalar fields. In the context of scalar–tensor theories (STTs), this is one way to understand the phenomenon of *spontaneous scalarization*, a novel non-perturbative effect arising in these theories. This effect predicts deviations from General Relativity (GR) that can be observationally tested [3–7]. Scalar fields are pivotal in cosmological scenarios, lead-

Jaziel G. Coelho, Rafael C. R. de Lima, Jonas P. Pereira, Jorge A. Rueda contributed equally to this work.

[a] e-mail: tulio.costa@edu.ufes.br (corresponding author)
[b] e-mail: jaziel.coelho@ufes.br
[c] e-mail: rafael.nuclear@gmail.com
[d] e-mail: jpereira@camk.edu.pl
[e] e-mail: jorge.rueda@icra.it

Published online: 30 December 2024

ing to well-established inflationary models [8–10]. A fundamental scalar field can modify compact objects structure and gravitational field depending on the Lagrangian coupling between the scalar field and ordinary matter. Such theoretically predicted modifications can be tested with astrophysical observations. On the other hand, some grand unification theories, like string theory, also predict scalar degrees of freedom in the low energy, classical regime (see, e.g., [11,12], and references therein).

We aim to extend previous efforts to constrain STTs using astrophysical observations of NSs, particularly the X-ray light curve profiles. This task can generally be done for STTs without specifying the origin of the scalar field. There is currently a broad class of astrophysical sources associated with NSs, with observations spanning the electromagnetic spectrum from the radio to high-energy X-rays and gamma rays. In particular, some systems exhibit periodic X-ray emissions modulated by the star's rotation period, which can be deduced from the pulsar timing of radio signals. The modeling of these pulse profiles can be compared to observations, such as those made by NICER [13], and global properties of NSs, like compactness ($\mathcal{C} \equiv GM/Rc^2$, where M is the NS mass and R its radius), can be inferred from the analysis. This, in turn, can constrain the equation of state of nuclear matter. Furthermore, modeling deviations from GR in the pulse profile can, in principle, constrain modified gravity models, such as STT.

A crucial and pertinent question regarding NSs revolves around the maximum mass allowed by gravitational instability, known as the Tolman–Oppenheimer–Volkov (TOV) limit. Presently, we have reliable mass measurements for high-mass pulsars, with masses around or greater than $2M_\odot$, such as PSR J0348+0432 with $2.01 \pm 0.04M_\odot$ [14], PSR J0740+6620 with $2.08 \pm 0.07M_\odot$ [15] and PSR J0952-0607 with $2.35\pm0.17M_\odot$ [16]. The first two pulsars are in a binary system, and the masses were estimated by standard timing techniques. At the same time, the last one is a "spider" system with more model-dependent uncertainty. But the message here is that such massive NSs are feasible, and such systems are ideal for testing strong gravity effects because of the high gravitational binding energy compared to low-mass NSs.

For a $\sim 2M_\odot$ star, several realistic equations of state (EOS) predict a radius such that the resultant compactness can be closer or higher than $GM/Rc^2 = 0.284$, the critical value in GR that makes light bending strong enough for the whole NS surface to be seen by an observer at rest at infinity [17]. As a result, considering multiple images is relevant to model realistic light curves of high-mass stars. From the point of view of STT predictions, deviations from GR generally increase with compactness, making these high-mass systems ideal for testing and constraining the strong field regime of alternative theories. This study focuses on scenarios of high compactness, which have been partially explored in the literature and are critical for understanding the differences between STT and GR. Our analysis emphasizes the effects of possible compactness values approaching the theoretical limits.

Significant research has been conducted on pulse profile modeling within the framework of STT [18–22]. Silva and Yunes [20] derived the flux of infinitesimal spots, incorporating the varying effects of bending, time delay, and kinematic factors specific to STT. Here, we use their expression but integrate it over a finite spot and a different regime of compactness. Furthermore, the work by [21,22] expanded these calculations to finite spots and linked them to particular scalar–tensor models with a massive scalar field. In this study, we investigate the impact of extended spots on the light curve of an isolated NS with high compactness [17,23], demonstrating that such compact systems, close to producing multiple images of the spot by a strong lensing effect, are promising for testing deviations from GR, as evidenced by the qualitative and quantitative differences in the light curves.

The structure of the paper is as follows. In Sect. 2, we review the fundamentals of scalar–tensor theory and examine specific models that predict spontaneous scalarization. Section 3 reviews pulse profile modeling techniques within the STT context. Finally, in Sect. 4, we present and discuss our findings. Throughout this paper, we adopt the units where $G = c = 1$.

2 Scalar–tensor theory

A general class of scalar–tensor theory that encodes a non-minimal coupling with geometry is described by the gravitational action

$$S_g = \frac{1}{16\pi} \int d^4x\sqrt{-\tilde{g}}[F(\Phi)\tilde{R} - -Z(\Phi)\nabla_\mu\Phi\nabla^\mu\Phi - V(\Phi)], \tag{1}$$

which is written in the so-called *Jordan* Frame, where the scalar field couples directly with the geometry via $F(\Phi)$ [24]. We get a particular theory within this general class once we specify a particular form of these functions.

In this work, we focus on the simpler case of a massless scalar field with no self-interactions so that we can neglect the potential term $V(\Phi) = 0$. Also, to take into account the stringent constraints from solar system experiments [see, e.g., 25], we set the background scalar field value to $\Phi_\infty = 0$ since parametrized pós Newtonian (PPN) deviations in this theory are generally proportional to this background value. Including the matter contribution, the total action reads

$$S = S_g + S_m[\Psi_m, \tilde{g}_{\mu\nu}], \tag{2}$$

where Ψ_m denotes the matter fields collectively. As usual, we assume a perfect fluid form for the energy-momentum tensor $T^{\mu\nu} \equiv (2/\sqrt{-g})\delta S_m/\delta \tilde{g}_{\mu\nu}$, i.e.,

$$T^{\mu\nu} = (\epsilon + p)u^{\mu}u^{\nu} + p\tilde{g}^{\mu\nu}. \tag{3}$$

For numerical computation, it is convenient to work in the so-called *Einstein* frame, where, after a conformal transformation of the metric $g_{\mu\nu} \equiv F(\Phi)\tilde{g}_{\mu\nu}$ and field redefinition $\Phi \rightarrow \varphi(\Phi)$, the action can be written as

$$S = \frac{1}{16\pi}\int d^4x\sqrt{-g}[R - 2\nabla_{\mu}\varphi\nabla^{\mu}\varphi] + S_m[\Psi_m, A^2(\phi)g_{\mu\nu}], \tag{4}$$

where we define $A(\varphi) \equiv F(\Phi(\varphi))^{-1/2}$ and now the scalar field is minimally coupled to gravity, but it couples directly with matter. We also chose the standard canonical kinetic term $Z(\Phi) = 1$. After varying the action with respect to $g_{\mu\nu}$ and φ, we get the following field equations:

$$G_{\mu\nu} - 2\partial_{\mu}\varphi_{\nu}\partial\varphi + g_{\mu\nu}g^{\alpha\beta}\partial_{\alpha}\varphi\partial_{\beta}\varphi = 8\pi T_{\mu\nu}A^2(\varphi). \tag{5}$$
$$\nabla^{\mu}\nabla_{\mu}\varphi = -4\pi A^4(\varphi)\alpha(\varphi)T, \tag{6}$$

where $T \equiv g_{\mu\nu}T^{\mu\nu} = 3p - \epsilon$ is the trace of the energy-momentum tensor,

$$\alpha(\varphi) \equiv \frac{d\ln A(\varphi)}{d\varphi}. \tag{7}$$

2.1 Spontaneous scalarization

The most distinct feature of the STT when compared to GR is the phenomenon of *spontaneous scalarization* of compact objects, discovered by Damour and Esposito-Farèse [6]. This scalarization is a violation of the strong equivalence principle associated with a gravitational phase transition [26,27]. It can be understood as a tachyonic instability of the scalar field [28]. To see this more clearly, we can study linear perturbations of the scalar field given by Eq. (6),

$$\Box\delta\varphi = -4\pi\beta(\varphi)T\delta\varphi, \tag{8}$$

where $\beta(\varphi) = d\alpha(\varphi)/d\varphi|_{\varphi_{\infty}}$. This equation is a Klein–Gordon equation of the background space-time, with an effective mass

$$\mu^2_{eff} = -4\pi\beta T. \tag{9}$$

The solutions are oscillatory for a positive effective mass squared, and the perturbations do not grow. This happens if β and T have opposite signs. But now, if they have the same sign, the instability grows until the linear approximation breaks down and the nonlinearities occur, quenching the scalar field's growth.

2.2 Models

Once we choose a specific form for the coupling function, we select a particular model within the general class of STTs. A simple model is described by an exponential coupling, first used in [6]

$$A(\varphi) = e^{\frac{\beta\varphi^2}{2}}, \tag{10}$$

frequently known as Damour–Esposito–Faresè (DEF) theory and has a significant historical value and simplicity, although incompatible with recent observations [29]. Another well-motivated form for the conformal factor comes from cosmology, especially from inflationary models [30,31]

$$A(\varphi) = \frac{1}{\sqrt{1 + \xi\Phi^2}}, \tag{11}$$

but the technical difficulty here is that we need to solve the relation between the fields numerically, and so there is no close form for $\alpha(\varphi)$ in the Einstein frame, for example, [32]. This difficulty can be overcome with the use of an analytical approximation using hyperbolic functions, where the conformal function is

$$A(\varphi) = (\cosh(-2\sqrt{3}\xi\varphi))^{-\frac{1}{6\xi}}, \tag{12}$$

while the coupling function is

$$\frac{1}{\sqrt{3}}\tanh(-2\sqrt{3}\xi\varphi). \tag{13}$$

This model was first discussed in [33], known as the Mendes–Ortiz (MO) theory. Finally, all three models are similar for $\xi = 2\beta$, showing the same linear behavior when expanded in powers of ϕ.

2.3 Exact external solution

In the scalar–tensor theory, an exact analytical solution for a spherically symmetric spacetime is the Just metric [34–36]. Written in the Einstein frame, it is

$$ds^2 = -f^{b/a}dt^2 + f^{-b/a}d\rho^2 + \rho^2 f^{1-b/a}d\Omega, \tag{14}$$

besides the spherical part, the radial coordinate ρ is related to Schwarzschild coordinate by

$$r = \rho(1 - a/\rho)^{(1-b/a)/2}, \tag{15}$$

which cannot be analytically inverted. Here, b is related to the gravitational (ADM) mass, $b \equiv 2M$, and

$$f \equiv 1 - a/\rho, \tag{16}$$

where a has length units and is related to the mass and the scalar field configuration. We recover GR when $a = b$.

The scalar field profile outside the star has the form

$$\varphi = \varphi_\infty + \frac{q}{a}\log\left(1 - \frac{a}{\rho}\right), \tag{17}$$

where φ_∞ is the background value of the scalar field, which is constrained to be very small by solar system experiments. For simplicity, we assume $\varphi_\infty = 0$. Far from the source, the scalar field behaves like an electric field of a point charge $\varphi \sim -q/\rho$, and thus, we make the identification of q as the scalar charge. The constants a, b and q are not independent:

$$a^2 - b^2 - (2q)^2 = 0. \tag{18}$$

It is more common to define a scalar-to-mass ratio $Q \equiv q/M$, so that

$$a/b = \sqrt{1 + Q^2} \tag{19}$$

2.4 Constraints

Since the formulation of GR, it has passed the scrutiny of experimental tests [37], and tight constraints were put in alternative theories of gravity. The most relevant constraint in the weak field regime and solar system scale comes from the Cassini bound [25]. Making the PPN expansion for the weak field/low velocities regime, the constraint on the γ parameter is usually proportional to the background value of the scalar field. We put $\Phi_\infty = \varphi_\infty = 0$, which automatically satisfies that. But even with a restricted weak field phenomenology, STTs can still have a rich, strong-field landscape, bigger than GR, which is precisely the essence of the phenomenon of spontaneous scalarization.

From the strong field perspective, the constraints usually come from the timing of binary systems [38–40]. These bounds are typically put in the microphysics of the theory, i.e., the restrictions on coupling parameters, which, in the case of the models discussed before, translates into a constraint on the coupling constant ξ. Indeed, the timing of radio pulsars in binary systems leads to the exclusion of the region $2\xi = \beta \lesssim -4.35$, mainly due to the effect of emission of dipolar gravitational radiation, which affects the dynamics of the two-body system at 1.5 post-Newtonian order (PN), in contrast with the quadrupolar emission of GR, that enter in a 2.5 PN order [38].

From the macroscopic phenomenological perspective, few constraints exist on the scalar charge Q. Horbatsch and Burgess [41], with model-independent analysis using the double pulsar, found $Q < 0.21$. But it is important to emphasize that a constraint on the scalar charge for a $\sim 1.4M_\odot$ NS does not necessarily translate into a constraint on the charge of a high mass $\sim 2.1M_\odot$ because there can be some models that allow spontaneous scalarization only for high mass NSs.

It is important to note also that pulsar timing of binary systems cannot constrain a massive STT when the orbital separation is larger than the characteristic length of the scalar field (Compton wavelength), $\lambda_\phi = (2\pi\hbar)/m_\varphi$. Thus, the scalar field is local, only affecting the NS structure and its immediate surroundings, leaving the orbital motion of wide binaries as in GR [see 42]. Another similar case arises when one considers fast rotation [43,44], with the strength of the scalar field increasing at the center and inside the star but decreasing quickly after some star radii.

For a massive STT, the main effect is the suppression of the scalar field proportional to the Yukawa term e^{-r/λ_ϕ} [42]. We stress that the constraints in the massive scenario differ significantly from those in the massless case. Observationally, the agreement between the orbital motion of close relativistic binaries and GR places constraints on STT, as STT predicts dipolar gravitational wave emission [38]. Given that the typical size of such compact binaries is about $r_{\rm bin} \sim 10^{10}$ m, dipolar gravitational radiation is suppressed if $r_{\rm bin} > \lambda_\phi$, which implies $m_\varphi > 10^{-16}$ eV. On the other hand, a maximum mass can be estimated by ensuring that scalarization is not suppressed inside the star. This condition requires $\lambda_\phi > R$, or equivalently, $m_\varphi < 10^{-9}$ eV. Therefore, the allowed mass range for the scalar field is $10^{-16}\,\text{eV} \lesssim m_\varphi \lesssim 10^{-9}\,\text{eV}$, which also accommodates a much broader range of the parameter ξ consistent with observations [42,45].

3 Pulse profile modeling

Pulse profile modeling is a powerful and crucial tool for analyzing localized surface emission of pulsars, such as the X-ray observations of NASA's NICER observatory [13]. Since the seminal work of Pechenick et al. [46], several studies have been made to model realistic pulse profile of neutrons stars [47–49], and by comparing them with data, its possible to infer the mass and radius of the star [50–54]. In addition, the magnetic field structure (related to the spot configurations [55]) and hot-spot temperatures could be obtained.

The basic idea is to make two transformations of the relevant quantities that describe the radiation emission. The first is from a frame co-rotating with the star to a frame just above the star's surface (a local Lorentz boost). The second transformation is from the star to the observer at infinity. The first transformation considers the special relativistic effects of the moving spot, such as aberration and Doppler boost. The second one, being non-local, collects the effect of gravity on photon propagation, such as the bending and time delay.

In the geometric optics approximation, the photon path is a null geodesic of the Just metric (14), whose Lagrangian is

$$\mathcal{L} = g_{\mu\nu} p^\mu p^\nu, \tag{20}$$

where p^α is the photon 4-momenta along the path $x^\alpha = (ct, \rho, \theta, \phi)$, parametrized by an affine parameter λ. The equations of motion follow from Euler–Lagrange equations, with two well-known constants of motion associated with energy and angular momentum conservation

$$dt/d\lambda = A^{-2}\epsilon f^{-b/a}, \tag{21}$$
$$d\rho/d\lambda = A^{-4}[c^2\epsilon^2 - (h/\rho)^2 f^{2b/a-1}], \tag{22}$$
$$d\theta/d\lambda = 0, \tag{23}$$
$$d\psi/d\lambda = A^{-2}(h/\rho^2) f^{b/a-1}. \tag{24}$$

We can make the identification of ψ with the azimuthal angle ϕ because of the spherical symmetry, i.e., the photon is always constrained to move on a plane, which we can choose as $\theta = \pi/2$. Also, from the two constants of motion (ϵ and h), we can define, as usual, the impact parameter of the photon as $\sigma \equiv h/\epsilon$.

Now we consider the emission angle α of the photon at the stellar surface, we have $\tan\alpha = [p^\psi p_\psi/(p^\rho p_\rho)]^{1/2}$ which gives a relation for the impact parameter σ:

$$\sin\alpha = \frac{\sigma}{\rho_s}(1 - \bar{a}_s)^{b/a-1/2}, \tag{25}$$

where $\bar{a}_s = a/\rho_s$, and ρ_s is the stellar radius in Just coordinates. Using the geodesic equations and the impact parameter, Silva and Yunes [20] were able to derive an integral expression for the angle ψ that generalizes the GR expression

$$\begin{aligned}\psi = 2\sin\alpha \int_0^1 dx\, x[1 - \bar{a}_s(1 - x^2)]^{b/a-1} \\ \times\{(1 - \bar{a}_s)^{2b/a-1} - (1 - x^2)^2 \\ [1 - \bar{a}_s(1 - x^2)]^{2b/a-1} \sin^2\alpha\}^{-1/2},\end{aligned} \tag{26}$$

where $x = \sqrt{1-y}$ and $y \equiv \rho_s/\rho$. (Although we do not use it in this work, in Appendix A we compare the Beloborodov approximation [56] for GR and its equivalent for STT.) In the GR limit, $a/b = 1$, and $\bar{a}_s$ becomes twice the compactness $2M/R$. In other words, in GR, the bending of the photon path will depend on the emission angle and the compactness, i.e., $\psi_{\rm GR} = \psi_{\rm GR}(\alpha, M/R)$. On the other hand, in STT, the bending will also depend on the scalar charge of the spacetime and the value of $\bar{a}_s$, i.e., $\psi_{\rm STT} = \psi_{\rm STT}(\alpha, \bar{a}_s, Q)$

In particular, the visible part of the star is defined by the light ray emitted tangentially to the local radial direction at the star's surface, i.e., $\alpha = \pi/2$. For low compactness, the value of ψ is close to α, and half of the star surface is visible.

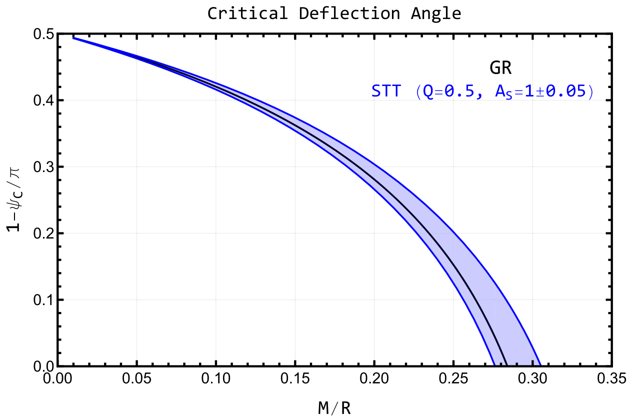

Fig. 1 Critical deflection angle in GR and scalar–tensor theory, with a charge of $Q = 0.5$ and a scale factor evaluated on the surface $A_s = 1 \pm 0.05$, where $A_s = 1.05$ correspond to the left boundary and $A_s = 0.95$ to the right boundary of the blue shaded area. Since the critical angle is equal to π, which means a star whose surface is fully visible, this affects the light curve and could be used to distinguish between the two theories. Notice that the relative changes of the critical view angle in STT and GR scale with the compactness in a nonlinear way

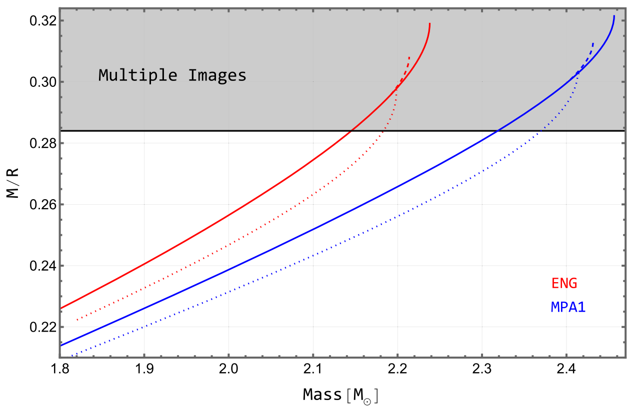

Fig. 2 Compactness versus ADM mass for two realistic EOS. The continuous lines represent the GR solution. The dotted lines correspond to scalarized solutions in STT for the MO coupling with $\xi = -3$, and the dashed lines at the end of each curve represent the scalarized solution with $\xi = 25$. We also mark the critical GR compactness that starts to produce a multiple-image region behind the star ($M/R = 0.284$)

But, as compactness increases, the bending increases, and ψ can become larger than π, meaning that there is a region behind the star where the light rays emitted can take two different paths to reach the observer, one in the direction of increasing ψ and the other of decreasing ψ. (An explicit example of such a phenomenon is given in the Appendix B.) As shown in Fig. 1, in GR $\psi_{\rm GR}(\pi/2, M/R) \equiv \psi_c = \pi$ for a compacteness $M/R = 0.284$, and the whole star surface is visible. We stress that ψ_c in STT changes nonlinearly with the compactness, as clear from Eq. (26). Thus, the same should happen with the relative changes of ψ_c and observables in STT and GR that depend on ψ.

In addition to the bending, the Shapiro time delay [57] also affects the photons. Working with the geodesics of the Just metric, Silva and Yunes [20] also derived an integral expression for the time delay, defined as

$$\Delta t \equiv t(\sigma) - t(\sigma = 0), \tag{27}$$

i.e., the time difference for a photon emitted directly towards the observer. With all these ingredients, the authors derive the differential flux formula in the context of the STT

$$dF = A_s^2 (1 - \bar{a}_s)^{\frac{1}{\sqrt{1+Q^2}}} \delta^5 \cos\alpha \frac{d\cos\alpha}{d\cos\psi} \frac{dA'}{D^2} I_0'(\alpha'), \tag{28}$$

where A_s is the conformal factor evaluated on the stellar surface, δ is the Doppler factor (whose expression can be seen in [20]), which takes into account the gravitational redshift, α is the local emission angle, dA' is the area element on the surface, D is the distance to the pulsar and I_0 is the specific intensity of radiation, which is naturally expressed in terms of α', the emission angle for an observer co-moving with the surface.

The values of A_s and Q for a given mass and compactness are needed to integrate the flux formula. With the mass, we can get the values of b and a using the scalar charge Q. The mass and compactness also specify the physical radius, which can be translated to ρ_s via the conformal factor A_s. We can perform an EOS-independent analysis using the exterior spacetime solution [20]. Namely, we can specify the mass and radius without integrating the interior relativistic structure equations and choosing suitable values for the scalar charge Q and conformal factor A_s, thus characterizing the exterior spacetime. We adopt a straightforward and intuitive approach of treating the stellar compactness as an independent parameter, which maintains theoretical consistency within observational limits and the predictions of STT and GR. This method allows for a flexible yet robust exploration of the differences between the theories, clearly demonstrating how compactness influences the phenomena of interest without requiring an explicit TOV (or modified TOV) solution. Table 1 lists the stellar models studied here.

To motivate possible compactness values to explore, we first present a specific solution following the model-dependent approach of integrating the interior equations for a given EOS to get the mass, radius, conformal factor at the surface, and the scalar charge via the asymptotic behavior of the external scalar field solution, Eq. (17). We choose a realistic EOS and an STT model, like the ones presented in 2.2. These models depend generally on just one free parameter, the value of the coupling constant ξ. Once we choose the value of ξ and a central pressure or density, we can integrate the equations outwards and obtain all the quantities needed to describe the exterior spacetime and compute the flux. As an example, Fig. 2 shows the equilibrium solutions for GR and STT ($\xi = -3, 25$) for the realistic ENG [58] and MPA1 [59] EOSs. GR and STT solutions have stellar configurations that go into the high compactness region to produce multiple images before reaching the maximum mass. One interesting case of specific coupling will be the one with $\xi > 0$ since they *scalarize* for stars with high mass and are still unconstrained by pulsar timing [33,60]. Unfortunately, in this case, the smallness of the scalar charge makes the difference in the light curve relative to the GR case negligible [60]. The differences between theories increase for high compactness, close to $M/R = 0.284$, especially for the tangentially emitted photons $\alpha \approx \pi/2$ (meaning $\psi \approx \psi_c$), as can be seen in Fig. 1.

The above solutions to the NS interior equilibrium equations with realistic EOSs demonstrate that GR and STT can result in high compactness configurations, allowing for multiple images in pulsars. To maintain generality, from now on, we adopt the previously mentioned model strategy of treating compactness as an independent parameter, having as references the critical threshold predicted by GR.

For the models considered here, following the choices of [20] with $Q = 0.5$ and a conformal factor varying 5% relative to 1, the critical angle ψ_C becomes π for a compactness in the range $[0.275, 0.305]$. This slight difference creates a large qualitative difference in the light curve because a star with $\psi_C > \pi$ develops a region behind it that produces multiple images so the photon can bend from one direction or another. Meanwhile, for a $\psi_C < \pi$, there is an invisible zone behind the star where the photons cannot reach the observer.

To make the model appropriate for astrophysical applications, one must go beyond the infinitesimal approximation, integrating the flux over an extended region of the star's surface. In this case,

$$F = F_0 A_s^2 (1 - \bar{a}_s)^{\frac{1}{\sqrt{1+Q^2}}} \iint_S \delta^5 \cos\alpha \sin\alpha \frac{d\alpha}{d\psi} \, d\psi \, d\phi, \tag{29}$$

where we choose spherical coordinates over the spot area S. Since we are dealing primarily with compact configurations, where the view bending angle can become larger than π, it is better to write the derivative as $\frac{d\alpha}{d\psi}$ to avoid the singularity when $\cos\psi = 0$. Also, F_0 is a phase-independent overall constant

$$F_0 \equiv \frac{I_0}{RD^2}. \tag{30}$$

Owing to the exploratory theoretical nature of the present work, we consider only one hot spot on the stellar surface, with a circular shape of semi-aperture angle $\Delta\psi$, to isolate the scalar-field effects. Likely, the light curve fitting of specific sources could require additional ingredients, such as complicated magnetic field structures over a simple-centered dipole or multiple spots [55,61,62]. The infinitesimal approximation works well for small spots ($\Delta\psi < 5^\circ$). For larger spots, one must integrate over the spot area. In this case, the difference between the theories increases because of the cumulative light bending, time delay, and gravitational redshift.

Let us briefly revisit the massive STT mentioned earlier. A high scalar field mass always suppresses the scalarization of the star, leading to a lower scalar field value at its surface [42]. For example, if one assumes that the flux equation (29) approximately holds for the massive case, Fig. 2 of Ref. [42] suggests that for $m_\varphi > 1.6 \times 10^{-12}$ eV, the flux differences between STT and GR become negligible. Therefore, the results presented in the next section for the massless case can be regarded as an upper limit on flux changes (see also [63] for a discussion of a massive scalar field in heavy NS with the "asymmetron" model). We leave precise details about the flux change in the case of highly compact NS with a massive scalar field for future work.

To characterize the flux, one must know the specific geometry of the source, which can be described by the angles (ι_0, θ_s), as illustrated in Fig. 3. Here, ι_0 is the angle between the rotational axis of the NS and line of sight (LoS), and θ_s is the colatitude of the spot's center relative to the rotational axis. The position of the spot's center will vary in time as the star rotates

$$\cos\psi_0 = \sin\iota_0 \sin\theta_s \cos\omega t + \cos\iota_0 \cos\theta_s, \tag{31}$$

where ω is the angular velocity of the star, and we choose $t = 0$ as the moment of closest approach between the spot and the observer. For the integration procedure, we follow [62,64,65]. The main difference here is the inclusion of the flux of the secondary image of the spot. The center of the secondary image is in the position $\psi_{sec} = 2\pi - \psi_0$, and we start to consider it when $\cos(\psi_0 + \Delta\psi) \leq \cos(\psi_c)$.

Here, we keep things simple enough to isolate the effects of STT on the light curves of compact NS. We do not include an atmosphere model, magnetic fields, and rotation effects on the exterior spacetime and star's structure. These ingredients must be included in STT [66] to be consistent.

4 Results

In Fig. 4, we show the bolometric flux of a spot with $\Delta\psi = 10^\circ$ for the compact stellar models of Table 1. In this case, we do not consider rotational effects (Doppler and time delay) and take the rotational frequency $\nu = 0$. For the GR star, the critical angle is $\psi_c = \pi$, and the whole surface of the star is visible, making a non-vanishing flux, even when the spot is behind the star. For the model STT1, according to Fig. 1, the critical angle is smaller than π ($\psi_c = 0.90\pi$), making an invisible zone of roughly $\sim 20^\circ$ behind the star, which eclipses the entire spot during a short period. In the case of the model STT2, the critical angle is a little greater than π ($\psi_c = 1.05\pi$), meaning that a zone of roughly $\sim 9^\circ$ starts to produce a second image when the spot reaches it, making that brightening observed in the light curve close to half the rational phase of the star.

One interesting fact about the light bending of compact stars is that visually, the star appears bigger than it is. For

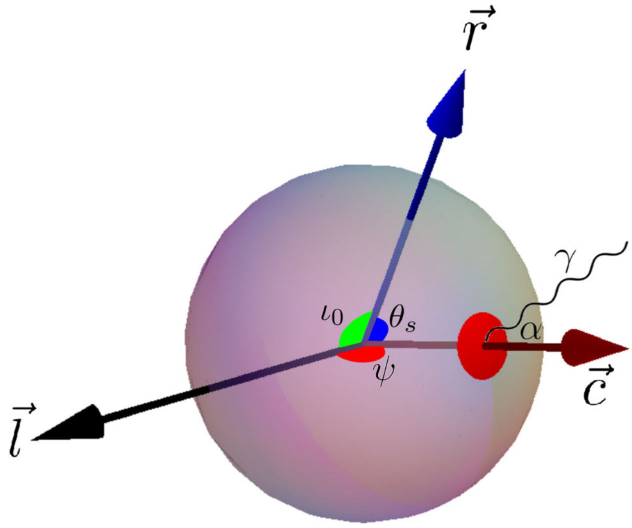

Fig. 3 Schematic representation of angles and vectors for the NS. **l** represents the line of sight, **r** denotes the axis of rotation, and **c** is normal to the center of the polar cap. The angle ψ is defined between **l** and **c**, and α represents the angle made by a photon leaving the star relative to **c**. Additionally, ι_0 is the angle between **l** and **r**, and θ_s is the angle between **c** and **r**

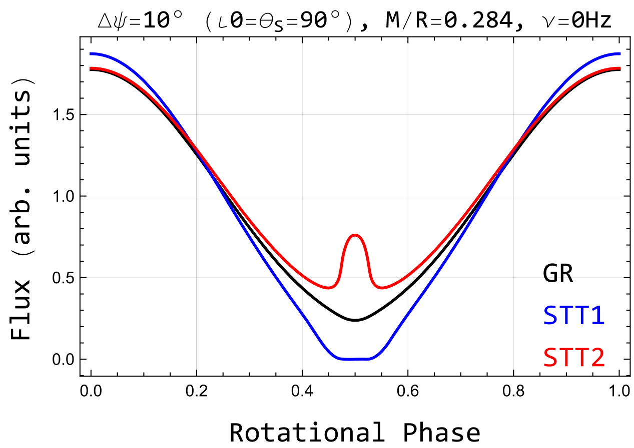

Fig. 4 Bolometric flux of the models relative to GR. The difference is more evident when the spot passes the area opposite the observer's line of sight, around half the rotational period. In one case there is an invisible zone and a multiple image zone in the other, producing a brightening in the flux. The huge difference between the fluxes is evident, both qualitatively and quantitatively

Table 1 Stellar models considered in the light curve analysis. We choose configurations that are doppelgängers of each other, with the same mass M and Jordan frame radius R, giving the same compactness value of $M/R = 0.284$. The STT models are chosen by fixing the conformal factor at the surface A_s and scalar charge Q. The values of ρ_s (Einstein Frame radius in Just coordinates), $\bar{a}_s = a/\rho_s$ and $\bar{b}_s = b/\rho_s$ are then obtained by Eq. (15), the b definition and Eq. (19), respectively

Stellar models								
Name	M/R	$M/M_\odot$	R/km	ρ_s/km	A_s	$\bar{a}_s$	$\bar{b}_s$	Q
GR	0.284	2.1	10.918	10.918	1	0.568	0.568	0
STT1	0.284	2.1	10.918	12.026	0.95	0.576	0.515	0.5
STT2	0.284	2.1	10.918	10.962	1.05	0.632	0.565	0.5

a $2.1M_\odot$ star, with compactness $M/R = 0.284$, the physical radius is 10.918 km. Still, using the impact parameter formula (25) for the last photon that we can see from the star surface ($\alpha = \pi/2$), we find a value of 16.611 km for GR, almost 50% bigger. A different gravitational field will of course also influence the visual appearance of the star, for the STT1 model the apparent radius is ~ 260 *m* bigger, and for STT2 ~ 340 m smaller, causing although a small perceptual difference of 1.6 and 2% respectively, with respect to GR.

These distinct features between the light curves can be appreciated for increasing compactness above $M/R = 0.275$ (see Appendix B) and a geometrical configuration where the spot crosses the invisible or multiple image region behind the star. To be more specific, the effect is evident when $\iota_0 + \theta_s - \pi \leq \Delta\psi$, meaning that the ideal configuration to test is with small hot spots seen edge-on that are near the stellar equator. Although it may sound particular, the analysis of Miller et al. [52] of NICER data from the massive ($2.08M_\odot$) pulsar PSR J0740+6620 is consistent with this geometrical configuration, making this source suitable for gravitational theory tests.

Although the light curves are qualitatively different for the same compactness, there is a degeneracy between the compactness and the scalar charge: a slightly more compact star in GR will start to produce the multiple image region, and a less compact one will produce an invisible zone. This is a reflex of the well-known degeneracy between the equation of state physics and the gravitational theory [see, e.g., 67]. To get a clear signature of the scalar charge on the light curve, one, in principle, needs an independent measurement of the mass and radius, which is difficult for millisecond pulsars, for example. The mass can be well measured by the radio timing of the pulses, while the radius measurement is way more elusive [68]. Still, multimessenger observations could help to break this degeneracy.

Even for geometric configurations where the spot does not cross the region opposite to the line of sight, the light curves of the models can be significantly different when we include rotational effects. Here, the spacetime is still spherically symmetric, and we keep the spherical shape of the star.

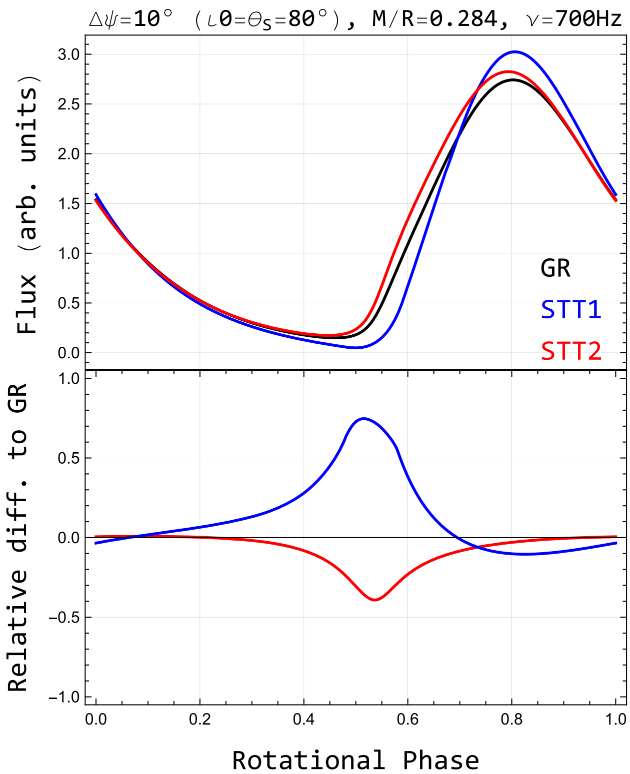

Fig. 5 Upper: Bolometric flux for a geometric configuration $\iota_0 = \theta_s = 80°$, where the spot's flux does not suffer the influence of the special region behind the star, so the differences are ascribed to the time-delay and gravitational redshift. Lower: STT cases relative difference relative to GR

Still, we include special relativity effects that depend crucially on the gravitational redshift and the time delay, which are small but enhanced by the integration over the extended spot. Motivated by observations, we choose, in the case of rotation, the frequency $\nu = 700$ Hz. In Fig 5, we show the bolometric light curve for a $\Delta\psi = 10°$ spot but for a configuration *almost equatorial*, with $\iota_0 = \theta_s = 80°$. In this case, we do not have the effect illustrated in Fig. 4 because the spot does not cross exactly the region behind the star. The difference is mainly due to the surface gravity that affects the special relativistic effects and the time delay integrated over the extended spot.

We emphasize that for a fast-rotating NS, one should include at least the dominant effect of the deformed stellar surface in the light curve analysis [48], but for geometrical configurations where $\iota_0 \approx \theta_s \approx 90°$, as discussed here, the approximation using a spherical surface works well and the effects of a rotating spacetime is subdominant, as demonstrated by Cadeau et al. [48] for the GR case.

5 Conclusion

While GR has passed all experimental tests, it remains imperative to scrutinize it for potential deviations, striving for greater precision. Among the notable alternative theories is scalar–tensor gravity, which posits an additional scalar degree of freedom alongside the metric tensor to describe gravitation and predict different phenomena, like *spontaneous scalarization* that affect both neutron stars structure and gravitational field.

In this work, we analyze a promising way to test STTs in the strong-field regime of high-mass pulsars: the pulse profile is very sensitive to the scalar charge when the compactness is close to $GM/(c^2R) \sim 0.284$. It makes compact systems with localized hot spot emission close to the equator, ideal for testing scalar-tensor theories and suggestively, alternative gravitational theories in general. Such an analysis needs the inclusion of all ingredients that enter the pulse profile analysis: gravitational redshift, light bending, time delay, and different stellar structures. The advantage of the STT used here is that it allows the analysis with an analytic, closed-form exterior spacetime solution for the light bending and time delay. The STT effects, especially for the light bending, are more pronounced for the light rays emitted tangentially relative to the stellar surface, as shown by the distinct features in Figs. 4 and 5. The latter shows flux differences of up to 80% in the spot's passage around the region opposite the line of sight (i.e., behind the star relative to the observer). This suggests that differences between GR and STT light curves can be significant in cases of high compactness. Therefore, that could be a promising observational approach to constrain deviations from GR. Due to the nonlinear dependence of the flux on compactness, slightly smaller values of the latter can result in much smaller relative changes of the former in STT and GR.

Figure 1 shows the nonlinearity of the differences between STTs and GR in the deflection angle. For a fixed scalar charge, configurations with a scale factor with the same excess or defect relative to the GR case lead to asymmetric stellar compactness values (relative to the GR case) at which the whole NS becomes visible. This is expected because STT changes are more relevant for more relativistic systems. The largest deviation of compactness is around 10% (when the star is not entirely visible ($\psi_c < \pi$), the relative changes are smaller). It is meaningful to compare the above numbers with NICER compactness constraints, which use GR, to gain insight into the feasibility of probing scalarization in compact stars. We use as reference pulsar PSR J0740+6620, constrained to having a radius [52,53] $R = 12.39^{+2.22}_{-1.50}$ km (90% credible interval). For the accurately-estimated mass of $2.08 M_\odot$, its compactness is 0.209–0.281, with a median of 0.248. Thus, the relative dispersion of compactness values is around 12–15%. Therefore, current NICER observations cannot yet differentiate GR from STTs. However, with the increasing accuracy of multimessenger constraints [52] or several gravitational-wave observations [69], it will be possible to differentiate theories using ray-tracing observables, especially for highly compact stars. The largest compactness dispersion produced by STT can also be used to estimate the radius uncertainty associated with scalarization. From the definition, $\mathcal{C} \equiv M/R$, it follows that $|\Delta R|/R = \Delta\mathcal{C}/\mathcal{C}$ for a well-constrained mass. Thus, $|\Delta R|/R \lesssim 10\%$ for the above parameters. This also suggests that $Q = 0.5$ is the maximum value of the charge parameter allowed by current radius constraints. Naturally, tighter constraints on Q and A or smaller values for ψ_c will reduce that uncertainty. Still, it is large enough to suggest that STT could generally impact radius inferences from light curves.

Large compactness values are generally associated with very dense systems where phase transitions can occur [70–72]. This means that probing scalarization could also be particularly relevant in hybrid stars [73]. If the surface tension of dense matter is large enough, the quark phase and the hadronic phase could be in direct touch (first-order phase transition). In this case, phase conversions could happen upon perturbations, and the matter would not be catalyzed anymore, meaning that the usual stability rules for NSs would be violated [73]. Such a violation would allow for an extended branch of (meta)stable NSs with large compactnesses (see, e.g., [74–78]). The terminal mass (where radial perturbations have null eigenfrequencies) within this branch is not known. Still, it could go down to values about ordinary stars [79]. All the above means that scalarization could be relevant for NSs of canonical mass, in addition to massive ones.

Gravitational theory tests using pulse profile modeling are still not sufficiently competitive compared to binary pulsar experiments for real astrophysical verification or for placing meaningful constraints. However, this subject remains a fresh and fertile area for research, as emphasized in [80]. In this work, we have presented promising configurations that could shed new light on the field. However, our model is still too simplified for application to real astrophysical sources. We must incorporate the possibility of multiple spots (e.g., [62,65]) with temperature distributions and account for atmospheric effects within the context of STT, which can attenuate tangentially emitted photons. Additionally, it is crucial to consider stellar oblateness. For instance, as an initial approximation, one could solve the structure equations up to second order in angular velocity [66] to obtain the star's quadrupole moment and shape, resulting in an oblate Just+Doppler model for the NS spacetime. With this more comprehensive theoretical model in hand, a statistical analysis can be performed, for example, using the NICER data for the high-mass pulsar PSR J0740+6620. This would enable us to obtain posterior values for the mass and radius and the parameters of the STT. We leave this analysis for future work.

Acknowledgements We thank the anonymous referee for their valuable suggestions and comments, which have helped improve this work. T. O. is grateful for the financial support of CAPES and the hospitality of the University of Ferrara. J.G.C. is grateful for the support of Fundação de Amparo à Pesquisa e Inovação do Espírito Santo (FAPES) (Grant nos. 1020/2022, 1081/2022, 976/2022, 332/2023), CNPq (Grant no. 311758/2021-5), and Fundação de Amparo à Pesquisa do Estado de São Paulo (FAPESP) (Grant no. 2021/01089-1). R.C.R.L. acknowledges the support of Fundação de Amparo à Pesquisa e Inovação do Estado de Santa Catarina (FAPESC) under Grant no. 2021TR912. J.P.P. is thankful for the financial support of FAPES under Grant no. 04/2022. This study was partly funded by the Coordenação de Aperfeiçoamento de Pessoal de Nível Superior - Brasil (CAPES)-Finance Code 001.

Data Availability Statement Data will be made available on reasonable request. [Authors' comment: The datasets generated during and/or analysed during the current study are available from the corresponding author on reasonable request].

Code Availability Statement Code/software will be made available on reasonable request. [Authors' comment: The code/software generated during and/or analysed during the current study is available from the corresponding author on reasonable request].

Funded by SCOAP[3].

Appendix A The Beloborodov approximation

Although this work focuses on the light curve of compact stars, a comment can be made about the well-established Beloborodov analytical approximation [56] in the context of STT. This approximation for the light bending integral, Eq. (26), is valid for compactness bellow $M/R \leq 0.25$, where we get an exact analytical formula without solving the integral numerically, saving computational time.

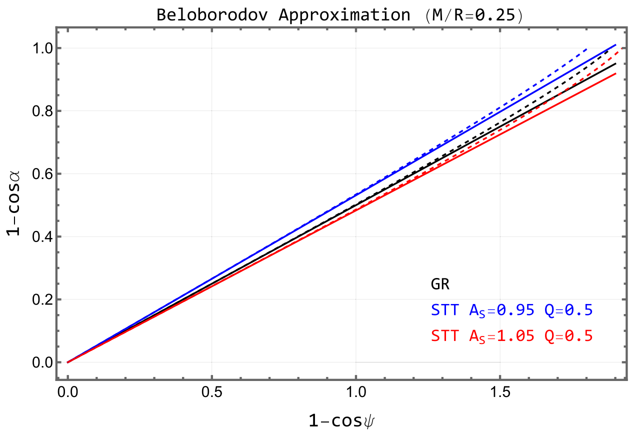

Fig. 6 Beloborodov approximation for compactness of $M/R = 0.25$. The dashed lines are the exact numerical result, and the solid lines are for the function $(1 - \cos\alpha) = (1 - 2x)(1 - \cos\psi)$, with $x = 0.25$ for GR and 0.234, 0.258 for the STT models. The fact that the lines run practically parallel shows compactness's main role in this geometric approximation. The error is a maximum of 7% for the emission angle $\alpha = \pi/2$

The Beloborodov formula reads

$$1 - \cos\alpha = (1 - 2\mathcal{C})(1 - \cos\psi) \tag{A1}$$

where $\mathcal{C}$ is the stellar compactness. In Fig. 6, we show the Beloborodov approximation for GR and the equivalent for the STT, choosing the value of the slope so that the error relative to the numerical results is similar. We fixed the scalar charge to be $Q = 0.5$ and the scale factor at the star's surface to vary 5% relative to 1. For the blue curve ($A_s = 0.95$), we put $\mathcal{C} = 0.234$, and for the red one ($A_s = 1.05$) $\mathcal{C} = 0.258$. We note that these values are very similar to the "effective compactness" in the STT solution $b_s/2 = GM/\rho_s c^2$, which are $b_s/2 = 0.228$ and $b_s/2 = 0.251$. We can interpret this as the compactness's key role in light bending, which dominates over the direct effect of the scalar charge [18]. The lines of GR and STT run almost parallel, and the error is a maximum of 7% for the emission angle $\alpha = \pi/2$.

Appendix B Increasing compactness and the appearance of multiple images of the spot

One of the key aspects of the results discussed here is the appearance of multiple images of the NS surface when the compactness increases over a critical value, which depends on the gravitational theory and crucially affects the light curve. The difference between the theories is small for compactness below the critical one, as seen from Fig. 7. The geometric configuration is similar to those of Fig. 5 of Hu et al. [22], and we also find within our model that the maximum

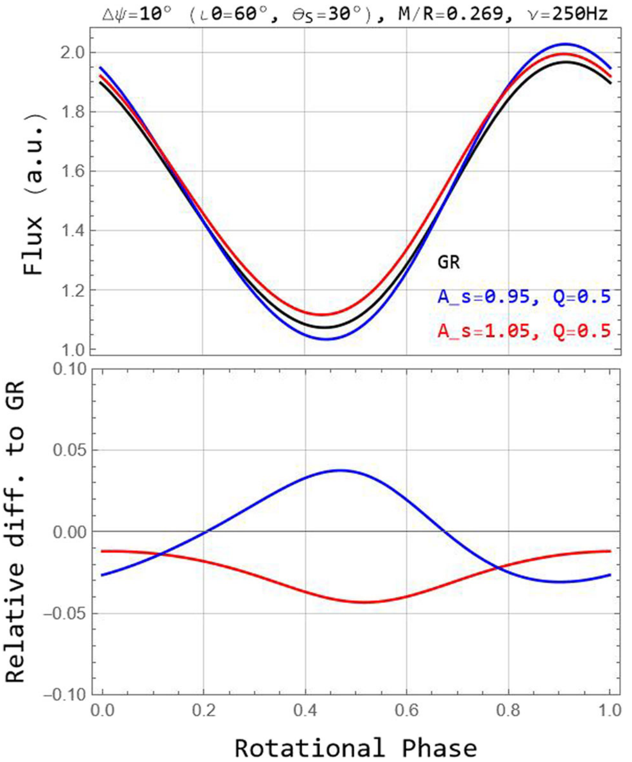

Fig. 7 The difference between the theories is small for compactness below critical and a geometrical configuration where the spot does not cross the region opposite to the LoS

relative change of the flux in STT and GR is smaller than 5%, in agreement with their findings.

But as compactness increases, the bending becomes strong enough so that the critical angle ψ_c can be greater than π, meaning that photons that leave a region behind the star, relative to the LoS, can take two paths to reach the observer, a phenomenon similar to gravitational lensing that can be seen in Fig. 8. We consider the Schwarzschild spacetime and a star with the critical compactness $\mathcal{C} = 0.284$.

One can appreciate in Fig. 9 the increasing sensitivity of the light curve as compactness increases in the interval [0.275, 0.305], where the GR solution (thick line) can be very different from the STT models considered (dotted and dashed). The brightening observed around half the rotational period, associated with the lensed secondary flux, can be compared with [17,23]. The peak of the brightening depends on the spot size, with smaller spots producing more pronounced peaks [23].

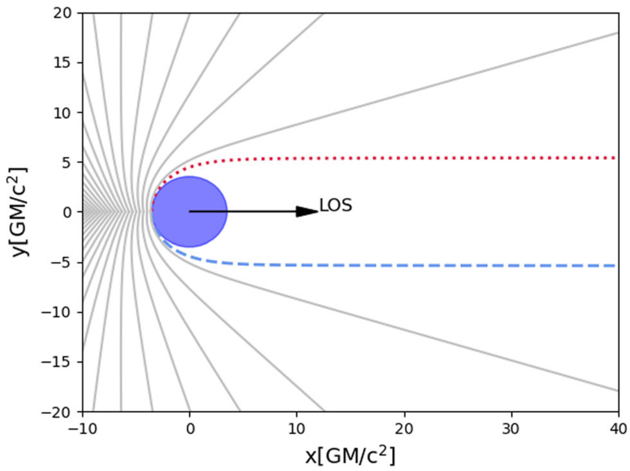

Fig. 8 Several geodesics starting from different heights relative to the NS equator are shown from an overhead view, with the line of sight (LOS) along the x-axis. The lensing effect of extreme bending is evident in two geodesics-red dotted and blue dashed-that originate from the same point behind the star's surface ($\psi = \pi$) and still reach the observer ($\psi = 0$) via two different paths. That is related to multiple images when the compactness is large enough. The NS compactness is $\mathcal{C} = 0.284$, and the spacetime is Schwarzschild

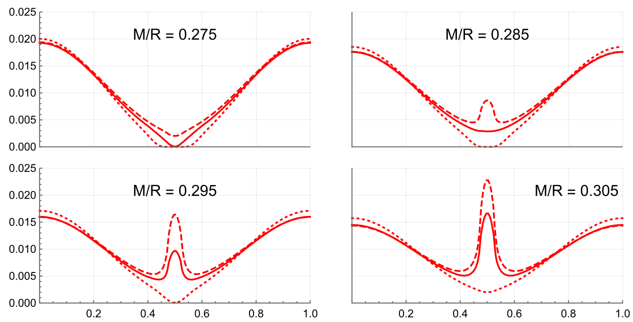

Fig. 9 Bolometric flux fixing the geometrical configuration to be $\iota_0 = \theta_s = 90°$ with a spot size $\Delta\psi = 10°$. The GR light curve is the thick one, while for the dotted one, we set $A_s = 0.95$, $Q = 0.5$ and for the dashed $A_s = 1.05$, $Q = 0.5$

References

1. J. Nättilä, J.J.E. Kajava, *Fundamental Physics with Neutron Stars* (Singapore, Springer Nature Singapore, 2022), pp.1–53. https://doi.org/10.1007/978-981-16-4544-0_105-1
2. E. Berti, E. Barausse, V. Cardoso, L. Gualtieri, P. Pani, U. Sperhake, L.C. Stein, N. Wex, K. Yagi, T. Baker, C.P. Burgess, F.S. Coelho, D. Doneva, A.D. Felice, P.G. Ferreira, P.C.C. Freire, J. Healy, C. Herdeiro, M. Horbatsch, B. Kleihaus, A. Klein, K. Kokkotas, J. Kunz, P. Laguna, R.N. Lang, T.G.F. Li, T. Littenberg, A. Matas, S. Mirshekari, H. Okawa, E. Radu, R. O'Shaughnessy, B.S. Sathyaprakash, C.V.D. Broeck, H.A. Winther, H. Witek, M.E. Aghili, J. Alsing, B. Bolen, L. Bombelli, S. Caudill, L. Chen, J.C. Degollado, R. Fujita, C. Gao, D. Gerosa, S. Kamali, H.O. Silva, J.G. Rosa, L. Sadeghian, M. Sampaio, H. Sotani, M. Zilhao, Testing general relativity with present and future astrophysical observations. Class. Quantum Gravity **32**(24), 243001 (2015). https://doi.org/10.1088/0264-9381/32/24/243001
3. Y. Fujii, K.I. Maeda, *The Scalar-Tensor Theory of Gravitation. Cambridge Monographs on Mathematical Physics* (Cambridge University Press, Cambridge, 2003)
4. D.D. Doneva, F.M. Ramazanoğlu, H.O. Silva, T.P. Sotiriou, S.S. Yazadjiev, Scalarization. (2022). https://doi.org/10.48550/arXiv.2211.01766

5. T. Damour, G. Esposito-Farese, Tensor-multi-scalar theories of gravitation. Class. Quantum Gravity **9**(9), 2093 (1992). https://doi.org/10.1088/0264-9381/9/9/015
6. T. Damour, G. Esposito-Farèse, Nonperturbative strong-field effects in tensor–scalar theories of gravitation. Phys. Rev. Lett. **70**, 2220–2223 (1993). https://doi.org/10.1103/PhysRevLett.70.2220
7. T. Damour, G. Esposito-Farèse, Tensor–scalar gravity and binary-pulsar experiments. Phys. Rev. D **54**, 1474–1491 (1996). https://doi.org/10.1103/PhysRevD.54.1474
8. V. Faraoni, A crucial ingredient of inflation. Int. J. Theor. Phys. **40**, 2259–2294 (2001). https://doi.org/10.1023/A:1012990305341. arXiv:hep-th/0009053
9. T. Clifton, P.G. Ferreira, A. Padilla, C. Skordis, Modified gravity and cosmology. Phys. Rep. **513**, 1–189 (2012). https://doi.org/10.1016/j.physrep.2012.01.001. arXiv:1106.2476 [astro-ph.CO]
10. D. Anderson, N. Yunes, E. Barausse, Effect of cosmological evolution on solar system constraints and on the scalarization of neutron stars in massless scalar–tensor theories. Phys. Rev. D **94**, 104064 (2016). https://doi.org/10.1103/PhysRevD.94.104064
11. S. Hollands, R.M. Wald, Quantum fields in curved spacetime. Phys. Rep. **574**, 1–35 (2015). https://doi.org/10.1016/j.physrep.2015.02.001. arXiv:1401.2026 [gr-qc]
12. J. Polchinski, *String Theory. Vol. 1: An Introduction to the Bosonic String. Cambridge Monographs on Mathematical Physics* (Cambridge University Press, Cambridge, 2007). https://doi.org/10.1017/CBO9780511816079
13. K.C. G et al., *The Neutron star Interior Composition Explorer (NICER): design and development*. in *Space Telescopes and Instrumentation 2016: Ultraviolet to Gamma Ray*, vol. 9905, eds. by J.W.A. den Herder, T. Takahashi, M. Bautz. International Society for Optics and Photonics (SPIE, 2016), p. 99051H. https://doi.org/10.1117/12.2231304
14. J. Antoniadis, P.C.C. Freire, N. Wex, T.M. Tauris, R.S. Lynch, M.H. van Kerkwijk, M. Kramer, C. Bassa, V.S. Dhillon, T. Driebe, J.W.T. Hessels, V.M. Kaspi, V.I. Kondratiev, N. Langer, T.R. Marsh, M.A. McLaughlin, T.T. Pennucci, S.M. Ransom, I.H. Stairs, J. van Leeuwen, J.P.W. Verbiest, D.G. Whelan, A massive pulsar in a compact relativistic binary. Science **340**(6131), 1233232 (2013). https://doi.org/10.1126/science.1233232
15. E. Fonseca, H.T. Cromartie, T.T. Pennucci, P.S. Ray, A.Y. Kirichenko, S.M. Ransom, P.B. Demorest, I.H. Stairs, Z. Arzoumanian, L. Guillemot, A. Parthasarathy, M. Kerr, I. Cognard, P.T. Baker, H. Blumer, P.R. Brook, M. DeCesar, T. Dolch, F.A. Dong, E.C. Ferrara, W. Fiore, N. Garver-Daniels, D.C. Good, R. Jennings, M.L. Jones, V.M. Kaspi, M.T. Lam, D.R. Lorimer, J. Luo, A. McEwen, J.W. McKee, M.A. McLaughlin, N. McMann, B.W. Meyers, A. Naidu, C. Ng, D.J. Nice, N. Pol, H.A. Radovan, B. Shapiro-Albert, C.M. Tan, S.P. Tendulkar, J.K. Swiggum, H.M. Wahl, W.W. Zhu, Refined mass and geometric measurements of the high-mass PSR J0740+6620. Astrophys. J. Lett. **915**(1), L12 (2021). https://doi.org/10.3847/2041-8213/ac03b8. arXiv:2104.00880 [astro-ph.HE]
16. R.W. Romani, D. Kandel, A.V. Filippenko, T.G. Brink, W. Zheng, PSR J0952–0607: the fastest and heaviest known galactic neutron star. Astrophys. J. **934**(2), L17 (2022). https://doi.org/10.3847/2041-8213/ac8007. arXiv:2207.05124 [astro-ph.HE]
17. H. Sotani, U. Miyamoto, Pulse profiles of highly compact pulsars in general relativity. Phys. Rev. D **98**, 044017 (2018). https://doi.org/10.1103/PhysRevD.98.044017
18. H. Sotani, Pulse profiles from a pulsar in scalar–tensor gravity. Phys. Rev. D **96**, 104010 (2017). https://doi.org/10.1103/PhysRevD.96.104010
19. H. Sotani, U. Miyamoto, Sensitivity of pulsar light curves to spacetime geometry and efficacy of analytic approximations. Phys. Rev. D **96**, 104018 (2017). https://doi.org/10.1103/PhysRevD.96.104018
20. H.O. Silva, N. Yunes, Neutron star pulse profiles in scalar–tensor theories of gravity. Phys. Rev. D **99**, 044034 (2019). https://doi.org/10.1103/PhysRevD.99.044034
21. R. Xu, Y. Gao, L. Shao, Strong-field effects in massive scalar–tensor gravity for slowly spinning neutron stars and application to X-ray pulsar pulse profiles. Phys. Rev. D **102**, 064057 (2020). https://doi.org/10.1103/PhysRevD.102.064057
22. Z. Hu, Y. Gao, R. Xu, L. Shao, Scalarized neutron stars in massive scalar–tensor gravity: X-ray pulsars and tidal deformability. Phys. Rev. D **104**, 104014 (2021). https://doi.org/10.1103/PhysRevD.104.104014
23. H. Sotani, Light curves from highly compact neutron stars with spot size effect. Phys. Rev. D **101**, 063013 (2020). https://doi.org/10.1103/PhysRevD.101.063013
24. T.P. Sotiriou, V. Faraoni, S. Liberati, Theory of gravitation theories: a no-progress report. Int. J. Mod. Phys. D **17**, 399–423 (2008). https://doi.org/10.1142/S0218271808012097. arXiv:0707.2748 [gr-qc]
25. B. Bertotti, L. Iess, P. Tortora, A test of general relativity using radio links with the Cassini spacecraft. Nature **425**, 374–376 (2003). https://doi.org/10.1038/nature01997
26. H.J. Kuan, A.G. Suvorov, D.D. Doneva, S.S. Yazadjiev, Gravitational waves from accretion-induced descalarization in massive scalar–tensor theory. Phys. Rev. Lett. **129**, 121104 (2022). https://doi.org/10.1103/PhysRevLett.129.121104
27. D.D. Doneva, C.J. Krüger, K.V. Staykov, P.Y. Yordanov, Neutron stars in Gauss–Bonnet gravity: nonlinear scalarization and gravitational phase transitions. Phys. Rev. D **108**, 044054 (2023). https://doi.org/10.1103/PhysRevD.108.044054
28. F.M. Ramazanoğlu, Spontaneous growth of vector fields in gravity. Phys. Rev. D **96**, 064009 (2017). https://doi.org/10.1103/PhysRevD.96.064009
29. J. Zhao, P.C.C. Freire, M. Kramer, L. Shao, N. Wex, Closing a spontaneous-scalarization window with binary pulsars. Class. Quantum Gravity **39**(11), 11LT01 (2022). https://doi.org/10.1088/1361-6382/ac69a3
30. V. Faraoni, Nonminimal coupling of the scalar field and inflation. Phys. Rev. D **53**, 6813–6821 (1996). https://doi.org/10.1103/PhysRevD.53.6813
31. D.S. Salopek, J.R. Bond, J.M. Bardeen, Designing density fluctuation spectra in inflation. Phys. Rev. D **40**, 1753–1788 (1989). https://doi.org/10.1103/PhysRevD.40.1753
32. A.S.M.C. Arapoğlu, K.Y. Ekşi, A.E. Yükselci, Neutron star structure in the presence of nonminimally coupled scalar fields. Phys. Rev. D **99**, 064055 (2019). https://doi.org/10.1103/PhysRevD.99.064055
33. R.F.P. Mendes, N. Ortiz, Highly compact neutron stars in scalar–tensor theories of gravity: spontaneous scalarization versus gravitational collapse. Phys. Rev. D **93**, 124035 (2016). https://doi.org/10.1103/PhysRevD.93.124035
34. K. Just, Notizen: the motion of mercury according to the theory of Thiry and Lichnerowicz. Zeitschrift für Naturforschung A **14**(8), 751 (1959). https://doi.org/10.1515/zna-1959-0810
35. R. Coquereaux, G. Esposito-Farese, The theory of Kaluza–Klein–Jordan–Thiry revisited. Ann. Inst. H. Poincare Phys. Theor. **52**, 113–150 (1990)
36. G. Creci, T. Hinderer, J. Steinhoff, Tidal properties of neutron stars in scalar–tensor theories of gravity. Phys. Rev. D **108**(12), 124073 (2023). https://doi.org/10.1103/PhysRevD.108.124073. arXiv:2308.11323 [gr-qc]
37. C.M. Will, *Theory and Experiment in Gravitational Physics*, 2nd edn. (Cambridge University Press, Cambridge, 2018). https://doi.org/10.1017/9781316338612
38. P.C.C. Freire, N. Wex, G. Esposito-Farèse, J.P.W. Verbiest, M. Bailes, B.A. Jacoby, M. Kramer, I.H. Stairs, J. Antoniadis, G.H. Janssen, The relativistic pulsar-white dwarf binary PSR

J1738+0333 – II. The most stringent test of scalar–tensor gravity. Mon. Not. Roy. Astron. Soc. **423**(4), 3328–3343 (2012). https://doi.org/10.1111/j.1365-2966.2012.21253.x. arXiv:1205.1450 [astro-ph.GA]
39. M. Kramer, I.H. Stairs, R.N. Manchester, N. Wex, A.T. Deller, W.A. Coles, M. Ali, M. Burgay, F. Camilo, I. Cognard, T. Damour, G. Desvignes, R.D. Ferdman, P.C.C. Freire, S. Grondin, L. Guillemot, G.B. Hobbs, G. Janssen, R. Karuppusamy, D.R. Lorimer, A.G. Lyne, J.W. McKee, M. McLaughlin, L.E. Münch, B.B.P. Perera, N. Pol, A. Possenti, J. Sarkissian, B.W. Stappers, G. Theureau, Strong-field gravity tests with the double pulsar. Phys. Rev. X **11**(4), 041050 (2021). https://doi.org/10.1103/PhysRevX.11.041050. arXiv:2112.06795 [astro-ph.HE]
40. P.C.C. Freire, N. Wex, Gravity experiments with radio pulsars. Living Rev. Relativ. **27**(1), 5 (2024). https://doi.org/10.1007/s41114-024-00051-y. arXiv:2407.16540 [gr-qc]
41. M.W. Horbatsch, C.P. Burgess, Model-independent comparisons of pulsar timings to scalar–tensor gravity. Class. Quantum Gravity **29**(24), 245004 (2012). https://doi.org/10.1088/0264-9381/29/24/245004. arXiv:1107.3585 [gr-qc]
42. F.M. Ramazanoğlu, F. Pretorius, Spontaneous scalarization with massive fields. Phys. Rev. D **93**, 064005 (2016). https://doi.org/10.1103/PhysRevD.93.064005
43. D.D. Doneva, S.S. Yazadjiev, N. Stergioulas, K.D. Kokkotas, Rapidly rotating neutron stars in scalar–tensor theories of gravity. (2014). arXiv:1309.0605
44. S.S. Yazadjiev, D.D. Doneva, D. Popchev, Slowly rotating neutron stars in scalar–tensor theories with a massive scalar field. (2016). arXiv:1602.04766
45. R. Rosca-Mead, C.J. Moore, U. Sperhake, M. Agathos, D. Gerosa, Structure of neutron stars in massive scalar–tensor gravity. Symmetry **12**(9), 1384 (2020). https://doi.org/10.3390/sym12091384
46. K.R. Pechenick, C. Ftaclas, J.M. Cohen, Hot spots on neutron stars – the near-field gravitational lens. Astrophys. J. **274**, 846–857 (1983). https://doi.org/10.1086/161498
47. J. Poutanen, A.M. Beloborodov, Pulse profiles of millisecond pulsars and their Fourier amplitudes. Mon. Not. Roy. Astron. Soc. **373**(2), 836–844 (2006). https://doi.org/10.1111/j.1365-2966.2006.11088.x. https://academic.oup.com/mnras/article-pdf/373/2/836/4106808/mnras0373-0836.pdf
48. C. Cadeau, S.M. Morsink, D. Leahy, S.S. Campbell, Light curves for rapidly rotating neutron stars. Astrophys. J. **654**(1), 458 (2007). https://doi.org/10.1086/509103
49. A.L. Watts, W. Yu, J. Poutanen, S. Zhang, S. Bhattacharyya, S. Bogdanov, L. Ji, A. Patruno, T.E. Riley, P. Bakala, A. Baykal, F. Bernardini, I. Bombaci, E. Brown, Y. Cavecchi, D. Chakrabarty, J. Chenevez, N. Degenaar, M. Del Santo, T. Di Salvo, V. Doroshenko, M. Falanga, R.D. Ferdman, M. Feroci, A.F. Gambino, M. Ge, S.K. Greif, S. Guillot, C. Gungor, D.H. Hartmann, K. Hebeler, A. Heger, J. Homan, R. Iaria, J.i. Zand, O. Kargaltsev, A. Kurkela, X. Lai, A. Li, X. Li, Z. Li, M. Linares, F. Lu, S. Mahmoodifar, M. Méndez, M. Coleman Miller, S. Morsink, J. Nättilä, A. Possenti, C. Prescod-Weinstein, J. Qu, A. Riggio, T. Salmi, A. Sanna, A. Santangelo, H. Schatz, A. Schwenk, L. Song, E. Šrámková, B. Stappers, H. Stiele, T. Strohmayer, I. Tews, L. Tolos, G. Török, D. Tsang, M. Urbanec, A. Vacchi, R. Xu, Y. Xu, S. Zane, G. Zhang, S. Zhang, W. Zhang, S. Zheng, X. Zhou, Dense matter with eXTP. Sci. China Phys. Mech. Astron. **62**(2), 29503 (2019). https://doi.org/10.1007/s11433-017-9188-4. arXiv:1812.04021 [astro-ph.HE]
50. T.E. Riley et al., A *NICER* view of PSR J0030+0451: millisecond pulsar parameter estimation. Astrophys. J. Lett. **887**(1), L21 (2019). https://doi.org/10.3847/2041-8213/ab481c. arXiv:1912.05702 [astro-ph.HE]
51. M.C. Miller et al., PSR J0030+0451 mass and radius from *NICER* data and implications for the properties of neutron star matter. Astrophys. J. Lett. **887**(1), L24 (2019). https://doi.org/10.3847/2041-8213/ab50c5. arXiv:1912.05705 [astro-ph.HE]
52. M.C. Miller, F.K. Lamb, A.J. Dittmann, S. Bogdanov, Z. Arzoumanian, K.C. Gendreau, S. Guillot, W.C.G. Ho, J.M. Lattimer, M. Loewenstein, S.M. Morsink, P.S. Ray, M.T. Wolff, C.L. Baker, T. Cazeau, S. Manthripragada, C.B. Markwardt, T. Okajima, S. Pollard, I. Cognard, H.T. Cromartie, E. Fonseca, L. Guillemot, M. Kerr, A. Parthasarathy, T.T. Pennucci, S. Ransom, I. Stairs, The radius of PSR J0740+6620 from NICER and XMM-Newton data. Astrophys. J. Lett. **918**(2), L28 (2021). https://doi.org/10.3847/2041-8213/ac089b. arXiv:2105.06979 [astro-ph.HE]
53. T.E. Riley, A.L. Watts, P.S. Ray, S. Bogdanov, S. Guillot, S.M. Morsink, A.V. Bilous, Z. Arzoumanian, D. Choudhury, J.S. Deneva, K.C. Gendreau, A.K. Harding, W.C.G. Ho, J.M. Lattimer, M. Loewenstein, R.M. Ludlam, C.B. Markwardt, T. Okajima, C. Prescod-Weinstein, R.A. Remillard, M.T. Wolff, E. Fonseca, H.T. Cromartie, M. Kerr, T.T. Pennucci, A. Parthasarathy, S. Ransom, I. Stairs, L. Guillemot, I. Cognard, A NICER view of the massive pulsar PSR J0740+6620 informed by radio timing and XMM-Newton spectroscopy. Astrophys. J. Lett. **918**(2), L27 (2021). https://doi.org/10.3847/2041-8213/ac0a81. arXiv:2105.06980 [astro-ph.HE]
54. D. Choudhury et al., A NICER view of the nearest and brightest millisecond pulsar: PSR J0437-4715. Astrophys. J. Lett. **971**(1), L20 (2024). https://doi.org/10.3847/2041-8213/ad5a6f. arXiv:2407.06789 [astro-ph.HE]
55. A.V. Bilous, A.L. Watts, A.K. Harding, T.E. Riley, Z. Arzoumanian, S. Bogdanov, K.C. Gendreau, P.S. Ray, S. Guillot, W.C.G. Ho, D. Chakrabarty, A nicer view of PSR J0030+0451: evidence for a global-scale multipolar magnetic field. Astrophys. J. Lett. **887**(1), L23 (2019). https://doi.org/10.3847/2041-8213/ab53e7
56. A.M. Beloborodov, Gravitational bending of light near compact objects. Astrophys. J. **566**(2), L85 (2002). https://doi.org/10.1086/339511
57. S.L. Shapiro, S.A. Teukolsky, Black holes, white dwarfs and neutron stars. Phys. Compact Objects (1983). https://doi.org/10.1002/9783527617661
58. L. Engvik, E. Osnes, M. Hjorth-Jensen, G. Bao, E. Ostgaard, Asymmetric nuclear matter and neutron star properties. Astrophys. J. **469**, 794 (1996). https://doi.org/10.1086/177827. arXiv:nucl-th/9509016 [nucl-th]
59. H. Müther, M. Prakash, T. Ainsworth, The nuclear symmetry energy in relativistic Brueckner–Hartree–Fock calculations. Phys. Lett. B **199**(4), 469–474 (1987). https://doi.org/10.1016/0370-2693(87)91611-X
60. R.F.P. Mendes, T. Ottoni, Scalar charges and pulsar-timing observables in the presence of nonminimally coupled scalar fields. Phys. Rev. D **99**, 124003 (2019). https://doi.org/10.1103/PhysRevD.99.124003
61. J. Pétri, Multipolar electromagnetic fields around neutron stars: exact vacuum solutions and related properties. Mon. Not. Roy. Astron. Soc. **450**(1), 714–742 (2015). https://doi.org/10.1093/mnras/stv598
62. R.C.R. de Lima, J.P. Pereira, J.G. Coelho, R.C. Nunes, P.E. Stecchini, M. Castro, P. Gomes, R.R. da Silva, C.V. Rodrigues, J.C.N. de Araujo, M. Bejger, P. Haensel, J.L. Zdunik, Evidence for 3XMM J185246.6+003317 as a massive magnetar with a low magnetic field. J. High Energy Astrophys. **42**, 52–62 (2024). https://doi.org/10.1016/j.jheap.2024.04.001. arXiv:2210.06648 [astro-ph.HE]
63. S. Morisaki, T. Suyama, Spontaneous scalarization with an extremely massive field and heavy neutron stars. Phys. Rev. D **96**, 084026 (2017). https://doi.org/10.1103/PhysRevD.96.084026
64. R. Turolla, L. Nobili, Pulse profiles from thermally emitting neutron stars. Astrophys. J. **768**(2), 147 (2013). https://doi.org/10.1088/0004-637X/768/2/147
65. R.C.R. de Lima, J.G. Coelho, J.P. Pereira, C.V. Rodrigues, J.A. Rueda, Evidence for a multipolar magnetic field in SGR J1745–

2900 from X-ray light-curve analysis. Astrophys. J. **889**(2), 165 (2020). https://doi.org/10.3847/1538-4357/ab65f4
66. P. Pani, E. Berti, Slowly rotating neutron stars in scalar–tensor theories. Phys. Rev. D **90**, 024025 (2014). https://doi.org/10.1103/PhysRevD.90.024025
67. L. Shao, Degeneracy in studying the supranuclear equation of state and modified gravity with neutron stars. AIP Conf. Proc. **2127**(1), 020016 (2019). https://doi.org/10.1063/1.5117806. https://pubs.aip.org/aip/acp/article-pdf/doi/10.1063/1.5117806/14067591/020016_1_online.pdf
68. S. Ascenzi, V. Graber, N. Rea, Neutron-star measurements in the multi-messenger era. Astropart. Phys. (2024). https://doi.org/10.1016/j.astropartphys.2024.102935
69. K. Chatziioannou, Uncertainty limits on neutron star radius measurements with gravitational waves. Phys. Rev. D **105**(8), 084021 (2022). https://doi.org/10.1103/PhysRevD.105.084021. arXiv:2108.12368 [gr-qc]
70. E. Annala, T. Gorda, A. Kurkela, J. Nättilä, A. Vuorinen, Evidence for quark-matter cores in massive neutron stars. Nat. Phys. **16**(9), 907–910 (2020). https://doi.org/10.1038/s41567-020-0914-9. arXiv:1903.09121 [astro-ph.HE]
71. J.P. Pereira, M. Bejger, J.L. Zdunik, P. Haensel, Differentiating between sharp and smoother phase transitions in neutron stars. Phys. Rev. D **105**(12), 123015 (2022). https://doi.org/10.1103/PhysRevD.105.123015. arXiv:2201.01217 [astro-ph.HE]
72. T. Gorda, K. Hebeler, A. Kurkela, A. Schwenk, A. Vuorinen, Constraints on strong phase transitions in neutron stars. Astrophys. J. **955**(2), 100 (2023). https://doi.org/10.3847/1538-4357/aceefb. arXiv:2212.10576 [astro-ph.HE]
73. J.P. Pereira, C.V. Flores, G. Lugones, Phase transition effects on the dynamical stability of hybrid neutron stars. Astrophys. J. **860**, 12 (2018). https://doi.org/10.3847/1538-4357/aabfbf. arXiv:1706.09371 [gr-qc]
74. F. Di Clemente, M. Mannarelli, F. Tonelli, Reliable description of the radial oscillations of compact stars. Phys. Rev. D **101**(10), 103003 (2020). https://doi.org/10.1103/PhysRevD.101.103003. arXiv:2002.09483 [gr-qc]
75. L. Tonetto, G. Lugones, Discontinuity gravity modes in hybrid stars: assessing the role of rapid and slow phase conversions. Phys. Rev. D **101**(12), 123029 (2020). https://doi.org/10.1103/PhysRevD.101.123029. arXiv:2003.01259 [astro-ph.HE]
76. G. Lugones, A.G. Grunfeld, Phase conversions in neutron stars: implications for stellar stability and gravitational wave astrophysics. Universe **7**(12), 493 (2021). https://doi.org/10.3390/universe7120493
77. V.P. Gonçalves, L. Lazzari, Impact of slow conversions on hybrid stars with sequential QCD phase transitions. Eur. Phys. J. C **82**(4), 288 (2022). https://doi.org/10.1140/epjc/s10052-022-10273-5. arXiv:2201.03304 [nucl-th]
78. P.B. Rau, A. Sedrakian, Two first-order phase transitions in hybrid compact stars: higher-order multiplet stars, reaction modes, and intermediate conversion speeds. Phys. Rev. D **107**(10), 103042 (2023). https://doi.org/10.1103/PhysRevD.107.103042. arXiv:2212.09828 [astro-ph.HE]
79. J.P. Pereira, M. Bejger, L. Tonetto, G. Lugones, P. Haensel, J.L. Zdunik, M. Sieniawska, Probing elastic quark phases in hybrid stars with radius measurements. Astrophys. J. **910**(2), 145 (2021). https://doi.org/10.3847/1538-4357/abe633. arXiv:2011.06361 [astro-ph.HE]
80. H.O. Silva, in *Recent Progress on Gravity Tests: Challenges and Future Perspectives*, ed. by C. Bambi, A. Cárdenas-Avendaño (Springer Nature, Singapore, 2024), pp. 101–147. https://doi.org/10.1007/978-981-97-2871-8_4

Impact of stratified rotation on the moment of inertia of neutron stars

Jonas P. Pereira,[1,2,3,*] Tulio Ottoni,[2,4] Jaziel G. Coelho,[2,5] Jorge A. Rueda,[6,7,8,9,10,†] and Rafael C. R. de Lima[11]

[1]*Departamento de Astronomia, Instituto de Astronomia, Geofísica e Ciências Atmosféricas (IAG), Universidade de São Paulo, São Paulo, 05508-090, Brazil*
[2]*Núcleo de Astrofísica e Cosmologia (Cosmo-Ufes) and Departamento de Física, Universidade Federal do Espírito Santo, Vitória, 29075-910, ES, Brazil*
[3]*Nicolaus Copernicus Astronomical Center, Polish Academy of Sciences, Warsaw, 00-716, Poland*
[4]*Università degli Studi di Ferrara, Via Saragat 1, I–44122 Ferrara, Italy*
[5]*Divisão de Astrofísica, Instituto Nacional de Pesquisas Espaciais, São José dos Campos, 12227-010, São Paulo, Brazil*
[6]*ICRANet, Piazza della Repubblica 10, I-65122 Pescara, Italy*
[7]*ICRA, Dipartimento di Fisica, Sapienza Università di Roma, Piazzale Aldo Moro 5, I-00185 Roma, Italy*
[8]*ICRANet-Ferrara, Dipartimento di Fisica e Scienze della Terra, Università degli Studi di Ferrara, Via Saragat 1, I–44122 Ferrara, Italy*
[9]*Dipartimento di Fisica e Scienze della Terra, Università degli Studi di Ferrara, Via Saragat 1, I–44122 Ferrara, Italy*
[10]*INAF, Istituto di Astrofisica e Planetologia Spaziali, Via Fosso del Cavaliere 100, 00133 Rome, Italy*
[11]*Universidade do Estado de Santa Catarina, Joinville, 89219-710, Brazil*

(Received 9 August 2024; accepted 17 October 2024; published 12 November 2024)

Rigid (uniform) rotation is usually assumed when investigating the properties of mature neutron stars (NSs). Although it simplifies their description, it is an assumption because we cannot observe the NS's innermost parts. Here, we analyze the structure of NSs in the simple case of "almost rigidity," where the innermost and outermost parts rotate with different angular velocities. This is motivated by the possibility of NSs having superfluid interiors, phase transitions, and angular momentum transfer during accretion processes. We show that, in general relativity, the relative difference in angular velocity between different parts of an NS induces a change in the moment of inertia compared to that of rigid rotation. The relative change depends *nonlinearly* on where the angular velocity jump occurs inside the NS. For the same observed angular velocity in both configurations, if the jump location is close to the star's surface—which is possible in central compact objects (CCOs) and accreting stars—the relative change in the moment of inertia is close to that of the angular velocity (which is expected due to total angular momentum aspects). If the jump occurs deep within the NS, for instance, due to phase transitions or superfluidity, smaller relative changes in the moment of inertia are observed; we found that if it is at a radial distance smaller than approximately 40% of the star's radius, the relative changes are negligible. Additionally, we outline the relevance of systematic uncertainties that nonrigidity could have on some NS observables, such as radius, ellipticity, and the rotational energy budget of pulsars, which could explain the x-ray luminosity of some sources. Finally, we also show that nonrigidity weakens the universal I-Love-Q relations.

DOI: 10.1103/PhysRevD.110.103014

I. INTRODUCTION

A reasonable picture of the neutron star (NS) structure has emerged after more than half a century since the discovery of pulsars [1]. First, there is an atmosphere of ionized matter, probably hydrogen or helium, with a composition that depends on the environment and can be affected by strong magnetic fields. Under the atmosphere, we have the ocean and then the crust, a lattice of increasingly heavy elements and neutron richness until the point of neutron drip density, which is energetically favorable to have free neutrons instead of being bound to nuclei. When the density increases, the lattice structure disappears, giving way to a liquid structure of primarily protons, neutrons, and electrons (outer core). Matter here is expected to be a superfluid. Going deeper into the inner core of an NS, several extra possibilities emerge, such as meson condensates [2], hyperons, and deconfined quarks [3]. The core of an NS is where most of its mass is concentrated, and the energy density can be several times the nuclear saturation density.

*Contact author: jpereira@camk.edu.pl
†Contact author: jorge.rueda@icra.it

As all NS are spinning with frequencies ranging from sub-Hz [4] to several hundreds of Hz [5,6], it is crucial to describe appropriately the rotation and its effects on the star's observables. With such a rich and complicated internal structure, is treating a spinning NS as a rigid body reasonable? Numerical simulations show that newborn NS in mergers, supernova explosions, and main sequence stars all present differential rotation [7]. But even in an old and evolved NS, we can imagine different rotations between the crust and a weakly coupled superfluid core component due to vortices. Moreover, if there is a phase transition to quark matter in the neutron star core [8], simple angular momentum conservation considerations will demand a differential rotation between the crust and the now more compact core.

A clear example where rotation stratification is relevant is in the Sun. An abrupt change in angular velocity is possible due to the tachocline [9], a very thin layer between the Sun's core and the convective envelope. In the case of NSs, the Ekman layer [10] between the core and the crust may also lead to an abrupt change in the rotation of the phases it splits. Of course, stars also have dissipation mechanisms such as viscosity [11], which leads to a uniform rotation inside some part of the star. However, there is still room for nonrigid rotation between two different phases of stars for those in the process of "settling in" (such as due to accretion) and those that are "old" (that could have superfluid parts).

Regarding the viscosity, it has been estimated (see [12] and references therein for details) the characteristic timescales for an NS to reach uniform rotation. Assuming that superfluids are present in the outer core of an NS, the shear viscosity of the liquid core (η) would be dominated by electron-electron scattering (η_{ee}), which is

$$\eta_{\mathrm{ee}} = 4.7 \times 10^{19} T_8^{-2} \left(\frac{\rho}{\rho_{\mathrm{sat}}}\right)^2 \mathrm{~g\,cm^{-1}\,s^{-1}}, \tag{1}$$

where ρ is the density, T_8 is the temperature in units of 10^8 K, and $\rho_{\mathrm{sat}} = 2.7 \times 10^{14}\ \mathrm{g\,cm^{-3}}$ is the nuclear saturation density. In addition, $\eta \equiv \rho\nu$, where ν is the kinematic shear viscosity. Finally, the viscosity timescale can be estimated as $t_{\mathrm{vis}} \sim R^2/\nu$, where R is the NS radius. From the above equation, one thus has

$$t_{\mathrm{vis}}^{\mathrm{supfl}} = 0.18 R_6^2 T_8^2 \left(\frac{\rho}{\rho_{\mathrm{sat}}}\right)^{-1} \left(\frac{\eta}{\eta_{\mathrm{ee}}}\right)^{-1} \mathrm{~yr}, \tag{2}$$

with $R_6 = R/(10^6\ \mathrm{cm})$. For instance, taking $T_8 = 1$, $R = 10$ km and $\rho = \rho_{\mathrm{sat}}$, it follows that $t_{\mathrm{vis}}^{\mathrm{supfl}} \approx 0.2$ yr. Thus, a superfluid phase in a star could be safely taken as having a uniform rotation. For the crust of an NS, analysis from [13] shows that $\eta_{\mathrm{crust}} \sim 10^{15}\ \mathrm{g\,cm^{-1}\,s^{-1}}$ for $\rho_{\mathrm{crust}} = \rho_{\mathrm{sat}}/2$ and $T_8 = 1$. Thus, $t_{\mathrm{vis}}^{\mathrm{crust}} = R^2 \rho_{\mathrm{crust}}/\eta_{\mathrm{crust}} \sim 10$ kyr, much longer than the superfluid region. Therefore, for old (i.e., aging more than the above timescale), nonaccreting NSs, assuming rigid rotation of the crust is reasonable. When it comes to the timescale it takes for a superfluid phase and a nonsuperfluid phase to equilibrate their rotations, the answer is much more complex. Up to now, there is no precise mechanism for the core-crust angular momentum transfer. The occurrence of glitches suggests that the timescale for the rigid rotation of the whole star to be attained may be significant. Although the star will eventually reach an equilibrium angular momentum, this does not mean that angular velocities will be equal. This is because the superfluid part of the star (outer core and inner crust) is generally much larger in mass than the nonsuperfluid part (outer crust) [1].

This work aims to draw attention to the implications of rotation stratification of NSs, where we examine its impact on some relevant stellar observables. In general relativity (GR), the total angular moment J appears as a constant of integration from the field equations [14] at the first order in the rotation parameter, associated with frame dragging. With the corresponding J, we find the moment of inertia I by simply dividing it by the observed angular velocity Ω of the NS surface, measured, for example, with radio pulse timing, i.e., $I \equiv J/\Omega$. Note that this result is intrinsically general relativistic because J comes directly from GR, and it generalizes the classical moment of inertia of stars with axial symmetry [14]. In the Newtonian framework, rotation generally influences the moment of inertia by altering the star's equilibrium shape, thereby affecting its mass distribution. However, for slow rotation (reasonable approximation for old NSs), the deviation from the moment of inertia in the static, spherically symmetric case remains small. On the other hand, when GR is also taken into account, boundary conditions for the angular velocity can have an imprint on I. That means that even in the perturbative case the background aspects of the star are enough in general. Thus, for NSs, the way internal parts rotate matters for the moment of inertia.

A relevant motivation for our study is that it will soon be possible to infer the moment of inertia directly from observations. For instance, further timing measurements of PSR J0737–3039A/B, the *double pulsar*, will allow for further improvement in the constraints of the system post-Keplerian parameters, e.g., the periastron advance [15–17]. Indeed, the inclusion of the pulsar A mass-energy loss owing to spindown will lead to a direct measurement of its moment of inertia with 11% accuracy by 2030 [17,18]. Another motivation is that the moment of inertia is important for several observables, such as the rotational energy, energy budget of stars, deformations, production of gravitational waves (GWs), the braking index and the physics of glitches [19].

The structure of the paper is as follows: In Sec. II, we give the basic details about slow rotation in general relativity, focusing on rigid rotation, differential rotation, the correct boundary conditions when there is rotation stratification in NSs, the general relativistic version of the moment of inertia for stars and their rotational energy in this context. Section III discusses some expected relative changes of the moment of inertia in the case of one-phase and hybrid stars when rotation stratification is present. Finally, in Sec. IV, we discuss the main points raised and show several astrophysical observables that could be affected by nonrigid rotation. We work with geometric units and metric signature +2 unless otherwise specified.

II. SLOW ROTATION IN GR, ANGULAR MOMENTUM, AND MOMENT OF INERTIA

After Hartle and collaborators [14,20–26], the problem of slowly rotating stars has been characterized and extensively explored. When it comes to the equations governing the motion of fluid elements and most metric components, they only appear in the second order of the rotation parameter Ω, supposed to be small ($R\Omega \ll 1$, where R is the stellar radius). However, the description of the angular rotation of the star's fluid, locally and for observers at infinity, is done in the first order of the rotation parameter. The structure of the star is described by the Tolman-Oppenheimer-Volkoff (TOV) equation, assuming spherical symmetry and a perfect-fluid description.

In particular, the background spacetime is defined as

$$ds^2 = -e^{\nu(r)}dt^2 + e^{\lambda(r)}dr^2 + r^2 d\theta^2 + r^2 \sin^2\theta d\varphi^2. \quad (3)$$

The unperturbed spacetime spherical symmetry allows the metric and variables decomposition into spherical harmonics (Y_l^m) or Legendre polynomials (P_l, $m = 0$).

A. Rigid rotation

Up to the first order in the rotation parameter (for $l = 1$), Hartle showed that the equation describing the rate of rotation of inertial frames, $\omega(r)$, is given by

$$\frac{1}{r^4}\frac{d}{dr}\left(r^4 j(r)\frac{d\omega}{dr}\right) - \frac{4}{r}\frac{dj}{dr}(\Omega - \omega) = 0, \quad (4)$$

where $j(r) \equiv e^{-(\lambda+\nu)/2}$. In addition, Ω is the velocity of the fluid as seen by an observer at rest in the fluid. Equation (4) is a direct consequence of the $t\varphi$-component of the Einstein equations, which becomes relevant when deducing the boundary conditions in the stratified case.

In rigid rotation, i.e., Ω constant, one could absorb it in the first term of the above equation and get [14]

$$\frac{1}{r^4}\frac{d}{dr}\left(r^4 j(r)\frac{d\bar{\omega}}{dr}\right) + \frac{4}{r}\frac{dj}{dr}\bar{\omega} = 0, \quad (5)$$

with $\bar{\omega} \equiv \Omega - \omega$, the fluid's angular velocity relative to a freely falling observer, or, in other words, the fluid's angular velocity relative to the local inertial frame.

B. Differential rotation

In the case of differential rotation, where $\Omega = \Omega(r)$ [23], the appropriate equation to be taken into account is (4). In addition, to solve it, a prescription for $\Omega(r)$ should be given. Based on the sun's case [27], one would expect that Ω would not be the same throughout the star. However, if the star is old enough, it seems reasonable to assume rigid rotation given the action of angular momentum loss mechanisms. At the same time, that is exactly when superfluidity would play a role in the star's angular momentum. Thus, even for old stars, differential rotation should not be overlooked.

Here, we *do not* work with differential rotation *per se*, but we approach it by considering a toy model where some parts of the star rotate with different angular velocities. That should be seen as a phenomenological model trying to capture some of the rich physics in stars that would lead to a spatially varying rotation rate. This model should be applicable for some time intervals during the lives of compact stars. For instance, a young NS star born in a core-collapse supernova or an NS binary merger should experience some form of differential rotation [28]; it should also exist, at least transiently, in the case of fallback accretion (e.g., associated with central compact objects—CCOs—and recycled pulsars) [29], or even during an NS phase transition by angular momentum conservation.

C. Boundary conditions

Given that, loosely speaking, the problem of perturbations of stars is a Sturm-Louiville problem, boundary conditions are paramount for their solutions. Hartle and collaborators have shown the necessary prescriptions for solving Eq. (5). Regularity at the origin imposes

$$\bar{\omega} = \text{const}, \qquad \left(\frac{d\bar{\omega}}{dr}\right)_{r=0} = 0. \quad (6)$$

Outside the star, where $j = 0$, one has a general solution

$$\bar{\omega} = \Omega - 2\frac{J}{r^3}, \quad (7)$$

where J is a constant identified with the total angular momentum of the star and in the absence of surface degrees of freedom, the function $\bar{\omega}$ and its derivative are continuous at the stellar surface. This implies that

$$J = \frac{1}{6}R^4\left(\frac{d\bar{\omega}}{dr}\right)_{r=R}, \qquad \Omega = \bar{\omega}(R) + 2\frac{J}{R^3}. \quad (8)$$

Given one has freedom in choosing $\bar{\omega}$ at the center of the star, one will generally end up with an Ω different from a desirable one (coming from observations, for example). In this case, one should just rescale $\bar{\omega}$ as follows

$$\bar{\omega}_{\rm new}(r) = \left(\frac{\Omega_{\rm new}}{\Omega_{\rm old}}\right)\bar{\omega}_{\rm old}(r). \tag{9}$$

When stratification is involved, further boundary conditions should be given. By stratification, we mean a sudden change in Ω at a given radial distance $R_\star$. Such a boundary condition could be obtained when promoting the relevant equations to distributions and collecting the Dirac delta terms. The appropriate equation to be promoted here is Eq. (4). Assume that there is a sudden change of Ω at $r = R_\star$, meaning that at such a radial distance, the "jump" of Ω is different from zero, i.e., $[\Omega]^+_- \neq 0$. Here, "$\pm$" represents a distance immediately above/below $r = R_\star$ ($r = R_\star \pm \epsilon$, with $\epsilon \to 0^+$). The question we want to answer is what $[\Omega]^+_- \neq 0$ implies for $[\omega]^+_-$ and $[\omega']^+_-$.

We stressed that it comes from the $t\varphi$-component of the Einstein equations, which should be the equation to be promoted to distributions. In this case, the energy-momentum tensor may have a surface term, contributing to a Dirac delta. Indeed, it appears when $[\omega']^+_- \neq 0$ [30]. By writing (promotion of ω to a distribution)

$$\omega = \omega^+\Theta(r - R_\star) + \omega^-\Theta(R_\star - r), \tag{10}$$

where Θ is the Heaviside function, and seeing Eq. (4) as a distributional equation with the right-hand side replaced by a term proportional to $[\omega']^+_-\delta(r - R_\star)$, it immediately follows that this equation only starts making distributional sense if

$$[\omega]^+_- = 0. \tag{11}$$

Working now with the second derivatives of Eq. (10), based on Eq. (4) and the energy-momentum tensor at $r = R_\star$, it follows that

$$[\omega']^+_- = 0. \tag{12}$$

From the above equations, it is simple to see the appropriate jump conditions for $\bar{\omega} \equiv \Omega - \omega$:

$$[\bar{\omega}]^+_- = [\Omega]^+_-, \qquad [\bar{\omega}']^+_- = 0. \tag{13}$$

We stress that it would have been incorrect to promote Eq. (5) to a distribution and then find the appropriate boundary conditions to $\bar{\omega}$ because it is valid only when Ω is a given constant. Equation (13) lead to the additional boundary conditions to be considered in the stratification case. One needs to solve Eq. (5) for each layer with a given Ω and implement Eq. (13) between them.

D. Moment of inertia in the stratified case

In the rigid (uniform) perturbative rotation case without stratification, the moment of inertia is $I = J/\Omega$. This makes sense because the constant J, the star's total angular momentum, must be of first order in Ω. It then ensues that I should be seen as the general relativistic counterpart of the star's moment of inertia.

The fact that I is a ratio of two first-order quantities does not mean it is free from the subtleties of $\bar{\omega}$, particularly its boundary conditions. To make matters more complicated, in the case of rotation stratification, it is in principle unclear which Ω (i.e., $\Omega^\pm$ in our case) to choose when writing J as a first-order quantity. However, the case of uniform rotation and the observables we have at hand are good guides to consistently define I for rotation stratification. To start with, for an isolated NS, the total angular momentum J is a conserved quantity for both stratified and uniform rotation cases. In addition, the angular frequency at the surface of the star (Ω^+) is an observable, easily obtained by timing analysis. Thus, the most natural definition for the moment of inertia in the stratified rotation case is also $I_{\rm strat} \equiv J/\Omega^+$.

This definition renders $I_{\rm strat}$ numerically different from $I_{\rm rig}$ in general because J is sensitive to boundary conditions. However, the functional form of J in the case of stratification is exactly the same as in the case of uniform rotation [given by Eq. (8)]. Indeed, from Hartle [23] we learn that

$$J = -\frac{2}{3}\int_0^R \frac{dj}{dr} r^3\bar{\omega}(r)dr = \frac{1}{6}R^4\left(\frac{d\bar{\omega}}{dr}\right)_{r=R}, \tag{14}$$

[see Eqs. (23), (28), (29), and (32) of Hartle [23] for the case $l = 1$, making use of $\int_\pi^0 d\theta \sin^2\theta(dP_1(\theta)/d\theta) = -\frac{4}{3}$ with $P_1(\theta)$ the first-order Legendre polynomial and taking into account Eq. (5), $j(R) = 1$ and $[\omega']^+_- = 0$]. From the above expression, one sees that different Js will arise in the case of stratified and rigid rotations because $\bar{\omega}'_{\rm strat}(R) \neq \bar{\omega}'_{\rm rig}(R)$. Note that (the constant) J is intrinsically general relativistic, which easily allows us to define a relativistic moment of inertia using Ω^+. In addition, J is a "global" quantity, which depends on the internal aspects and dynamics of a star, in agreement with what is expected for its moment of inertia. Finally, $I = J/\Omega^+$ is physically relevant because J (and also Ω^+) can be directly inferred from observations [15,17].

E. Rotational energy

Another relevant issue for energy-balance considerations is the rotational energy of a star. Reference [23] clarifies this point using the seminal work of Bardeen [31]. In summary, Hartle has shown that the rotational energy (which is a positive quantity [23]) of a star with uniform rotation (for which case $\omega_l = 0$ for $l > 1$) is given by

$$E_{\rm rot} = -\frac{1}{3}\int_0^R drr^3\frac{dj}{dr}\Omega(\Omega - \omega(r)), \tag{15}$$

where it is now understood that $\Omega = \Omega^+\Theta(r - R_\star) + \Omega^-\Theta(R_\star - r)$, which is the generalization of the uniform rotation case for stratification. Since Eq. (15) comes from a variational principle, it should also hold in the case of stratification. However, its integrant is not continuous in the whole star, and thus this integral should be properly split. One has

$$E_{\rm rot} = -\frac{1}{3}\left[\Omega^- \int_0^{R_\star} drr^3 \frac{dj}{dr}\bar{\omega}^- + \Omega^+ \int_{R_\star}^{R} drr^3 \frac{dj}{dr}\bar{\omega}^+\right], \tag{16}$$

where we have used that $\bar{\omega}(r) = \Omega - \omega(r)$ for each phase. With Eq. (16), one can use Eq. (5) and obtain

$$E_{\rm rot} = \frac{1}{2}\left[J\Omega^+ - \frac{1}{6}R_\star^4 j(R_\star)\bar{\omega}'(R_\star)[\Omega]_-^+\right]. \tag{17}$$

Therefore, from our definition of the moment of inertia,

$$E_{\rm rot} = \frac{1}{2}\left[I - \frac{1}{6}R_\star^4 j(R_\star)\frac{\bar{\omega}'(R_\star)}{\Omega^+}\frac{[\Omega]_-^+}{\Omega^+}\right](\Omega^+)^2. \tag{18}$$

We stress that the second term of the above equation is generally much smaller than the first due to $R_\star < R$, $j(R_\star) < 1$, and $|[\Omega]_-^+|/\Omega^+ < 1$. In general, it would have been misleading to read off the moment of inertia from Eq. (18) because energy is not trivially extended from Newtonian dynamics to general relativity in general. Finally, we note that Eq. (18) is only valid for the case of 'almost rigidity," i.e., when $\Omega^\pm$ are constants. The case where $\Omega^\pm = \Omega^\pm(r)$ is much more complicated because it involves $l > 1$ [23]. We leave this to be studied in future work.

III. RESULTS

Our main goal here is to compare the outcomes of J and I in the cases of rigid rotation and stratification. For simplicity, in the case of stratification, we assume that two regions of a star rotate with different Ωs and that a surface splits them at $r = R_\star$. The case with more layers with different values of Ω can be trivially extended.

The motivations for different parts of the star rotating with different angular velocities stem from various stellar possibilities: (i) sharp phase transitions leading to a quark core and a hadronic phase (crust); (ii) superfluidity in the neutron star, which tends to preserve a certain angular velocity up to a critical lag; (iii) burying of the star's surface by supernova remnant material, which in general has different angular momentum than the star's; and (iv) nuclear reactions and gravitational and electromagnetic wave emission in some regions of the star, which also take away angular momentum.

A. Modeling

We will work with two main models: (i) the SLy4 equation of state (EOS) [32] for one-phase stars and (ii) stars presenting sharp phase transitions with different quark-hadron energy density jumps $(\eta + 1)$–hybrid stars. Many models could be used for the hybrid star EOS. Here we limit to some examples given in Pereira *et al.* [33]. Particular details can be found there. For the $M - R$ relations (or $M - R$ diagrams) of the representative EOSs that we will make use of here, see Fig. 1.

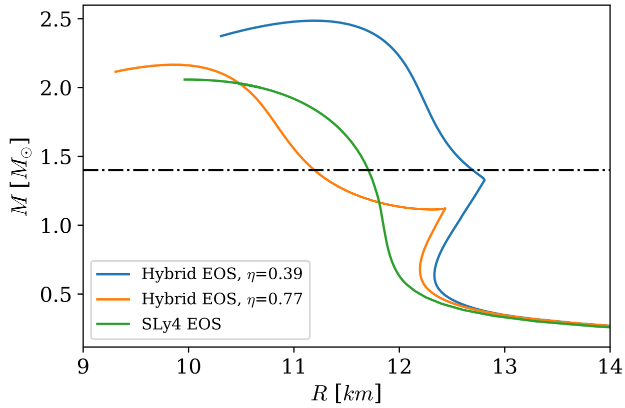

FIG. 1. M-R relations for the SLy4 EOS and the hybrid models of Ref. [33], for selected values of the $1 + \eta \equiv$ top of the quark phase over the bottom of the hadronic phase energy density ratio, 0.39 and 0.77. The dot-dashed horizontal line represents $M = 1.4M_\odot$ and is highlighted to facilitate the identification of the canonical NS mass radius.

In case (i), we assume that $R_\star$ is chosen at will. It would allow one to build intuition about changes in J and I for different angular velocity stratification depths compared to the rigid rotation scenario. In case (ii), $R_\star$ will be identified with the phase transition radius and hence will be fixed for given quark and hadronic equations of state and stellar masses. The idea of this work is not to make an exhaustive EOS analysis but to find the main trends to focus on in future works and to make back-of-the-envelope estimates of the relative changes relative to the rigid rotation case.

B. One-phase stars with rotational stratification

Let us focus first on stars without phase transitions described by the (realistic) SLy4 model. We will assume that the star's inner and outer parts rotate with different Ωs. The inner part encompasses radii up to $R_\star$, which will be freely chosen. The outer part goes from $R_\star$ to the star's surface (R). Motivated by the sun's case, where relative changes in Ω for the core and the convective envelope could be around 10%–20% [34] (associated with the presence of a very thin layer where the angular velocity changes rapidly—the tachocline [9]), we will assume this also to be the case of NSs roughly. Because we work with $\bar{\omega}$ in the numerical integrations, we will assume that $[\Omega]_-^+/\bar{\omega}^- = \text{given} \equiv \mathcal{C}$. From it, it trivially follows that $[\Omega]_-^+/\Omega^+ = \mathcal{C}(\bar{\omega}^-/\Omega^+)$. Here, $\Omega^-(\Omega^+)$ is the angular velocity of the inner(outer) phase of the star. We aim to work with cases where $[\Omega]^{\pm}_{-}/\Omega^{+} \sim 10\%$–$20\%$. For a given $\mathcal{C}$, Eq. (5) could be easily integrated out, and $\bar{\omega}$ could be known throughout the star. For a given Ω^{+}, which directly comes from observations of NS surfaces, one could easily find the right $\mathcal{C}$ for any given $[\Omega]^{\pm}_{-}/\Omega^{+}$. As a rule of thumb, $\mathcal{C}$ is not much different from $[\Omega]^{\pm}_{-}/\Omega^{+}$.

An important issue when comparing I and J with and without rigid rotation is fulfilling Eqs. (8) and (9) if the Ω that we get at the star's surface is not the one we would like to link with observations. That is not the case, given that Ω at R depends on the choice of $\bar{\omega}(0)$. However, this is not a problem, as we show now. From our definition of I and Eqs. (8) and (9), it follows that $I = J_{\mathrm{new}}/\Omega_{\mathrm{new}} = J_{\mathrm{old}}/\Omega_{\mathrm{old}}$, meaning that it is independent of the choice of $\bar{\omega}$ at the center of the star. For J in both the stratified and rigid rotation cases, one can use Eq. (14) after solving Eq. (5). Note from Eq. (14) that when $R_\star \to R$, it follows that $J_{\mathrm{strat}} \to J_{\mathrm{rig}}$ due to Eq. (12).

We start by analyzing the relative differences of I between stratification and rigid rotation for different depths in the NS (different $R_\star$). We use as a representative EOS the SLy4 EOS (see Fig. 1 for its $M-R$ relation). Figure 2 shows that the largest differences in $\Delta I/I_{\mathrm{rig}} \equiv (I_{\mathrm{rig}} - I_{\mathrm{strat}})/I_{\mathrm{rig}}$ happen close to the surface of the star ($\sim[\Omega]^{\pm}_{-}/\Omega^{+}$). This is expected since the total angular momenta in the cases of stratified and uniform rotation tend to the same value, meaning that $\Delta I/I_{\mathrm{rig}} \to [(1/\Omega^{-}) - (1/\Omega^{+})]\Omega^{-} = [\Omega]^{\pm}_{-}/\Omega^{+}$. What is not intuitive is how it does so. It decreases nonlinearly when the angular velocity jumps deeper inside the star. Further, the smaller the mass, the larger the relative difference for a given $R_\star$. Roughly speaking, relative differences in I grow much quicker and become relevant for $R_\star \gtrsim 0.6R$. The sign of $\Delta I/I_{\mathrm{rig}}$ is always the same as $[\Omega]^{\pm}_{-}/\Omega^{+}$, but the relative changes in the moment of inertia are not exactly symmetric to the relative changes in Ω.

C. Hybrid stars

We consider EOSs with different (and controllable) energy density jumps for hybrid stars as in [35,36]. In other words, we use the SLy4 EOS [32] for the crust, smoothly connected to a polytropic EOS for the hadronic outer core, followed by a sharp phase transition with a given energy density jump, $\eta + 1$, to an inner quark core modeled by a simple MIT baglike model, with the sound speed equal to unity (as suggested by Bayesian inferences using GW and electromagnetic data [37–39]). Further details about these EOSs can be found in Ref. [33]. The mass-radius relations for the hybrid EOSs we use are shown in Fig. 1 and they lead to radii around 11–13 km for $1.4M_\odot$, in agreement with multimessenger results [40–43].

Figures 3 and 4 show the results for $\Delta I/I_{\mathrm{rig}}$ for several choices of $\mathcal{C}$ and different masses. Qualitatively, the results are similar to the case without phase transitions: relative changes are roughly limited by $[\Omega]^{\pm}_{-}/\Omega^{+}$, and the deeper the phase transition occurs, the smaller the change in the moment of inertia relative to the rigid case. As is clear from

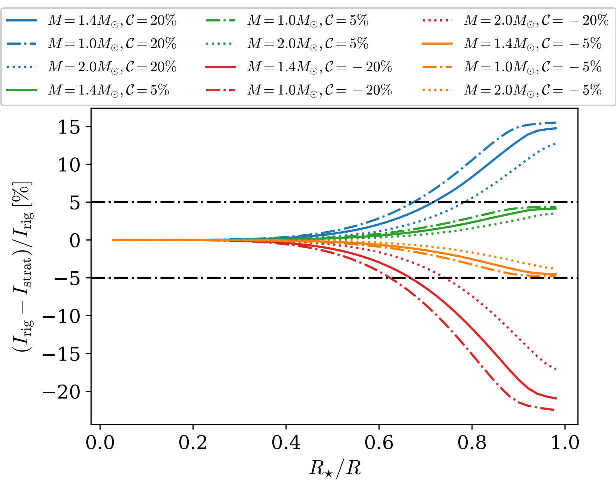

FIG. 2. $\Delta I/I_{\mathrm{rig}}$ for the SLy4 EOS assuming a relative angular velocity jump $\mathcal{C}$ at $R_\star$. Several $\mathcal{C}$s have been included, as well as NS masses. Each color represents a given $\mathcal{C} \sim [\Omega]^{\pm}_{-}/\Omega^{+}$, while each curve dashing relates to a given NS mass. Non-negligible relative differences start showing up for $R_\star/R \gtrsim 0.6$, increasing nonlinearly. If we can infer an NS moment of inertia with a 5% uncertainty, that would also be the minimum level of uncertainty for the relative angular velocity difference between the two phases we could resolve.

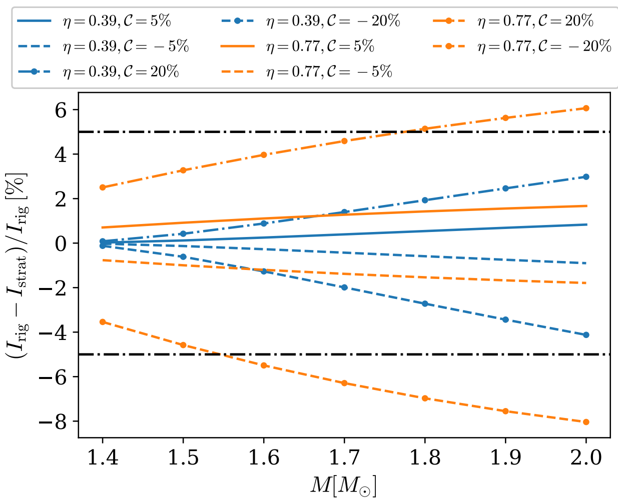

FIG. 3. $\Delta I/I_{\mathrm{rig}}$ for hybrid EOS models with $\eta = 0.39$ (weak phase transition) and $\eta = 0.77$ (strong phase transition) as a function of the NS's mass assuming an angular velocity jump $\mathcal{C}$ at the phase transition radius ($R_\star$). Several $\mathcal{C}$ and NS masses have been included. Each color represents a given energy density jump, while each curve dashing relates to a given $\mathcal{C} \sim [\Omega]^{\pm}_{-}/\Omega^{+}$. Non-negligible relative differences ($\gtrsim$5%) start showing up only for $\mathcal{C} \sim 20\%$ for these models given that the $R_\star$ are at most around $0.8R$ (see Fig. 4).

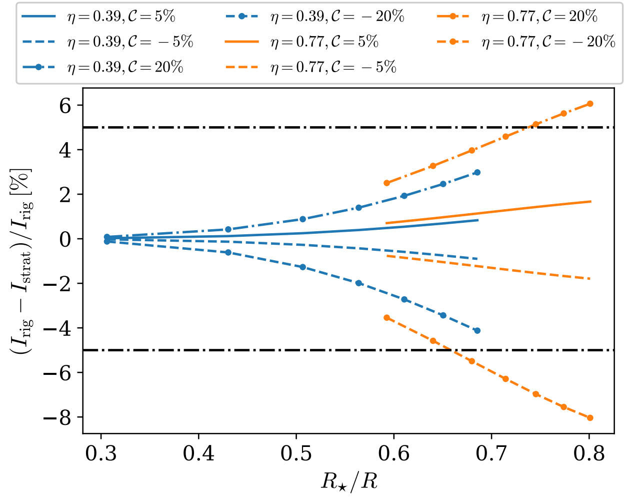

FIG. 4. $\Delta I/I_{\rm rig}$ for hybrid EOS models with $\eta = 0.39$ (weak phase transition) and $\eta = 0.77$ (strong phase transition) assuming an angular velocity jump of $\mathcal{C}$ at the phase transition radius ($R_\star$) as a function of $R_\star/R$. Several $\mathcal{C}$ and NS masses have been included, related to the different $R_\star/R$ values for a given η. Each color on the curves relates to a given energy density jump, while each curve shape relates to a given $\mathcal{C} \sim [\Omega]_-^+/\Omega^+$. Non-negligible relative differences ($\gtrsim 5\%$) start showing up only for $R_\star/R \gtrsim 0.8$ and $\mathcal{C} \sim 20\%$ (because it represents the same models of Fig. 3).

Fig. 2, a relevant aspect is where the jump in rotation occurs in the star. This depends on the star's mass relative to the phase transition mass for a given microphysics of the quark and hadronic phases. Another relevant aspect of $\Delta I/I_{\rm rig}$ as a function of the angular rotation jump depth, as evident in Figs. 2 and 4, is its nonlinearity. Instead, in the case of $\Delta I/I_{\rm rig}$ versus the stellar mass, as shown in Fig. 3, an almost linear behavior is observed, mainly because the phase transition does not vary significantly with the mass in the range $(1.4–2.0)M_\odot$. The larger the mass, the greater the relative change in the moment of inertia because larger masses have larger transition radii, meaning that the radius where the angular velocity jump occurs is closer to the stellar surface.

IV. DISCUSSION AND CONCLUSIONS

The internal composition and rotational dynamics of NSs are not directly observable, necessitating theoretical assumptions for predictions. A prevalent assumption is the rigid rotation of NSs, simplifying the model by reducing the number of variables. However, this assumption may introduce biases in astrophysical constraints. Observations of the Sun and other stars suggest that differential rotation is a more natural assumption. However, modeling this requires a specific rotational law, which introduces its own set of challenges. Moreover, as a main-sequence star, the Sun differs significantly from NSs regarding composition, dynamics, and phenomena. Additionally, temperature effects significantly influence the Sun's differential rotation and are less significant in NSs.

Despite these differences, the Sun is a practical reference point without direct observables for NS internal rotation. Our study shows that nonrigid rotation in NSs introduces systematic uncertainties when calculating their moment of inertia. We adopted a simplified model of nonrigid rotation, characterized by two phases, separated at $r = R_\star$, and having different angular velocities. Though rudimentary and predicated on stellar viscosity properties, this model aims to identify angular velocity jumps that significantly impact I. Our findings indicate that the maximum relative differences in I correspond to the relative changes in the angular velocity, especially when the discontinuity in rotation occurs near the stellar surface. Considering that future observations could constrain I within 5%–10%, our results highlight the potential inaccuracies in assuming rigid rotation for stars.

We now discuss the implications of rotational stratification and changes in I for various stellar observables. Incorporating nonrigid rotation models, which could mitigate many current challenges in understanding stellar dynamics, may help address these issues. Here we focus on the impact of the maximum changes in I on certain observables to assess their systematic errors.

A. Direct measurements of *I*

From the above, it becomes clear that direct measurement of the NS moment of inertia can be the most relevant probe of the NS interior stratification. Such measurement might soon be fulfilled as pulsar timing precision and data increase and improve [17], but models must be more accurate. We have just reached the level where higher-order post-Keplerian parameters can be assessed because the double pulsar mass loss cannot be ignored anymore. Among such higher-order parameters, the moment of inertia of a pulsar can be constrained. The results of Kramer *et al.* [17] have constrained the moment of inertia of a pulsar with mass $1.338M_\odot$ to $I_{45} \equiv I/(10^{45}\ {\rm g\,cm^2}) = 1.15–1.48$ at 95% confidence. It takes into account multimessenger constraints on the radius of NSs. Although the uncertainty about this result is around 10%–20%, it is remarkable that such a direct inference can be made. In the future, this uncertainty is expected to decrease significantly.

Another possibility for constraining the moment of inertia of an NS in a binary system is due to measurements of its periastron advance [15], which will be possible for some sources [16]. That is a higher-order spin-orbit effect, and the expected precision for moment-of-inertia measurements is around 10%–20% [16]. Based on our results, the above accuracies suggest the maximum uncertainties for the rigid rotation of neutron stars. At the same time, it shows that phases rotating with relative differences up to 10%–20% could not be differentiated from those rotating with a uniform angular velocity. However, this stratified rotation could have an impact on other observables, and combined measurements may be able to provide further information. In the best-case scenario, stratified rotation will lead to systematic uncertainties, and they should be duly characterized and not ignored.

Systematic uncertainties to I can have important implications for the constraint of superdense matter in NSs. Suppose there is an intrinsic $\Delta I/I$ due to nonrigid rotation. In that case, it follows that radius inferences will also have uncertainties, and they can be estimated as $\Delta R/R = (1/2)\Delta I/I$ if the mass of an NS is well-constrained. If $\Delta I/I \sim 10\%$, then $\Delta R/R \sim 5\%$. For reference, that already competes with combined multimessenger constraints using ray-tracing techniques for light-curve modeling and tidal deformation constraints [42]. We have shown that $\Delta I/I$ around a few percent can already occur for small angular velocity jumps (~5%). Thus, unless the rotation stratification is small, direct measurements of I may constrain superdense matter less strongly than combined multimessenger techniques.

B. Central compact objects (CCOs)

CCOs are a distinctive class of neutron stars, typically found near the centers of young supernova remnants (SNRs) [see, e.g., 44, for a review]. As these remnants evolve from the aftermath of a supernova, they undergo dynamic processes, including the potential accretion of surrounding material.

The assumption of rigid (uniform) rotation, often applied to older neutron stars, may not be valid for these young and dynamically evolving objects. Specifically, it is expected that the accreted layer rotates differently from the rest of the star, at least transiently, over timescales characterized by viscosity in the outermost regions of the NS. Our estimates suggest that this transient period lasts approximately up to 10 kyr, which is significant for most CCOs given the typical ages of their associated SNRs [see 45].

Due to the thinness of these accreted layers, which are much smaller than the radius of the NS, our analysis suggests that their moments of inertia might differ considerably from other NSs with similar masses if their layers rotate at different rates compared to the rest of the star. When rotation is considered and is not negligible in ray-tracing techniques used to characterize CCOs (or even rotation-powered pulsars), fluctuations in the moment of inertia may affect the spacetime geometry due to variations in total angular momentum and the quadrupole moment. In addition, fluctuations in I can also influence the inference of the dipolar component of the magnetic field of CCOs. Indeed, $B \propto I^{\frac{1}{2}}$, meaning that $\Delta B/B = (1/2)\Delta I/I$ for given values of the star's period and its derivative. For instance, a $\Delta I/I \sim 10\%$ would imply $\Delta B/B \sim 5\%$. Thus, the stratified rotation will not significantly affect the values inferred for the dipolar component of B of CCOs.

The differential rotation within the accreted layers of CCOs has a broader impact beyond just influencing magnetic fields; it can also affect the emission of x-rays. Specifically, variations in the accretion rate, the angular momentum deposited, and the temperature distribution on the NS surface may lead to measurable fluctuations in x-ray emission. These aspects should be investigated further, as such modulations could provide additional information about the internal structure and dynamical evolution of CCOs. We leave this for future studies.

C. Energy budget of neutron stars

Here we focus on back-of-the-envelope consequences of the rotational energy of stratified NSs. We have checked numerically that the second term of Eq. (18) is up to around 1% of the first term for all EOSs that we used. Therefore, we will neglect it and consider $E_{\rm rot} \simeq (1/2)I(\Omega^+)^2$. A relative change of 10%–20% in the moment of inertia due to stratified rotation might significantly impact the energy budget of some sources previously classified as nonrotation-powered pulsars. We identified at least five sources that could be explained by rotation alone in the stratified regime by applying the SLy4 equation of state to compute each pulsar's moment of inertia. This was done using the period (P) and period derivative ($\dot{P}$) data from the third catalog of gamma-ray pulsars [46]. For convenience, we define $\alpha \equiv L_\gamma/E_{\rm rot}$, where L_γ is the luminosity and $E_{\rm rot}$ is the rotational energy. Thus, a rotation-powered pulsar (RPP) has $\alpha \leq 1$.

In our analysis, we selected two reference points from the EOS: the fiducial configuration for SLy4, i.e., a mass $M = 1.45 M_\odot$ for which we find a moment of inertia $I_0 = 1.06 \times 10^{46}$ g cm^2, and the maximum mass configuration, $M = 2.04 M_\odot$, where we calculated $I_0 = 6.55 \times 10^{45}$ g cm^2. Table I displays our results. Considering the fiducial mass, we find that for a 10% increase in the moment of inertia ($I_{+10\%}$), the source J1522–5735 has a value of $\alpha = 0.99$, indicating it is an

TABLE I. Comparison of αs for pulsars with rigid-rotation and stratified-rotation moments of inertia.

$(M, I_0) = (1.45 M_\odot, 1.06 \times 10^{46}$ g cm$^2)$			
PSR	$\alpha(I_0)$	$\alpha(I_{+10\%})$	$\alpha(I_{+20\%})$
J1057-5851	1.19	>1	0.99
J1522-5735	1.09	0.99	0.911
J1650-4601	1.11	>1	0.92
$(M, I_0) = (2.04 M_\odot, 6.55 \times 10^{45}$ g cm$^2)$			
PSR	$\alpha(I_0)$	$\alpha(I_{+10\%})$	$\alpha(I_{+20\%})$
J1429-5911	1.03	0.94	0.86
J1817-1742	1.04	0.95	0.87

RPP, in contrast to $\alpha = 1.19$ found for I_0. Additionally, when we increase the change in the moment of inertia to 20% ($I_{+20\%}$) for the fiducial mass case, we identify three sources within the rotation-powered zone: J1057–5851, J1522–5735, and J1650–4601. Stratified rotation will not address the issue of RPPs for all pulsars, but it is an aspect that must be considered for energy budget assessments. A reasonable upper limit correction would be 10%–20%.

D. Mass changes due to stratification

Within the Hartle formalism for slowly rotating stars, the boundary conditions discussed in Sec. II C for the first-order quantity $\omega(r)$ will affect all the second-order metric perturbation functions. In particular, the total mass-energy of the rotating star is given by [20]

$$M = m(R) + m_0(R) + \frac{J^2}{R^3} \equiv m(R) + \delta M \qquad (19)$$

where $m(R)$ is the mass of the nonrotating star and δM is the mass increase due to rotation, with a contribution coming from m_0, a second-order metric perturbation function, and the rotational energy, which is proportional to J^2. The stratification will affect J (in the same way I, as shown in Sec. III) and the function m_0 since its differential equation depends on the value of ω throughout the star. Thus, a stratified NS has a different gravitational mass relative to a rigidly rotating one, as shown in Fig. 5 for different Ωs in the reference rigid case (20% and 50% of the Newtonian Keplerian frequency, $\Omega_k = \sqrt{Gm(R)/R^3}$). We chose a situation where the sharp angular velocity change happens close to the star's surface, $R = 0.9R$, and a large rotation jump, $|\mathcal{C}| = 20\%$, to obtain the largest differences. For the case, $\Omega = 0.2\Omega_k$, stratification contributes little to the mass related to rigid rotation ($\lesssim 1\%$). However, the contribution to the rigid mass due to stratified rotation when $\Omega = 0.5\Omega_k$ can be more significant, up to around 10%. The above happens essentially because the mass variation $\delta M_{\rm strat}$ can differ significantly concerning $\delta M_{\rm rig}$ (up to $\approx 45\%$ for the case $\mathcal{C} = -20\%$ and $R_\star$ close to the star surface), but the total mass is still dominated by the nonrotating term $m(R)$, making less relevant the global change in the mass.

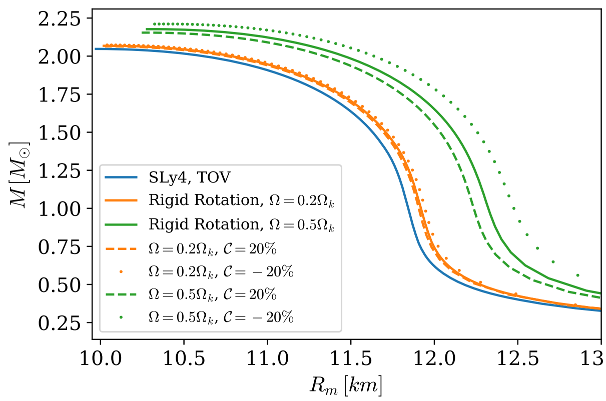

FIG. 5. Gravitational mass (M) versus mean radius (R_m) relation, where $R_m = (R_p + 2R_{\rm eq})/3$ (R_p and $R_{\rm eq}$ are the NSs radius at the pole and equator, respectively). The SLy4 EOS was used as the equation of state of the nonrotating seed. Concerning the rigid rotations, we chose the exemplary cases of $\Omega = 0.2\Omega_k$ and $\Omega = 0.5\Omega_k$, where $\Omega_k = \sqrt{Gm(R)/R^3}$ is the Newtonian Keplerian frequency. For the stars with stratified rotation, we assumed a rotation jump of $\mathcal{C} = \pm 20\%$ close to the surface $R_* = 0.9R$.

E. I-Love-Q universal relations

Many uncertainties are associated with the NS interior structure, mainly because of our lack of knowledge about the equation of the state of the NS core. Nevertheless, some universal relations between the moment of inertia I, the quadrupole moment Q, and the tidal Love number λ have been discovered some time ago [47]. These relations are very powerful from an astrophysical point of view since measuring any of the variables in the trio could lead to direct information about the other two. The assumptions behind the I-Love-Q relations derivation are slow and uniform rotation, small tidal perturbations, and GR gravity. As discussed in this work, letting go of uniform rigid rotation will naturally alter the moment of inertia, as shown previously. But what happens with the quadrupole moment and the universal relations?

The spin-induced quadrupole moment Q is a second-order quantity that will be affected by the boundary condition in ω through nonlinear terms in the differential equation. The expression for Q is given by [20]

$$Q = -\frac{J^2}{m(R)} - \frac{8}{5}Am^3(R). \qquad (20)$$

As we have shown, the first term is sensitive to stratification, hence the second term, since second-order equations are seeded by the solutions of first-order equations in the rotation parameter.

The universal relations are expressed in terms of the dimensionless moment of Inertia $\bar{I} \equiv I/m(R)^3$ and dimensionless quadrupole moment $\bar{Q} \equiv -Qm(R)/J^2$ [47]. Since the normalization is done with the nonrotating mass $m(R)$, the relative change due to stratification in the dimensionless moment of inertia will be

$$\frac{\Delta \bar{I}}{\bar{I}} = \frac{\Delta J}{J} = \frac{\Delta I}{I}, \qquad (21)$$

while the relative change in the dimensionless quadrupole moment is

$$\frac{\Delta \bar{Q}}{\bar{Q}} = \frac{\frac{8}{5}\frac{A}{J^2} m^4(R)\left(\frac{\Delta A}{A} - \frac{2\Delta J}{J}\right)}{\left(1 + \frac{8}{5} A \frac{m^4(R)}{J^2}\right)}. \tag{22}$$

One sees that $\Delta \bar{I}$ and $\Delta \bar{Q}$ will not be proportional to each other due to the presence of $\Delta A/A$. Thus, we expect, in general, that the universal relation between $\bar{I}$ and $\bar{Q}$ will no longer hold/will be weakened in the presence of stratified rotation. We leave further examination of that for future work.

F. Gravitational wave production

For isolated NSs, mountains can be built on their surfaces for a variety of reasons (see [33] and references therein), and they could lead to the emission of GWs due to a resultant ellipticity (quadrupole moment). It depends on the moment of inertia of the star and is defined as [33,48,49]

$$\varepsilon \equiv \sqrt{\frac{8\pi}{15}} \frac{Q_{22}}{I}, \tag{23}$$

where I is the principal moment of inertia, Q_{22} is the $l = m = 2$ quadrupole moment of the star. The GW strain is [50]

$$h = \frac{4\pi \varepsilon I f_{\mathrm{GW}}^2}{d}, \tag{24}$$

where d is the source distance and f_{GW} is the GW frequency. Thus, from the above equations, ε (and to a lesser extent h because of the product εI) will have systematic uncertainties associated with the NS unknown internal rotation. The relative uncertainties of ε will be proportional to $\Delta I/I$. Uncertainties today are large for h, and only upper limits can be set for ε, meaning that $\Delta I/I \lesssim 10\%$–20% will not be problematic for NS constraints with them. However, in the future, systematics about I will become relevant for GW astronomy. That motivates further studies on the internal rotation of NSs.

Future missions promise much tighter constraints on GW observables, such as the GW strain, tidal deformations, ellipticities, and quasinormal modes, which all depend on the moment of inertia. At the same time, when uncertainties for GW observables decrease, it might also be possible to constrain rotation aspects of NSs with them. Statistical studies of GW observables may also constrain where, inside the star, an abrupt rotation change happens. Our analysis suggests that relative changes of a few percent in the moment of inertia happen for $R_\star/R \gtrsim 0.6$. If no systematic fluctuation in the observables is found, it would suggest that rotation changes happen much deeper in the star.

ACKNOWLEDGMENTS

We thank the anonymous referee for their valuable suggestions and comments, which have helped improve this work. J. P. P. is thankful for the financial support of Fundação de Amparo à Pesquisa e Inovação do Espírito Santo (FAPES) under Grant No. 04/2022 and CNPq–Conselho Nacional de Desenvolvimento Científico e Tecnológico–under Grant No. 174612/2023-0. J. G. C. is grateful for the support of FAPES (1020/2022, 1081/2022, 976/2022, 332/2023), CNPq (311758/2021-5), and FAPESP (2021/01089-1). T. O. is grateful for the financial support of CAPES and the hospitality of the University of Ferrara. This study was financed in part by the Coordenação de Aperfeiçoamento de Pessoal de Nível Superior—Brasil (CAPES)—Finance Code 001.

[1] P. Haensel, A. Y. Potekhin, and D. G. Yakovlev, *Neutron Stars 1: Equation of State and Structure* (Springer, New York, USA, 2007), Vol. 326.

[2] A. Ramos, J. Schaffner-Bielich, and J. Wambach, Kaon condensation in neutron stars, in *Physics of Neutron Star Interiors*, edited by D. Blaschke, N. K. Glendenning, and A. Sedrakian (Springer, Berlin, Germany, 2001), Vol. 578, p. 175.

[3] D. D. Ivanenko and D. F. Kurdgelaidze, Hypothesis concerning quark stars, Astrophysics (Engl. Transl.) **1**, 251 (1965).

[4] M. Caleb *et al.*, Discovery of a radio-emitting neutron star with an ultra-long spin period of 76 s, Nat. Astron. **6**, 828 (2022).

[5] J. W. T. Hessels, S. M. Ransom, I. H. Stairs, P. C. C. Freire, V. M. Kaspi, and F. Camilo, A radio pulsar spinning at 716 Hz, Science **311**, 1901 (2006).

[6] A. K. Harding, The neutron star zoo, Front. Phys. **8**, 679 (2013).

[7] B. Margalit, A. S. Jermyn, B. D. Metzger, L. F. Roberts, and E. Quataert, Angular-momentum transport in proto-neutron stars and the fate of neutron star merger remnants, Astrophys. J. **939**, 51 (2022).

[8] N. K. Glendenning, First-order phase transitions with more than one conserved charge: Consequences for neutron stars, Phys. Rev. D **46**, 1274 (1992).

[9] E. A. Spiegel and J. P. Zahn, The solar tachocline, Astron. Astrophys. **265**, 106 (1992), https://articles.adsabs.harvard.edu/full/1992A%26A...265..106S.

[10] K. Glampedakis and N. Andersson, Ekman layer damping of r modes revisited, Mon. Not. R. Astron. Soc. **371**, 1311 (2006).

[11] R. F. Sawyer, Bulk viscosity of hot neutron-star matter and the maximum rotation rates of neutron stars, Phys. Rev. D **39**, 3804 (1989).

[12] D. Lai, Resonant oscillations and tidal heating in coalescing binary neutron stars, Mon. Not. R. Astron. Soc. **270**, 611 (1994).
[13] D. G. Yakovlev, M. E. Gusakov, and P. Haensel, Bulk viscosity in a neutron star mantle, Mon. Not. R. Astron. Soc. **481**, 4924 (2018).
[14] J. B. Hartle, Slowly rotating relativistic stars. I. Equations of structure, Astrophys. J. **150**, 1005 (1967).
[15] T. Damour and G. Schafer, Higher-order relativistic periastron advances and binary pulsars, Nuovo Cimento **101B**, 127 (1988).
[16] S. K. Greif, K. Hebeler, J. M. Lattimer, C. J. Pethick, and A. Schwenk, Equation of state constraints from nuclear physics, neutron star masses, and future moment of inertia measurements, Astrophys. J. **901**, 155 (2020).
[17] M. Kramer *et al.*, Strong-field gravity tests with the double pulsar, Phys. Rev. X **11**, 041050 (2021).
[18] H. Hu, M. Kramer, N. Wex, D. J. Champion, and M. S. Kehl, Constraining the dense matter equation-of-state with radio pulsars, Mon. Not. R. Astron. Soc. **497**, 3118 (2020).
[19] D. Antonopoulou, B. Haskell, and C. M. Espinoza, Pulsar glitches: Observations and physical interpretation, Rep. Prog. Phys. **85**, 126901 (2022).
[20] J. B. Hartle and K. S. Thorne, Slowly rotating relativistic stars. II. Models for neutron stars and supermassive stars, Astrophys. J. **153**, 807 (1968).
[21] J. B. Hartle and K. S. Thorne, Slowly rotating relativistic stars. III. Static criterion for stability, Astrophys. J. **158**, 719 (1969).
[22] J. B. Hartle, Slowly rotating relativistic stars. IIIA. The static stability criterion recovered, Astrophys. J. **195**, 203 (1975).
[23] J. B. Hartle, Slowly-rotating relativistic stars. IV. Rotational energy and moment of inertia for stars in differential rotation, Astrophys. J. **161**, 111 (1970).
[24] J. B. Hartle and M. W. Munn, Slowly rotating relativistic stars. V. Static stability analysis of $n = 3/2$ polytropes, Astrophys. J. **198**, 467 (1975).
[25] J. B. Hartle, K. S. Thorne, and S. M. Chitre, Slowly rotating relativistic stars. VI. Stability of the quasiradial modes, Astrophys. J. **176**, 177 (1972).
[26] J. B. Hartle and J. L. Friedman, Slowly rotating relativistic stars. VIII. Frequencies of the quasi-radial modes of an $N = 3/2$ polytrope, Astrophys. J. **196**, 653 (1975).
[27] M. H. Pinsonneault, S. D. Kawaler, S. Sofia, and P. Demarque, Evolutionary models of the rotating sun, Astrophys. J. **338**, 424 (1989).
[28] S. L. Shapiro, Differential rotation in neutron stars: Magnetic braking and viscous damping, Astrophys. J. **544**, 397 (2000).
[29] A. G. Suvorov and A. Melatos, Recycled pulsars with multipolar magnetospheres from accretion-induced magnetic burial, Mon. Not. R. Astron. Soc. **499**, 3243 (2020).
[30] J. P. Pereira, J. G. Coelho, and J. A. Rueda, Stability of thin-shell interfaces inside compact stars, Phys. Rev. D **90**, 123011 (2014).
[31] J. M. Bardeen, A variational principle for rotating stars in general relativity, Astrophys. J. **162**, 71 (1970).
[32] F. Douchin and P. Haensel, A unified equation of state of dense matter and neutron star structure, Astron. Astrophys. **380**, 151 (2001).
[33] J. P. Pereira, M. Bejger, P. Haensel, and J. L. Zdunik, Crustal failure as a tool to probe hybrid stars, Astrophys. J. **950**, 185 (2023).
[34] R. Howe, Solar interior rotation and its variation, Living Rev. Solar Phys. **6**, 1 (2009).
[35] J. P. Pereira, M. Bejger, N. Andersson, and F. Gittins, Tidal deformations of hybrid stars with sharp phase transitions and elastic crusts, Astrophys. J. **895**, 28 (2020).
[36] J. P. Pereira, M. Bejger, L. Tonetto, G. Lugones, P. Haensel, J. L. Zdunik, and M. Sieniawska, Probing elastic quark phases in hybrid stars with radius measurements, Astrophys. J. **910**, 145 (2021).
[37] W.-J. Xie and B.-A. Li, Bayesian inference of the dense-matter equation of state encapsulating a first-order hadron-quark phase transition from observables of canonical neutron stars, Phys. Rev. C **103**, 035802 (2021).
[38] A. Li, Z. Miao, S. Han, and B. Zhang, Constraints on the maximum mass of neutron stars with a quark core from GW170817 and NICER PSR J0030 + 0451 data, Astrophys. J. **913**, 27 (2021).
[39] I. Legred, K. Chatziioannou, R. Essick, S. Han, and P. Landry, Impact of the PSR J 0740 + 6620 radius constraint on the properties of high-density matter, Phys. Rev. D **104**, 063003 (2021).
[40] M. C. Miller *et al.*, PSR J0030 + 0451 mass and radius from NICER data and implications for the properties of neutron star matter, Astrophys. J. Lett. **887**, L24 (2019).
[41] T. E. Riley, A. L. Watts, S. Bogdanov, P. S. Ray, R. M. Ludlam, S. Guillot, Z. Arzoumanian, C. L. Baker, A. V. Bilous, D. Chakrabarty, K. C. Gendreau, A. K. Harding, W. C. G. Ho, J. M. Lattimer, S. M. Morsink, and T. E. Strohmayer, A NICER view of PSR J0030 + 0451: Millisecond pulsar parameter estimation, Astrophys. J. Lett. **887**, L21 (2019).
[42] M. C. Miller *et al.*, The radius of PSR J0740 + 6620 from NICER and XMM-Newton data, Astrophys. J. Lett. **918**, L28 (2021).
[43] T. E. Riley *et al.*, A NICER view of the massive pulsar PSR J0740 + 6620 informed by radio timing and XMM-Newton spectroscopy, Astrophys. J. Lett. **918**, L27 (2021).
[44] A. De Luca, Central compact objects in supernova remnants, J. Phys. Conf. Ser. **932**, 012006 (2017).
[45] A. Borghese, Exploring the neutron star zoo: An observational review, IAU Symp. **363**, 51 (2020).
[46] https://fermi.gsfc.nasa.gov/ssc/data/access/lat/3rd_PSR_catalog/.
[47] K. Yagi and N. Yunes, I-Love-Q, Science **341**, 365 (2013).
[48] B. J. Owen, Maximum elastic deformations of compact stars with exotic equations of state, Phys. Rev. Lett. **95**, 211101 (2005).
[49] N. K. Johnson-McDaniel and B. J. Owen, Maximum elastic deformations of relativistic stars, Phys. Rev. D **88**, 044004 (2013).
[50] N. Andersson, Gravitational-wave astronomy: Exploring the dark side of the universe (Oxford University Press, Oxford, UK, 2019).

Eur. Phys. J. C (2024) 84:1166
https://doi.org/10.1140/epjc/s10052-024-13459-1

THE EUROPEAN PHYSICAL JOURNAL C

Regular Article

Theoretical Physics

Kerr black hole energy extraction, irreducible mass feedback, and the effect of captured particles charge

J. A. Rueda[1,2,3,4,5,a], **R. Ruffini**[1,2,6,b]

[1] ICRANet, Piazza della Repubblica 10, 65122 Pescara, Italy
[2] ICRA, Dipartimento di Fisica, Sapienza Università di Roma, P.le Aldo Moro 5, 00185 Rome, Italy
[3] ICRANet-Ferrara, Dipartimento di Fisica e Scienze della Terra, Università degli Studi di Ferrara, Via Saragat 1, 44122 Ferrara, Italy
[4] Dipartimento di Fisica e Scienze della Terra, Università degli Studi di Ferrara, Via Saragat 1, 44122 Ferrara, Italy
[5] INAF, Istituto de Astrofisica e Planetologia Spaziali, Via Fosso del Cavaliere 100, 00133 Rome, Italy
[6] INAF, Viale del Parco Mellini 84, 00136 Rome, Italy

Received: 17 June 2024 / Accepted: 6 October 2024

Abstract We analyze the extraction of the rotational energy of a Kerr black hole (BH) endowed with a test charge and surrounded by an external test magnetic field and ionized low-density matter. For a magnetic field parallel to the BH spin, electrons move outward(inward) and protons inward(outward) in a region around the BH poles(equator). For zero charge, the polar region comprises spherical polar angles $-60^\circ \lesssim \theta \lesssim 60^\circ$ and the equatorial region $60^\circ \lesssim \theta \lesssim 120^\circ$. The polar region shrinks for positive charge, and the equatorial region enlarges. For an isotropic particle density, we argue the BH could experience a *cyclic* behavior: starting from a zero charge, it accretes more polar protons than equatorial electrons, gaining net positive charge, energy and angular momentum. Then, the shrinking(enlarging) of the polar(equatorial) region makes it accrete more equatorial electrons than polar protons, gaining net negative charge, energy, and angular momentum. In this phase, the BH rotational energy is extracted. The extraction process continues until the new enlargement of the polar region reverses the situation, and the cycle repeats. We show that this electrodynamical process produces a relatively limited increase of the BH irreducible mass compared to gravitational mechanisms like the Penrose process, hence being a more efficient and promising mechanism for extracting the BH rotational energy.

1 Introduction

This paper discusses a specific electrodynamic process to extract the Kerr black hole (BH) rotational energy and analyze its efficiency. For this task, taking into account and differentiating the concepts of extractable energy, extracted energy, and the inevitable increase of the BH irreducible mass in processes interacting with the BH are essential. This fact has been recently exemplified for the gravitational Penrose process [1] in [2] (hereafter Paper I) and in [3] (hereafter Paper II). Paper I assesses the efficiency of the single Penrose process, while Paper II analyzes the case of repetitive processes. Paper II conclusion is dramatic: applying the Penrose processes repetitively either poorly reduces the BH spin, hence the BH rotational energy, leaving most of it yet to be extracted, or it can approach a final Schwarzschild BH state, but by converting the BH rotational energy into irreducible mass. In either case, very little or even no energy extraction occurs. The former case results from Penrose processes occurring near the BH horizon, and the latter near the ergosphere border. Papers I and II have revealed that the nonlinear increase of the BH irreducible mass is responsible for the Penrose process's inefficiency.

The main consequence of the above result is that any Kerr BH rotational energy extraction process must account for the irreducible mass increase effect. Therefore, the efficiency of any BH energy extraction process is ultimately linked to its ability to approach reversibility, i.e., to cause an as-low-as-possible increase of the BH irreducible mass.

In the context of the Wald electromagnetic field [4] for a Kerr BH immersed in an asymptotically aligned (with the BH spin), uniform test magnetic field, it was shown in

[a] e-mail: jorge.rueda@icra.it (corresponding author)
[b] e-mail: ruffini@icra.it

Ref. [5] that the capture and ejection of positively and negatively charged particles by a Kerr BH can extract its energy when the BH captures more particles with negative than positive energy (and angular momentum). These conditions are attainable in an ionized anisotropic medium with density increasing toward the equator. The process showed the BH extracted energy increases more than the irreducible mass, representing a first step towards an efficient process of BH energy extraction. Indeed, in the sequence of gravitational Penrose processes of Paper II, the increase of the BH irreducible mass relative to the decrease of the mass becomes as large as $\sim 500\%$, which contrasts with the ~ 1–10% relative change obtained in the electrodynamical process in [5].

This paper extends the above analysis by accounting for the fact that the BH also gains charge. As a first step in understanding the process, we consider the BH charge to be a test charge, i.e., it affects the exterior electromagnetic field but not the spacetime geometry, which will still be given by the Kerr metric. The main new result is that including the BH (test) charge allows the BH energy extraction for isotropic surrounding particle density and is more efficient than the previous case.

The paper is organized as follows. Section 2 discusses the concepts of *extractable* energy, *extracted* energy, and the role of the BH irreducible mass in differentiating the two. Section 3 describes the electromagnetic field structure leading to outgoing and ingoing charged particles. In Sect. 4, we calculate the energy and angular momentum of the particles captured by the BH. Section 5 estimates the total change in the BH parameters mass, angular momentum, and irreducible mass. Finally, we outline the conclusions, consequences, and future research directions from the paper's results in Sect. 6.

2 Extractable, extracted energy, and irreducible mass

Let us start by recalling the concept of *extractable energy* (see, e.g., [6,7])

$$E_{\rm ext} \equiv M - M_{\rm irr}, \tag{1}$$

where M and $M_{\rm irr}$ are the BH mass and irreducible mass. Unless otherwise specified, we use geometric ($G = c = 1$) units throughout. The relation between the BH mass, angular momentum (J), charge (Q), and irreducible mass is dictated by the Christodoulou-Ruffini-Hawking BH mass-energy formula [8–10]

$$M^2 = \left(M_{\rm irr} + \frac{Q^2}{4M_{\rm irr}^2}\right)^2 + \frac{J^2}{4M_{\rm irr}^2}. \tag{2}$$

The BH horizon is $r_+ = M + \sqrt{M^2 - a^2 - Q^2}$, being $a = J/M$ the BH angular momentum per unit mass, so $M_{\rm irr}$ can be readily written as

$$M_{\rm irr} = \frac{1}{2}\sqrt{2Mr_+ - Q^2}. \tag{3}$$

For a Schwarzschild BH ($Q = 0$ and $J = 0$), $M_{\rm irr} = M$, so $E_{\rm ext} = 0$. For the extreme Kerr BH ($Q = 0$ and $J = M^2$), $M_{\rm irr} = M/\sqrt{2} \approx 0.71M$, leading to $E_{\rm ext} = (1-1/\sqrt{2})M \approx 0.29M$. For an extreme Reissner–Nordström BH ($J = 0$ and $Q = M$), $M_{\rm irr} = M/2$, so $E_{\rm ext} = 0.5M$. Thus, a non-rotating BH has no energy to be extracted, while up to 29% (50%) of the mass of an extremely rotating (charged) BH could be extracted. However, astrophysical processes have to deal with the BH surface area increase theorem [10]

$$dS_+ \geq 0, \quad S_+ = 4\pi(r_+^2 + a^2) = 16\pi M_{\rm irr}^2, \tag{4}$$

which implies that $dM_{\rm irr}^2 \geq 0$ for any process acting on the BH. Hence, the extractable energy given by Eq. (1) is the maximum amount of energy that can be *extracted*. If an energy extraction process reduces the BH mass by an amount dM, then the extracted energy is defined as

$$dE_{\rm extracted} \equiv -dM, \tag{5}$$

and from Eq. (1), the extractable energy changes by

$$dE_{\rm ext} = dM - dM_{\rm irr} = -dE_{\rm extracted} - dM_{\rm irr}. \tag{6}$$

Thus, the extracted energy can approach the maximum possible value, the extractable energy, only if the process of extraction occurs without increasing the BH irreducible mass, namely if it is reversible in the Christodoulou-Ruffini sense [8,9], i.e., if $dM_{\rm irr} = 0$.

Reversibility is hard to approach, so in general, we seek *efficient* processes able to extract the BH energy causing a relatively small change of the irreducible mass [5,11], i.e.,

$$|dM| = dE_{\rm extracted} \gg dM_{\rm irr}, \tag{7}$$

such that $dE_{\rm extracted} = -dM \approx dE_{\rm ext}$.

Let us now focus on the case of a Kerr BH. Equation (3) tells that an infinitesimal change in the BH mass (dM) and angular momentum (dJ) leads to a change in the horizon surface area

$$dS_+ = 16\pi\, dM_{\rm irr}^2 = 32\pi M_{\rm irr}^2 \frac{dM - \Omega_+ dJ}{\sqrt{M^2 - a^2}}, \tag{8}$$

where $\Omega_+ = a/(2Mr_+)$. The condition (7) is not trivial. It challenges energy extraction processes by particles or fields as they could convert the BH rotational energy into irreducible mass rather than in energy extracted.

When the BH captures a particle of energy E and angular momentum L, from Eq. (8) we have $dM_{\rm irr}^2 \propto E - \Omega_+ L \propto |p^r|_+$, being the latter the radial momentum of the particle crossing the horizon [5,11–13]. Therefore, a reversible transformation is achieved only by capturing particles *grazing* the horizon [8,9]. Otherwise, $|p^r|_+ > 0$, $dS_+ > 0$ and $dM_{\rm irr}^2 > 0$, so $M_{\rm irr}$ necessarily increases.

We have already recalled the results of Paper II, which shows the high irreversibility of a repetitive Penrose process, even approaching the limit of being completely irreversible when it occurs near the ergosphere, i.e., approaching a complete conversion of the BH rotational energy into the irreducible mass without energy extracted: $dE_{\rm ext} \to -dM_{\rm irr}$ and $dE_{\rm extracted} = -dM \to 0$.

We now turn to the electrodynamical processes. We recall that the electrostatic potential for charged particles allows them to have negative energy states outside the ergosphere, a fact first noticed for the Reissner–Nordström BH leading to the concept of *generalized ergosphere* [14]. This property has been used in the extension of the Penrose process in the presence of magnetic fields (see, e.g., [15–20], and references therein).

However, the presence of electromagnetic fields does not guarantee an improvement in efficiency. An astrophysically relevant example is a Kerr BH immersed in a test magnetic field, asymptotically inclined relative to the BH rotation axis. Two seminal papers [21,22] showed, in the slow-rotation regime and the full Kerr metric, that the exerted torque by the fields onto the BH induces the alignment between the BH angular momentum and the magnetic moment. The process fully converts the BH rotational energy into irreducible mass, with no energy being released to infinity at any time in the alignment process. The above result was also independently obtained using a different theoretical framework for the general Kerr BH metric in [23].

In the meantime, several energy extraction mechanisms using electromagnetic fields have been proposed. The matter-dominated plasma accreting onto a Kerr BH [24] inspired the Blandford-Znajek mechanism [25], which has seen a recently boosted interest from relativistic magnetohydrodynamics and particle-in-cell simulations (e.g., [26–28]). Further works involve magnetohydrodynamic inflows [29], electric and magnetic generalizations of the Penrose process [15–20], and references therein), and more recently, relativistic magnetic reconnection in the BH vicinity [30]. Because of the critical role of the BH irreducible mass increase discussed above, it remains to verify whether or not the efficiency condition (7) is approached in these processes. However, such a study goes beyond the scope of the present work and is left as a prospect.

Next, we follow our plan of setting the physical picture of present interest to assess the conditions for the energy extraction to occur and its efficiency by monitoring the increase of the BH irreducible mass.

3 Electromagnetic field structure

In spheroidal Boyer–Lindquist coordinates (t, r, θ, ϕ), the Kerr metric reads [31]

$$ds^2 = g_{00}dt^2 + g_{11}dr^2 + g_{22}d\theta^2 + g_{33}d\phi^2 + 2g_{03}dtd\phi, \tag{9a}$$

$$g_{00} = -\left(1 - \frac{2Mr}{\Sigma}\right), \quad g_{11} = \frac{\Sigma}{\Delta}, \quad g_{22} = \Sigma, \tag{9b}$$

$$g_{33} = \frac{A}{\Sigma}\sin^2\theta, \quad g_{03} = -\frac{2aMr}{\Sigma}\sin^2\theta, \tag{9c}$$

where, being M and $a = J/M$, respectively, the BH mass and angular momentum per unit mass.

The electromagnetic four-potential of the Wald solution in the case of a slightly charged Kerr BH, embedded in a magnetic field of strength B_0 asymptotically aligned with the BH rotation axis is given by [4],

$$A_\mu = \frac{B_0}{2}\,\psi_\mu + a\,B_0\eta_\mu - \frac{Q}{2M}\eta_\mu, \tag{10}$$

where $\eta^\mu = \delta^\mu_0$ and $\psi^\mu = \delta^\mu_3$ are the time-like and space-like Killing vectors of the Kerr metric. Thus, the electromagnetic four-potential is $A_\mu = (A_0, 0, 0, A_3)$, where the non-vanishing components are given by (see Appendix A)

$$A_0 = -aB_0\left[1 - \frac{Mr}{\Sigma}(1+\cos^2\theta)\right] + \frac{Q}{2M}\left(1 - \frac{2Mr}{\Sigma}\right), \tag{11a}$$

$$A_3 = \frac{1}{2}B_0\sin^2\theta\left[r^2 + a^2 - \frac{2Mra^2}{\Sigma}(1+\cos^2\theta)\right] + \frac{Qar\sin^2\theta}{\Sigma}. \tag{11b}$$

With the knowledge of A_μ, we can now calculate the Faraday tensor, $F_{\alpha\beta} = \partial_\alpha A_\beta - \partial_\beta A_\alpha$, whose non-vanishing components result to be (see Appendix A)

$$F_{01} = \frac{(r^2 - a^2\cos^2\theta)}{\Sigma^2}\left[aB_0M(1+\cos^2\theta) - Q\right], \tag{12a}$$

$$F_{02} = \frac{2ar\sin\theta\cos\theta}{\Sigma^2}\left[B_0M(r^2 - a^2) + aQ\right] \tag{12b}$$

$$F_{13} = B_0 r\sin^2\theta\left[1 + \frac{Ma^2(r^2 - a^2\cos^2\theta)(1+\cos^2\theta)}{r\Sigma^2}\right] - \frac{Qa(r^2 - a^2\cos^2\theta)\sin^2\theta}{\Sigma^2}, \tag{12c}$$

$$F_{23} = \frac{B_0\sin\theta\cos\theta}{\Sigma^2}\Big[\Sigma^2(r^2+a^2) - 2Ma^2r\Sigma(1+\cos^2\theta) + 2Ma^2r(r^2-a^2)\sin^2\theta\Big] + \frac{2Qar^3\sin\theta\cos\theta}{\Sigma^2}. \tag{12d}$$

To better depict the electromagnetic field structure and the expected charged particle motion, we calculate the electromagnetic invariant (see Appendix A)

$$\vec{E}\cdot\vec{B} = -\frac{1}{4}F_{\alpha\beta}\tilde{F}^{\alpha\beta} = \frac{F_{02}F_{13} - F_{01}F_{23}}{\Sigma\sin\theta}, \tag{13}$$

where $\tilde{F}^{\alpha\beta}$ is the dual of the electromagnetic tensor, defined by $\sqrt{-g}\tilde{F}^{\alpha\beta} = (1/2)\epsilon^{\alpha\beta\mu\nu}F_{\mu\nu}$, being $\epsilon^{\alpha\beta\mu\nu}$ the Levi-Civita symbol, and $g = -\Sigma^2\sin^2\theta$ the determinant of the Kerr spacetime metric (9).

We are interested in obtaining the polar angle at which $\vec{E}\cdot\vec{B} = 0$, which separates regions where the scalar product is positive and negative and can be calculated at the BH horizon radius. By replacing the corresponding expressions of $F_{\alpha\beta}$ given in Eq. (12) into Eq. (13), it follows the quadratic equation $(\vec{E}\cdot\vec{B})_+ = \lambda Q^2 + \sigma Q + \gamma = 0$, whose two roots are

$$Q = \frac{-\sigma \pm \sqrt{\sigma^2 - 4\lambda\gamma}}{2\lambda}, \tag{14}$$

where we have defined

$$\lambda = \frac{2ar_+(r_+^2 - a^2\cos^2\theta)\cos\theta}{\Sigma^4}, \tag{15}$$

$$\sigma = -\frac{2B_0a^2r_+\cos\theta}{\Sigma^4}[M(r_+^2 - a^2\cos^2\theta)(1+\cos^2\theta) - r_+\sin^2\theta(r_+^2 + a^2\cos^2\theta)], \tag{16}$$

$$\gamma = \sigma\frac{B_0M(r_+^2 - a^2)}{a}. \tag{17}$$

The background color in Fig. 1 shows the regions where the invariant (13) is positive (bluer), negative (redder), and zero (blue dashed lines). For example, for a magnetic field aligned with the BH spin (i.e., vertically upward), positively charged particles will follow the magnetic field lines downward in the red and upward in the blue regions. Negatively charged particles have the opposite behavior.

Given the invariant character of $\vec{E}\cdot\vec{B}$, we can use any observer to exemplify the above situation, e.g., the *locally non-rotating* observer, also called the *zero angular momentum* (ZAMO) observer [32,33]. The ZAMO carries a tetrad with vectors $e_{\hat{0}} = u_{(Z)}$, $e_{\hat{1}} = \sqrt{\Delta/\Sigma}\,e_1$, $e_{\hat{2}} = e_2/\sqrt{\Sigma}$, and $e_{\hat{3}} = \sqrt{\Sigma/A}\,e_3/\sin\theta$, where $u^\nu_{(Z)}$ the ZAMO four-velocity as seen for an observer at rest at infinity, $u^\nu_{(Z)} = \Gamma(1,0,0,\omega)$, with $\Gamma = \sqrt{A/(\Sigma\Delta)}$ and $\omega = 2\,Mar/A$.

The electric and magnetic field components measured by the ZAMO are $E_{\hat{i}} = E_\mu e^\mu_{\hat{i}}$ and $B_{\hat{i}} = B_\mu e^\mu_{\hat{i}}$, where $E_\mu = F_{\mu\nu}u^\nu_{(Z)}$ and $B_\mu = \tilde{F}_{\mu\nu}u^\nu_{(Z)}$. Using the above ZAMO tetrad and the electromagnetic tensor components (12), the resulting electric and magnetic fields measured by the ZAMO are $E_{\hat{i}} = (E_{\hat{1}}, E_{\hat{2}}, 0)$ and $B_{\hat{i}} = (B_{\hat{1}}, B_{\hat{2}}, 0)$, where

$$E_{\hat{1}} = -\frac{B_0aM}{\Sigma^2\sqrt{A}}\Big[(r^2+a^2)(r^2 - a^2\cos^2\theta)(1+\cos^2\theta) - 2r^2\sin^2\theta\,\Sigma\Big] + Q\frac{(r^2+a^2)(r^2-a^2\cos^2\theta)}{\Sigma^2\sqrt{A}}, \tag{18a}$$

$$E_{\hat{2}} = \frac{2ra^2\sin\theta\cos\theta}{\Sigma^2}\left[B_0aM(1+\cos^2\theta) - Q\sqrt{\frac{\Delta}{A}}\right], \tag{18b}$$

and

$$B_{\hat{1}} = -\frac{B_0\cos\theta}{\Sigma^2\sqrt{A}}\Big\{2Mra^2[2r^2\cos^2\theta + a^2(1+\cos^4\theta)] - (r^2+a^2)\Sigma^2\Big\} + Qa\frac{2r(r^2+a^2)\cos\theta}{\sqrt{A}\Sigma^2}, \tag{19a}$$

$$B_{\hat{2}} = \sqrt{\frac{\Delta}{A}}\frac{\sin\theta}{\Sigma^2}\{-B_0[Ma^2(r^2-a^2\cos^2\theta)(1+\cos^2\theta) + r\Sigma^2] + Qa(r^2 - a^2\cos^2\theta)\}. \tag{19b}$$

Figure 1 shows the electric and magnetic field lines in the ZAMO frame. In the northern and southern regions (hereafter polar regions), comprised at polar angles $-\theta_c^{(Q)} < \theta < \theta_c^{(Q)}$ and $\pi - \theta_c^{(Q)} < \theta < \pi + \theta_c^{(Q)}$, respectively, the electric field accelerates electrons outward and protons inward. In the eastern and western regions (hereafter equatorial regions), $\theta_c^{(Q)} \leq \theta \leq \pi - \theta_c^{(Q)}$ and $-\pi + \theta_c^{(Q)} \leq \theta \leq -\theta_c^{(Q)}$, respectively, the electric field accelerates electrons inward and protons outward. Notice that this result is independent of the ZAMO observer since it arises from the analysis of the Maxwell invariant associated with $\vec{E}\cdot\vec{B}$ (see Eq. 13).

Introducing the charge parameter, $\xi = Q/Q_W$, where $Q_W = Q_{\rm eff} = 2JB_0 = 2aMB_0$ is the so-called Wald charge (or effective charge; see [6,34,35], for this concept), and normalizing the radial coordinate to M and the electric and magnetic field to B_0, by fixing a value of a/M, the angle $\theta_c^{(Q)}$ depends only on ξ. Figure 1 shows the electric field lines (blue arrows) and the magnetic field lines (contours of constant A_ϕ, in red color) for a BH with $a/M = 0.7$. In this case, the solution of Eq. (14) gives, besides the trivial solution $\theta_c^{(Q)} = 90°$, $\theta_c^{(Q)} \approx 56.12°$ ($\xi = 0$), 46.87° ($\xi = 0.2$), and 38.44° ($\xi = 0.4$), so the polar region shrinks with the increase of the positive charge. On the contrary, the increase of a negative charge enlarges it, e.g., $\theta_c^{(Q)} \approx 67.86°$ ($\xi = -0.2$).

4 Particle energy and angular momentum

The conserved energy and angular momentum of massive, charged, test particle of mass m_i and charge q_i are

$$E_i = -\pi_\mu\eta^\mu = -\pi_0 = -p_0 - qA_0, \tag{20a}$$

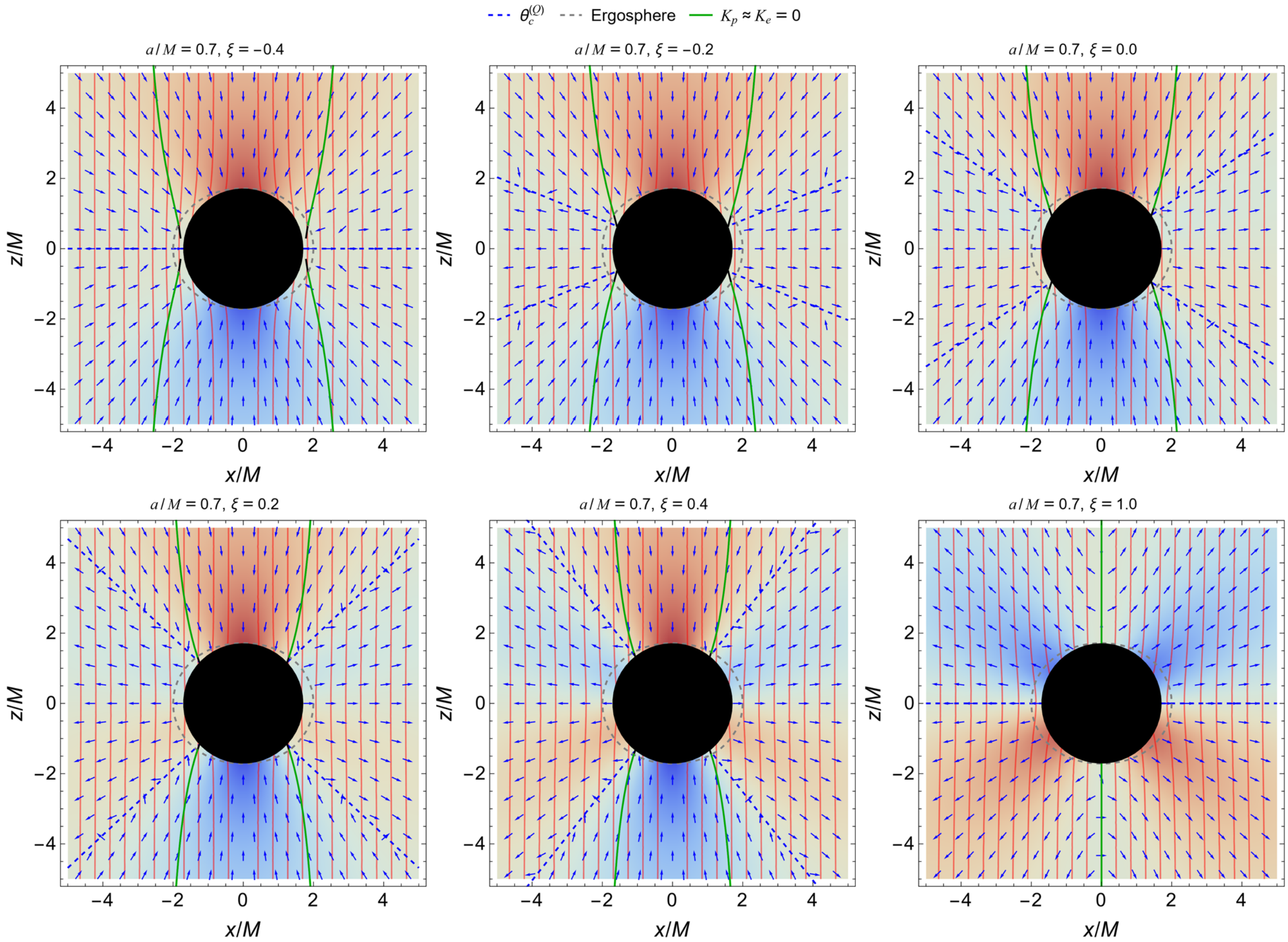

Fig. 1 BH horizon (filled-black), ergosphere (dashed-gray), $K_p = 0$ boundary (green), electric field lines (blue arrows) and magnetic field lines (red, contours of constant A_3) for selected values of the charge parameter, $\xi = Q/Q_W$, where $Q_W = 2JB_0 = 2aMB_0$. By normalizing the radial coordinate to M and the electric and magnetic field intensity to B_0, the EM field expressions depend only on a/M and ξ. In this example, the BH spin parameter is $a/M = 0.7$, in the upper panel, $\xi = -0.4$ (left), -0.2 (center), and 0.0 (right), and in the lower panel, $\xi = 0.2$ (left), 0.4 (center), and 1.0 (right). The lower panel shows how the angle at which $\vec{E}\cdot\vec{B} = 0$ (besides the equator), marked by the dashed-blue lines, shrinks with the increase of the positive charge, for instance, $\theta_c^{(Q)} \approx 56.12°$ ($\xi = 0$), $46.87°$ ($\xi = 0.2$), and $38.44°$ ($\xi = 0.4$). The background color maps the value of $\vec{E}\cdot\vec{B}$, i.e., the redder color is negative and the bluer positive

$$L_i = \pi_\mu \psi^\mu = \pi_3 = p_3 + qA_3, \tag{20b}$$

where $p_\alpha = m_i u_\alpha$ the four-momentum, u_α the four-velocity, A_μ is the electromagnetic four-potential given by Eq. (10), and $i = p, e$ stands for protons or electrons. We also refer the reader to the discussions of charged particle motion, energy, and angular momentum in the case of the Wald solution presented in [12,13,36].

As in Ref. [5], we study test particles initially at rest at the position (r_i, θ_i, ϕ_i), outside the ergosphere. Hence, $\Sigma_i > 2Mr_i$, with $r_i > r_{\rm erg} = M + \sqrt{M^2 - a^2\cos^2\theta_i}$, and the initial four-velocity is $u_i^\alpha = u_i^0\delta_0^\alpha$, with $u_i^0 = (1-2Mr_i/\Sigma_i)^{-1/2}$. The kinetic energy of a particle crossing the BH horizon is

$$K_i = -p_\mu l^\mu|_+ = E_i - \Omega_+ L_i. \tag{21}$$

where $l^\mu = \eta^\mu + \Omega_+\psi^\mu$ [37]. By inspecting Eq. (8), it can be seen that the condition $K_i > 0$ implies the increase of the square of the BH irreducible mass.

Charged particles will follow the magnetic field lines, which are nearly vertical (see Fig. 1), so the BH can capture particles at initial positions $r_i \sin\theta_i \lesssim r_H$. For example, let us set initial particle positions $r_i \sin\theta_i = r_H$. The upper panel of Fig. 2 shows E_e, L_e, E_p, L_p, K_e, K_p, and indicates the spherical polar angles $\theta_c^{(Q)}$, θ_{K_p}, and $\theta_{i,\rm cyl}(r_i = r_{\rm erg})$. The angle $\theta_{i,\rm cyl}(r_i = r_{\rm erg})$ is the maximum value at which the initial position is along the set cylinder and above the ergosphere, i.e., the solution of the equation $r_{\rm erg}\sin\theta_i = r_H$. The angle θ_{K_p} is that where $K_p = 0$. Thus, the BH captures polar protons (in the northern hemisphere) in the region $0 \le \theta \le {\rm Min}(\theta_c^{(Q)}, \theta_{i,\rm cyl}, \theta_{K_p})$. Let us analyze the neutral case, $\xi = 0$ (upper right figure). We have $\theta_{K_p} \approx 41°$, $\theta_c^{(Q)} \approx 57°$, and $\theta_{i,\mathrm{cyl}}(r_i = r_{\mathrm{erg}}) \approx 62°$. The BH captures protons in the region $0 \leq \theta_{K_p}$. These protons have positive energy and angular momentum (see solid and dashed orange curves). For larger angles, proton trajectories do not cross the event horizon (the red curve, K_p, becomes negative), and the BH captures electrons (the blue curve, K_e, becomes positive). Those electrons have negative energy and angular momentum (solid and dashed green curves). An analogous analysis can be done for non-zero values of the charge parameter: it turns out that the proton(electron) capture region shrinks(enlarges) for positive values of the charge parameter and vice-versa for negative values, as expected from Fig. 1.

5 BH mass, angular momentum, and irreducible mass change

By capturing a particle, the BH mass and angular momentum change by $dM_i = E_i$ and $dJ_i = L_i$. Because $dM_i - \Omega_+ dJ_i = E_i - \Omega_+ L_i = K_i \geq 0$ (see Fig. 2), we have $dM_{\mathrm{irr}}^2 \geq 0$ (see Eq. 8), as expected from the BH reversible and irreversible transformations [8,9] or the horizon surface area increase theorem [10].

For a particle number density n, we can estimate the net energy and angular momentum transferred to the BH by the captured particles as [5]

$$\begin{aligned}\mathscr{E}_i &= 2\pi \iint E_i n\sqrt{-g}\, dr_i d\theta_i \\ &= 2\pi \iint E_i n \Sigma_i \sin\theta_i\, dr_i d\theta_i, \qquad (22a)\\ \mathscr{L}_i &= 2\pi \iint L_i n\sqrt{-g}\, dr_i d\theta_i \\ &= 2\pi \iint L_i n \Sigma_i \sin\theta_i\, dr_i d\theta_i, \qquad (22b)\end{aligned}$$

where the integration is carried out in the region covering all initial positions of particles captured by the BH, as discussed in the previous section. We calculate the conserved energy and angular momentum at the initial position (r_i, θ_i) of the electrons ($i = e$) and protons ($i = p$), where we assume they start their motion at rest, so $u_e^0 = u_p^0 = 1/\sqrt{-g_{00}} = (1 - 2Mr_{e,p}/\Sigma_{e,p})^{-1/2}$. Hence, Eq. (20) become

$$E_e = m_e\sqrt{-g_{00}} + eA_0, \quad E_p = m_p\sqrt{-g_{00}} - eA_0, \qquad (23a)$$

$$L_e = m_e\frac{g_{03}}{\sqrt{-g_{00}}} - eA_3, \quad L_p = m_p\frac{g_{03}}{\sqrt{-g_{00}}} + eA_3, \qquad (23b)$$

where we have denoted with $m_{e,p}$ the electron and proton rest-mass and $q_e = -e$ and $q_p = +e$ their charge, and the electromagnetic four-potential components are given by Eq. (11). Therefore, we obtain the total energy and angular momentum absorbed by the BH are

$$\mathscr{E} = \mathscr{E}_e + \mathscr{E}_p, \quad \mathscr{L} = \mathscr{L}_e + \mathscr{L}_p \qquad (24)$$

where

$$\begin{aligned}\mathscr{E}_e &= 2\pi \iint n\Sigma_e \sin\theta_e \left[m_e\sqrt{-g_{00}} + \frac{eB_0}{2}g_{03} + \left(eaB_0 - \frac{eQ}{2M}\right)g_{00}\right] dr_e\theta_e, \qquad (25a)\\ \mathscr{L}_e &= 2\pi \iint n\Sigma_e \sin\theta_e \left[m_e\frac{g_{03}}{\sqrt{-g_{00}}} - \frac{eB_0}{2}g_{33} - \left(eaB_0 - \frac{eQ}{2M}\right)g_{03}\right] dr_e\theta_e, \qquad (25b)\\ \mathscr{E}_p &= 2\pi \iint n\Sigma_p \sin\theta_p \left[m_p\sqrt{-g_{00}} - \frac{eB_0}{2}g_{03} - \left(eaB_0 - \frac{eQ}{2M}\right)g_{00}\right] dr_p\theta_p, \qquad (25c)\\ \mathscr{L}_p &= 2\pi \iint n\Sigma_p \sin\theta_p \left[m_p\frac{g_{03}}{\sqrt{-g_{00}}} + \frac{eB_0}{2}g_{33} + \left(eaB_0 - \frac{eQ}{2M}\right)g_{03}\right] dr_p\theta_p, \qquad (25d)\end{aligned}$$

where we have used the expression of A_μ given in Eq. (A.2) in Appendix A, Eq. (23), and the involved metric functions are given in Eq. (9).

With the above, the total change of the mass, angular momentum, and irreducible mass are

$$\Delta M = \mathscr{E}, \quad \Delta J = \mathscr{L}, \quad \Delta M_{\mathrm{irr}} = M_{\mathrm{irr}}\frac{\mathscr{E} - \Omega_+\mathscr{L}}{\sqrt{M^2 - a^2}}, \qquad (26)$$

where we have assumed the changes as infinitesimal (relative to the BH initial parameters) and used Eq. (3) to estimate the change of the irreducible mass.

Figure 3 shows in the upper panels $\mathscr{E}_e$ and $\mathscr{E}_p$, in the middle panels, $\mathscr{L}_e$ and $\mathscr{L}_p$, and in the lower panels, ΔM, ΔJ, and ΔM_{irr}, for selected values of the charge parameter, $\xi = 0$ (first column), 0.3 (central column), 0.5 (last column), as a function of the BH spin parameter. We assume a spherically symmetric density, $n(r) = n_+(r_+/r)^m$, with $m = 3$. It is clear from Eq. (25) that the parameter n_+ is only a scaling factor, so we do not need to specify it for the general discussion. However, we must remember that the particle density around the BH must be lower than the Goldreich-Julian density to avoid the screening of the accelerating electric field (see discussion in [5]). For instance, for a BH of mass $M = 4M_\odot$, spin $a = M$, surrounded by a magnetic field of 10^{13} G, the density must be lower than a few 10^{-9} g cm^{-3}, so $n_+ \lesssim 10^{15}$ cm^{-3}. Further, for these astrophysical BH and magnetic field parameters, the electric potential energy largely dominates over the gravitational one [5], which implies, from Eq. (23),

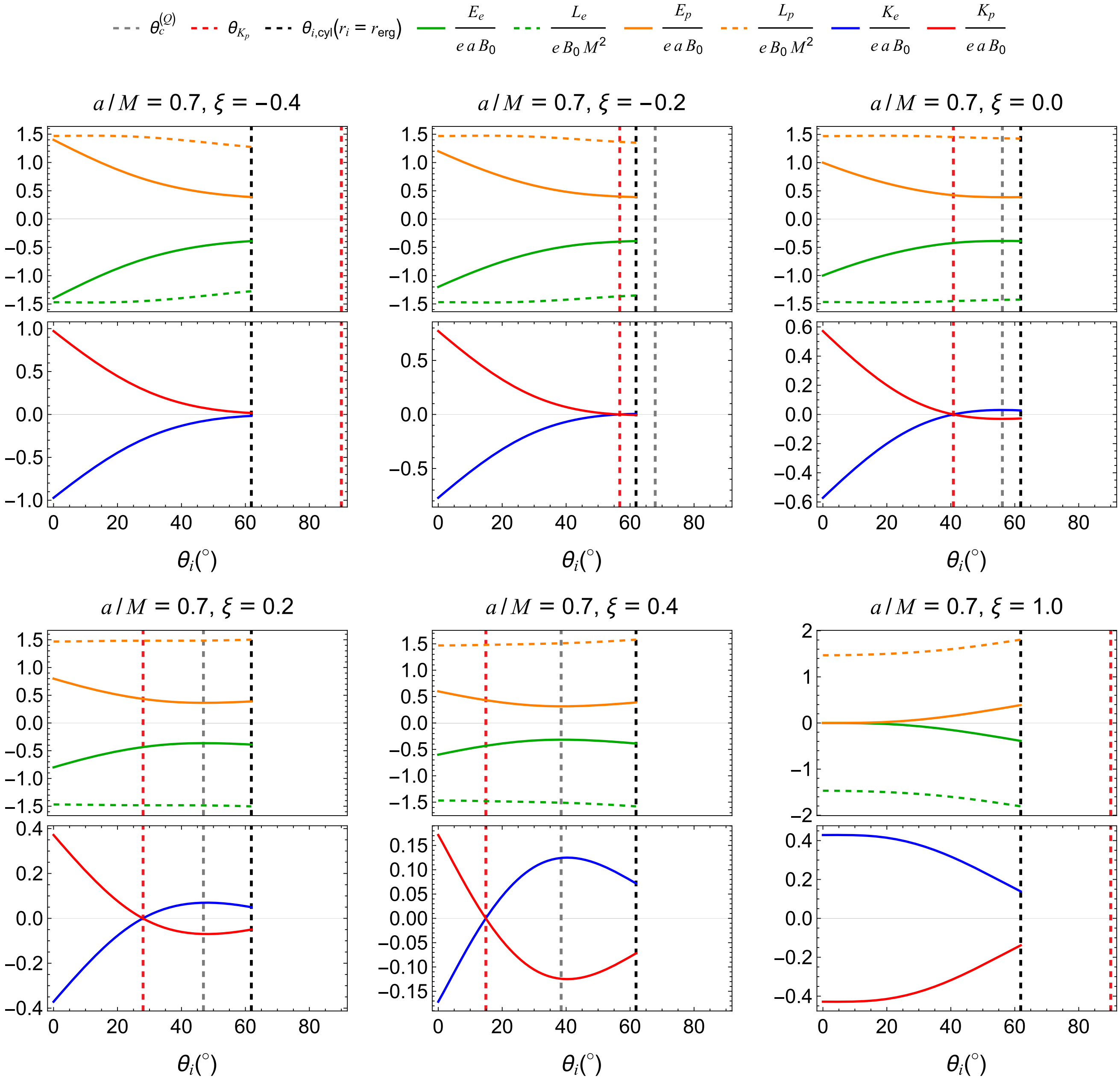

Fig. 2 E_i, L_i, given by Eqs. (20a)–(20b), and K_i given by Eq. (21), at initial positions outside the ergosphere ($r_i > r_{\mathrm{erg}}$) leading to the particle capture by the BH (see Fig. 1). In this example, the initial radial coordinate is set by $r_i = r_H / \sin\theta_i$, and the polar angle by $0 \leq \theta_i \leq \theta_{i,\mathrm{cyl}}(r_i = r_{\mathrm{erg}})$, and the polar angle is $\theta_{i,\mathrm{cyl}}(r_i = r_{\mathrm{erg}}) \approx 61.86^\circ$ is the angle at which $r_i = r_{\mathrm{erg}}$

that $E_{e,p} \approx \pm e A_0$ and $L_{e,p} \approx \mp e A_3$, which do not depend upon the particle mass. Under these conditions, and recalling that $Q = \xi Q_W = \xi 2 a M B_0$, $E_{e,p}$ and $L_{e,p}$ scale with $e a B_0$ and $e B_0 M^2$, respectively, which explains the normalization used in Fig. 3.

The figure suggests the BH could follow a cyclic behavior. Let us start with a neutral BH ($\xi = 0$, left column plots). As already discussed in [5], and shown by this plot, the BH in this initial phase absorbs more protons than electrons, so it gains energy and angular momentum ($\Delta M > 0$ and $\Delta J > 0$), and becomes positively charged ($\xi > 0$). Figures 1 and 2 show that, for $\xi > 0$, the polar region shrinks (the equatorial enlarges), so the positive contribution of protons to the energy and angular momentum reduces, and the negative one of electrons increases, as shown by the central column panels. The process can continue this way until the BH starts to absorb more electrons than protons, and it gains net negative energy and angular momentum ($\Delta M < 0$

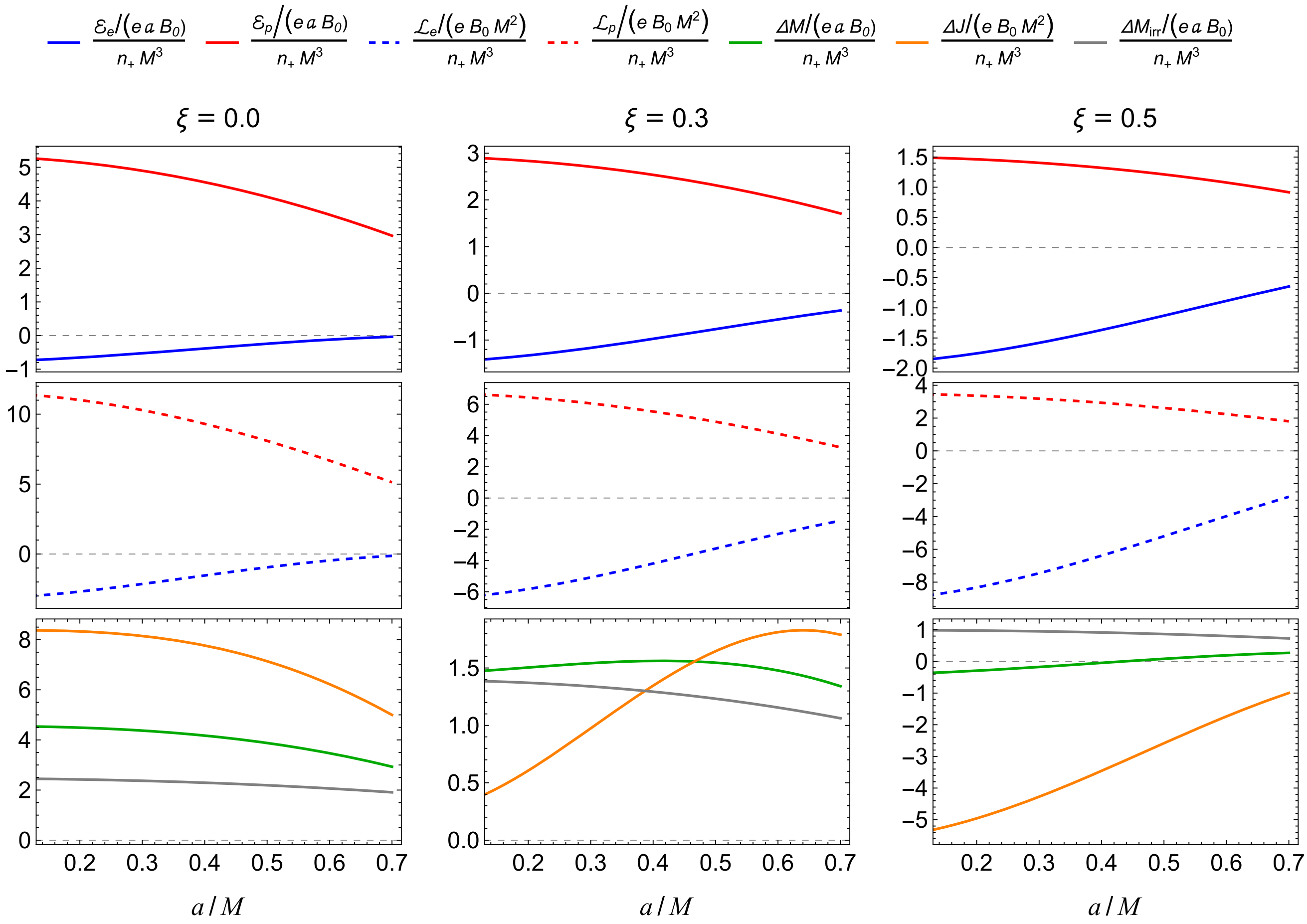

Fig. 3 Upper and middle panels: total energy and angular momentum, $\mathscr{E}_i/(eB_0a)$ and $\mathscr{L}_i/(eB_0M^2)$, of the polar protons (solid and dashed red) and equatorial electrons (solid and dashed blue) absorbed by the BH, given by Eq. (25). Lower panels: The net change of the BH mass-energy ΔM (green), angular momentum ΔL (orange), and irreducible mass $\Delta M_{\rm irr}$ (gray), according to Eq. (26)

and $\Delta J < 0$), as shown in the last column panels. In this stage, the BH energy is extracted. It can be shown that for $\xi > \xi_c = (3 - \sqrt{1-(a/M)^2})/2$, the polar region is entirely contained in the cylinder of radius r_+, leading to a considerable reduction of absorbed protons. The electrons can take over, causing the BH charge to reduce. The BH energy extraction continues. However, the decrease in the BH charge reverses the shrinking of the polar region and the equatorial region enlargement. The charge becomes again $\xi < \xi_c$, and at some instant, the enlargement of the polar region is such that protons take over once again. The BH energy extraction stops, and the cycle repeats.

6 Conclusions

We have generalized the analysis of Ref. [5] of the energy extraction from a Kerr BH, immersed in a magnetic field asymptotically aligned to the BH spin, which captures positively and negatively charged particles from its surroundings, considering the effects of the BH charge. For this task, we used the charged Wald solution [4], i.e., for test BH charge. We have estimated the change of the BH mass, angular momentum, and irreducible mass for different values of the BH spin and charge parameter.

We have shown the changes of the region of capturable protons and electrons as a function of the BH charge parameter (see Figs. 1, 2). The changing polar and equatorial regions with the charge parameter leads to new results relative to the previously uncharged analysis in [5].

For the present case, energy extraction occurs for a particle density that is isotropic and falls with distance as a power-law, e.g., $n \propto 1/r^3$, unlike the uncharged case [5]. The increase of the irreducible mass in this process is relatively low compared to purely gravitational processes like the Penrose process recently evaluated in Paper II.

For isotropic ionized matter density, our analysis for various spin and charge values suggests the BH could evolve in cycles where its charge increases and decreases, alternating periods without and with energy and angular momentum extraction (see Figs. 2, 3).

As we have made some assumptions, it is worth mentioning possible extensions and generalizations of this work. Two main extensions are particularly promising and relevant. First, abandoning the assumption of the BH charge as a test charge. Such an extension would allow us to verify how much the maximum extractable energy of 50% of the energy of an extremely charged BH is approachable. Second, in our estimate of the increase of the irreducible mass, we have carried out the integrals (22) over the entire region where the charged particles can be captured by the BH of some mass and angular momentum. The above method implicitly assumes all those particles are captured simultaneously. Thus, an improvement would be calculating the equal capture time regions. The above extension is necessary for understanding the dynamic behavior of this system. Further, they will lead to an improved assessment of the BH irreducible mass increase in time, hence the efficiency of the energy extraction process.

Data Availability Statement My manuscript has no associated data. [Authors' comment: Data sharing not applicable to this article as no datasets were generated or analysed during the current study.]

Code Availability Statement My manuscript has no associated code/software. [Authors' comment: Code/Software sharing not applicable to this article as no code/software was generated or analysed during the current study.]

Funded by SCOAP[3].

Appendix A Expressions of the electromagnetic four-potential, Faraday tensor and its dual

This appendix shows the explicit, full expressions, i.e., vanishing and non-vanishing components, of the electromagnetic four-potential, A_μ, the Faraday tensor, $F_{\alpha\beta}$, and its dual, $\tilde{F}_{\alpha\beta}$. We start with A_μ, so for this task, following Eq. (10), we must know the covariant and contravariant time-like and space-like Killing vectors

$$\eta^\mu = \delta^\mu_0, \quad \eta_\mu = g_{\mu\alpha}\eta^\alpha = g_{\mu 0} = g_{00}\delta^0_\mu + g_{03}\delta^3_\mu, \tag{A.1a}$$

$$\psi^\mu = \delta^\mu_3, \quad \psi_\mu = g_{\mu\alpha}\psi^\alpha = g_{\mu 3} = g_{03}\delta^0_\mu + g_{33}\delta^3_\mu. \tag{A.1b}$$

Using Eq. (A.1), A_μ can be written as

$$A_\mu = \left[\frac{B_0}{2}g_{03} + \left(aB_0 - \frac{Q}{2M}\right)g_{00}\right]\delta^0_\mu + \left[\frac{B_0}{2}g_{33} + \left(aB_0 - \frac{Q}{2M}\right)g_{03}\right]\delta^3_\mu, \tag{A.2}$$

where the metric tensor is

$$g_{\alpha\beta} = \begin{pmatrix} g_{00} & 0 & 0 & g_{03} \\ 0 & g_{11} & 0 & 0 \\ 0 & 0 & g_{22} & 0 \\ g_{03} & 0 & 0 & g_{33} \end{pmatrix} \tag{A.3}$$

with the components given in Eq. (9). The inverse metric tensor is

$$g^{\alpha\beta} = \begin{pmatrix} g^{00} & 0 & 0 & g^{03} \\ 0 & g^{11} & 0 & 0 \\ 0 & 0 & g^{22} & 0 \\ g^{03} & 0 & 0 & g^{33} \end{pmatrix}, \tag{A.4}$$

where

$$g^{00} = \frac{g_{33}}{g_{00}g_{33} - g_{03}^2} = -\frac{A}{\Sigma\Delta}, \tag{A.5a}$$

$$g^{11} = \frac{1}{g_{11}} = \frac{\Delta}{\Sigma}, \tag{A.5b}$$

$$g^{22} = \frac{1}{g_{22}} = \frac{1}{\Sigma}, \tag{A.5c}$$

$$g^{33} = \frac{g_{00}}{g_{00}g_{33} - g_{03}^2} = \frac{\Delta - a^2\sin^2\theta}{\Sigma\Delta\sin^2\theta}, \tag{A.5d}$$

$$g^{03} = -\frac{g_{03}}{g_{00}g_{33} - g_{03}^2} = -\frac{2Mar}{\Sigma\Delta}. \tag{A.5e}$$

Thus, by replacing the metric functions in Eq. (A.2), we obtain the electromagnetic four-potential

$$A_\mu = (A_0, 0, 0, A_3), \tag{A.6}$$

where A_0 and A_3 are given in Eq. (11).

The Faraday tensor is defined as $F_{\alpha\beta} = \partial_\alpha A_\beta - \partial_\beta A_\alpha$. Thus, using Eq. (A.6), and that A_0 and A_3 are only functions of r and θ because of the axial symmetry, we obtain

$$F_{\alpha\beta} = \partial_1 A_0(\delta^1_\alpha\delta^0_\beta - \delta^1_\beta\delta^0_\alpha) + \partial_2 A_0(\delta^2_\alpha\delta^0_\beta - \delta^2_\beta\delta^0_\alpha) + \partial_1 A_3(\delta^1_\alpha\delta^3_\beta - \delta^1_\beta\delta^3_\alpha) + \partial_2 A_3(\delta^2_\alpha\delta^3_\beta - \delta^2_\beta\delta^3_\alpha), \tag{A.7}$$

which can be written in matrix form as

$$F_{\alpha\beta} = \begin{pmatrix} 0 & F_{01} & F_{02} & 0 \\ F_{10} & 0 & 0 & F_{13} \\ F_{20} & 0 & 0 & F_{23} \\ 0 & F_{31} & F_{32} & 0 \end{pmatrix}, \tag{A.8}$$

where

$$F_{01} = -F_{10} = -\partial_1 A_0, \quad F_{02} = -F_{20} = -\partial_2 A_0, \tag{A.9a}$$
$$F_{13} = -F_{31} = \partial_1 A_3, \quad F_{23} = -F_{32} = \partial_2 A_3, \tag{A.9b}$$

leading to the expressions given by Eq. (12). For completeness, we give the expressions of the two-contravariant Faraday tensor $F^{\alpha\beta} = g^{\alpha\mu} g^{\beta\nu} F_{\mu\nu}$, in matrix form

$$F^{\alpha\beta} = \begin{pmatrix} 0 & F^{01} & F^{02} & 0 \\ F^{10} & 0 & 0 & F^{13} \\ F^{20} & 0 & 0 & F^{23} \\ 0 & F^{31} & F^{32} & 0 \end{pmatrix}, \tag{A.10}$$

where

$$F^{01} = -F^{10} = g^{11}(g^{00} F_{01} + g^{03} F_{31}), \tag{A.11a}$$
$$F^{02} = -F^{20} = g^{22}(g^{00} F_{02} + g^{03} F_{32}), \tag{A.11b}$$
$$F^{13} = -F^{31} = g^{11}(g^{03} F_{10} + g^{33} F_{13}), \tag{A.11c}$$
$$F^{23} = -F^{32} = g^{22}(g^{03} F_{20} + g^{33} F_{23}), \tag{A.11d}$$

with the inverse metric given by Eqs. (A.4) and (A.5).

For the determination of the electromagnetic scalars, we must compute the electromagnetic dual tensor, defined by $\sqrt{-g}\tilde{F}^{\alpha\beta} = (1/2)\epsilon^{\alpha\beta\mu\nu} F_{\mu\nu}$, being $\epsilon^{\alpha\beta\mu\nu}$ the Levi-Civita symbol given by

$$\epsilon^{\alpha\beta\mu\nu} = \begin{cases} +1, & \text{for even permutations of 0,1,2,3} \\ -1, & \text{for odd permutations of 0,1,2,3} \\ 0, & \text{otherwise.} \end{cases} \tag{A.12}$$

With the above definition, we obtain

$$\sqrt{-g}\tilde{F}^{\alpha\beta} = \begin{pmatrix} 0 & F_{23} & -F_{13} & 0 \\ -F_{23} & 0 & 0 & -F_{02} \\ F_{13} & 0 & 0 & F_{01} \\ 0 & F_{02} & -F_{01} & 0 \end{pmatrix}. \tag{A.13}$$

It is straightforward to check that the matrix product of Eqs. (A.8) and (A.13) leads to the electromagnetic invariant (13).

References

1. R. Penrose, Nuovo Cimento Rivista Serie **1**, 252 (1969)
2. R. Ruffini, M. Prakapenia, H. Quevedo, S. Zhang, Submitted. https://doi.org/10.48550/arXiv.2405.08229. arXiv:2405.08229 (2024)
3. R. Ruffini, C.L. Bianco, M. Prakapenia, H. Quevedo, J.A. Rueda, S.R. Zhang, Submitted. https://doi.org/10.48550/arXiv.2405.10459. arXiv:2405.10459 (2024)
4. R.M. Wald, Phys. Rev. D **10**, 1680 (1974). https://doi.org/10.1103/PhysRevD.10.1680
5. J.A. Rueda, R. Ruffini, Eur. Phys. J. C **83**(10), 960 (2023). https://doi.org/10.1140/epjc/s10052-023-12153-y
6. R. Moradi, J.A. Rueda, R. Ruffini, Y. Wang, Astron. Astrophys. **649**, A75 (2021). https://doi.org/10.1051/0004-6361/201937135
7. J.A. Rueda, R. Ruffini, R.P. Kerr, Astrophys. J. **929**(1), 56 (2022). https://doi.org/10.3847/1538-4357/ac5b6e
8. D. Christodoulou, Phys. Rev. Lett. **25**(22), 1596 (1970). https://doi.org/10.1103/PhysRevLett.25.1596
9. D. Christodoulou, R. Ruffini, Phys. Rev. D **4**, 3552 (1971). https://doi.org/10.1103/PhysRevD.4.3552
10. S.W. Hawking, Phys. Rev. Lett. **26**, 1344 (1971). https://doi.org/10.1103/PhysRevLett.26.1344
11. J.A. Rueda, R. Ruffini, Astron. Rep. **67**, S93 (2023). https://doi.org/10.1134/S1063772923140184
12. J. Levin, D.J. D'Orazio, S. Garcia-Saenz, Phys. Rev. D **98**(12), 123002 (2018). https://doi.org/10.1103/PhysRevD.98.123002
13. K. Gupta, Y.T.A. Law, J. Levin, Phys. Rev. D **104**(8), 084059 (2021). https://doi.org/10.1103/PhysRevD.104.084059
14. G. Denardo, R. Ruffini, Phys. Lett. B **45**(3), 259 (1973). https://doi.org/10.1016/0370-2693(73)90198-6
15. S.V. Dhurandhar, N. Dadhich, Phys. Rev. D **30**(8), 1625 (1984). https://doi.org/10.1103/PhysRevD.30.1625
16. S. Parthasarathy, S.M. Wagh, S.V. Dhurandhar, N. Dadhich, Astrophys. J. **307**, 38 (1986). https://doi.org/10.1086/164390
17. A. Tursunov, N. Dadhich, Universe **5**(5), 125 (2019). https://doi.org/10.3390/universe5050125
18. M. Kološ, A. Tursunov, Z. Stuchlík, Phys. Rev. D **103**(2), 024021 (2021). https://doi.org/10.1103/PhysRevD.103.024021
19. A. Tursunov, B. Juraev, Z. Stuchlík, M. Kološ, Phys. Rev. D **104**(8), 084099 (2021). https://doi.org/10.1103/PhysRevD.104.084099
20. Z. Stuchlík, M. Kološ, A. Tursunov, Universe **7**(11), 416 (2021). https://doi.org/10.3390/universe7110416
21. M.D. Pollock, Proc. Roy. Soc. Lond. Ser. A **350**(1661), 239 (1976). https://doi.org/10.1098/rspa.1976.0105
22. M.D. Pollock, W.P. Brinkmann, Proc. Roy. Soc. Lond. Ser. A **356**(1686), 351 (1977). https://doi.org/10.1098/rspa.1977.0138
23. A.R. King, J.P. Lasota, Astron. Astrophys. **58**(1–2), 175 (1977)
24. R. Ruffini, J.R. Wilson, Phys. Rev. D **12**(10), 2959 (1975). https://doi.org/10.1103/PhysRevD.12.2959
25. R.D. Blandford, R.L. Znajek, Mon. Not. Roy. Astron. Soc. **179**, 433 (1977). https://doi.org/10.1093/mnras/179.3.433
26. S.S. Komissarov, Mon. Not. Roy. Astron. Soc. **350**(2), 427 (2004). https://doi.org/10.1111/j.1365-2966.2004.07598.x
27. S.S. Komissarov, Mon. Not. Roy. Astron. Soc. **359**(3), 801 (2005). https://doi.org/10.1111/j.1365-2966.2005.08974.x
28. K. Parfrey, A. Philippov, B. Cerutti, Phys. Rev. Lett. **122**(3), 035101 (2019). https://doi.org/10.1103/PhysRevLett.122.035101
29. M. Takahashi, S. Nitta, Y. Tatematsu, A. Tomimatsu, Astrophys. J. **363**, 206 (1990). https://doi.org/10.1086/169331
30. L. Comisso, F.A. Asenjo, Phys. Rev. D **103**(2), 023014 (2021). https://doi.org/10.1103/PhysRevD.103.023014
31. B. Carter, Phys. Rev. **174**(5), 1559 (1968). https://doi.org/10.1103/PhysRev.174.1559
32. J.M. Bardeen, Astrophys. J. **162**, 71 (1970). https://doi.org/10.1086/150635
33. J.M. Bardeen, W.H. Press, S.A. Teukolsky, Astrophys. J. **178**, 347 (1972). https://doi.org/10.1086/151796
34. R. Ruffini, R. Moradi, J.A. Rueda, L. Becerra, C.L. Bianco, C. Cherubini, S. Filippi, Y.C. Chen, M. Karlica, N. Sahakyan, Y. Wang, S.S. Xue, Astrophys. J. **886**(2), 82 (2019). https://doi.org/10.3847/1538-4357/ab4ce6
35. J.A. Rueda, R. Ruffini, Eur. Phys. J. C **80**(4), 300 (2020). https://doi.org/10.1140/epjc/s10052-020-7868-z
36. S.S. Komissarov, Mon. Not. Roy. Astron. Soc. **512**(2), 2798 (2022). https://doi.org/10.1093/mnras/stab2686
37. B. Carter, in Black Holes (Les Astres Occlus) (1973), pp. 57–214

The Astrophysical Journal, 976:80 (14pp), 2024 November 20 https://doi.org/10.3847/1538-4357/ad82ea

Occurrence of Gravitational Collapse in the Accreting Neutron Stars of Binary-driven Hypernovae

L. M. Becerra[1,2], F. Cipolletta[3], C. L. Fryer[4], Débora P. Menezes[5], Constança Providência[6], J. A. Rueda[2,7,8,9,10], and R. Ruffini[2,7,11]

[1] Centro Multidisciplinario de Física, Vicerrectoría de Investigación, Universidad Mayor, Santiago de Chile 8580745, Chile; laura.becerra7@correo.uis.edu.co
[2] IICRANet, Piazza della Repubblica 10, I-65122 Pescara, Italy
[3] Barcelona Supercomputing Center, Plaça Eusebi Güell 1–3, I–08034 Barcelona, Spain
[4] CCS-2, Los Alamos National Laboratory, Los Alamos, NM 87545, USA
[5] Departamento de Física—CFM, Universidade Federal de Santa Catarina, Florianópolis/SC, CEP 88.040–900, Brazil
[6] CFisUC, Department of Physics, University of Coimbra, 3004–516 Coimbra, Portugal
[7] ICRA, Dipartimento di Fisica, Sapienza Università di Roma, P.le Aldo Moro 5, 00185 Rome, Italy
[8] ICRANet-Ferrara, Dipartimento di Fisica e Scienze della Terra, Università degli Studi di Ferrara, Via Saragat 1, I–44122 Ferrara, Italy
[9] Dipartimento di Fisica e Scienze della Terra, Università degli Studi di Ferrara, Via Saragat 1, I–44122 Ferrara, Italy
[10] INAF, Istituto di Astrofisica e Planetologia Spaziali, Via Fosso del Cavaliere 100, 00133 Rome, Italy
[11] INAF, Viale del Parco Mellini 84, 00136 Rome, Italy
Received 2023 December 4; revised 2024 September 30; accepted 2024 October 1; published 2024 November 14

Abstract

The binary-driven hypernova (BdHN) model proposes long gamma-ray bursts (GRBs) originate in binaries composed of a carbon–oxygen (CO) star and a neutron star (NS) companion. The CO core collapse generates a newborn NS and a supernova that triggers the GRB by accreting onto the NSs, rapidly transferring mass and angular momentum to them. This article aims to determine the conditions under which a black hole (BH) forms from NS collapse induced by the accretion and the impact on the GRB's observational properties and taxonomy. We perform three-dimensional, smoothed particle hydrodynamics simulations of BdHNe using up-to-date NS nuclear equations of state, with and without hyperons, and calculate the structure evolution in full general relativity. We assess the binary parameters leading either NS in the binary to the critical mass for gravitational collapse into a BH and its occurrence time, t_{col}. We include a nonzero angular momentum of the NSs and find that t_{col} ranges from a few tens of seconds to hours for decreasing NS initial angular momentum values. BdHNe I are the most compact (about 5 minute orbital period), promptly form a BH, and release $\gtrsim 10^{52}$ erg of energy. They form NS–BH binaries with tens of kiloyears merger timescales by gravitational-wave emission. BdHNe II and III do not form BHs, and release $\sim 10^{50}$–10^{52} erg and $\lesssim 10^{50}$ erg of energy, respectively. They form NS–NS binaries with a range of merger timescales larger than for NS–BH binaries. In some compact BdHNe II, either NS can become supramassive, i.e., above the critical mass of a nonrotating NS. Magnetic braking by a 10^{13} G field can delay BH formation, leading to BH–BH or NS–BH with tens of kiloyears merger timescales.

Unified Astronomy Thesaurus concepts: Gamma-ray bursts (629); Neutron stars (1108); Black holes (162); Gravitational collapse (662); Core-collapse supernovae (304); Close binary stars (254); Compact binary stars (283)

1. Introduction

Understanding the physical and astrophysical conditions under which a neutron star (NS) can reach the point of gravitational collapse into a black hole (BH) is essential for understanding the final stages of binary stellar evolution, which are associated with the most energetic and powerful cataclysms in the Universe: gamma-ray bursts (GRBs).

In a few seconds, a GRB can produce a gamma-ray luminosity comparable to the luminosity of all stars in the observable Universe, which makes a GRB detectable to cosmological redshifts $z \sim 10$, close to the dawn of galaxy and stellar formation. Observationally, they are classified as short or long depending on whether T_{90} is shorter or longer than 2 s. The time T_{90} is the time interval in the observer frame where 90% of the isotropic energy in gamma rays (E_{iso}) is released (E. P. Mazets et al. 1981; J.-P. Dezalay et al. 1992; R. W. Klebesadel 1992; C. Kouveliotou et al. 1993; M. Tavani 1998). This article focuses on assessing the BH formation in long GRBs within the binary-driven hypernova (BdHN) scenario (details below).

Despite a few peculiar exceptions of short bursts that shows hybrid properties of long GRBs, pointing to alternative scenarios (e.g., see the discussion in J. A. Rueda et al. 2018; B.-B. Zhang et al. 2021), NS binary (NS–NS) and NS–BH mergers are widely accepted as the progenitors of short GRBs (J. Goodman 1986; B. Paczynski 1986; D. Eichler et al. 1989; R. Narayan et al. 1991). This view has gained additional attention by the proposed first electromagnetic counterpart associated with a gravitational-wave event, i.e., GW170817 and GRB 170817A (B. P. Abbott et al. 2017).

For long GRBs, the model (see, e.g., P. Mészáros 2002; T. Piran 2004, for reviews) based on a relativistic jet, a fireball of an optically thick $e^{-}e^{+}$–photon–baryon plasma (G. Cavallo & M. J. Rees 1978; J. Goodman 1986; B. Paczynski 1986; R. Narayan et al. 1991, 1992), with bulk Lorentz factor $\Gamma \sim 10^2$–10^3 (A. Shemi & T. Piran 1990; M. J. Rees & P. Meszaros 1992; P. Meszaros et al. 1993; T. Piran et al. 1993; S. Mao & I. Yi 1994), powered by a massive disk accreting onto a BH, became the traditional GRB model. The formation of such a BH–massive disk structure has been theorized by the collapsar model (S. E. Woosley 1993; A. I. MacFadyen & S. E. Woosley 1999), i.e., the core collapse of a single, massive, fast-rotating star. In parallel, it has also been explored as GRB central engine, a highly magnetized, newborn NS (V. V. Usov 1992; J. C. Wheeler et al. 2000; B. D. Metzger et al. 2011), currently referred to as the millisecond magnetar scenario. This model has gained attention in the literature mainly in the explanation of low to moderate luminosity GRBs (see, e.g., T. A. Thompson et al. 2004; N. Bucciantini et al. 2007; B. D. Metzger et al. 2007; P. Beniamini et al. 2017; B. D. Metzger et al. 2018; S. Dall'Osso et al. 2023; C.-Y. Song & T. Liu 2023, and references therein); see also B. Zhang (2018) for a recent review of the traditional GRB model.

Meanwhile, GRB astronomy has made significant advances that challenge the traditional picture of long GRBs and evidence the need to explore alternatives. In particular, there is mounting evidence of the necessity of accounting for binary progenitors, as discussed below.

First, we recall the X-ray afterglow discovery by the BeppoSAX satellite (E. Costa et al. 1997) and the confirmation of the GRB cosmological nature (M. R. Metzger et al. 1997). The accurate source localization provided by BeppoSAX allowed the optical follow-up by ground-based telescopes. This led to one of the most significant discoveries: the observation of long GRBs in coincidence with Type Ic supernovae (SNe). The first GRB-SN association was GRB 980425–SN 1998bw (T. J. Galama et al. 1998). The number of associations has since then increased thanks to the optical afterglow follow-up by the Neil Gehrels Swift Observatory (S. D. Barthelmy et al. 2005; D. N. Burrows et al. 2005; P. W. A. Roming et al. 2005), leading to about twenty robust cases with spectroscopic coverage as of today (S. E. Woosley & J. S. Bloom 2006; M. Della Valle 2011; J. Hjorth & J. S. Bloom 2012; Z. Cano et al. 2017; Y. Aimuratov et al. 2023). Further potential GRB-SN associations have been claimed, although they are uncertain owing to the lack of spectral verification (see, e.g., the discussion in Z. Cano et al. 2017; M. G. Dainotti et al. 2022).

Interestingly, all SNe associated with long GRBs show similar luminosity and time of occurrence (from the GRB trigger). In contrast, the associated GRBs show energy releases that span nearly 7 orders of magnitude (see Y. Aimuratov et al. 2023, for details). It seems challenging to reconcile this observational result with a model based on a single massive stellar collapse.

The association of GRB-SN systems to massive star explosions has been set statistically (A. S. Fruchter et al. 2006; P. L. Kelly et al. 2008; C. Raskin et al. 2008) and from the modeling of photometric and spectroscopic observations of the optical emission of GRB-associated SNe (see P. A. Mazzali et al. 2003; K. Nomoto et al. 2003; K. Maeda et al. 2006; P. A. Mazzali et al. 2006; S. E. Woosley & J. S. Bloom 2006; M. Tanaka et al. 2009; F. Bufano et al. 2012; C. Ashall et al. 2019, for specific examples). Thus, further constraints and drawbacks of a single-star collapse model for long GRBs arise from observational evidence pointing out the ubiquitous role of binaries in the stellar evolution of massive stars.

Observations show that most massive stars belong to binaries (H. A. Kobulnicky & C. L. Fryer 2007; H. Sana et al. 2012). For a more recent analysis, we refer to K. F. Neugent et al. (2020). The ubiquitousness of massive binaries across the universe has also caught the attention of the James Webb Space Telescope with the recent observations of Mothra, a likely binary of two supergiants at redshift $z = 2.091$ (J. M. Diego et al. 2023). A new observational exploration era has started, looking for binary companions of SN explosions in binaries (see, e.g., M. Ogata et al. 2021; O. D. Fox et al. 2022; H.-P. Chen et al. 2023; T. Moore et al. 2023; P. Chen et al. 2024, and references therein).

This makes particular contact with GRBs since they are associated with SNe of Type Ic. These SNe lack hydrogen (H) and helium (He), and most Type Ic SN models acknowledge binary interactions as the most effective mechanism to get rid of the H and He layers of the pre-SN star (see, e.g., K. Nomoto & M. Hashimoto 1988; K. Iwamoto et al. 1994; C. L. Fryer et al. 2007; S.-C. Yoon et al. 2010; N. Smith et al. 2011; H.-J. Kim et al. 2015; S.-C. Yoon 2015).

From the theoretical side, it appears an extreme assumption that the gravitational collapse of a single massive star forms a collapsar, a jetted fireball, and an SN explosion, although some proposals have been made to mitigate this difficulty (see, e.g., A. I. MacFadyen & S. E. Woosley 1999; K. Kohri et al. 2005; C. C. Lindner et al. 2012; M. Milosavljević et al. 2012; J. Fuller et al. 2015). Theoretical models fail to produce the fast rotation to produce a GRB jet and an SN-like explosion from a single stellar collapse (C. L. Fryer et al. 2007). Moreover, stellar evolution suggests that the angular momenta in the stellar cores of single stars are even less than what earlier models obtained (J. Fuller et al. 2015). Binary interactions are likely required to produce the high angular momenta needed for the BH–accretion disk mechanism of the traditional GRB model. However, extreme fine-tuning appears necessary to reach the requested physical conditions, challenging to reproduce the GRB density rates (see, e.g., J. Fuller & W. Lu 2022).

S. J. Smartt et al. (2009) and S. J. Smartt (2009, 2015) analyzed archival images of the locations of past SNe to pinpoint their pre-SN stars. The result has been that the inferred zero-age main-sequence (ZAMS) progenitors masses are $\lesssim 18\ M_\odot$. These observations agree with standard stellar evolution, i.e., ZAMS stars with mass $\lesssim 25\ M_\odot$ evolve to core-collapse SNe, forming NSs. Direct BH formation occur for ZAMS stars with mass above 20–25 $M_\odot$, without an SN (e.g., C. L. Fryer 1999; A. Heger et al. 2003; H.-J. Park et al. 2022). Instead, they are at odds with the traditional GRB model, which requests a single-star core collapse to produce a BH and an SN.

All the above facts on GRB-SNe strongly suggest that most GRBs, if not all, should occur in binaries. In their pioneering work, this possibility was envisaged by C. L. Fryer et al. (1999). The alternative BdHN model has been developed complementing and joining the SN and binary evolution community results, filling the gap between the increasing observational evidence of the role of binaries in the stellar evolution of massive stars and theoretical modeling of long GRBs. Specifically, the BdHN model proposes the GRB event occurs in a binary composed of a carbon–oxygen (CO) star and an NS companion. We refer the reader to L. Izzo et al. (2012), J. A. Rueda & R. Ruffini (2012), C. L. Fryer et al. (2014, 2015), L. Becerra et al. (2015, 2016, 2019), and L. M. Becerra et al. (2022) for theoretical details on the model.

The core of the CO star collapses, generating a newborn NS (hereafter, νNS) and the SN. The latter triggers the GRB event, which shows up to seven emission episodes in the most energetic sources, associated with specific physical processes that occur in a BdHN, scrutinized in recent years (see Y. Aimuratov et al. 2023, and references therein). Numerical three-dimensional (3D) smoothed particle hydrodynamics (SPH) simulations of the SN explosion in a CO–NS binary (L. Becerra et al. 2019; L. M. Becerra et al. 2022) show the CO–NS fates explain the diversity of GRBs: BdHNe I are the most extreme with energies of 10^{52}–10^{54} erg and orbital periods of a few minutes. In these sources, the material ejected in the SN is easily accreted by the NS companion, so it reaches the point of gravitational collapse, forming a rotating BH. In BdHNe II, the orbital period is of a few tens of minutes and emit energies of 10^{50}–10^{52} erg. The accretion is lower, so the NS remains stable. The energy threshold of 10^{52} erg for BdHN I and II is set by the energy released when bringing the NS to the critical mass and forming a rotating BH (R. Ruffini et al. 2016, 2018). The BdHNe III have orbital periods of hours, and the accretion is negligible. They explain GRBs with energies lower than 10^{50} erg.

Therefore, the BdHN scenario complements and joins the SN and binary evolution community results, leading to a more comprehensive and global picture of GRB progenitors. Section 6.1 describes the connection between the CO–NS binary and the BdHN I, II, and III features. In this line, a crucial point is the determination of the conditions under which BH formation occurs since it separates BdHNe I from Types II and III. This is the topic of this work. The article is organized as follows. Section 2 describes the SPH numerical simulations of the GRB-SN event, focusing on determining the accretion rate of material from the SN explosion onto the νNS and the NS companion. Section 3 details the up-to-date nuclear equations of state (EOSs) used in the numerical simulations to describe the NS interiors. Section 4 sets the theoretical framework to determine the evolution of the NS structure during the accretion process and the critical mass limit for gravitational collapse into a rotating BH. Specific results of numerical simulations and the evolution of the NSs and the collapse times are shown in Section 5. We discuss in Section 6 the impact of the results of this work on the BdHN scenario. Finally, in Section 7, we discuss and draw the main conclusions.

2. Simulation of the Binary-driven Hypernova Early Evolution

We perform SPH simulations with the SNSPH code adapted to the binary progenitor of the BdHN presented in L. Becerra et al. (2019). This Newtonian, 3D Lagrangian code calculates the evolution of the position, momentum (linear and angular), and thermodynamics (pressure, density, and temperature) of pseudoparticles, which are of mass m_i, assigned according to the mass–density distribution of the ejecta. The code estimates the baryonic mass accretion rate at every time $t = t_0 + \Delta t$, where t_0 is the simulation's starting time, i.e., the time of the SN explosion set by the time when the SN shock front reaches the CO star surface, given as

$$\dot{M}_{\nu\mathrm{NS}}^{\mathrm{cap}} = \sum_i m_i \frac{N_{\nu\mathrm{NS}}^{\mathrm{cap}}(\Delta t,\, m_i)}{\Delta t}, \tag{1}$$

$$\dot{M}_{\mathrm{NS}}^{\mathrm{cap}} = \sum_i m_i \frac{N_{\mathrm{NS}}^{\mathrm{cap}}(\Delta t,\, m_i)}{\Delta t}, \tag{2}$$

where $N_{\nu\mathrm{NS}}^{\mathrm{cap}}$ and $N_{\mathrm{NS}}^{\mathrm{cap}}$ are the number of particles gravitationally captured by the νNS and the NS companion, respectively at time t. The Newtonian scheme suffices for the accretion rate estimate because the size of the gravitational capture region (i.e., the Bondi–Hoyle radius) of the NSs is 100–1000 larger than their Schwarzschild radius (L. Becerra et al. 2019). The gravitational mass and angular momentum of the NSs are calculated in full general relativity by solving, at every time step, the Einstein equations in axial symmetry (see Section 4).

The top panel of Figure 1 shows snapshots of the mass and density of the SN ejecta in the x–y plane, the binary equatorial plane at different times. In this simulation, the mass of the CO star, just before its collapse, is around 8.89 $M_\odot$. This pre-SN configuration is obtained from the thermonuclear evolution of a ZAMS star of $M_{\mathrm{ZAMS}} = 30\, M_\odot$. The NS companion has a mass of 1.9 $M_\odot$, and the pre-SN orbital period is 5.77 minutes, which is the shortest orbital period for the system to avoid Roche-lobe overflow before the SN explosion of the CO core (see, e.g., C. L. Fryer et al. 2014).

The SPH simulation maps to a 3D SPH configuration, the 1D core-collapse SN simulation of C. L. Fryer et al. (2018). At this moment, the collapse of the CO star has formed a νNS of mass of 1.75 $M_\odot$, and around 7.14 $M_\odot$ of mass is ejected by the SN explosion of energy 3.26×10^{51} erg. In the simulation, the νNS and NS companion are modeled as point-like masses, interacting only gravitationally with the SN particles and between them. We allow these two point-like particles to increase their mass by accreting other SN particles following the algorithm described in L. Becerra et al. (2019).

The top panel of Figure 1 shows that the SN ejecta, which are gravitationally captured by the NS companion, first form a tail behind the star and then circularize around it, forming a thick disk. At the same time, the particles from the innermost layers of the SN ejecta that could not escape from the νNS gravitational field fallback are accreted by the νNS. After a few minutes, part of the material in the disk around the NS companion is also attracted by the νNS, enhancing the accretion process onto the νNS.

The bottom panel of Figure 1 corresponds to a simulation with a CO star coming from a $M_{\mathrm{ZAMS}} = 15\, M_\odot$ progenitor with a 1.4 $M_\odot$ companion. At the beginning of the simulation, the CO core collapses into a νNS of 1.4 $M_\odot$, and around 1.6 $M_\odot$ of mass is ejected by the SN explosion with a total energy of 1.1×10^{51} erg. Almost all the SN ejecta leave the system without being affected by the NS companion's gravitational field.

The hydrodynamics of matter infalling and accreting onto an NS at hypercritical rates has been extensively studied in different astrophysics contexts taking into account details on the neutrino emission, e.g., fallback accretion in SNe (Y. B. Zel'dovich et al. 1972; C. L. Fryer et al. 1996, 2006a; C. L. Fryer 2009), accreting NSs in X-ray binaries (R. Ruffini & J. Wilson 1973), and for the case of BdHNe, we refer to C. L. Fryer et al. (2014) and L. Becerra et al. (2016, 2018) for details. The latter include a formulation in a general relativistic background and account for neutrino flavor oscillations. The relevant, not obvious result is that these simulations show that the NS can accrete matter at a hypercritical rate at which

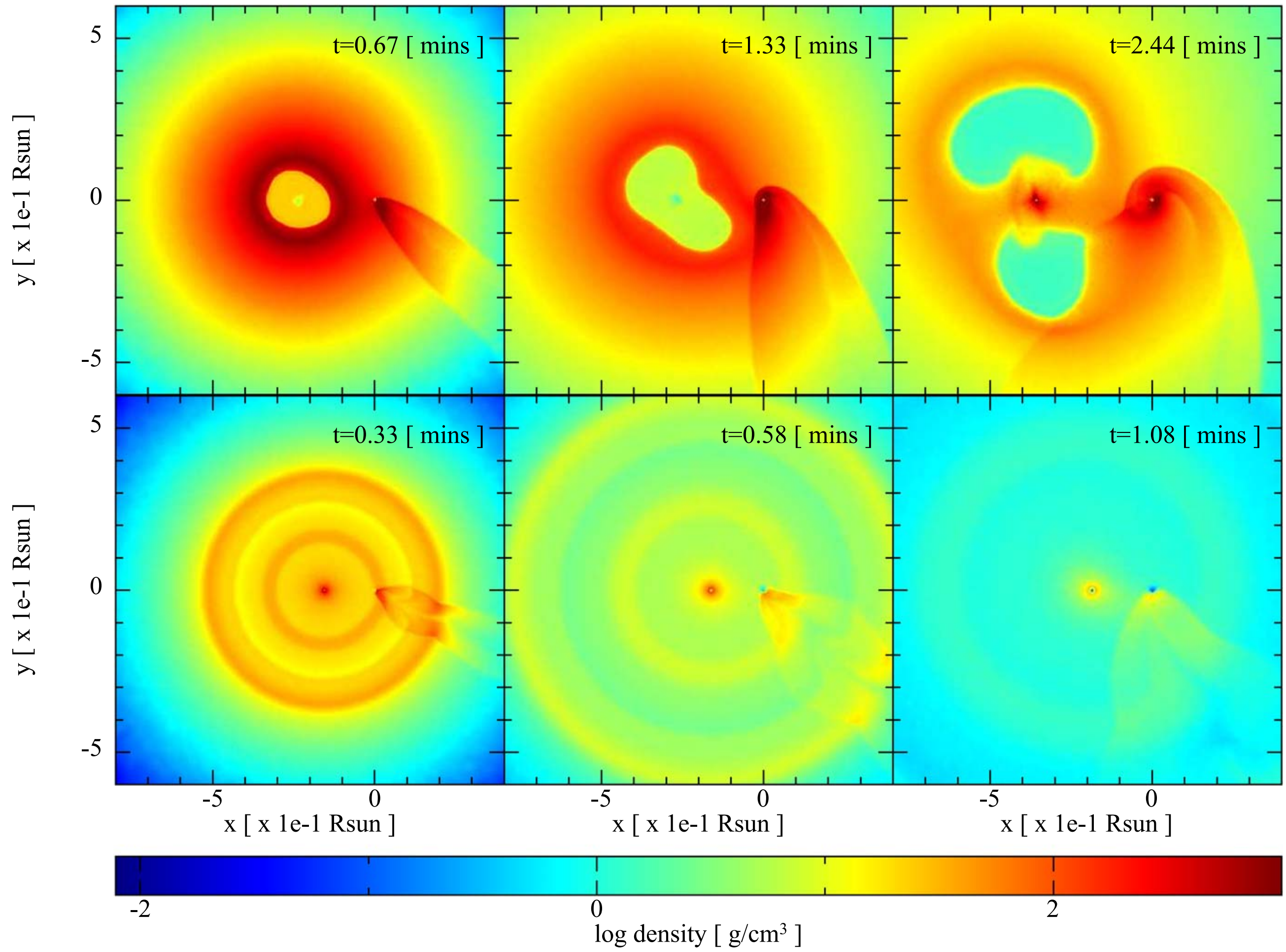

Figure 1. SPH simulations of BdHNe: model "30m1p1eb" (top) and "15m1p05e" (bottom) of Table 2 in L. Becerra et al. (2019). Top: the binary progenitor comprises a CO star of mass $\approx 9\ M_\odot$, produced by a ZAMS star of 30 $M_\odot$, and a 1.9 $M_\odot$ NS companion. The orbital period is $\approx$6 minutes and the energy of the SN is 3.26×10^{51} erg. Bottom: the binary progenitor is a CO star of mass $\approx 3\ M_\odot$, produced by a ZAMS star of 15 $M_\odot$, and a 1.4 $M_\odot$ NS companion. The orbital period is $\approx$5 minutes and the energy of the SN is 1.1×10^{51} erg. Each frame corresponds to selected increasing times from left to right with $t = 0$ s the instant of the SN shock breakout. They show the mass and density on the equatorial plane. The reference system is rotated and translated to align the x-axis with the line joining the binary components. The origin of the reference system is located at the NS companion position. Top: the first frame corresponds to $t = 0.6$ minutes, showing that the particles entering the NS capture region form a tail behind them. These particles then circularize around the NS, forming a thick disk already visible in the second frame at $t = 1.3$ minutes. Part of the SN ejecta are also attracted by the νNS accreting onto it; this is appreciable in the third frame at $t = 2.4$ minutes. Bottom: in all three panels, it can be seen how the material leaves the system almost without being affected by the NS companion. This figure has been produced with the SNsplash visualization program (D. J. Price 2011).

baryonic mass from the SN ejecta falls into the gravitational capture region of the NS. The simulations show the accretion rate in BdHNe is hypercritical, reaching peak values of up to $10^{-3}\ M_\odot\ \mathrm{s}^{-1}$. This implies the accretion flow reaches densities $\sim 10^8\ \mathrm{g\ cm}^{-3}$ near the NS surface (see, e.g., Appendix B in L. Becerra et al. 2016; Table 1 in L. Becerra et al. 2018), which is about 12 orders of magnitude larger than the densities of Eddington-limited accretion flows in low-mass X-ray binaries.

Therefore, we assume that the accretion rate inferred with the SPH code is the effective baryonic mass accretion rate onto the NS, i.e.,

$$\dot{M}_{b,\nu\mathrm{NS}} = \dot{M}_{\nu\mathrm{NS}}^{\mathrm{cap}}, \quad \dot{M}_{b,\mathrm{NS}} = \dot{M}_{\mathrm{NS}}^{\mathrm{cap}}. \tag{3}$$

Figure 2 shows the accretion rate onto the νNS and the NS companion obtained from SPH simulations for selected orbital periods and progenitor for the CO star: $M_{\mathrm{ZAMS}} = 30\ M_\odot$ and $M_{\mathrm{ZAMS}} = 15\ M_\odot$, with an NS companion with 1.9 $M_\odot$ and 1.4 $M_\odot$, respectively (see Table 1).

For systems with a CO progenitor of mass $M_{\mathrm{ZAMS}} = 30\ M_\odot$, the accretion rate onto the νNS shows two prominent peaks. The second peak of the fallback accretion onto the νNS is a unique feature of BdHNe because, as explained above (see, also, L. Becerra et al. 2019, for additional details), it is caused by the influence of the NS companion. The accretion rate onto the NS companion shows a single-peak structure, accompanied by additional peaks of smaller intensity and shorter timescales. This feature is more evident in short-period binaries. Such small peaks are produced by higher and lower accretion episodes as the NS companion orbits across the ejecta and finds higher- and lower-density regions.

For systems with a CO progenitor with $M_{\mathrm{ZAMS}} = 15\ M_\odot$, the second peak in the mass accretion rate for the νNS does not occur, while the accretion rate for the NS companion is much lower. This is due to the small amount of mass ejected in the SN explosion and its high velocity.

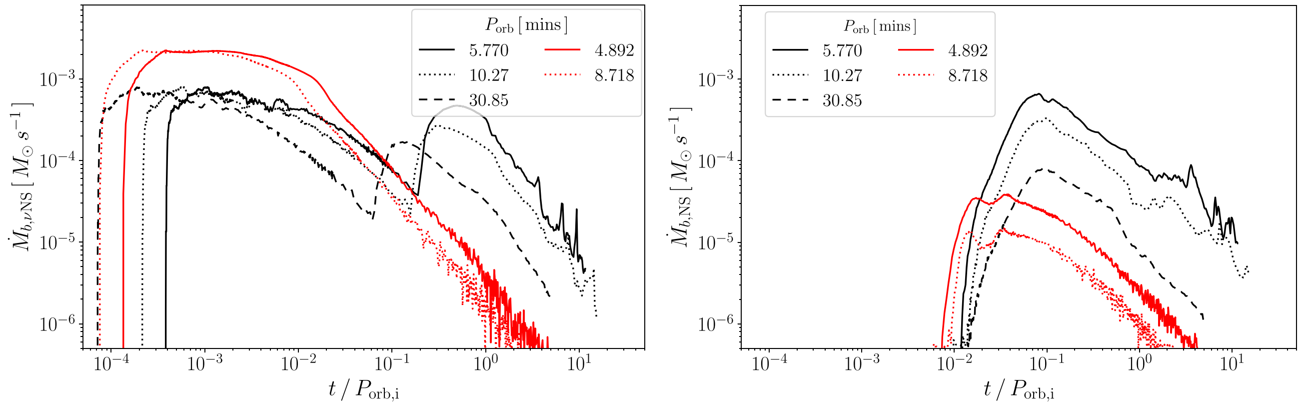

Figure 2. Accretion rate onto the νNS (left) and the NS companion (right) as a function of time, obtained from SPH simulations of BdHNe with various orbital periods and CO star progenitors. The black curves correspond to binaries formed by a CO star evolved from a ZAMS with $M_{ZAMS} = 30\ M_\odot$ and a 1.9 $M_\odot$ NS companion. The CO star undergoes collapse, ejecting an SN with an energy of 3.26×10^{51} erg. The red curves correspond to binaries formed by a CO star from a ZAMS star with $M_{ZAMS} = 15\ M_\odot$ and a 1.4 $M_\odot$ NS companion, where the corresponding SN energy is 1.1×10^{51} erg. We refer to Table 1 for the CO–NS binary properties.

Table 1
Properties of the Carbon–Oxygen Star–Neutron Star Binary before the Carbon–Oxygen Core Gravitationally Collapses

M_{ZAMS} ($M_\odot$)	$M_{\nu NS}$ ($M_\odot$)	M_{ej} ($M_\odot$)	M_{NS} ($M_\odot$)	P_{orb} (min)	$\Delta M_{b,NS}$ ($M_\odot$)	$\Delta M_{b,\nu NS}$ ($M_\odot$)
30	1.8	7.14	1.9	5.77	0.328	0.414
				10.27	0.281	0.391
				30.85	0.117	0.322
15	1.4	1.6	1.4	4.89	0.006	0.029
				8.72	0.006	0.023

Note. The CO star mass is $M_{CO} = M_{\nu NS} + M_{ej}$, where the mass of the CO unstable iron core gives the νNS mass.

3. Equation of State

To consider the scenario proposed in the present paper, nuclear matter EOSs that can describe NS macroscopic properties are necessary. In recent decades, many relativistic EOSs were proposed and analyzed in light of bulk nuclear matter properties (M. Dutra et al. 2014). The detection of massive NSs (P. B. Demorest et al. 2010; J. Antoniadis et al. 2013; H. T. Cromartie et al. 2020; E. Fonseca et al. 2021; R. W. Romani et al. 2022), imposes strong constraints on the density dependence of the EOS and the EOSs that passed the test of satisfying nuclear bulk properties were confronted with the observational data in several works, see for instance M. Dutra et al. (2016a, 2016b) and M. Fortin et al. (2016). More recently, the data on GW170817 (B. P. Abbott et al. 2017) by the LIGO/Virgo Collaboration have been used to constrain the radius of the canonical NS (i.e., of a mass of 1.4 $M_\odot$) by the tidal polarizabilities of the stars involved in the merger (see, e.g., O. Lourenço et al. 2019). In the last years, data from the Neutron star Interior Composition Explorer (NICER) X-ray telescope for a canonical NS (M. C. Miller et al. 2019; T. E. Riley et al. 2019) and a massive NS (M. C. Miller et al. 2021; T. E. Riley et al. 2021) have also been used to constrain the EOS, with both measurements imposing further restrictions on the EOS. Another interesting object is the NS in the quiescent low-mass X-ray binary in NGC 6397 (J. E. Grindlay et al. 2001; S. Guillot et al. 2011; C. O. Heinke et al. 2014), which provided reliable constraints, as seen in F. Özel & P. Freire (2016) and A. W. Steiner et al. (2018). It is also worth mentioning other observations that have been used as constraints, but they must be considered carefully due to their specific nature. One refers to a massive, fast black widow with a large error bar (R. W. Romani et al. 2022). Another one is the gravitational-wave emission resulting from the merger of a BH with another object that can be either the smallest BH or the most massive NS ever detected, GW190814 (R. Abbott et al. 2020). The last one is a very compact object, perhaps a quark star, known as XMMU J173203.3–344518 (V. Doroshenko et al. 2022). Notice, however, that the present observations are still not very restrictive, as discussed in several works where a Bayesian inference approach has been used to constrain the parameters of relativistic mean-field (RMF) models (S. Traversi et al. 2020; T. Malik et al. 2022; M. V. Beznogov & A. R. Raduta 2023; T. Malik et al. 2023; C. Huang et al. 2024).

Having all those considerations in mind, we have chosen to work with two different RMF parameterizations that satisfy all of the constraints mentioned above, namely eL3$\omega\rho$ (L. L. Lopes 2022), and NL3$\omega\rho$ (C. J. Horowitz & J. Piekarewicz 2001; M. Fortin et al. 2016; H. Pais & C. Providência 2016; L. L. Lopes & D. P. Menezes 2022). One should notice that the nonlinear Lagrangian density terms are presented differently in the literature. Any reader interested in a uniform and clear notation is referred to C. Biesdorf et al. (2023). One aspect that remains to be mentioned is the hyperon puzzle. While including hyperons seems to be natural from the theoretical point of view, it softens the EOS with a consequent decrease in the maximum NS mass, possibly not attaining 2 $M_\odot$; see, for instance, the discussions in T. Malik & C. Providência (2022), T. Malik et al. (2023), and X. Sun et al. (2023), where the inclusion of hyperons has been considered within a Bayesian inference approach. There are different ways to circumvent this problem in the literature, and we cannot say it is completely solved. Hence, one of the models we use next fails to describe the highly massive objects detected so far when hyperons are included. Nevertheless, it remains a good choice if other aspects are considered, as discussed in L. L. Lopes et al. (2022). We consider these two EOSs as representatives of EOSs with similar properties allowing for 2 $M_\odot$ stars, also including hyperons, see for instance (T. Malik et al. 2023).

The Lagrangian density of these models is given by (C. J. Horowitz & J. Piekarewicz 2001; F. J. Fattoyev et al.

2010)

$$\mathcal{L}_{\rm QHD} = \bar{\psi}_B[\gamma^\mu(i\partial_\mu - g_{B\omega}\omega_\mu - g_{B\rho}\frac{1}{2}\boldsymbol{\tau}\cdot\boldsymbol{\rho}_\mu) - (M_B - g_{B\sigma}\sigma)]\psi_B - U(\sigma) + \frac{1}{2}(\partial_\mu\sigma\partial^\mu\sigma - m_s^2\sigma^2) - \frac{1}{4}\Omega^{\mu\nu}\Omega_{\mu\nu} + \frac{1}{2}m_v^2\omega_\mu\omega^\mu - \frac{1}{4}\boldsymbol{P}^{\mu\nu}\cdot\boldsymbol{P}_{\mu\nu} + \frac{1}{2}m_\rho^2\boldsymbol{\rho}_\mu\cdot\boldsymbol{\rho}^\mu\mathcal{L}_{\omega\rho} + \mathcal{L}_\phi, \quad (4)$$

in natural units. Here ψ_B represents the Dirac field, where B can stand either for nucleons only (N) or nucleons (N) and hyperons (H). σ, ω_μ, and $\boldsymbol{\rho}_\mu$ are the mesonic fields and $\boldsymbol{\tau}$ are the Pauli matrices. The gs are the Yukawa coupling constants, M_B is the baryon mass, and m_s, m_v, and m_ρ are the masses of the σ, ω, and ρ mesons respectively. $U(\sigma)$ is a self-interaction term (J. Boguta & A. R. Bodmer 1977)

$$U(\sigma) = \frac{1}{3!}\kappa\sigma^3 + \frac{1}{4!}\lambda\sigma^4, \quad (5)$$

where the ω^4 term was introduced in Y. Sugahara & H. Toki (1994), which softens the EOS at high densities (see the discussion in T. Malik et al. 2023), and $\mathcal{L}_{\omega\rho}$ is the nonlinear ω–ρ coupling interaction discussed in C. J. Horowitz & J. Piekarewicz (2001)

$$\mathcal{L}_{\omega\rho} = \Lambda_{\omega\rho}(g_{N\rho}^2\boldsymbol{\rho}^\mu\cdot\boldsymbol{\rho}_\mu)(g_{N\omega}^2\omega^\mu\omega_\mu), \quad (6)$$

necessary to correct the slope of the symmetry energy (L). The last term $\mathcal{L}_\phi$ is related the hidden strangeness ϕ vector meson, which couples only with hyperons (H), not affecting the properties of nuclear matter

$$\mathcal{L}_\phi = g_{H\phi}\bar{\psi}_H(\gamma^\mu\phi_\mu)\psi_H + \frac{1}{2}m_\phi^2\phi_\mu\phi^\mu - \frac{1}{4}\Phi^{\mu\nu}\Phi_{\mu\nu}. \quad (7)$$

To account for the chemical stability and charge neutrality of the NS, leptons have to be considered, and the corresponding Lagrangian density reads

$$\mathcal{L}_l = \sum_{l=e,\mu}\bar{\psi}_l[\gamma^\mu(i\partial_\mu - m_l)]\psi_l, \quad (8)$$

where l represents electrons and muons, and β-equilibrium conditions establish a relation between the different chemical potentials

$$\mu_B = \mu_n - q_B\mu_e, \quad \mu_\mu = \mu_e, \quad (9)$$

where μ_i designates the chemical potential of the baryons (B), neutrons (n), electrons (e), and muons (μ), and q_B is the electric charge of baryon B. The imposition of these relations defines the NS composition. In the present study, we consider the νNS is already in a neutrino-free regime.

Given the Lagrangian density, the equations of motion are obtained and solved with the help of an RMF approximation. All details can be found in the literature (see for instance B. D. Serot 1992; N. K. Glendenning 2012; L. L. Lopes & D. P. Menezes 2022) and are not reproduced here. The first step is to obtain expressions for the pressure (P_B), energy density (ε_B), and baryonic density (n_B) at zero temperature, which are used as input to the calculation of the NS's macroscopic properties via Einstein equations. The next step is to calculate the EOS at fixed entropy per baryon (s_B/n_B) for neutrino-free matter (e.g., M. Prakash et al. 1997). For this case, the Fermi distribution functions are no longer step functions, and antiparticles have to be taken into account as

$$f_{B\pm} = \frac{1}{1 + \exp[(E_B \mp \mu_B^*)/T]}, \quad (10)$$

with energy $E_B = \sqrt{k^2 + M_B^{*2}}$, where M_B^* is the effective mass and μ_B^* is the effective chemical potential. The entropy density can be easily obtained from the expression

$$s_B = \frac{\varepsilon_B + P_B - \sum_B\mu_B n_B}{T}, \quad (11)$$

or computed as the entropy density of a free Fermi gas.

The top panel of Figure 3 shows the pressure as a function of the energy density for the eL3$\omega\rho$ and NL3$\omega\rho$ EOSs at zero temperature. For both parameterizations, we considered the case of matter formed only by nucleons and the case of nucleons mixed with hyperons. The middle panel of Figure 3 shows the mass–radius relation for the nonrotating and cold NS configurations (see also Table 2), obtained including a crust. We have considered the Baym, Pethick and Sutherland (BPS) model for the outer crust (G. Baym et al. 1971) and a Thomas–Fermi calculation of the inner crust (S. S. Avancini et al. 2008; F. Grill et al. 2012). The core–crust transition occurs at $n_B = 0.082\ \mathrm{fm}^{-3}$ ($\rho_B = \varepsilon_B/c^2 = 1.39 \times 10^{14}\ \mathrm{g\ cm}^{-3}$) for the NL3$\omega\rho$ model. As discussed in M. Fortin et al. (2016), it is important to consider an inner crust EOS described by the same model as the core. We will take for both EOSs the same crust model because they have similar symmetry energy at subsaturation densities, and, therefore, it is expected that the two inner crust EOSs do not differ much (H. Pais & C. Providência 2016). The bottom panel of Figure 3 shows the mass–radius relation for nonrotating and hot NS configurations for the eL3$\omega\rho$ and NL3$\omega\rho$ EOS parameterizations with nucleons mixed with hyperons. The hot EOS generally produces less compact configurations than the cold one, but the maximum allowed mass remains roughly the same for both cases (see also Table 2). In the last two plots, we have also colored the regions corresponding to the observational constraints discussed at the beginning of this section. We have used two constant values of entropy per baryon, $s_B/n_B = 1$ and 2, which we designate as S1 and S2, respectively, in Table 2 and Figure 3.

4. Evolution of the Neutron Star Structure

To calculate the time evolution of the νNS and the NS companion structure during the accretion process, we have implemented a code that uses the RNS code (N. Stergioulas & J. L. Friedman 1995; with the quadrupole correction performed in F. Cipolletta et al. 2015). Given the EOS, the code calculates the stable, rigidly rotating, corresponding NS configuration of equilibrium in axial symmetry for the baryonic mass, M_b, and angular momentum, J, at a given time. The value of M_b is updated using the baryonic mass accretion rate from the SPH numerical simulation (see

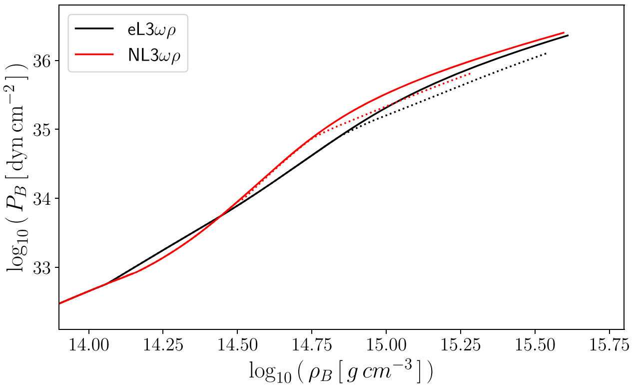

(a)

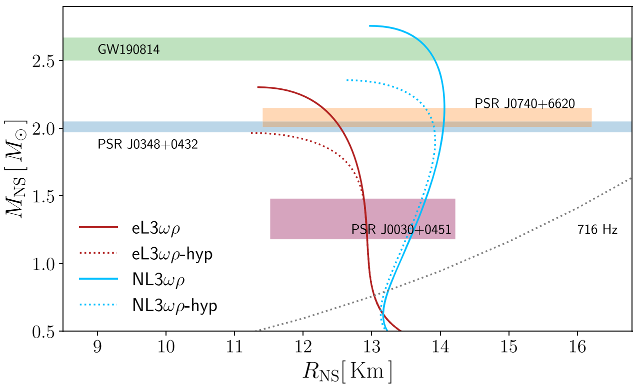

(b)

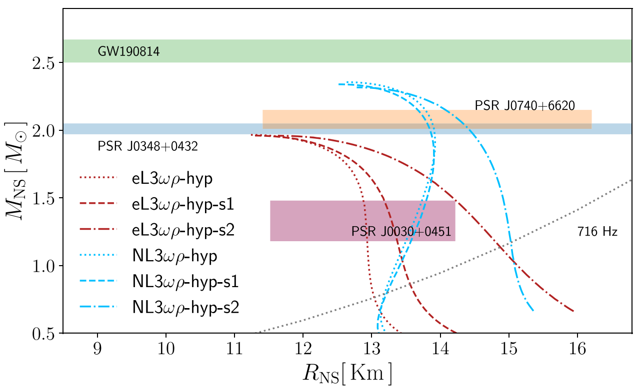

(c)

Figure 3. Top: pressure–energy density relation for the cold NS EOS with the matter with nucleons only (solid line) and nucleons and hyperons (dotted line). Middle: mass–radius relation for nonrotating NSs. The color bands represent observational constraints given by the pulsar mass of PSR J0348+0432 (J. Antoniadis et al. 2013); on mass and radius from NICER measurements for pulsars PSR J0030+0451 (M. C. Miller et al. 2019; T. E. Riley et al. 2019) and PSR J0740+662 (M. C. Miller et al. 2021; T. E. Riley et al. 2021); and the mass of the secondary compact object of the GW190814 event (R. Abbott et al. 2020). The dashed gray line corresponds to the fastest observed radio pulsar, PSR J1748–2446ad (J. W. T. Hessels et al. 2006). Bottom: same as middle panel but adding the hot NS EOS with nucleons mixed with hyperons for two constant entropy per baryon values, $s_B/n_B = 1$ and 2.

Section 2). The value of J is obtained by angular momentum conservation (L. M. Becerra et al. 2022)

$$\dot{J} = \tau_{\rm acc} + \tau_{\rm mag}, \tag{12}$$

Table 2

For Selected Equations of State, the Table Lists the Maximum Stable Mass for the Nonrotating and Uniformly Rotating Configurations, $M_{\rm max}^{j=0}$ and $M_{\rm max}^{\rm Kep}$, and the Maximum Rotation Frequency, $\Omega_{\rm max}^{\rm Kep}$

EOS	$M_{\rm max}^{j=0}$ $(M_\odot)$	$M_{\rm max}^{\rm Kep}$ $(M_\odot)$	$\Omega_{\rm max}^{\rm Kep}$ $(10^4\ {\rm s}^{-1})$
eL3ωρ	2.30	2.75	1.08
eL3ωρ-hyperons	1.96	2.35	0.98
eL3ωρ-hyperons-S1	1.96	2.32	0.97
eL3ωρ-hyperons-S2	1.96	2.27	0.92
NL3ωρ	2.76	3.36	0.98
NL3ωρ-hyperons	2.35	2.88	0.91
NL3ωρ-hyperons-S1	2.34	2.84	0.91
NL3ωρ-hyperons-S2	2.32	2.75	0.88

Note. S1 and S2 stand for the two constant values of entropy per baryon, $s_B/n_B = 1$ and 2, respectively.

where the torques acting on the stars are specified as follows. Our numerical simulations indicate that the infalling material forms a disk around the star before being accreted. Therefore, the accreted matter exerts a (positive) torque on the star

$$\tau_{\rm acc} = \chi\, l\, \dot{M}_b, \tag{13}$$

where $\chi \leqslant 1$ is an efficiency parameter of angular momentum transfer, and l is the specific (i.e., per unit mass) angular momentum of the inner disk radius, $R_{\rm in}$, and it is given by

$$l = \begin{cases} l_{\rm isco}, & \text{if } R_{\rm in} \geqslant R_{\rm NS}, \\ \Omega R_{\rm NS}^2, & \text{if } R_{\rm in} < R_{\rm NS}, \end{cases} \tag{14}$$

with $l_{\rm isco}$ the specific angular momentum of the innermost stable circular orbit around the NS, while $R_{\rm NS}$ and Ω are, respectively, the NS radius and angular velocity. All these quantities are obtained from the numerical solution of the Einstein equations directly from the RNS code. It is worth noting that due to the high accretion rates (see Figure 2), the NSs evolve in the regime where $R_{\rm mag} < R_{\rm NS}$, with $R_{\rm mag}$ the magnetospheric radius (J. E. Pringle & M. J. Rees 1972)

$$R_{\rm mag} = \left(\frac{\mu_{\rm dip}^2}{\dot{M}\sqrt{2GM_{\rm NS}}}\right)^{2/7}, \tag{15}$$

where $\mu_{\rm dip} = B_{\rm dip} R_{\rm NS}^3$ is the dipole magnetic moment. Additionally, if the magnetic field is not buried by the accretion (e.g., D. J. B. Payne & A. Melatos 2007), the star is subjected to (negative) torque by the magnetic field. We adopt the dipole + quadrupole magnetic field model (see J. Pétri 2015, for details)

$$\tau_{\rm mag} = -\frac{2}{3}\frac{\mu_{\rm dip}^2\Omega^3}{c^3}\sin^2\theta_1\left(1 + \eta^2\frac{16}{45}\frac{R_{\rm NS}^2\Omega^2}{c^2}\right), \tag{16}$$

where η defines the quadrupole-to-dipole magnetic field strength ratio

$$\eta \equiv \sqrt{\cos^2\theta_2 + 10\sin^2\theta_2}\,\frac{B_{\rm quad}}{B_{\rm dip}}. \tag{17}$$

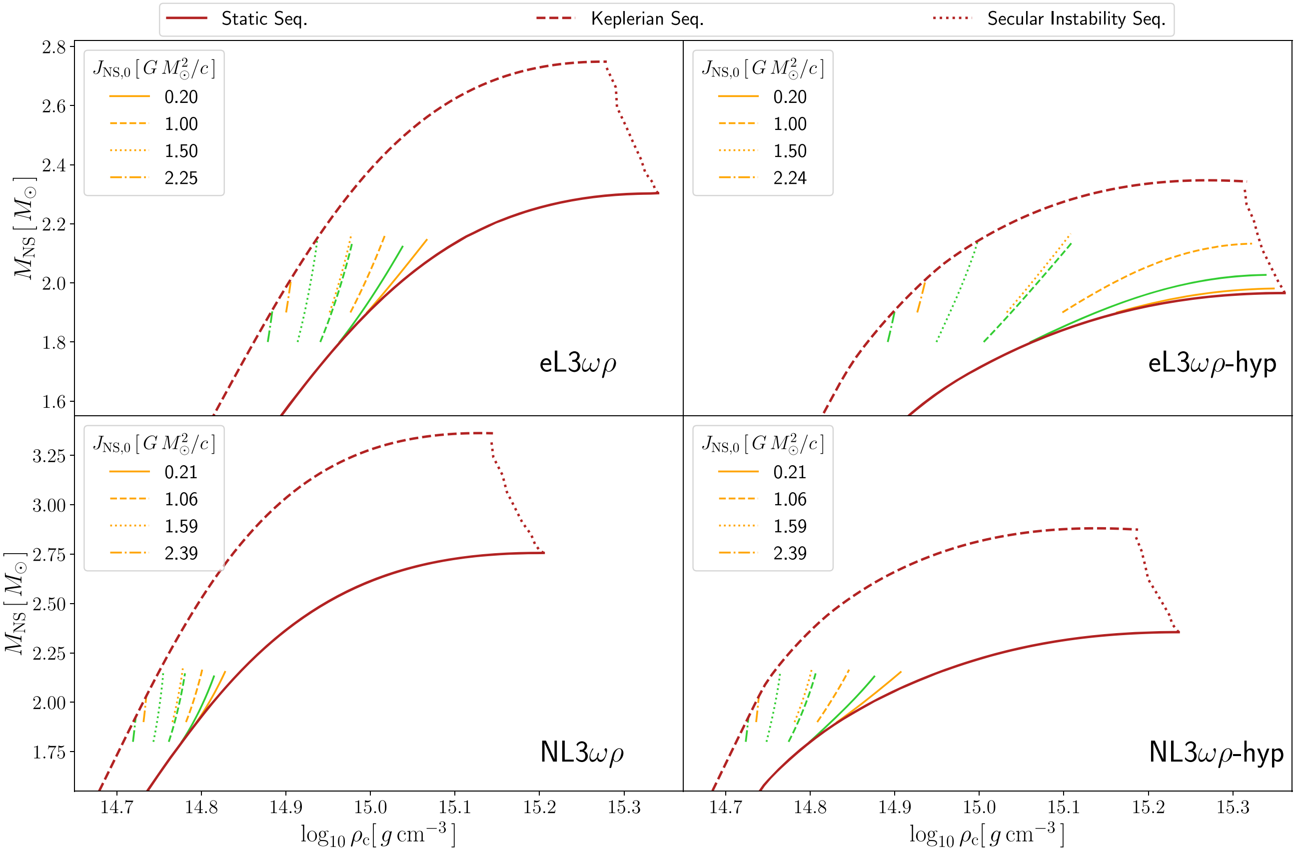

Figure 4. Evolution of the NS (orange lines) and the νNS (green lines) in the ρ_c–$M_{\rm NS}$ plane for different initial values of the angular momentum, J. Each panel corresponds to each EOS summarized in Table 2. We set the strength of the magnetic field to $B_{\rm ns} = 10^{13}$ G and the angular momentum transfer efficiency $\chi = 0.5$. The initial binary system is formed by a 1.9 $M_\odot$ NS and a CO star, whose progenitor is a star with $M_{\rm ZAMS} = 30\,M_\odot$, and the orbital period is $P_{\rm orb} = 5.77$ minutes. The stability zone is delimited by the static (red solid line), Keplerian (red dashed line), and secular instability sequences (red dotted line).

In this model, the $m = 0$ mode is set by $\theta_1 = 0$ and any value of θ_2; the $m = 1$ mode is given by $(\theta_1, \theta_2) = (90°, 0°)$; and the $m = 2$ mode is given by $(\theta_1, \theta_2) = (90°, 90°)$.

In the following, we analyze systems with a CO star evolving from a progenitor with $M_{\rm ZAMS} = 30\,M_\odot$. For the case of a CO star with a progenitor with $M_{\rm ZAMS} = 15\,M_\odot$, we do not find any initial condition in which the star evolves outside the stability zone. These systems remain gravitationally bound after the SN explosion and produce binary NS systems that will eventually merge, driven by gravitational-wave emission.

5. Results

5.1. Newborn Neutron Star and Neutron Star Evolution

Figure 4 shows, for the EOSs summarized in Table 2, the evolution of the NS and the νNS in the central density, ρ_c–gravitational mass, $M_{\rm NS}$ plane, where ρ_c is $\rho_B = \varepsilon_B/c^2$ at the stellar center, $r = 0$. The baryonic mass accretion rate on the NS is taken from the SPH simulation of the BdHN event, which begins with the SN explosion of a CO star in a binary system with a 1.9 $M_\odot$ NS companion. The CO star evolved from a star with $M_{\rm ZAMS} = 30\,M_\odot$. When the CO core collapses, it leaves a 1.85 $M_\odot$ proto-NS and ejects about 7 $M_\odot$ of material in the SN explosion. The orbital period is $P_{\rm orb} = 5.77$ minutes. The star increases its central density in all cases as it accretes baryonic mass and angular momentum. The equatorial radius and angular velocity also increase when the secular instability limit is not reached.

For sufficiently high initial angular momentum, the stars reach the mass-shedding limit. As shown by 3D numerical simulations of uniformly rotating NSs by M. Shibata et al. (2000), the mass-shedding limit leads to a dynamical instability point near secular instability, which, in turn, leads to gravitational collapse into a BH. They show this situation will occur by an NS accreting at the mass-shedding limit. Therefore, we here assume the mass-shedding limit and the secular instability as points of BH formation. Configurations that can reach this limit are discussed in the next section.

5.2. Time to Black Hole Formation

We now analyze how the initial star's angular momentum affects the occurrence of gravitational collapse by accretion. For the same binary systems in Figure 4, Figure 5 shows the time taken for the stars to become unstable during the accretion process and probably collapse to a BH as a function of the star's initial angular momentum, for different values for the angular momentum transfer efficiency, χ. We recall the orbital period is $P_{\rm orb} = 5.77$ minutes. The NS companion only reaches the secular instability limit when the eL3$\omega\rho$ EOS with hyperons is assumed. The time the star needs to reach it shortens for larger initial angular momentum or larger χ. On the other hand, independently of the EOS assumed, for $j_{\rm NS,0} \equiv cJ/(GM_\odot^2) \gtrsim 1$ and $\chi = 0.9$, the star reaches the

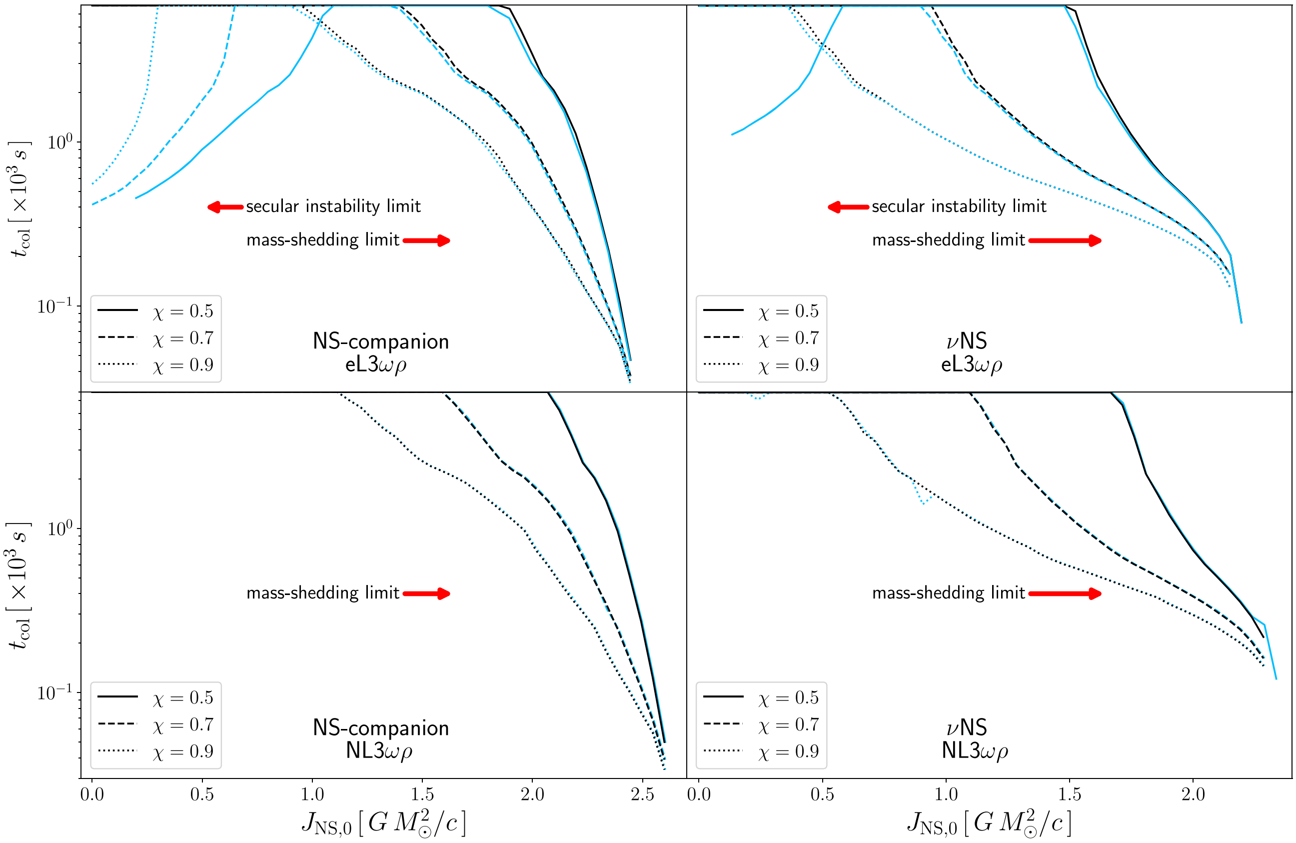

Figure 5. Time to collapse, defined as the time it takes the stars to leave the stability zone, as a function of the star's initial angular momentum, for different values of the angular momentum efficiency, χ. The upper panels show the results assuming the eL3$\omega\rho$ parameterization for the EOS, while for the lower panels, we use the NL3$\omega\rho$ one. Black lines correspond to matter with nucleons, and blue lines correspond to matter with nucleons mixed with hyperons. The initial binary is the same as in Figure 4.

mass-shedding limit, and the time it takes to do so decreases as its initial angular momentum increases. Under certain conditions, with high initial angular momentum, the star could reach the mass-shedding limit in less than 50 s. In contrast, an initially nonrotating star needs more than 300 s to reach the secular instability limit. The νNS reaches the secular instability limit for the eL3$\omega\rho$ EOS with hyperons and only for $\chi = 0.5$. For the νNS, the mass-shedding limit can be reached for $j_{\rm NS,0} \gtrsim 0.5$, if $\chi = 0.9$, for example.

Figure 6 shows the collapse time as done in Figure 5, for the same binary system stars but with different initial binary periods (see Figure 2) and employing the eL3$\omega\rho$ EOS parameterization with nucleons mixed with hyperons. As shown in Figure 2, an increase in the initial binary period results in a decrease in the accretion rate of the binary stars, which subsequently requires more time to reach an instability limit. When the initial binary period is greater than 31 minutes, the NS companion does not reach the secular instability limit for any value of the χ parameter, while the νNS reaches it only for $\chi < 0.5$. The initial angular momentum required for the stars to reach the mass-shedding limit increases with the initial binary period. It is worth noting that the mass loss by the SN explosion disrupts the final binary system only for larger initial binary periods ($P_{\rm orb} > 31$ minutes). In contrast, the system remains gravitationally bound for the two shorter ones, forming BH–BH or NS–NS binaries. We refer to L. M. Becerra et al. (2024) for the latest simulations of the unbinding process in BdHN systems and Section 6.2 for further discussions on the implications.

Figure 7 shows the collapse time for the νNS described by a hot EOS with uniform entropy (see also bottom panel of Figure 3). For these cases, the hotter the star, the mass-shedding limit or the secular instability limit is reached in less time, independent of the EOS parameterization used. For the eL3$\omega\rho$ parameterization, hotter stars can get to the secular instability limit with greater values for the angular momentum transfer efficiency, χ, while cold stars do not.

5.3. Delayed Black Hole Formation

When the stars do not collapse and if the magnetic field is not buried by the accretion (e.g., D. J. B. Payne & A. Melatos 2007), they will continue losing angular momentum driven by the magnetic field torque after the end of the accretion process. When the final mass of the stars is smaller than the maximum mass allowed for a static star, $M_{\rm TOV}^{\rm max}$, they evolve toward the static sequences as they lose angular momentum. But, when the final mass of either star is larger than $M_{\rm TOV}^{\rm max}$, the stars evolve toward the secular instability limit, leading to a long-delayed collapse into a BH. This will be the case for stars that do not collapse in the accretion process. On the other hand, if the binary remains gravitationally bound, gravitational-wave emission makes the stars merge in a time $t_{\rm GW}$ (see below). Thus, for the BdHN event to occur, the collapse delay time must be shorter than the merger time. We refer to Section 6.1

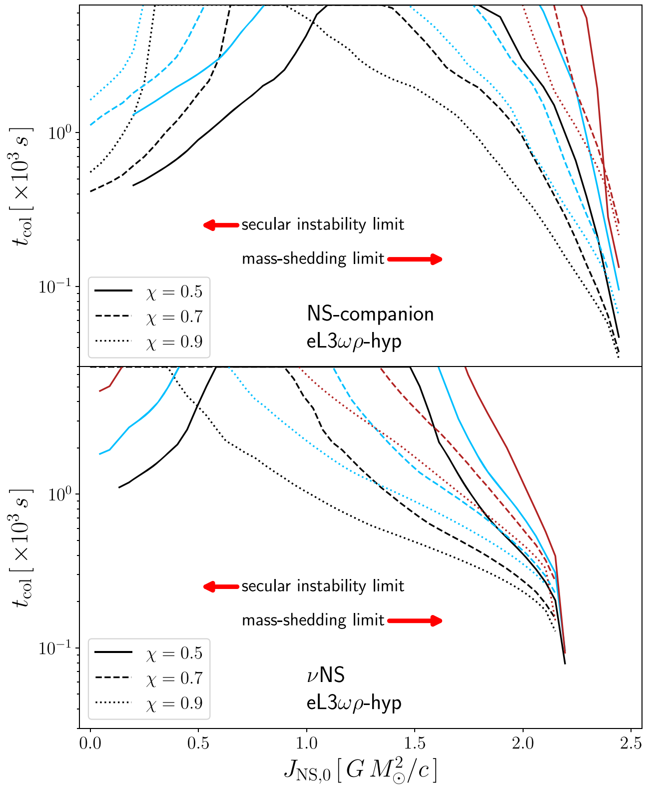

Figure 6. Same as Figure 5 but using an EOS with the eL3$\omega\rho$ parameterization with hyperons. The initial binary system is formed by a 1.9 $M_\odot$ NS and a CO star, whose progenitor is a star with $M_{\rm ZAMS} = 30\ M_\odot$. The initial binary period is about 5.7 minutes for the black lines, 10.2 minutes for the blue ones, and 31 minutes for the red ones.

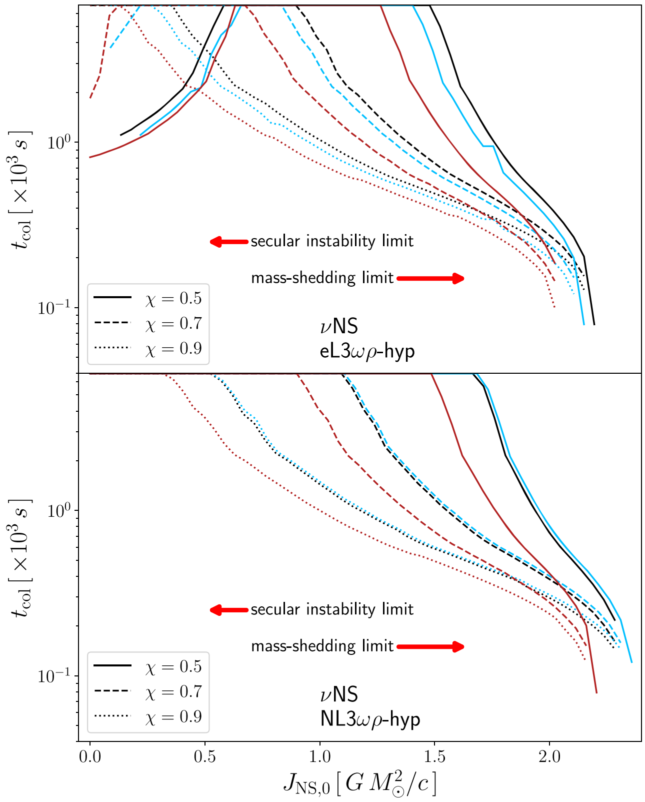

Figure 7. Same as Figure 5 but for a hot NS using the eL3$\omega\rho$ and NL3$\omega\rho$ parameterizations with hyperons for the EOS. The black lines correspond to the cold EOS, the blue ones for an EOS with constant entropy $S1(s_B/n_B = 1)$, and the red ones for an EOS with constant entropy $S2(s_B/n_B = 2) > S1$. The initial binary system is formed by a 1.9 $M_\odot$ NS and a CO star, whose progenitor is a star with $M_{\rm ZAMS} = 30\ M_\odot$ in an initial binary period of about 5.7 minutes.

for further discussion on the consequences of the delayed collapse for the BdHN classifications.

To assess the above scenario, we analyze as specific examples the stars described by the eL3$\omega\rho$ EOS with hyperons (Figure 4 and top panel of Figure 5).

The time to reach the secular instability limit by magnetic-dipole braking is

$$t_{\rm col}^{\rm dip} = -\frac{3}{2}\frac{c^3}{B^2}\int_{J_i}^{J_{\rm sec}}\frac{dJ}{R^6\Omega^3}, \tag{18}$$

where J_i and $J_{\rm sec}$ are the NS angular momentum at the end of accretion and the secularly unstable configuration with the same baryon mass, respectively. Equation (18) refers to a spherical dipole, so we approximate its radius with the authalic radius, $R \approx (2R_{\rm eq} + R_p)/3$. The merger time is (see, e.g., Equation (4.135) in M. Maggiore 2007)

$$t_{\rm GW} = \frac{c^5}{G^3}\frac{5}{256}\frac{a_{\rm orb}^4}{\mu M^2}\frac{48}{19}\frac{1}{g(e)^4}\int_0^e\frac{g(e)^4(1-e^2)^{5/2}}{e(1+\frac{121}{304}e^2)}de, \tag{19}$$

where $g(e) = e^{12/19}(1-e^2)^{-1}(1+121e^2/304)^{870/2299}$, $a_{\rm orb}$ is the orbital separation at the end of the accretion process, and M and μ are the total and reduced binary mass, respectively. The BdHN event of an initial binary with a 1.9 $M_\odot$ NS and a CO star from a $M_{\rm ZAMS} = 30\ M_\odot$ progenitor leaves a binary of approximately equal masses ($\sim$2.1 $M_\odot$), orbital separation $a_{\rm orb} \sim 3.3\times 10^{10}$ cm, and eccentricity $e = 0.71$. Equation (19) says this system will merge in $t_{\rm GW} = 33$ kyr. Figure 8 shows

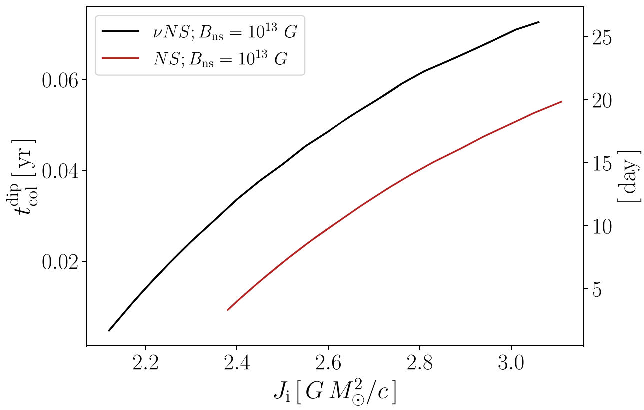

Figure 8. Time to the secular instability limit by magnetic-dipole braking as a function of the initial angular momentum of the νNS and the NS companion, which do not collapse to a BH in the BdHN event but reach a mass greater than $M_{\rm TOV}^{\rm max}$. The EOS is the eL3$\omega\rho$ parameterization with hyperons. The star's initial mass is about 2.1 $M_\odot$, and its radius is between 13 and 16 km, depending on its angular momentum. The star reaches secular instability when $J = J_{\rm sec} \approx 3GM_\odot^2/c$.

that $t_{\rm col}^{\rm dip}$ is of the order of 0.05 yr ($\approx$18 days) for a magnetic field strength of 10^{13} G. Equation (18) shows this time increases as the square of the magnetic field strength decreases. For the above numbers, we obtain that these stars will gravitationally collapse to a BH before the binary merges for magnetic fields above 10^{10} G. Given the shortness of $t_{\rm col}^{\rm dip}$

relative to t_{GW}, we can conclude that in ∼33 kyr, this system leads to a BH–BH merger.

6. Discussion

6.1. Carbon–Oxygen Star–Neutron Star Parameters and Binary-driven Hypernova Types

We recalled in Section 1 that the various possible fates of the binary imply the three types of sources, BdHNe I, II, and III. In particular, the main parameters of the classification are the GRB energy and the orbital period of the CO–NS progenitor. These two parameters are naturally connected in the BdHN model (L. Becerra et al. 2016; R. Ruffini et al. 2016; L. Becerra et al. 2019), as follows.

The minimum energy release of a BdHN is the energy released by the NS companion accretion process when increasing its mass from $M_{\rm NS,0}$ to $M_{\rm NS,f}$, i.e., $\Delta E_{\rm acc} \approx \eta_{\rm acc} \Delta M_{\rm acc} c^2$, where $\Delta M_{\rm acc} = M_{\rm NS,f} - M_{\rm NS,0}$, and $\eta_{\rm acc}$ is the efficiency in converting gravitational into electromagnetic energy. Because the BH forms when the NS reaches the critical mass for gravitational collapse, $M_{\rm crit}$, the energy released to the BH formation trigger point, assuming typical order-of-magnitude values $\Delta M_{\rm acc} = M_{\rm crit} - M_{\rm NS,0} \sim 0.1\ M_\odot$ and $\eta_{\rm acc} \sim 0.1$, one obtains $\Delta E_{\rm acc} \sim 10^{52}$ erg. This estimate shows the reason BdHNe I are expected to explain the most energetic GRBs with $E_{\rm iso} \gtrsim 10^{52}$ erg. The connection with the CO–NS progenitor orbital period follows from the relation between the latter and the accreted mass. L. Becerra et al. (2019) showed that for a given SN explosion energy, the amount of accreted matter approximately scales as $\Delta M_{\rm acc} \propto M_{\rm NS,0}^2 / P_{\rm orb}^{1/3}$. This expression implies there is a maximum orbital period, $P_{\rm orb,max} \propto M_{\rm NS,0}^6 / (M_{\rm crit} - M_{\rm NS,0})^3$, over which no BH is formed by the accretion process. It turns out that $P_{\rm orb,max}$ is of the order of a few minutes for typical CO–NS parameters. The above suggests that the shorter the orbital period, the shorter the time the NS takes to reach the collapse point. The peak time of accretion scales as $t_{\rm peak} \propto P_{\rm orb}^{2/3}$ (L. Becerra et al. 2019). Besides, there is a strong dependence on the initial NS angular momentum, as shown in this article (e.g., Figures 5 and 6). Examples of BdHNe I are GRB 130427A (R. Ruffini et al. 2019), GRB 180720B (J. A. Rueda et al. 2022), and GRB 190114C (R. Moradi et al. 2021a, 2021b). BdHNe I show seven observable emission episodes in the sequence of physical processes triggered by the SN explosion in the CO–NS: GRB precursors, MeV prompt emission, GeV and TeV emissions, X-ray–optical–radio afterglow, and optical SN emission. These emissions involve the physics of the early SN, NS accretion, BH formation, synchrocurvature radiation, and quantum and classic electrodynamics processes. We refer to Y. Aimuratov et al. (2023) and the appendix in C. L. Bianco et al. (2024) for details.

Therefore, binaries with $P_{\rm orb} > P_{\rm orb,max}$ do not form a BH. These binaries lead to the subclasses BdHNe II and III. The divide between these two subclasses is given by the fact that as the period and orbital separation increase, the role of the NS companion diminishes, becoming negligible for binaries with periods of hours. Thus, BdHNe III are expected to release an energy similar to that of a single core-collapse event without any companion. Accretion is expected only from fallback onto the νNS, which has a maximum peak accretion rate of $10^{-3}\ M_\odot$ $\rm s^{-1}$ for about seconds (e.g., Figure 2), so $\Delta M_{\rm acc} \sim 10^{-3}\ M_\odot$, leading to $\Delta E_{\rm acc} \sim 10^{50}$ erg. We refer to Y. Wang et al. (2023) for a detailed analysis of GRB 171205A as an example of a BdHN III.

The sources with energies in the range 10^{50}–10^{52} erg are explained by BdHNe II, with orbital periods from tens of minutes to hours. We refer to Y. Wang et al. (2022) for an analysis of GRB 190829A as a BdHN II. At this stage, it is worth recalling that Section 5.3 has shown that the NS companion, in some cases, could lie at the supramassive metastable region at the end of the accretion phase. For those systems, delayed BH formation is expected to occur under the action of braking mechanisms, e.g., by a magnetic field. A natural question arises as to whether these systems should be classified as a BdHN I or II. Figure 8 shows that the delay time of BH formation could be a few 10^6 s (10 days or longer for magnetic fields lower than 10^{13} G) after the SN breakout. Whether the BH formation implies BdHN I signatures in a binary that would lead to a BdHN II depends on the emission processes related to the BH and the differences in the system properties relative to a BdHN I. In this sense, the delay time could be crucial (e.g., the density surrounding the system decreases with time). It might be that these are borderline sources with energies of the order of 10^{52} erg and show hybrid properties between BdHNe I and II. However, this situation is new for us and needs further analysis and simulations to arrive at a definite answer.

6.2. The Long–Short Gamma-Ray Burst Connection

The above classification implies a unique prediction of this scenario: BdHNe I lead to NS–BH systems and BdHN II to NS–NS systems if the binary holds bound in the cataclysmic event. The BdHN III most likely unbinds the progenitor binary. Gravitational-wave emission drives the bound compact-object binaries to merge, leading to short GRBs (C. L. Fryer et al. 2015; L. Becerra et al. 2019; L. M. Becerra et al. 2022, 2023; C. L. Bianco et al. 2024). The above long–short GRB connection is a unique prediction of the BdHN scenario with verifiable observational consequences (L. M. Becerra et al. 2024).

If the system remains bound, the typical outcome of a BdHN I is an NS–BH, and of a BdHN II, an NS–NS. Gravitational-wave emission leads the NS–BH and NS–NS to merge, with the likely consequent emission of a short GRB (C. L. Fryer et al. 2015; L. M. Becerra et al. 2023; C. L. Bianco et al. 2024). Recent numerical simulations of the BdHN scenario for various binary parameters show a wide range of merger timescales $\sim 10^4$–10^9 yr (L. M. Becerra et al. 2024). The rapidly merging (e.g., tens of kiloyears timescale) binaries are those of short orbital periods (e.g., of a few minutes), so they are NS–BH. The wider binaries are NS–NS and lead to longer merger times. The fact that the mass loss in BdHNe should unbind a considerable amount of binaries (see L. M. Becerra et al. 2024, for the latest simulations) and the broad range of merger times is essential to explain the lower observed rate of short GRBs relative to that of long GRBs (see, e.g., R. Ruffini et al. 2016, 2018) and their shifted redshift distributions (see, e.g., M. H. P. M. van Putten et al. 2014; C. L. Bianco et al. 2024). Figure 9 shows a scheme of the above scenarios predicted by the BdHN model.

Section 5.3 has shown the possibility of forming BH–BH systems in some BdHNe II if the νNS and the NS do not collapse by accretion but reach a final mass larger than the maximum mass allowed for the nonrotating configuration, i.e.,

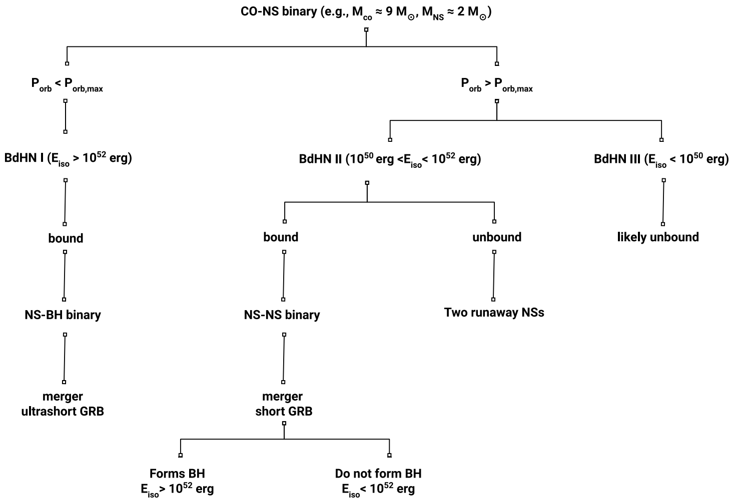

Figure 9. Scheme of the BdHN I, II, and III scenarios, depending upon the pre-SN CO–NS orbital period. We recall that $P_{\rm orb,max}$ is the maximum orbital period for the NS companion to reach an instability point of BH formation, given CO and NS masses and SN kinetic energy.

if they end the accretion process in the NS supramassive region. This happens for soft EOS as the EOS with the eL3$\omega\rho$ parameterization with matter formed by a mix of nucleons and hyperons. These stars may reach secular instability by losing angular momentum by magnetic torque if the magnetic field is not buried by accretion. We showed they could form a BH–BH or a BH–NS (if only one of them is supramassive) in a timescale shorter than the merger timescale by gravitational-wave emission. Following the BH formation, in a timescale of tens of kiloyears, gravitational-wave emission leads the BH–BH or BH–NS system to merge.

7. Conclusions

In this paper, we have followed the evolution of the νNS and its NS companion during their accretion of SN ejecta in a BdHN event leading to a long GRB. We have aimed to determine the conditions under which these stars evolve into unstable configurations, reaching either the secular instability or the mass-shedding limit, collapsing into a rotating, Kerr BH. We assume the stars evolve through stable configurations as they accrete baryonic mass and angular momentum from the SN ejecta. The accretion rate onto the NSs is obtained from 3D SPH simulations using the adapted SNSPH code of the Los Alamos National Laboratory (C. L. Fryer et al. 2006b). To perform the evolution of the NS structure, we adapted the RNS code (N. Stergioulas & J. L. Friedman 1995) to compute uniformly rotating NS configurations and used different parameterizations for the EOS, eL3$\omega\rho$, and NL3$\omega\rho$ both for cold and hot matter, respectively, with varying compositions including nucleons only and hyperons mixed with nucleons.

Our findings indicate that for low-mass progenitors of the CO star, the mass accretion rate onto the binary stars is insufficient to push them toward an unstable point. This holds, for instance, in the case of the CO progenitor with $M_{\rm ZAMS} = 15\ M_\odot$. On the other hand, for the progenitors of the CO star with $M_{\rm ZAMS} = 30\ M_\odot$, the configurations reach the mass-shedding limit under the same conditions regardless of the assumed EOS. This happens for configurations with $j_{\rm NS,0} > 1.0$ and efficient angular momentum accretion. The secular instability limit is reached when the EOS with the eL3$\omega\rho$ parameterization is used for matter with a mix of nucleons and hyperons and configuration with $j_{\rm NS,0} < 1.0$. This is the softer EOS we have considered in our study.

The time required to collapse can be as short as 10 s for rapidly rotating initial stars reaching the mass-shedding limit or as short as 50 s for slowly rotating initial stars reaching the secular instability limit and modeled by a soft EOS. As expected, this time increases with the binary period of the CO–NS system. There is the possibility of the appearance of the νNS at times of the order of 100 s, e.g., owing to the second accretion peak (see, e.g., the simulation with an orbital period of about 10 minutes in the left panel of Figure 2 and the discussion in L. M. Becerra et al. 2022), and BH formation at comparable times (see left panel of Figure 5) could have been individuated in three sources: GRB 221009A, GRB 221001A, and GRB 160625B (R. Ruffini et al. 2024, in preparation).

Summarizing, we confirm results from previous simulations (L. Becerra et al. 2019; L. M. Becerra et al. 2022) that short-period CO–NS binaries can lead to BH formation in an orbital timescale. In this work, we showed the effect of the NS angular momentum: the time to reach the conditions for gravitational collapse shortens if the NS has nonzero angular momentum before the accretion process. It can become as short as tens of seconds for a rapidly rotating NS before the SN explosion triggers the GRB event. This present approach is based on the simplest BdHN model based on core collapse in a CO star of mass of about 10 $M_\odot$, forming the νNS and the SN, in the presence of an NS companion. However, the quality of data from the early phases of BdHNe, particularly identifying the SN rise (R. Ruffini et al. 2024), opens the possibility to explore alternative scenarios for the νNS and the SN formation (R. Ruffini et al. 2024, in preparation).

All the above results provide an additional step toward a comprehensive understanding of binary stellar evolution, starting from binaries of main-sequence massive stars to intermediate stages like binary X-ray sources, whose further evolution leads to the most powerful transients in the Universe, long GRBs, and finally to compact-star binaries merging producing short GRBs.

Acknowledgments

D.P.M. is partially supported by project INCT-FNA Proc. No. 464898/2014-5 and Conselho Nacional de Desenvolvimento Científico e Tecnológico (CNPq/Brazil) under grant 303490/2021-7. C.P. acknowledges support from FCT (Fundação para a Ciência e a Tecnologia, I.P, Portugal) under Projects UIDP/04564/2020, UIDB/04564/2020, and 2022.06460.PTDC.

ORCID iDs

F. Cipolletta https://orcid.org/0000-0001-7894-1028
C. L. Fryer https://orcid.org/0000-0003-2624-0056
Débora P. Menezes https://orcid.org/0000-0003-0730-6689
Constança Providência https://orcid.org/0000-0001-6464-8023
J. A. Rueda https://orcid.org/0000-0003-4904-0014
R. Ruffini https://orcid.org/0000-0003-0829-8318

References

Abbott, B. P., Abbott, R., Abbott, T. D., Acernese, F., et al. 2017, PhRvL, 119, 161101
Abbott, R., Abbott, T. D., Abraham, S., et al. 2020, ApJL, 896, L44
Aimuratov, Y., Becerra, L. M., Bianco, C. L., et al. 2023, ApJ, 955, 93
Antoniadis, J., Freire, P. C. C., Wex, N., et al. 2013, Sci, 340, 448
Ashall, C., Mazzali, P. A., Pian, E., et al. 2019, MNRAS, 487, 5824
Avancini, S. S., Menezes, D. P., Alloy, M. D., et al. 2008, PhRvC, 78, 015802
Barthelmy, S. D., Barbier, L. M., Cummings, J. R., et al. 2005, SSRv, 120, 143
Baym, G., Pethick, C., & Sutherland, P. 1971, ApJ, 170, 299
Becerra, L., Bianco, C. L., Fryer, C. L., Rueda, J. A., & Ruffini, R. 2016, ApJ, 833, 107
Becerra, L., Cipolletta, F., Fryer, C. L., Rueda, J. A., & Ruffini, R. 2015, ApJ, 812, 100
Becerra, L., Ellinger, C. L., Fryer, C. L., Rueda, J. A., & Ruffini, R. 2019, ApJ, 871, 14
Becerra, L., Guzzo, M. M., Rossi-Torres, F., et al. 2018, ApJ, 852, 120
Becerra, L. M., Fryer, C., Rodriguez, J. F., Rueda, J. A., & Ruffini, R. 2023, Univ, 9, 332
Becerra, L. M., Fryer, C. L., Rueda, J. A., & Ruffini, R. 2024, arXiv:2401.15702
Becerra, L. M., Moradi, R., Rueda, J. A., Ruffini, R., & Wang, Y. 2022, PhRvD, 106, 083002
Beniamini, P., Giannios, D., & Metzger, B. D. 2017, MNRAS, 472, 3058
Beznogov, M. V., & Raduta, A. R. 2023, PhRvC, 107, 045803
Bianco, C. L., Mirtorabi, M. T., Moradi, R., et al. 2024, ApJ, 966, 219
Biesdorf, C., Menezes, D. P., & Lopes, L. L. 2023, BrJPh, 53, 137
Boguta, J., & Bodmer, A. R. 1977, NuPhA, 292, 413
Bucciantini, N., Quataert, E., Arons, J., Metzger, B. D., & Thompson, T. A. 2007, MNRAS, 380, 1541
Bufano, F., Pian, E., Sollerman, J., et al. 2012, ApJ, 753, 67
Burrows, D. N., Hill, J. E., Nousek, J. A., et al. 2005, SSRv, 120, 165
Cano, Z., Wang, S.-Q., Dai, Z.-G., & Wu, X.-F. 2017, AdAst, 2017, 8929054
Cavallo, G., & Rees, M. J. 1978, MNRAS, 183, 359
Chen, H.-P., Rau, S.-J., & Pan, K.-C. 2023, ApJ, 949, 121
Chen, P., Gal-Yam, A., Sollerman, J., et al. 2024, Natur, 625, 253
Cipolletta, F., Cherubini, C., Filippi, S., Rueda, J. A., & Ruffini, R. 2015, PhRvD, 92, 023007
Costa, E., Frontera, F., Heise, J., et al. 1997, Natur, 387, 783
Cromartie, H. T., Fonseca, E., Ransom, S. M., et al. 2020, NatAs, 4, 72
Dainotti, M. G., De Simone, B., Islam, K. M., et al. 2022, ApJ, 938, 41
Dall'Osso, S., Stratta, G., Perna, R., De Cesare, G., & Stella, L. 2023, ApJL, 949, L32
Della Valle, M. 2011, IJMPD, 20, 1745
Demorest, P. B., Pennucci, T., Ransom, S. M., Roberts, M. S. E., & Hessels, J. W. T. 2010, Natur, 467, 1081
Dezalay, J.-P., Barat, C., Talon, R., et al. 1992, AIP Conf. Ser. 265, American Institute of Physics Conference Series, ed. W. S. Paciesas & G. J. Fishman, (Melville, NY: AIP), 304
Diego, J. M., Sun, B., Yan, H., et al. 2023, A&A, 679, A31
Doroshenko, V., Suleimanov, V., Pühlhofer, G., & Santangelo, A. 2022, NatAs, 6, 1444
Dutra, M., Lourenço, O., Avancini, S. S., et al. 2014, PhRvC, 90, 055203
Dutra, M., Lourenço, O., & Menezes, D. P. 2016a, PhRvC, 94, 049901
Dutra, M., Lourenço, O., & Menezes, D. P. 2016b, PhRvC, 93, 025806
Eichler, D., Livio, M., Piran, T., & Schramm, D. N. 1989, Natur, 340, 126
Fattoyev, F. J., Horowitz, C. J., Piekarewicz, J., & Shen, G. 2010, PhRvC, 82, 055803
Fonseca, E., Cromartie, H. T., Pennucci, T. T., et al. 2021, ApJL, 915, L12
Fortin, M., Providência, C., Raduta, A. R., et al. 2016, PhRvC, 94, 035804
Fox, O. D., Van Dyk, S. D., Williams, B. F., et al. 2022, ApJL, 929, L15
Fruchter, A. S., Levan, A. J., Strolger, L., et al. 2006, Natur, 441, 463
Fryer, C. L. 1999, ApJ, 522, 413
Fryer, C. L. 2009, ApJ, 699, 409
Fryer, C. L., Andrews, S., Even, W., Heger, A., & Safi-Harb, S. 2018, ApJ, 856, 63
Fryer, C. L., Benz, W., & Herant, M. 1996, ApJ, 460, 801
Fryer, C. L., Herwig, F., Hungerford, A., & Timmes, F. X. 2006a, ApJL, 646, L131
Fryer, C. L., Mazzali, P. A., Prochaska, J., et al. 2007, PASP, 119, 1211
Fryer, C. L., Oliveira, F. G., Rueda, J. A., & Ruffini, R. 2015, PhRvL, 115, 231102
Fryer, C. L., Rockefeller, G., & Warren, M. S. 2006b, ApJ, 643, 292
Fryer, C. L., Rueda, J. A., & Ruffini, R. 2014, ApJL, 793, L36
Fryer, C. L., Woosley, S. E., & Hartmann, D. H. 1999, ApJ, 526, 152
Fuller, J., Cantiello, M., Lecoanet, D., & Quataert, E. 2015, ApJ, 810, 101
Fuller, J., & Lu, W. 2022, MNRAS, 511, 3951
Galama, T. J., Vreeswijk, P. M., van Paradijs, J., Kouveliotou, C., et al. 1998, Natur, 395, 670
Glendenning, N. K. 2012, Compact Stars: Nuclear Physics, Particle Physics, and General Relativity (New York, NY: Springer)
Goodman, J. 1986, ApJL, 308, L47
Grill, F., Providência, C., & Avancini, S. S. 2012, PhRvC, 85, 055808
Grindlay, J. E., Heinke, C. O., Edmonds, P. D., Murray, S. S., & Cool, A. M. 2001, ApJL, 563, L53
Guillot, S., Rutledge, R. E., & Brown, E. F. 2011, ApJ, 732, 88
Heger, A., Fryer, C. L., Woosley, S. E., Langer, N., & Hartmann, D. H. 2003, ApJ, 591, 288
Heinke, C. O., Cohn, H. N., Lugger, P. M., et al. 2014, MNRAS, 444, 443
Hessels, J. W. T., Ransom, S. M., Stairs, I. H., et al. 2006, Sci, 311, 1901
Hjorth, J., & Bloom, J. S. 2012, in Cambridge Astrophysics Series, Vol. 51, The Gamma-Ray Burst—Supernova Connection, ed. C. Kouveliotou, R. A. M. J. Wijers, & S. Woosley (Cambridge: Cambridge Univ. Press), 169
Horowitz, C. J., & Piekarewicz, J. 2001, PhRvL, 86, 5647
Huang, C., Raaijmakers, G., Watts, A. L., Tolos, L., & Providencia, C. 2024, MNRAS, 529, 4650
Iwamoto, K., Nomoto, K., Höflich, P., et al. 1994, ApJL, 437, L115
Izzo, L., Rueda, J. A., & Ruffini, R. 2012, A&A, 548, L5
Kelly, P. L., Kirshner, R. P., & Pahre, M. 2008, ApJ, 687, 1201
Kim, H.-J., Yoon, S.-C., & Koo, B.-C. 2015, ApJ, 809, 131
Klebesadel, R. W. 1992, in The Durations of Gamma-ray Bursts, ed. C. Ho, R. I. Epstein, & E. E. Fenimore (Cambridge: Cambridge Univ. Press), 161
Kobulnicky, H. A., & Fryer, C. L. 2007, ApJ, 670, 747
Kohri, K., Narayan, R., & Piran, T. 2005, ApJ, 629, 341
Kouveliotou, C., Meegan, C. A., Fishman, G. J., et al. 1993, ApJL, 413, L101
Lindner, C. C., Milosavljević, M., Shen, R., & Kumar, P. 2012, ApJ, 750, 163
Lopes, L. L. 2022, CoTPh, 74, 015302
Lopes, L. L., Biesdorf, C., & Menezes, D. P. 2022, MNRAS, 512, 5110
Lopes, L. L., & Menezes, D. P. 2022, ApJ, 936, 41
Lourenço, O., Dutra, M., Lenzi, C. H., Flores, C. V., & Menezes, D. P. 2019, PhRvC, 99, 045202
MacFadyen, A. I., & Woosley, S. E. 1999, ApJ, 524, 262
Maeda, K., Nomoto, K., Mazzali, P. A., & Deng, J. 2006, ApJ, 640, 854
Maggiore, M. 2007, Gravitational Waves. Vol. 1: Theory and Experiments (Oxford: Oxford Univ. Press)
Malik, T., Ferreira, M., Agrawal, B. K., & Providência, C. 2022, ApJ, 930, 17
Malik, T., Ferreira, M., Albino, M. B., & Providência, C. 2023, PhRvD, 107, 103018
Malik, T., & Providência, C. 2022, PhRvD, 106, 063024
Mao, S., & Yi, I. 1994, ApJL, 424, L131
Mazets, E. P., Golenetskii, S. V., Ilinskii, V. N., et al. 1981, Ap&SS, 80, 3
Mazzali, P. A., Deng, J., Pian, E., et al. 2006, ApJ, 645, 1323
Mazzali, P. A., Deng, J., Tominaga, N., et al. 2003, ApJL, 599, L95
Mészáros, P. 2002, ARA&A, 40, 137
Meszaros, P., Laguna, P., & Rees, M. J. 1993, ApJ, 415, 181
Metzger, B. D., Beniamini, P., & Giannios, D. 2018, ApJ, 857, 95
Metzger, B. D., Giannios, D., Thompson, T. A., Bucciantini, N., & Quataert, E. 2011, MNRAS, 413, 2031

Metzger, B. D., Thompson, T. A., & Quataert, E. 2007, ApJ, 659, 561
Metzger, M. R., Djorgovski, S. G., Kulkarni, S. R., et al. 1997, Natur, 387, 878
Miller, M. C., Lamb, F. K., Dittmann, A. J., et al. 2019, ApJL, 887, L24
Miller, M. C., Lamb, F. K., Dittmann, A. J., et al. 2021, ApJL, 918, L28
Milosavljević, M., Lindner, C. C., Shen, R., & Kumar, P. 2012, ApJ, 744, 103
Moore, T., Smartt, S. J., Nicholl, M., Srivastav, S., et al. 2023, ApJL, 956, L31
Moradi, R., Rueda, J. A., Ruffini, R., & Wang, Y. 2021a, A&A, 649, A75
Moradi, R., Rueda, J. A., Ruffini, R., et al. 2021b, PhRvD, 104, 063043
Narayan, R., Paczynski, B., & Piran, T. 1992, ApJL, 395, L83
Narayan, R., Piran, T., & Shemi, A. 1991, ApJL, 379, L17
Neugent, K. F., Levesque, E. M., Massey, P., Morrell, N. I., & Drout, M. R. 2020, ApJ, 900, 118
Nomoto, K., & Hashimoto, M. 1988, PhR, 163, 13
Nomoto, K., Maeda, K., Nakamura, T., et al. 2003, in Origin of Matter and Evolution of Galaxies, ed. T. Kajino et al. (Singapore: World Scientific), 223
Ogata, M., Hirai, R., & Hijikawa, K. 2021, MNRAS, 505, 2485
Özel, F., & Freire, P. 2016, ARA&A, 54, 401
Paczynski, B. 1986, ApJL, 308, L43
Pais, H., & Providência, C. 2016, PhRvC, 94, 015808
Park, H.-J., Kim, S.-J., Kim, S., & van Putten, M. H. P. M. 2022, ApJ, 938, 69
Payne, D. J. B., & Melatos, A. 2007, MNRAS, 376, 609
Pétri, J. 2015, MNRAS, 450, 714
Piran, T. 2004, RvMP, 76, 1143
Piran, T., Shemi, A., & Narayan, R. 1993, MNRAS, 263, 861
Prakash, M., Bombaci, I., Prakash, M., et al. 1997, PhR, 280, 1
Price, D. J. 2011, SPLASH: An Interactive Visualization Tool for Smoothed Particle Hydrodynamics Simulations, Astrophysics Source Code Library, ascl:1103.004
Pringle, J. E., & Rees, M. J. 1972, A&A, 21, 1
Raskin, C., Scannapieco, E., Rhoads, J., & Della Valle, M. 2008, ApJ, 689, 358
Rees, M. J., & Meszaros, P. 1992, MNRAS, 258, 41P
Riley, T. E., Watts, A. L., Bogdanov, S., et al. 2019, ApJL, 887, L21
Riley, T. E., Watts, A. L., Ray, P. S., et al. 2021, ApJL, 918, L27
Roming, P. W. A., Kennedy, T. E., Mason, K. O., et al. 2005, SSRv, 120, 95
Romani, R. W., Kandel, D., Filippenko, A. V., Brink, T. G., & Zheng, W. 2022, ApJL, 934, L17
Rueda, J. A., Li, L., Moradi, R., et al. 2022, ApJ, 939, 62
Rueda, J. A., & Ruffini, R. 2012, ApJL, 758, L7
Rueda, J. A., Ruffini, R., Wang, Y., et al. 2018, JCAP, 2018, 006
Ruffini, R., Bianco, C. L., Li, L., et al. 2024, arXiv:2405.08231
Ruffini, R., Moradi, R., Rueda, J. A., et al. 2019, ApJ, 886, 82
Ruffini, R., Rodriguez, J., Muccino, M., et al. 2018, ApJ, 859, 30
Ruffini, R., Rueda, J. A., Muccino, M., et al. 2016, ApJ, 832, 136
Ruffini, R., & Wilson, J. 1973, PhRvL, 31, 1362
Sana, H., de Mink, S. E., de Koter, A., et al. 2012, Sci, 337, 444
Serot, B. D. 1992, RPPh, 55, 1855
Shemi, A., & Piran, T. 1990, ApJL, 365, L55
Shibata, M., Baumgarte, T. W., & Shapiro, S. L. 2000, PhRvD, 61, 044012
Smartt, S. J. 2009, ARA&A, 47, 63
Smartt, S. J. 2015, PASA, 32, e016
Smartt, S. J., Eldridge, J. J., Crockett, R. M., & Maund, J. R. 2009, MNRAS, 395, 1409
Smith, N., Li, W., Silverman, J. M., Ganeshalingam, M., & Filippenko, A. V. 2011, MNRAS, 415, 773
Song, C.-Y., & Liu, T. 2023, ApJ, 952, 156
Steiner, A. W., Heinke, C. O., Bogdanov, S., et al. 2018, MNRAS, 476, 421
Stergioulas, N., & Friedman, J. L. 1995, ApJ, 444, 306
Sugahara, Y., & Toki, H. 1994, NuPhA, 579, 557
Sun, X., Miao, Z., Sun, B., & Li, A. 2023, ApJ, 942, 55
Tanaka, M., Yamanaka, M., Maeda, K., et al. 2009, ApJ, 700, 1680
Tavani, M. 1998, ApJL, 497, L21
Thompson, T. A., Chang, P., & Quataert, E. 2004, ApJ, 611, 380
Traversi, S., Char, P., & Pagliara, G. 2020, ApJ, 897, 165
Usov, V. V. 1992, Natur, 357, 472
van Putten, M. H. P. M., Lee, G. M., Della Valle, M., Amati, L., & Levinson, A. 2014, MNRAS, 444, L58
Wang, Y., Becerra, L. M., Fryer, C. L., Rueda, J. A., & Ruffini, R. 2023, ApJ, 945, 95
Wang, Y., Rueda, J. A., Ruffini, R., et al. 2022, ApJ, 936, 190
Wheeler, J. C., Yi, I., Höflich, P., & Wang, L. 2000, ApJ, 537, 810
Woosley, S. E. 1993, ApJ, 405, 273
Woosley, S. E., & Bloom, J. S. 2006, ARA&A, 44, 507
Yoon, S.-C. 2015, PASA, 32, e015
Yoon, S.-C., Woosley, S. E., & Langer, N. 2010, ApJ, 725, 940
Zel'dovich, Y. B., Ivanova, L. N., & Nadezhin, D. K. 1972, SvA, 16, 209
Zhang, B. 2018, The Physics of Gamma-Ray Bursts (Cambridge: Cambridge Univ. Press)
Zhang, B.-B., Liu, Z.-K., Peng, Z.-K., et al. 2021, NatAs, 5, 911